Computational Materials Science 158 (2019) 420–478

Contents lists available at ScienceDirect

Computational Materials Science

journal homepage: www.elsevier.com/locate/commatsci

Editor's Choice

DAMASK – The Düsseldorf Advanced Material Simulation Kit for modeling multi-physics crystal plasticity, thermal, and damage phenomena from the single crystal up to the component scale

F. Roters[a,*], M. Diehl[a], P. Shanthraj[a,b], P. Eisenlohr[c], C. Reuber[a], S.L. Wong[a], T. Maiti[c], A. Ebrahimi[d], T. Hochrainer[e], H.-O. Fabritius[a], S. Nikolov[f], M. Friák[a,g,h], N. Fujita[i], N. Grilli[j], K.G.F. Janssens[j], N. Jia[k], P.J.J. Kok[l], D. Ma[m], F. Meier[n], E. Werner[n], M. Stricker[o], D. Weygand[o], D. Raabe[a]

[a] Max-Planck-Institut für Eisenforschung GmbH, Max-Planck-Straße 1, 40237 Düsseldorf, Germany
[b] School of Materials, University of Manchester, Oxford Road, Manchester M13 9PL, UK
[c] Chemical Engineering and Materials Science, Michigan State University, East Lansing, MI 48824, USA
[d] Bremer Institut für Strukturmechanik und Produktionstechnik, Universität Bremen, Am Biologischen Garten 2, 28359 Bremen, Germany
[e] Institut für Festigkeitslehre, Technische Universität Graz, Kopernikusgasse 24, 8010 Graz, Austria
[f] Institute of Mechanics, Bulgarian Academy of Sciences, Acad. G. Bontchev St., bl. 4, 1113 Sofia, Bulgaria
[g] Institute of Physics of Materials, Academy of Sciences of the Czech Republic, v.v.i., Žižkova 22, 61662 Brno, Czech Republic
[h] Faculty of Science, Masaryk University, Kotlářská 2, 61137 Brno, Czech Republic
[i] Steel Research Laboratory, JFE Steel Corporation, 1 Mizushima Kawasaki-dori, Kurashiki-shi, Okayama 712-8511, Japan
[j] Laboratory for Nuclear Materials, Nuclear Energy and Safety Department, Paul Scherrer Institut, 5232 Villigen PSI, Switzerland
[k] Key Laboratory for Anisotropy and Texture of Materials (Ministry of Education), School of Material Science and Engineering, Northeastern University, Shenyang 110819, China
[l] Research & Development, Tata Steel Europe, PO Box 10 000, (3G37)1970 CA IJmuiden, The Netherlands
[m] Leichtmetallkompetenzzentrum Ranshofen GmbH, AIT Austrian Institute of Technology, Lamprechtshausenerstraße 61, 5282 Ranshofen-Braunau, Austria
[n] Institute of Materials Science and Mechanics of Materials, Technische Universität München, Boltzmannstraße 15, 85748 Garching b. München, Germany
[o] Institute for Applied Materials IAM, Karlsruhe Institute of Technology, Kaiserstraße 12, 76131 Karlsruhe, Germany

ARTICLE INFO

Keywords:
Crystal plasticity
Simulation
Open source software
Multi-physics

ABSTRACT

Crystal Plasticity (CP) modeling is a powerful and well established computational materials science tool to investigate mechanical structure–property relations in crystalline materials. It has been successfully applied to study diverse micromechanical phenomena ranging from strain hardening in single crystals to texture evolution in polycrystalline aggregates. However, when considering the increasingly complex microstructural composition of modern alloys and their exposure to—often harsh—environmental conditions, the focus in materials modeling has shifted towards incorporating more constitutive and internal variable details of the process history and environmental factors into these structure–property relations. Technologically important fields of application of enhanced CP models include phase transformations, hydrogen embrittlement, irradiation damage, fracture, and recrystallization. A number of niche tools, containing multi-physics extensions of the CP method, have been developed to address such topics. Such implementations, while being very useful from a scientific standpoint, are, however, designed for specific applications and substantial efforts are required to extend them into flexible multi-purpose tools for a general end-user community. With the Düsseldorf Advanced Material Simulation Kit (DAMASK) we, therefore, undertake the effort to provide an open, flexible, and easy to use implementation to the scientific community that is highly modular and allows the use and straightforward implementation of different types of constitutive laws and numerical solvers. The internal modular structure of DAMASK follows directly from the hierarchy inherent to the employed continuum description. The highest level handles the partitioning of the prescribed field values on a material point between its underlying microstructural constituents and the subsequent homogenization of the constitutive response of each constituent. The response of each microstructural constituent is determined, at the intermediate level, from the time integration of the underlying constitutive laws for elasticity, plasticity, damage, phase transformation, and heat generation among other coupled multi-physical processes of interest. Various constitutive laws based on evolving internal state variables can be implemented to provide this response at the lowest level. DAMASK already contains various CP-

* Corresponding author.
E-mail address: f.roters@mpie.de (F. Roters).

https://doi.org/10.1016/j.commatsci.2018.04.030
Received 24 January 2018; Received in revised form 12 April 2018; Accepted 13 April 2018
Available online 01 December 2018

based models to describe metal plasticity as well as constitutive models to incorporate additional effects such as heat production and transfer, damage evolution, and athermal transformations. Furthermore, the implementation of additional constitutive laws and homogenization schemes, as well as the integration of a wide class of suitable boundary and initial value problem solvers, is inherently considered in its modular design.

1. Introduction

Predicting, understanding, and controlling the mechanical behavior is critical when designing structural materials and using them during service. In modern alloy systems—where multiple deformation mechanisms, phases, and defects are introduced—the engineering of mechanical properties such as strength and ductility can quickly turn into a combinatorial challenge, rendering traditional, experimental-based alloy development workflows inappropriate. It is thus becoming increasingly important to complement the resource consuming step of material processing and testing with modeling and simulation to address this challenge [1–3]. In particular, continuum modeling approaches are a natural choice for this task since they are capable of predicting the mechanical behavior in dependence of alloy composition, microstructure, crystallographic texture and phase fractions at relevant engineering time and length scales [4]. Also, validation and calibration of continuum simulation results can be readily achieved by direct comparison to corresponding experimental data [5–15].

In the case of crystalline matter, the Crystal Plasticity (CP) method (see [4,16] and references therein), which is based on the behavior of a single crystal, has been successfully applied in predicting the mechanical response of polycrystals up to the industrially relevant component scale. CP models account for the tensorial nature of inelastic deformation modes such as dislocation glide, displacive transformation, or mechanical twinning in individual grains.

A constitutive description of the defect evolution and the associated interaction laws describing strain hardening are assigned to individual deformation systems either in the form of phenomenological or physics-based viscoplastic laws. These microscopically derived deformation mechanisms are then composed into an inelastic velocity gradient, which is embedded in a finite-strain continuum framework to enable the calculation of local shape changes and lattice rotations of a single crystal. Furthermore, by accounting for intergranular interactions, effective properties of polycrystalline aggregates can be derived.

Physics-based constitutive models reflect the kinetics of the various types of lattice defect populations in a mechanism-oriented fashion including phenomena such as thermally activated slip, build-up of geometrically necessary dislocations, the role of the stacking fault energy and the non-linear interaction among dislocations, grain boundaries, twins, and displacive transformations. A critical issue here is the extent to which microstructural detail needs to be incorporated in the parameterization of a constitutive law. In the classical works of Mecking and Kocks [17] it was observed that strain hardening properties of polycrystalline single phase materials can be expressed—in a rather coarse approximation—in terms of a global dislocation density alone. However, predicting more complex phenomena such as transitions in the strain hardening behavior, caused either by dislocation structure evolution or the activation of other deformation carriers such as mechanical twins at higher loads, can require a much richer description of the microstructure. An example where the interplay of compositional changes with various interacting deformation mechanisms has been studied in detail is the dependence of dislocation (cross-) slip, mechanical twinning, and the formation of ε- and α'-martensite on the Stacking Fault Energy (SFE) in face-centered cubic (fcc) Iron (Fe)-Manganese (Mn) [18,19]. Such development of chemical composition-sensitive constitutive models is of high relevance since practically all engineering materials are multicomponent systems. It becomes even more important when considering also chemical reactions between a mechanically loaded material and its environment such as encountered in the fields of stress corrosion cracking or hydrogen embrittlement [20,21].

Another important aspect of constitutive modeling lies in the consideration of grain softening phenomena, such as dislocation and cell recovery, primary static recrystallization, discontinuous or continuous subgrain coarsening, grain growth, dynamic recrystallization, post-dynamic recrystallization, or metadynamic recrystallization to name but a few essential effects that can reduce the critical shear stress and alter the crystallographic texture [22,23].

To complete the description of a constitutive model, the required constitutive parameters for the relevant physical quantities of a given material can be identified either from experiments [24] or from simulations at smaller length and time scales [25,26].

The behavior of a single crystal, described by a constitutive model, forms the basis for modeling the co-deformation of multiple constituents in a polycrystalline aggregate. The interaction between different grains can be modeled either in full-field simulations, where each grain is spatially resolved by a large number of material points, or in a homogenized way, where one material point aggregates the behavior of multiple grains. Full-field simulations provide spatial distribution of field values, including their extrema, in real or synthetic microstructures. While real microstructures are especially attractive to benchmark the constitutive description against experimental results, synthetic microstructures and their systematic permutations are of special importance for microstructure optimization. Moreover, if the probed Volume Element (VE) is large enough, it can serve as a Representative Volume Element (RVE) to derive effective quantities [1,27,28]. For large-scale forming simulations, determination of the local material response by such full-field simulations is often computationally prohibitive and requires subsequent model order reduction [29–31]. Alternatively, when applying CP to macroscopic loading situations, *e.g.* in the field of sheet forming operations, homogenization schemes based on coarse-graining from the single crystal up to the macroscopic scale can be used.

In a continuum setting, the constitutive stress response to the applied loading is required to be in mechanical equilibrium. Hence, to predict the overall mechanical response of the region of interest, the governing boundary value problem for mechanical equilibrium needs to be solved. A large number of numerical methods that utilize different discretizations of the geometry are available for this purpose. However, in the field of CP, only the Finite Element Method (FEM) and spectral methods based on Fast Fourier Transforms (FFTs) are commonly used. While FEM approaches offer the flexibility for simulating problems that are characterized by complex boundary conditions on arbitrarily shaped geometries, spectral methods are more efficient for dealing with VEs subjected to periodic boundary conditions. Hence, the former types of solvers are typically employed for component-scale simulations and the latter—working on a regular grid of material points—can be used for micromechanical investigations, often in direct conjunction with microscopic imaging techniques such as Electron Backscatter Diffraction (EBSD) [32–34] or Differential-Aperture X-ray Microscopy (DAXM) [35–37].

The features outlined above reflect the status of conventional CP models that are routinely used for polycrystal micromechanics, forming simulations, crystallographic texture predictions, and computational homogenization. Present efforts in developing constitutive models aim at further enhancing the predictive capabilities beyond classical CP to treat effects associated with heat transfer, chemical composition changes, phase transformation, and the evolution of microstructure and

damage under given service conditions including harsh environmental exposure. A strongly coupled approach is required to consistently treat the interactions among the constitutive (sub-) models describing these individual effects. Constitutive models for temperature evolution need to account for heat generation and transport. In a thermo-mechanically coupled setting, the heat generation resulting from plastic deformation in turn eases thermally activated dislocation motion and causes lattice expansion. Therefore, to enable full coupling, the underlying constitutive laws for elastic and plastic deformation should be rendered temperature dependent. The chemical composition in multicomponent alloy systems determines to a large extent the deformation mechanics. As an example, in the Fe-Mn steels mentioned above, the specific Carbon (C)- and Mn-content influences phase stability and activation of deformation twins and ε-martensite via the SFE. A chemo-mechanically coupled simulation taking local solubility and diffusion into account is hence desirable for the design of such alloy systems. The nucleation and propagation of microcracks, driven by stress and strain, redistributes these fields drastically, thus affecting subsequent micromechanical deformation pathways [38–41]. Finally, hydrogen embrittlement phenomena in concert with their associated effects such as hydrogen enhanced local plasticity (HELP), hydrogen stabilized vacancy and nanopore formation, or hydrogen-related interfacial decohesion and stress corrosion cracking are prominent examples where the interplay of all above mentioned effects is essential for arriving at a microstructure based understanding of material failure.

At the continuum level, additional solvers for the individual field problems are required. While various approaches are available, the strong multi-field coupling poses severe numerical challenges [42,43]. Therefore, tackling and solving the challenges associated with the inclusion of enhanced and strongly coupled constitutive models and related numerical solvers can serve as a great vehicle for profound progress in the field of Integrated Computational Materials Engineering (ICME) projects [2,3]. In the context of ICME, simulations are performed to efficiently identify relevant micromechanical mechanisms, enabling more rapid discovery and maturation of novel alloys, microstructures, forming methods, and thermo-chemo-mechanical processing routes.

The wide range of topics that can be tackled by such a modeling and simulation package capable of tackling complex ICME tasks requires to design it in a highly modular and flexible way to enable straightforward integration of additional metallurgical, chemistry related, or physics effects for expert users and developers. At the same time, as modeling becomes increasingly important for experimentalists to analyze and understand their observations or even design corresponding experimental set-ups, a suitable package should be designed in a user-friendly way for lowering the barrier to entry for non-expert users.

The present article reflects these different aspects regarding the current developmental status of the Düsseldorf Advanced Material Simulation Kit (DAMASK) in providing a comprehensive, flexible, modular, and easy-to-use multi-physics software tool for conducting advanced microstructure–property simulations to the scientific community as an open source freeware package. Other than previous overviews of the field of continuum modeling [4,16,44–47], this contribution places the focus on those kinematic and constitutive features available in DAMASK together with numerical and technical details of their implementation, which are complemented by illustrative application examples. It should, however, be mentioned that the DAMASK package is steadily extended and improved—hopefully also by contributors attracted by this work—so that this paper can only reflect the status at the time of writing. Yet, this article has been written and compiled in a way that the principal setup and the modularity of the DAMASK package are outlined so as to enable current and future users to understand its basic structure, apply it, and further help modifying and enhancing it.

This article is organized as follows: In Section 2 the overall concept and design of DAMASK is presented. Section 3 introduces the types of conservation laws that can be treated using DAMASK and the available corresponding solvers and their interfaces. In Sections 4 and 5 the upper and intermediate hierarchical levels of the DAMASK Material Point Model, namely the Partitioning and Homogenization and the Constituent Level, are discussed in detail. Section 6 presents all the models implemented at the Constitutive Level, forming the lowest rank of DAMASK. Application examples for these models are presented in Section 7 including case studies demonstrating the extensibility of DAMASK starting from Section 7.15. In Section 8 possible work flows including setup, running, and evaluation of DAMASK simulations are presented before Section 9 gives an outlook on current and future developments. In the Appendix, the scheme of notation and other technical information is compiled.

2. Concept

DAMASK has been designed to reproduce the multi-scale hierarchy and multi-physics structure inherent in the underlying material physics that is associated with thermo-mechanical loading of complex materials. Therefore, template functions are defined linking numerical solvers, homogenization schemes, and constitutive laws. For extended flexibility, multiple constitutive laws and homogenization schemes can be combined in the same model together with a specific set of solvers for the associated boundary and/or initial value problems. In this way a choice can be made between model accuracy and numerical effort to best address the problem at hand.

2.1. Background

The development of DAMASK started in 2006 with the establishment of a new research group named Computational Mechanics of Polycrystals (CMC^n) at the Max-Planck-Institut für Eisenforschung (MPIE). The aim of this joint research group between the Max-Planck-Gesellschaft and the Fraunhofer-Gesellschaft was the development of enhanced material models and simulation technologies from the single crystal up to the component scale [48]. In the course of the CMC^n project, it turned out that the Crystal Plasticity (CP) codes existing in the public domain at that time were not flexible enough for this purpose. Therefore, a new CP implementation was initiated, aiming at a strict modularization to allow for flexible incorporation of material models on all length scales. Within the CMC^n project, two different homogenization schemes and various constitutive models for plasticity have been incorporated into the new code. The capability to choose from a set of different available constitutive models within a single simulation is a unique feature of the developed simulation framework. Together with R.A. Lebensohn from the Los Alamos National Lab (LANL), Humboldt awardee at MPIE in 2010, a spectral method based mechanical boundary value problem solver was added to complement the existing user material interfaces to commercial Finite Element Method (FEM) solvers. In addition to the core routines, numerous utilities for pre- and post-processing have been added to the package now referred to as DAMASK.

In September 2011, a website (https://damask.mpie.de) was launched to release the code to the public domain as free software according to GPL 3. The idea of a flexible open source CP implementation was very well received by the scientific community. Presently, more[1] than 50 groups across the world use DAMASK, including universities such as University of California Los Angeles (UCLA), research facilities such as LANL, and multinational companies such as Tata Steel. These groups contribute to the further code development as well, *e.g.* by adding features such as new or modified constitutive models.

In 2015, multi-physics extensions were incorporated into DAMASK to consistently treat coupled problems, such as thermo-mechanics, chemo-mechanics, and damage-mechanics. Since early 2016, the code

[1] The exact number of users is unknown since downloads are not tracked.

is hosted in a public repository using GitLab (see Appendix A for details) to enable and assist collaborative development among the growing user community.

2.2. Hierarchical structure

DAMASK is designed to reproduce the multi-scale structure inherent to the underlying material physics of materials deformation, bridging the anisotropy introduced at the atomic scale to the global field description. A schematic representation of its hierarchical structure is shown in Fig. 1(a).

The global evolution of the field quantities is described by their respective conservation laws for static or dynamic equilibrium. Conservation of the field quantities (*e.g.* temperature, displacement) is build on the description of the corresponding fluxes (*e.g.* heat flux, stress) and sources (*e.g.* heat source, body forces) provided by constitutive descriptions. The conservation laws and associated numerical solution methods are outlined in Section 3.

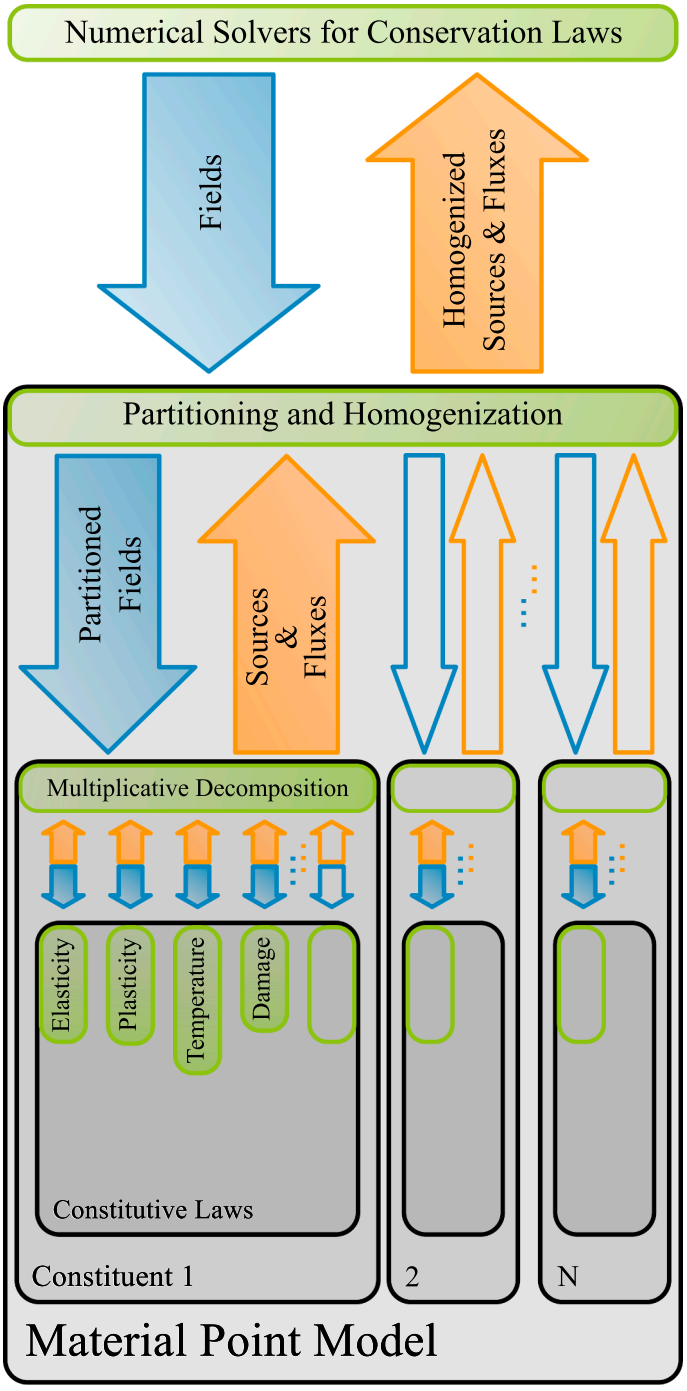

(a) Hierarchical structure at a material point.

- Numerical Solvers
  - Mechanical Equilibrium (elliptic/hyperbolic PDE)
    - Finite Element Method
      - Abaqus (implicit/explicit) & Msc.Marc
    - Spectral Method
  - Heat Conduction (parabolic PDE)
    - Finite Element Method
      - Abaqus (implicit) & Msc.Marc
    - Spectral Method
  - Phase Field Damage (parabolic PDE)
    - Spectral Method
- Partitioning and Homogenization
  - Mechanical Fields
    - Direct Scheme for Single Constituents
    - Isostrain
    - Relaxed Grain Cluster
  - Thermal Fields
  - Damage Fields
- Constitutive Laws
  - Elasticity
    - Generalized Hooke's law
  - Plasticity
    - Isotropic Plasticity
    - Phenomenological Crystal Plasticity
    - Dislocation Density Based Crystal Plasticity
    - Crystal Plasticity Including Dislocation Flux
    - Atomistically-Informed Crystal Plasticity for Tungsten
  - Temperature
    - Heat Flux
      - Fourier's law
    - Heat Generation
      - Plastic Dissipation
      - External Heat Source
    - Thermal Expansion
      - Linear Thermal Expansion
  - Damage
    - Phase Field Damage
      - Griffith's Criterion
    - Damage Driving Force
      - Brittle Damage
      - Ductile Damage

(b) Modular structure at the hierarchical levels.

Fig. 1. Concept of DAMASK. Each material point, which is part of a discretized body on which conservation laws are solved, is made up of multiple constituents that comprise of various constitutive laws.

A Material Point Model is a structured multi-scale description of the fluxes and sources required by the conservation laws. It has the following three-level hierarchy: The partitioning of the prescribed field values on a material point among its underlying microstructural constituents and the subsequent homogenization of the constitutive response of each constituent are handled at the highest level by a Partitioning and Homogenization scheme as outlined in Section 4. Section 5 details how, at the intermediate Constituent Level, the response of each microstructural constituent is determined from the time integration of the underlying constitutive laws for fluxes and sources. At the Constitutive Level (Section 6), constitutive laws based on evolving internal state variables are implemented in DAMASK to provide this response at this lowest level.

2.3. Modularization

In order to facilitate a flexible and extensible implementation, the code is organized in a modular structure. The Material Point Model is build from abstract modules for Partitioning and Homogenization and the Constitutive Level presented in the previous section. The purpose behind the introduction of these abstract modules is to facilitate branching into the different specific sub-modules available in DAMASK as sketched in Fig. 1(b). Each of these sub-modules needs to provide a standard set of functions with defined interfaces. For example, each mechanical homogenization sub-module has to partition the average deformation gradient to the individual constituents and homogenize their stress response. The abstract module on the Constituent Level (Fig. 1(a)) then derives additional field quantities from the primary fields and their gradients. For example, in the case of a "plain" elasto-plastic response, plastic and elastic deformation gradients are computed from the total deformation gradient. The elastic deformation gradient is used by an elasticity constitutive sub-module to calculate the stress. Finally, each constitutive sub-module for plasticity has to provide the plastic velocity gradient as a function of this stress, based on the current material state and possibly additional derived fields. Such an encapsulation of the Material Point Model provides the flexibility to interface it with different types of solvers for the conservation laws, such as FEM solvers or spectral solvers.

3. Conservation laws

The mechanical, thermal, structural, and chemical behavior of materials is of primary interest in microstructure physics. It is described by the concurrent evolution of multiple field quantities and is uniquely determined by a coupled system of governing Partial Differential Equations (PDEs) together with initial and/or boundary conditions. The solution of this system describes the conservation of physical quantities such as linear momentum, mass, or energy. Mathematically, these conservation laws can be categorized as elliptic (*e.g.* static mechanical equilibrium), hyperbolic (*e.g.* dynamic mechanical equilibrium), or parabolic (*e.g.* heat conduction, phase field) PDEs. Currently implemented in DAMASK are conservation laws for mechanical equilibrium, heat conduction, and phase field damage. However, the modular structure of the code allows to readily add additional conservation laws of the same mathematical categories, *e.g.* electrical conduction for the case of elliptic PDEs.

3.1. Formulation

The large-strain formulation employed in DAMASK is based on the assumption of a continuum body $\mathcal{B}$ that occupies the region $\mathcal{B}_0$ in the reference configuration and $\mathcal{B}_t$ in the current configuration. The location of the material points in the reference state is given by $\mathbf{x} \in \mathcal{B}_0$ and in a deformed configuration by $\mathbf{y} \in \mathcal{B}_t$. A deformation map $\chi(\mathbf{x})$: $\mathbf{x} \in \mathcal{B}_0 \rightarrow \mathbf{y} \in \mathcal{B}_t$ maps points $\mathbf{x}$ in the reference configuration to points $\mathbf{y}$ in the current configuration.

A line segment $\mathrm{d}\mathbf{x}$ in an infinitesimal neighborhood of a material point $\mathbf{x}$ is pushed forward by:

$$\mathbf{y} + \mathrm{d}\mathbf{y} = \mathbf{y} + \frac{\partial \mathbf{y}}{\partial \mathbf{x}} \cdot \mathrm{d}\mathbf{x} + O(\mathrm{d}\mathbf{x}^2). \tag{1}$$

Neglecting terms of higher order, $\mathrm{d}\mathbf{y}$ can be expressed as:

$$\begin{aligned} \mathrm{d}\mathbf{y} &= \frac{\partial \mathbf{y}}{\partial \mathbf{x}} \cdot \mathrm{d}\mathbf{x} \\ &= \underbrace{\mathrm{Grad}\, \boldsymbol{\chi}}_{=:\mathbf{F}(\mathbf{x})} \cdot \mathrm{d}\mathbf{x} \end{aligned} \tag{2}$$

where $\mathbf{F}(\mathbf{x})$ is the deformation gradient. $\mathbf{F}(\mathbf{x})$ maps the infinitesimal line segment $\mathrm{d}\mathbf{x}$ in the reference configuration to $\mathrm{d}\mathbf{y}$ in the current configuration.

3.1.1. Mechanical equilibrium

Mechanical equilibrium conserves linear momentum during a continuous deformation process[2] and describes a state where zero net forces are acting on a material volume. Mathematically, this is described by the divergence of stress being balanced by the inertia forces everywhere in $\mathcal{B}$. The finite deformation stress measure used in DAMASK, *i.e.* the first Piola–Kirchhoff stress ($\mathbf{P}$) or Cauchy stress ($\boldsymbol{\sigma}$), depends on the configuration (for conversion between the configurations see Appendix C) in which the conservation law is solved, *i.e.* the PDE can assume different forms that are equivalent in an infinitesimal deformation formulation [49]:

$$\mathrm{Div}\, \mathbf{P} = \rho_0 \ddot{\mathbf{y}} \qquad \text{in } \mathcal{B}_0, \tag{3a}$$

$$\mathrm{div}\, \boldsymbol{\sigma} = \rho_t \ddot{\mathbf{y}} \qquad \text{in } \mathcal{B}_t, \tag{3b}$$

where ρ is the mass density. These hyperbolic equations reduce to elliptic ones for static equilibrium, *i.e.* when $\ddot{\mathbf{y}} = \mathbf{0}$. The boundary conditions are prescribed as traction and/or displacement on the boundaries of $\mathcal{B}$ and need to be accompanied by initial conditions for dynamic situations.

3.1.2. Heat conduction

Thermal equilibrium describes a state where zero net heat flux occurs within a material volume. This is described by the divergence of the heat flux being balanced by the heat generated, *e.g.* due to plastic deformation, everywhere in $\mathcal{B}$. The parabolic PDE associated with non steady-state heat conduction in the reference configuration takes the form:

$$\mu_T \dot{T} = f_T - \mathrm{Div}\, \mathbf{f}_T \quad \text{in } \mathcal{B}_0, \tag{4}$$

where $\mu_T = \rho_0 C_\mathrm{p}$ is a viscosity-like term with heat capacity C_p. The temperature is denoted by T, f_T is the heat generation rate, and $\mathbf{f}_T$ the heat flux. The boundary conditions are prescribed as a heat flux and/or temperature on the boundaries of $\mathcal{B}$ and need to be accompanied by initial conditions for the temperature.

3.1.3. Phase field damage

The prediction of crack initiation and propagation is an inherently non-local process. The Phase Field Method for Fracture (PFMF) [38,42,50] has emerged as a powerful and versatile tool to formulate this process in terms of an Allen–Cahn [51] parabolic PDE.

A non-conserved scalar damage field φ is introduced, which indicates a phase transition between undamaged, *i.e.* $\varphi = 1$, and fully damaged, *i.e.* $\varphi = 0$, regions.[3] The damage process conserves the total energy in the sense of Griffith [52]. The resulting PDE associated with the evolution of φ takes the general form:

[2] Continuous deformation implies kinematic compatibility of the resulting deformation gradient field $\mathbf{F}$, *i.e.* Curl $\mathbf{F} = \mathbf{0}$.

[3] To avoid numerical difficulties associated with a fully damaged material description, in practice the damage field is restricted to a small but finite value, *i.e.* $\varphi \geqslant \varepsilon$.

$$\mu_\varphi \dot{\varphi} = f_\varphi - \mathrm{Div}\, \mathbf{f}_\varphi \quad \text{in } \mathcal{B}_0, \tag{5}$$

where μ_φ is the damage viscosity, f_φ the driving force, and $\mathbf{f}_\varphi$ the flux. The boundary conditions are typically prescribed as zero flux on the boundaries of $\mathcal{B}$ and need to be accompanied by initial conditions for the damage field.

3.2. Numerical solvers

PDEs (3) to (5) can be solved analytically only for a few simple cases. In general, a numerical approach such as the Finite Element Method (FEM), Finite Volume Method (FVM), or Finite Difference Method (FDM) is required to find an approximate solution. The FEM is most popular in micromechanics owing to its high flexibility in considering complex topologies and multiple types of non-homogeneous boundary conditions. In cases where less flexibility is acceptable, Fast Fourier Transform (FFT) based spectral methods have emerged as a powerful alternative [53–59]. Currently implemented in DAMASK are interfaces to the commercial FEM solvers Msc.Marc and Abaqus (standard and explicit) for thermo-mechanical or damage-mechanical problems as well as in-house developed spectral solvers for general multi-physics problems.

In order to arrive at an equilibrium solution, the solver of the PDE needs to be informed about the flux and source response to a given field at every material (discretization) point. More precisely, for each time increment Δt the PDE solver requests a stress and body force, heat flux and heat generation, and/or flux and driving force for damage that results from a change in the deformation gradient, temperature, and/or damage field from t_0 to $t = t_0 + \Delta t$. For some solution algorithms the solver also requires the tangents of the respective quantity, *e.g.* implicit mechanical FEM solvers require the tangent stiffness.

3.2.1. Finite element method

The FEM was introduced in 1943 by Courant [60] and its breakthrough came through the publication of "The Finite Element Method in Structural and Continuum Mechanics" in 1967 by Zienkiewicz [61]. These and the succeeding volumes are considered the most important monographs in the field to date.

The FEM approximates the weak form of the PDE by discretizing the body into finite elements within which a set of compact shape functions is defined. This compactness enables the assembly of many small local element tangent matrices into one large but sparse global matrix. The global solution is then obtained by inverting this global matrix by direct or iterative numerical methods. The material problems handled using DAMASK are typically non-linear in character and thus need to be solved iteratively.

In the following, only DAMASK-specific implementation details are presented as a large amount of general FEM literature is available [62,63].

3.2.1.1. Interfaces to finite element method software. DAMASK has been coupled to the commercial FEM packages Msc.Marc and Abaqus (explicit and implicit) via their respective user subroutine interfaces.

The user material subroutines for hyperelastic material behavior (`Hypela2` for Msc.Marc and (V)`Umat` for Abaqus) are employed to obtain the mechanical response, which requires DAMASK to provide the stress for a given deformation gradient in an updated Lagrangian setting. Hence, any distinction between elastic and inelastic deformation is handled internally by DAMASK and hidden from the FEM package. Msc.Marc and Abaqus require the material response to be provided in terms of the Cauchy stress[4] which can be computed as $\boldsymbol{\sigma} = (\det\mathbf{F})^{-1}\,\mathbf{P}\mathbf{F}^{\mathrm{T}}$ from the more general quantities $\mathbf{P}$ and $\mathbf{F}$ used in DAMASK (see Appendix C). Furthermore, for any implicit solver, a corresponding transformation step (push forward) detailed by Tjahjanto [64] is also required for the stress tangent $\mathrm{d}\mathbf{P}/\mathrm{d}\mathbf{F}$. The properties of the DAMASK Material Point Model are determined by the Partitioning and Homogenization scheme and the set of underlying laws at the Constitutive Level. These are locally selected through two numerical IDs, *i.e.* `State Variable`s 2 and 3 in Msc.Marc and `Constant`s 1 and 2 of the user material in Abaqus.

For thermo-mechanical simulations, the source term f_T in Eq. (4) provided by DAMASK is passed to the user heat flux subroutines `Flux` (for Msc.Marc) or `Dflux` (for Abaqus). The same procedure is followed for damage-mechanical simulations, where all thermal quantities in Eq. (4) are interpreted as their damage counterparts in Eq. (5) to solve for the evolution of φ instead of T.

The interaction between the Material Point Model of DAMASK and the FEM solvers via these interfaces occurs independently for each integration point.[5] For non-local constitutive models, which rely on neighborhood information, a special solution scheme, originally developed by Ma et al. [65], is implemented into DAMASK. This scheme discriminates even and odd iterations of the global FEM solution process. Odd iterations are used for gathering consistent field information to enable the evaluation of constitutive equations that require information about the state of neighboring points. This is done in parallel for all material points in the even iterations. While this approach is imperative to evaluate non-local constitutive models, DAMASK by default uses it for the local constitutive models as well to enable DAMASK-internal thread parallelization. It is important to note that this scheme conflicts with some parallelization options of the commercial FEM solvers.

The material point results requested are returned in the form of so called user defined variables (called `User Defined Var` in Msc.Marc and `Sdv` in abaqus), which in both cases can be given descriptive names with the help of a DAMASK script.

3.2.2. Spectral method

The spectral method using FFT was introduced to material mechanics by Moulinec and Suquet [53]. It has since been extended to a wide range of constitutive descriptions [54,57,66–68], reformulated to finite deformation [57,59,69,70], and numerically improved [58,71–76]. A systematic comparison to FEM approaches is given in [59,70,77].

The spectral solver variants included in DAMASK are based on the methods outlined in [57,76] for mechanical equilibrium (Eq. (3)), and on the approach introduced in [43] for heat conduction (Eq. (4)) and phase field damage (Eq. (5)). The field equations are solved using fully implicit time stepping. Strong coupling between multiple fields is achieved in a self-consistent manner through a staggered iterative procedure.

3.2.2.1. Mechanical equilibrium. Following the ideas of Eshelby [78], the deformation map $\chi(\mathbf{x})$ introduced in Section 3.1 is expressed as a sum of a homogeneous deformation gradient $\overline{\mathbf{F}}$, and a superimposed deformation fluctuation field $\widetilde{\mathbf{w}}$,

$$\chi(\mathbf{x}) = \overline{\mathbf{F}}\mathbf{x} + \widetilde{\mathbf{w}}(\mathbf{x}), \tag{6}$$

for which periodicity conditions hold, *i.e.* $\widetilde{\mathbf{w}}^- = \widetilde{\mathbf{w}}^+$ on corresponding surfaces $\partial\mathcal{B}^-$ and $\partial\mathcal{B}^+$ on $\mathcal{B}$.

Eq. (6) allows writing the deformation gradient $\mathbf{F}$ as the sum of a spatially homogeneous part, $\overline{\mathbf{F}}$, and a locally fluctuating part, $\widetilde{\mathbf{F}}$:

$$\mathbf{F} = \overline{\mathbf{F}} + \widetilde{\mathbf{F}}. \tag{7}$$

[4] The Cauchy stress is returned as a 6-vector with components ordered differently between Msc.Marc and abaqus.

[5] Msc.Marc and Abaqus implicit require the stress response for exactly one integration point while Abaqus explicit handles several integration points at a time.

The stress response is formally expressed through a strain energy density functional $\mathcal{W}$:

$$\mathbf{P}(\mathbf{x}) = \frac{\delta \mathcal{W}}{\delta \mathbf{F}}(\mathbf{x}, \mathbf{F}, T, \varphi, \ldots). \tag{8}$$

In the following, a spectral method is derived from the direct variational formulation, while numerically more robust solution schemes based on a mixed variational formulation are presented in [72,76]. In this so-called "basic" scheme, the equilibrated deformation field is obtained by minimizing $\mathcal{W}$ over all deformation fields that fulfill Eq. (6) for an externally imposed average deformation. Static equilibrium expressed in real and Fourier[6] space follows as:

$$\min_{\chi} \mathcal{W} \Rightarrow \text{Div } \mathbf{P}(\mathbf{x}) = \mathscr{F}^{-1}[\mathbf{P}(\mathbf{k}) i\mathbf{k}] = \mathbf{0}, \tag{9}$$

which is equivalent to finding the root of the residual body force field

$$\mathcal{F}[\chi(\mathbf{k})] \coloneqq \mathbf{P}(\mathbf{k}) i\mathbf{k} = \mathbf{0}. \tag{10}$$

The differential Eq. (10) in Fourier space is numerically difficult to solve because of its high condition number. Introducing, in the spirit of Eshelby [78] and Mura [79], a linear reference material of stiffness $\mathbb{D}$ allows reformulation of Eq. (10) into an equivalent problem $\mathbf{P}(\mathbf{x}) = \mathbb{D}\,\mathbf{F}(\mathbf{x}) = \mathbb{D}\,\text{Grad}\,\chi$ with better numerical properties, *i.e.* a lower condition number. Equilibrium in this reference material is fulfilled if, for a given deformation map χ, the residual body force field vanishes:

$$\mathcal{P}[\chi(\mathbf{k})] \coloneqq \mathbb{D}[\chi(\mathbf{k}) \otimes i\mathbf{k}] i\mathbf{k} = \mathbf{A}(\mathbf{k})\chi(\mathbf{k}) = \mathbf{0}. \tag{11}$$

The acoustic tensor $\mathbf{A}(\mathbf{k})$ is a shorthand notation for $\mathbf{A}(\mathbf{k})\mathbf{a}(\mathbf{k}) \coloneqq \mathbb{D}[\mathbf{a}(\mathbf{k}) \otimes i\mathbf{k}] i\mathbf{k}$ for any given vector field $\mathbf{a}(\mathbf{k})$. It corresponds to an operator on a deformation map producing the body forces resulting in the reference material. The inverse $\mathbf{A}^{-1}$ therefore gives the deformation map that would result from a known body force field in the reference material; this deformation map vanishes if the body force field vanishes, *i.e.* in static equilibrium and for a positive-definite $\mathbb{D}$. This formulation thus allows defining an operator that results in the deformation map causing the same body force field in the reference material as a given deformation map in the original material, which corresponds to a preconditioning operation of $\mathcal{P}^{-1}$ on the nonlinear operator $\mathcal{F}$. $\mathcal{P}$ is straightforward to invert since it is local in $\mathbf{k}$, with $\mathcal{P}^{-1} = \mathbf{A}(\mathbf{k})^{-1}$. The preconditioned system thus reads ($\forall\ \mathbf{k} \neq \mathbf{0}$):

$$\mathcal{P}^{-1}\mathcal{F}[\chi(\mathbf{k})] = \mathbf{A}(\mathbf{k})^{-1}\mathbf{P}(\mathbf{k}) i\mathbf{k} = \mathbf{0}. \tag{12}$$

The deformation gradient field corresponding to this deformation map is obtained from the gradient in real space of Eq. (12) as

$$\mathcal{P}^{-1}\mathcal{F}[\chi(\mathbf{k})] \otimes i\mathbf{k} = [\mathbf{A}(\mathbf{k})^{-1}\mathbf{P}(\mathbf{k}) i\mathbf{k}] \otimes i\mathbf{k} = \mathbf{0}, \tag{13}$$

which is equivalent to Eq. (12) except for a constant residual field, *i.e.* at $\mathbf{k} = \mathbf{0}$ where the prescribed average deformation gradient is known to hold. Expressed in terms of the deformation gradient field, Eq. (13) reads

$$\mathcal{F}_{\text{mech}}[\mathbf{F}(\mathbf{k})] \coloneqq \mathbb{\Gamma}(\mathbf{k})\mathbf{P}(\mathbf{k}) = \mathbf{0}, \tag{14}$$

where the Gamma operator $\mathbb{\Gamma}(\mathbf{k})$ is defined as a shorthand notation to $\mathbb{\Gamma}(\mathbf{k})\mathbf{T}(\mathbf{k}) \coloneqq [\mathbf{A}(\mathbf{k})^{-1}\mathbf{T}(\mathbf{k}) i\mathbf{k}] \otimes i\mathbf{k}$ for a tensor field $\mathbf{T}(\mathbf{k})$.

3.2.2.2. Heat conduction and phase field damage. The spectral method presented above for mechanical problems can be reformulated to solve the heat conduction and the phase field damage PDEs. Since Eqs. (4) and (5) have a similar form, the formulation is outlined here for the heat conduction PDE, but can be analogously applied to the phase field PDE.

A backward Euler time discretization is used to express the time-dependent Eq. (4) in the following semi-discrete form:

$$\mu_T \frac{T(\mathbf{x}, t) - T(\mathbf{x}, t_0)}{\Delta t} = f_T(\mathbf{x}) - \text{Div } \mathbf{f}_T(\mathbf{x}) \tag{15}$$

The flux, $\mathbf{f}_T$, is additively split into a linear homogeneous term and a fluctuating field:

$$\mathbf{f}_T(\mathbf{x}) = -\mathbf{K}\ \text{Grad}\ T(\mathbf{x}, t) - \widetilde{\tau_T}(\mathbf{x}) \tag{16}$$

where $\mathbf{K}$ is the homogenous reference tensor of the linear term. Similarly, the viscosity-like term, μ_T, is split into spatially averaged and fluctuating parts, *i.e.*

$$\mu_T = \overline{\mu_T} + \widetilde{\mu_T}. \tag{17}$$

With Eqs. (16) and (17), Eq. (15) can be expressed in Fourier space as

$$(\overline{\mu_T} + \Delta t \mathbf{k}\cdot\mathbf{K}\mathbf{k}) T(\mathbf{k}, t) = \tau_T(\mathbf{k}) \tag{18}$$

where the temperature polarisation field, $\tau_T(\mathbf{x})$, which implicitly depends on $T(\mathbf{x}, t)$, is given by

$$\tau_T(\mathbf{x}) = \Delta t (f_T(\mathbf{x}) + \text{Div } \widetilde{\tau_T}(\mathbf{x})) + \mu_T\ T(\mathbf{x}, t_0) - \widetilde{\mu_T}\ T(\mathbf{x}, t) \tag{19}$$

The solution of the heat conduction PDE can therefore be expressed as the root of the following residual function

$$\mathcal{F}_T[T(\mathbf{k}, t)] \coloneqq T(\mathbf{k}, t) - \mathbf{G}(\mathbf{k})\tau_T(\mathbf{k}) = 0 \tag{20}$$

where $\mathbf{G}^{-1}(\mathbf{k}) \coloneqq \overline{\mu_T} + \Delta t \mathbf{k}\cdot\mathbf{K}\mathbf{k}$.

The same procedure is followed for solving phase field damage problems, where all thermal quantities in Eq. (4) are interpreted as their damage counterparts in Eq. (5) to solve for the evolution of φ instead of T.

3.2.2.3. Implementation details. In the following, details concerning the implementation of the methods outlined above are concisely presented.

Fast Fourier Transform: Eqs. (14) and (20) are solved on a hexahedral domain $\mathcal{B}_0$ with side lengths d_x, d_y, d_z, which is discretized into a regular grid of $N_x \times N_y \times N_z = N$ points. The solution field is approximated in the discrete Fourier space associated with this real space grid using the FFT. Specifically, the Fastest Fourier Transform in the West (FFTW), a free FFT implementation that has shown excellent performance [80] is employed. To save memory and computation time, the complex conjugate symmetry resulting from the real space field data is exploited.

Calculation of Gradients: While the deformation, temperature, and damage fields are necessarily continuous, their spatial gradients are allowed to be discontinuous, *e.g.* across phase boundaries. A numerical artifact associated with Fourier representations of such discontinuous gradient fields is the formation of spurious oscillations which is referred to as Gibbs phenomenon. This can deteriorate the performance of the solution schemes as well as the quality of the solution [81]. Various techniques exist to reduce these effects, such as a low-pass filtering to effectively dampen high-frequency modes associated with the spurious oscillations [82]. Finite difference approximations of the gradient fields, which can be—as outlined by Kaßbohm et al. [55], Willot [58], and Vidyasagar et al. [83]—easily obtained in Fourier space, are employed to reduce such spurious oscillations.

The gradient Grad g of a field $g(\mathbf{x})$ is expressed in Fourier space as $g(\mathbf{k}) \otimes \mathbf{k}'$. Working with continuous derivatives results in the straightforward relation $\mathbf{k}' = i\mathbf{k}$. The forward–backward finite difference variant introduced by Willot [58] reads then as:

$$\mathbf{k}' = \begin{pmatrix} \frac{N_x}{4d_x}(e^{i\mathbf{k}_1} - 1)(e^{i\mathbf{k}_2} + 1)(e^{i\mathbf{k}_3} + 1) \\ \frac{N_y}{4d_y}(e^{i\mathbf{k}_1} + 1)(e^{i\mathbf{k}_2} - 1)(e^{i\mathbf{k}_3} + 1) \\ \frac{N_z}{4d_z}(e^{i\mathbf{k}_1} + 1)(e^{i\mathbf{k}_2} + 1)(e^{i\mathbf{k}_3} - 1) \end{pmatrix} \tag{21}$$

A more detailed discussion on alternative finite difference schemes applicable for this purpose has been conducted by Schneider et al. [84].

[6] Quantities in real space and Fourier space are distinguished by notation $Q(\mathbf{x})$ and $Q(\mathbf{k})$, respectively, with $\mathbf{x}$ the position in real space, $\mathbf{k}$ the frequency vector in Fourier space, and the imaginary unit i. $\mathscr{F}^{-1}[\cdot]$ denotes the inverse Fourier transform.

Reference Tensors: The choice of the reference stiffness has a strong influence on stability and convergence rate as shown by Michel et al. [72]. In absence of an analytic expression for the large-strain formulation [72], the reference stiffness $\mathbb{D}$ for the mechanical problem is selected as

$$\mathbb{D} = \frac{1}{2}\left(\operatorname{argmax}\left\|\frac{\mathrm{d}\mathbf{P}}{\mathrm{d}\mathbf{F}}(\mathbf{x})\right\|_{\mathrm{F}} + \operatorname{argmin}\left\|\frac{\mathrm{d}\mathbf{P}}{\mathrm{d}\mathbf{F}}(\mathbf{x})\right\|_{\mathrm{F}}\right). \tag{22}$$

Similarly, the choices for the reference thermal conductivity and damage gradient tensors are formulated as

$$\mathbf{K} = \frac{1}{2}\left(\operatorname{argmax}\left\|\frac{\mathrm{d}\mathbf{f}_T}{\mathrm{d}\ \mathrm{Grad}\ T}(\mathbf{x})\right\| + \operatorname{argmin}\left\|\frac{\mathrm{d}\mathbf{f}_T}{\mathrm{d}\ \mathrm{Grad}\ T}(\mathbf{x})\right\|\right), \tag{23}$$

$$\mathbf{D} = \frac{1}{2}\left(\operatorname{argmax}\left\|\frac{\mathrm{d}\mathbf{f}_\varphi}{\mathrm{d}\ \mathrm{Grad}\ \varphi}(\mathbf{x})\right\| + \operatorname{argmin}\left\|\frac{\mathrm{d}\mathbf{f}_\varphi}{\mathrm{d}\ \mathrm{Grad}\ \varphi}(\mathbf{x})\right\|\right). \tag{24}$$

Note that, unlike in the isotropic case, such convenient choice of the reference tensors does not guarantee convergence. The rate of convergence depends on the property contrast present in the material, as discussed by Shanthraj et al. [76] for the case of mechanical equilibrium.

Boundary and Initial Conditions: The applied boundary conditions on $\mathcal{B}$ are volume averages, *i.e.* for the mechanical boundary value problem $\overline{\mathbf{F}}$ is set to the applied load $\mathbf{F}_{\mathrm{BC}}$. To this end, the desired change of $\mathbf{F}_{\mathrm{BC}}$ is conveniently expressed in rate form, *i.e.* $\Delta\mathbf{F}_{\mathrm{BC}} = \dot{\mathbf{F}}_{\mathrm{BC}}\Delta t$ for a given time increment of length Δt. In order to allow the (component-wise) prescription of stress boundary conditions $\mathbf{P}_{\mathrm{BC}}$, an iterative adjustment of $\mathbf{F}_{\mathrm{BC}}$ needs to be done until the stress boundary conditions are fulfilled. The solution for the deformation gradient field, *i.e.* the actual spectral method procedure, is performed in parallel to these iterations. Within Δt, the volume element is then subjected to a set of complementary (component-wise mutually exclusive) boundary conditions in terms of deformation rate $\dot{\mathbf{F}}_{\mathrm{BC}}$ and stress $\mathbf{P}_{\mathrm{BC}}$, where stress boundary conditions must preclude rigid body rotations. In the following, $\dot{\mathbf{F}}_{\mathrm{BC}}$ and stress $\mathbf{P}_{\mathrm{BC}}$ are mutually exclusive and set to zero when undefined. These mixed boundary conditions are translated into pure deformation boundary conditions at iteration $n+1$ by setting

$$\{\mathbf{F}_{\mathrm{BC}}(t)\}_{n+1} = \mathbf{F}_{\mathrm{BC}}(t_0) + \dot{\mathbf{F}}_{\mathrm{BC}}\Delta t - \left\{\left(\frac{\partial\mathbf{F}}{\partial\mathbf{P}}\right)\right\}_n (\{\overline{\mathbf{P}}\}_n - \mathbf{P}_{\mathrm{BC}}). \tag{25}$$

The last term in Eq. (25) corrects for deviations from the prescribed stress boundary conditions. The average compliance $\overline{\partial\mathbf{F}/\partial\mathbf{P}}$ is estimated from the local responses $\partial\mathbf{P}/\partial\mathbf{F}$ [57]. In DAMASK, the use of two coordinate systems enables the definition of boundary conditions that are rotated with respect to the discretization of $\mathcal{B}$ [85]. In contrast to the mechanical equilibrium, the PDEs describing heat conduction and phase field damage require specification of their respective initial field values $T(\mathbf{x}, 0)$ and $\varphi(\mathbf{x}, 0)$.

Numerical solution: The resulting system of discretized equations is solved by non-linear solution methods. Originally, a fix-point scheme [86] was employed while recent approaches use more advanced solving techniques [74,87].

In DAMASK, iterative solution methods, such as the non-linear Richardson method [88], the non-linear GMRES method [89], and the inexact Newton-GMRES method [90] implemented in the Portable, Extensible Toolkit for Scientific Computation (PETSc) [91] are used. The use of PETSc allows to use advanced algorithms that exploit the characteristics of the problem at hand as discussed in [42] for the case of PFMF. In all these algorithms, an existing solution $\{\mathbf{F}(\mathbf{x})\}_n$ for the mechanical equilibrium problem, $\{T(\mathbf{x})\}_n$ for the heat conduction problem, or $\{\varphi(\mathbf{x})\}_n$ for the phase field damage problem at iteration n is iteratively improved until the prescribed convergence criteria are satisfied.

Algorithm: For a given time interval, $\Delta t = t - t_0$, the solution for individual fields can be found iteratively as described above. The multiphysics coupling approach followed in this work involves solving the coupled system Eqs. (14) and (20) within a staggered iterative loop until a consistent solution, within specified tolerances, is achieved for the time interval. The procedure is detailed in Algorithm 1. The advantage of such a staggered approach is that the solution scheme of each field can be selected independently and additional fields are easily implemented.

Algorithm 1. Self-consistent staggered iterative procedure for multiphysics coupling in the time increment $[t_0, t]$.

Data: $\mathbf{F}(\mathbf{x}, t_0)$, $T(\mathbf{x}, t_0)$, $\varphi(\mathbf{x}, t_0)$
Result: $\mathbf{F}(\mathbf{x}, t)$, $T(\mathbf{x}, t)$, $\varphi(\mathbf{x}, t)$

Initialization:

$$\mathbf{F}^0(\mathbf{x}, t) = \mathbf{F}(\mathbf{x}, t_0),$$
$$T^0(\mathbf{x}, t) = T(\mathbf{x}, t_0),$$
$$\varphi^0(\mathbf{x}, t) = \varphi(\mathbf{x}, t_0),$$
$$j = 1$$

while $\|T^j(\mathbf{x}, t) - T^{j-1}(\mathbf{x}, t)\|_2 \geq \epsilon_T^{\mathrm{stag}}$ and $\|\varphi^j(\mathbf{x}, t) - \varphi^{j-1}(\mathbf{x}, t)\|_2 \geq \epsilon_\varphi^{\mathrm{stag}}$ **do**
  solve $\mathcal{F}_{\mathrm{mech}}\left[\mathbf{F}^j(\mathbf{x}, t)\right] = \mathbf{0}$ using $T^{j-1}(\mathbf{x}, t)$ and $\varphi^{j-1}(\mathbf{x}, t)$;
  solve $\mathcal{F}_T\left[T^j(\mathbf{x}, t)\right] = 0$ using $\mathbf{F}^j(\mathbf{x}, t)$ and $\varphi^{j-1}(\mathbf{x}, t)$;
  solve $\mathcal{F}_\varphi\left[\varphi^j(\mathbf{x}, t)\right] = 0$ using $\mathbf{F}^j(\mathbf{x}, t)$ and $T^j(\mathbf{x}, t)$;
  $j = j+1$
end

Result:

$$\mathbf{F}(\mathbf{x}, t) = \mathbf{F}^j(\mathbf{x}, t),$$
$$T(\mathbf{x}, t) = T^j(\mathbf{x}, t),$$
$$\varphi(\mathbf{x}, t) = \varphi^j(\mathbf{x}, t)$$

Convergence Criteria: To ensure that the resulting mechanical stress field is in equilibrium, the Root Mean Square (RMS) value of the divergence of the stress field, evaluated in Fourier space, is reduced below a prescribed tolerance. The corresponding equilibrium criterion reads:

$$\max(\varepsilon_{\mathrm{eq,abs}}, \varepsilon_{\mathrm{eq,rel}}\|\overline{\mathbf{P}}\|_{\max}) \geqslant \mathrm{RMS}(\|\mathrm{Div}\ \mathbf{P}(\mathbf{x})\|_2), \tag{26}$$

where $\varepsilon_{\mathrm{eq,rel}}$ and $\varepsilon_{\mathrm{eq,abs}}$ are the relative and absolute stress divergence tolerance limits, respectively.

The fulfillment of the stress boundary conditions is checked by

$$\max(\varepsilon_{\mathrm{BC,abs}}, \varepsilon_{\mathrm{BC,rel}}\|\overline{\mathbf{P}}\|_{\max}) \geqslant \|\Delta\mathbf{P}_{\mathrm{BC}}\|_{\max}, \tag{27}$$

where $\Delta\mathbf{P}_{\mathrm{BC}} = \mathbf{P}_{\mathrm{BC}} - \overline{\mathbf{P}}$ is defined only for components where stress boundary conditions are given. $\varepsilon_{\mathrm{BC,rel}}$ and $\varepsilon_{\mathrm{BC,abs}}$ are the corresponding relative and absolute boundary condition tolerances, respectively.

The residual norm of Eq. (20) is evaluated as a convergence test for the heat conduction and phase field damage PDEs.

4. Partitioning and homogenization

For component-scale simulations, *e.g.* deep drawing of automotive structure parts, the volume represented by each material point is typically not composed of a single constituent but instead of an aggregate of

constituents with different phases and/or crystallographic orientations.

For example, sheet materials typically have a non-random Crystallographic Orientation Distribution Function (CODF) [92,93], also referred to as crystallographic texture, and hence show anisotropic behavior [94,95]. The CODF can be experimentally measured and approximated by a population of individual crystal orientations [96]. However, the number of orientations needed for a sufficiently close approximation of the crystallographic texture is usually much larger than the number of orientations that can be computationally handled at a single material point. Therefore, DAMASK contains the HybridIA algorithm to optimally approximate a crystallographic texture with a given number of individual orientations [97] and distribute those onto the material points.

Given an aggregate of constituents, the task at this highest hierarchical level is twofold: firstly to partition the prescribed field values between the microstructural constituents and subsequently to homogenize their constitutive response. In the field of mechanics, a vast body of literature exits on this topic ranging from simple schemes [98–101], which are computationally efficient yet limited in accuracy, to complex ones [102–107] with higher computational demands and accuracy. When detailed resolution of local fields is required, two-scale approaches [56,108–111] can be employed as accurate but computationally expensive homogenization schemes. To address this trade-off, DAMASK contains fast iso-field schemes for all field quantities and the more involved Relaxed Grain Cluster (RGC) scheme [105] for mechanical homogenization.

4.1. Mechanical fields

In the framework of DAMASK, mechanical homogenization requires to compute the average stress response $\overline{\mathbf{P}}$ over N_g constituents comprising a material point for a given average deformation gradient $\overline{\mathbf{F}}$.[7] $\overline{\mathbf{F}}$ is partitioned onto the constituents $g = 1, ...,N_g$ such that the volume-averaged deformation gradient is consistent:

$$\overline{\mathbf{F}} = \sum_{g=1}^{N_g} \nu^{(g)} \mathbf{F}^{(g)}, \tag{28}$$

where $\nu^{(g)}$ represents the volume fraction contributed by constituent g to the material point in its reference (or undeformed) configuration.

The homogenized stress at the material point is calculated as the volumetric average of the resulting stresses $\mathbf{P}^{(g)}$ of all constituents

$$\overline{\mathbf{P}} = \sum_{g=1}^{N_g} \nu^{(g)} \mathbf{P}^{(g)}. \tag{29}$$

The specific homogenization schemes presented in the following essentially differ in the procedure for partitioning $\overline{\mathbf{F}}$ (Eq. (28)).

4.1.1. Direct scheme for single constituents

For full-field simulations, where each material point represents a single constituent, *i.e.* $N_g = 1$, a homogenization scheme is not required. Nevertheless, the modular structure of DAMASK formally requires a homogenization to be specified for every material point. Therefore, in order to avoid any overhead, this scheme passes $\mathbf{F}^{(1)} = \overline{\mathbf{F}}$ directly on to the lower level and returns the computed stress directly as $\overline{\mathbf{P}} = \mathbf{P}^{(1)}$.

4.1.2. Isostrain

The isostrain assumption states that all constituents comprising a material point are subjected to the same deformation. It is often referred to as "full constraint (FC) Taylor" assumption since Taylor [100] first applied it to predict the deformation behavior of polycrystals.

Within the finite strain framework employed in DAMASK, it is expressed by equating the deformation gradient of each constituent g with the average deformation gradient $\overline{\mathbf{F}}$ of the material point

$$\mathbf{F}^{(g)} = \overline{\mathbf{F}}, \quad g = 1, ...,N_g. \tag{30}$$

In general, a different stress $\mathbf{P}^{(g)}$ will result in each constituent g due to, for instance, different orientation or constitutive behavior (strength). The isostrain scheme, therefore, generally violates stress equilibrium between the constituent grains.

The isostrain homogenization can also be used to model viscoelastic material behavior by combining a linear elastic with a viscoplastic constituent. The stress homogenization (Eq. (29)) can be changed to

$$\overline{\mathbf{P}} = \sum_{g=1}^{N_g} \mathbf{P}^{(g)} \tag{31}$$

in order to reflect this case.

4.1.3. Relaxed grain cluster

The RGC homogenization scheme [4,105,112] is an extension of other grain cluster approaches such as the Grain Interaction (GIA) [104,113] and the (A)LAMEL [102,103,114,115] models. Contrary to mean-field approaches, such as the isostrain assumption mentioned before, direct neighborhood interactions between the constituents, *i.e.* "grains", comprising a material point are taken into account by these cluster models, albeit in a simplified, homogeneous fashion. These interactions are defined to approximate strain compatibility and stress equilibrium between the constituents. The implementation of the RGC scheme in DAMASK is briefly outlined here following Tjahjanto et al. [105].

4.1.3.1. Kinematics of deformation relaxation. A cluster of $N_g = p \times q \times r$ hexahedral constituents is considered at each material point. The neighborhood of each constituent is determined by a periodic repetition of the cluster. Fig. 2 shows a $4 \times 5 \times 3$ cluster as an example.

Interactions between neighboring constituents are described using "relaxation vectors" that represent the rigid-body translation of their interface relative to the average deformation of the cluster (see Fig. 3). The average deformation gradient of each cluster member is, therefore, augmented by the translation modes on the six interfaces (indexed by α) such that

$$\mathbf{F}^{(g)} = \overline{\mathbf{F}} + \sum_{\alpha=1}^{6} \frac{1}{r_\alpha^{(g)}} \left(\mathbf{a}_\alpha^{(g)} \otimes \mathbf{n}_\alpha^{(g)}\right), \tag{32}$$

where $\mathbf{a}_\alpha^{(g)}$ and $\mathbf{n}_\alpha^{(g)}$ are, respectively, the relaxation vector and unit normal of the interface α of constituent g, and $r_\alpha^{(g)}$ is the constituent dimension along the interface normal $\mathbf{n}_\alpha^{(g)}$. Since each interface is shared by two constituents (i) relaxation vectors at the interface of two adjacent constituents are set identical and (ii) relaxation vectors that correspond to the "exterior" surface of the cluster fulfill a periodic boundary condition.

4.1.3.2. Interface incompatibility and penalty. In the above presented formalism of the constituent cluster deformation, the kinematic constraint on the relaxation vectors at shared interfaces ensures compatibility for isolated relaxation modes. Nevertheless, incompatible deformations can result from the superposition of these modes. To quantify the resulting incompatibility across interface α of constituent g, the concept of Bilby's planar dislocation tensor[8] [117–120] is adopted to define a "mismatch tensor" $\mathbf{M}_\alpha^{(g)}$ as (see also *e.g.* [121])

[7] Note that here $\overline{\mathbf{T}}$ denotes the average of a tensor $\mathbf{T}$ over one material point, while in Section 3.2.2 it denotes the average over the whole domain $\mathcal{B}$.

[8] Corresponding to the Nye [117] dislocation tensor in the limit of zero thickness.

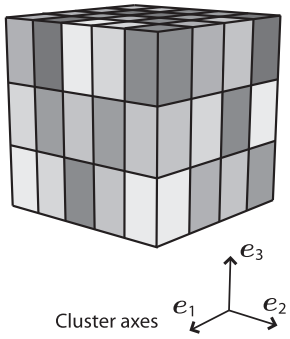

Fig. 2. Example of a 4 × 5 × 3 cluster considered by the Relaxed Grain Cluster (RGC) scheme. The different gray shades indicate different crystallographic orientations and/or phases of the constituents ("grains"). Figure adopted from [16] with permission from John Wiley and Sons.

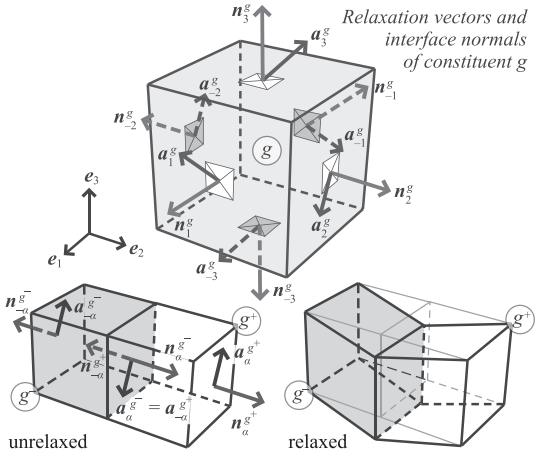

Fig. 3. Illustration of the relaxation vectors of constituent ("grain") g. Figure adopted from [105,112,116] with permission from Springer Nature.

$$\mathbf{M}_{\alpha}^{(g)} = -\left(\mathbf{n}_{\alpha}^{(g)} \times \Delta\mathbf{F}_{\alpha}^{(g)\mathrm{T}}\right)^{\mathrm{T}}, \tag{33}$$

where $\Delta\mathbf{F}_{\alpha}^{(g)\mathrm{T}}$ corresponds to the jump, *i.e.* difference, in the deformation gradient between constituent g and its neighbor across an interface α. By correlating the incompatibility with a density of accommodating "geometrically necessary" dislocations, a surface energy function is proposed that penalizes the incompatibility at interface α of constituent g:

$$\mathcal{R}_{\alpha}^{(g)} = \frac{b^{(g)}\mu^{(g)}\xi}{2c}\sinh\left(c\,\|\mathbf{M}_{\alpha}^{(g)}\|\right), \tag{34}$$

where $\mu^{(g)}$ denotes the isotropic equivalent shear modulus of a possibly anisotropic constituent g [122], $b^{(g)}$ the magnitude of the Burgers vector of the dislocations and $\|\mathbf{M}_{\alpha}^{(g)}\|$ the magnitude of the mismatch. Two dimensionless scalars are introduced in Eq. (34): ξ sets the effective weight of the penalty function, and c controls the over-proportionality of the penalty function with respect to the mismatch magnitude, such that Eq. (34) shows a linear behavior if $c \to 0$. Setting $\xi = 0$ renders the model "penalty-free", *i.e.* incompatibility between neighboring constituents is tolerated, whereas $\xi \to \infty$ results in a very strong penalty function which imposes a "fully compatible" deformation mode. The overall mismatch penalty density (per unit reference volume) $\mathcal{R}$ is computed as the volumetric average of the penalties at all interfaces of all constituents, *i.e.*

$$\mathcal{R} = \sum_{g=1}^{N_{\mathrm{g}}} \nu^{(g)} \left(\sum_{\alpha=1}^{6} \frac{\mathcal{R}_{\alpha}^{(g)}}{r_{\alpha}^{(g)}} \right). \tag{35}$$

4.1.3.3. Energy minimization. The deformation energy (or mechanical work) density of constituent g per unit reference volume at time t, denoted by $\mathcal{W}^{(g)}$, is given by

$$\mathcal{W}^{(g)} = \int_0^t \mathbf{P}^{(g)}(\tau)\cdot\dot{\mathbf{F}}^{(g)}(\tau)\,\mathrm{d}\tau, \tag{36}$$

where $\dot{\mathbf{F}}^{(g)} = \partial\mathbf{F}^{(g)}/\partial t$ is the rate of the deformation gradient. The overall work density of the cluster, $\mathcal{W}$, can be obtained as the volumetric average of the work density of all constituents as

$$\mathcal{W} = \sum_{g=1}^{N_{\mathrm{g}}} \nu^{(g)}\mathcal{W}^{(g)}. \tag{37}$$

In the RGC model, all relaxation vectors $\mathbf{a}_{\alpha}^{(g)}$ are determined such that the total energy density (including the mismatch penalty) of the cluster is minimum for a given $\overline{\mathbf{F}}$, *i.e.* $\widetilde{\mathbf{a}}_{\alpha}^{(g)} = \mathrm{argmin}\{\mathcal{W}(\mathbf{a}_{\alpha}^{(g)}) + \mathcal{R}(\mathbf{a}_{\alpha}^{(g)})\}$. Assuming convexity of the total energy density $\mathcal{W} + \mathcal{R}$, the solution of the energy minimization problem is equivalent to the stationary point, $\partial(\mathcal{W} + \mathcal{R})/\partial\mathbf{a}_{\alpha}^{(g)} = \mathbf{0}$, for each interface α of constituent g. Evaluating the above derivatives, the solution of the energy minimization leads to the following balance of traction (or equilibrium condition) at each interface α of constituent g:

$$\left(\mathbf{P}^{(g)} + \mathbf{R}^{(g)}\right)\mathbf{n}_{\alpha}^{g} - \left(\mathbf{P}^{(g^*)} + \mathbf{R}^{(g^*)}\right)\mathbf{n}_{\alpha}^{(g)} = \mathbf{0}, \tag{38}$$

where g^* denotes the constituent opposite to g across the interface α. In the above equilibrium condition, $\mathbf{R}^{(g)}$ represents a tensor analogous to the first Piola–Kirchhoff stress tensor obtained as the derivative of the total mismatch penalty with respect to the constituent deformation gradient, *i.e.* $\mathbf{R}^{(g)} = \partial\mathcal{R}/\partial\mathbf{F}^{(g)}$. A more detailed discussion on the "penalty stress" tensor $\mathbf{R}^{(g)}$ can be found in [105].

4.2. Thermal fields

The average temperature field $\overline{T}$ acting on a material point is partitioned onto the N_{g} constituents $g = 1, \ldots, N_{\mathrm{g}}$ such that

$$\overline{T} = \sum_{g=1}^{N_{\mathrm{g}}} \nu^{(g)}T^{(g)}. \tag{39}$$

An iso-field homogenization assumption is used, whereby the equality of the temperature field $T^{(g)}$ of each constituent g with the average temperature field $\overline{T}$ is enforced:

$$T^{(g)} = \overline{T}, \quad g = 1, \ldots, N_{\mathrm{g}}. \tag{40}$$

Typically, a different flux $\mathbf{f}_T^{(g)}$ and driving force $f_T^{(g)}$ results in each constituent g, which can, for instance, be due to anisotropy or different constitutive behavior. The flux and driving force at the material point are calculated as the average of all constituents:

$$\overline{\mathbf{f}_T} = \sum_{g=1}^{N_{\mathrm{g}}} \nu^{(g)}\mathbf{f}_T^{(g)} \tag{41a}$$

$$\overline{f_T} = \sum_{g=1}^{N_{\mathrm{g}}} \nu^{(g)}f_T^{(g)}. \tag{41b}$$

4.3. Damage fields

Similar to the partitioning of $\overline{T}$ given in Eq. (39), the average damage field $\overline{\varphi}$ acting on a material point is partitioned onto the N_{g} constituents $g = 1, \ldots, N_{\mathrm{g}}$ such that

$$\overline{\varphi} = \sum_{g=1}^{N_{\mathrm{g}}} \nu^{(g)}\varphi^{(g)}. \tag{42}$$

As for the temperature (Eq. (40)), the iso-field homogenization assumption is used, whereby the equality of the damage field $\varphi^{(g)}$ of each constituent g with the average damage field $\overline{\varphi}$ is enforced:

$$\varphi^{(g)} = \overline{\varphi}, \quad g = 1, \ldots, N_g. \tag{43}$$

In general, different fluxes $\mathbf{f}_\varphi^{(g)}$ and driving forces $f_\varphi^{(g)}$ will result in the different constituents. The flux and driving force at the material point are calculated as the average of all constituents:

$$\overline{\mathbf{f}_\varphi} = \sum_{g=1}^{N_g} \nu^{(g)} \mathbf{f}_\varphi^{(g)} \tag{44a}$$

$$\overline{f_\varphi} = \sum_{g=1}^{N_g} \nu^{(g)} f_\varphi^{(g)}. \tag{44b}$$

5. Single constituent kinematics

The intermediate Constituent Level connects the Partitioning and Homogenization and the Constitutive Level defined according to the hierarchical structure of DAMASK (Section 2.2). An abstract procedure is established at this level to encapsulate all model-specific aspects in the constitutive descriptions (Section 6).

The purpose of this level is therefore twofold: (i) to consistently decompose the partitioned deformation gradient based on multiple deformation sources and (ii) to integrate the internal state of the underlying constitutive laws for fluxes and sources over time. As outcome, the stress and its tangent with respect to the deformation gradient are provided to the Partitioning and Homogenization level.

5.1. Multiplicative decomposition

The decomposition of the partitioned deformation gradient $\mathbf{F}$ is required to determine the stress response $\mathbf{P}$.[9] The physical motivation for this partitioning is a clear distinction between different deformation modes: Elastic deformation, resulting from stretching of atomic bonds, plastic deformation, resulting from, for instance, dislocation motion, and lastly eigenstrains, arising in connection with, for instance, damage, phase transformations, or changes in temperature fields.

In the finite strain framework of DAMASK, the multiplicative decomposition of the deformation gradient $\mathbf{F}$ reads as

$$\mathbf{F} = \mathbf{F}_\mathrm{e}\mathbf{F}_\mathrm{i}\mathbf{F}_\mathrm{p}, \tag{45}$$

where $\mathbf{F}_\mathrm{p}$ is a lattice-preserving, inelastic deformation gradient that maps to the plastic configuration, $\mathbf{F}_\mathrm{i}$ is a lattice-distorting, inelastic deformation gradient, *e.g.* thermal expansion or crack opening [123], mapping further to the eigenstrain configuration, and $\mathbf{F}_\mathrm{e}$ is an elastic deformation gradient that maps from the inelastic to the deformed configuration. This decomposition is schematically shown in Fig. 4.

The specific order in Eq. (45) allows to conveniently account for anisotropy, *i.e.* dependence on crystallographic orientation, of the constitutive laws in the isoclinic plastic configuration. To avoid unnecessary rotations of tensorial quantities naturally defined in the lattice coordinate frame, $\mathbf{F}_\mathrm{p}$ is initialized with the initial crystal orientation $\mathbf{O}_0$, *i.e.* $\mathbf{F}_\mathrm{p}(t=0) = \mathbf{F}_\mathrm{e}^\mathrm{T}(t=0) = \mathbf{O}_0$ such that the plastic configuration of each crystal corresponds to a common cube orientation [65]. The current crystallographic orientation $\mathbf{O}$ can then always be calculated from $\mathbf{F}_\mathrm{e}$ through a polar decomposition $\mathbf{F}_\mathrm{e} = \mathbf{O}^\mathrm{T}\mathbf{U}$, where $\mathbf{U}$ is the right stretch tensor.

5.2. Time integration

The constitutive laws for inelastic deformation, *i.e.* the flow rules, are formulated in rate form.[10] This requires time integration of kinematic quantities from t_0 to $t = t_0 + \Delta t$. In addition, for flow rules depending on an internal material state, this time integration has to be performed consistently with the evolving state.

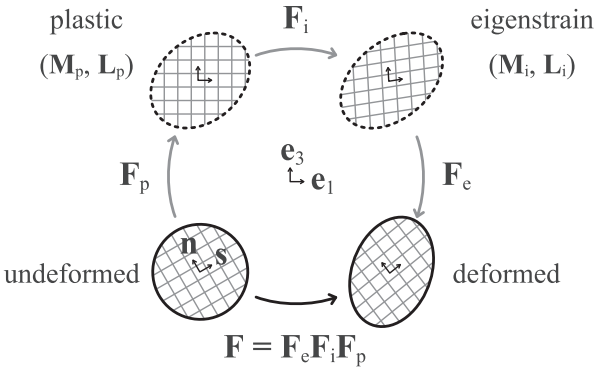

Fig. 4. Illustration of the intermediate configurations resulting from the multiplicative decomposition of the deformation gradient. Selecting the crystal orientation as initial value of $\mathbf{F}_\mathrm{p}(t=0) = \mathbf{O}_0$ guarantees that the lattice coordinate system in the plastic configuration always coincides with the lab coordinate system [65].

5.2.1. Inelastic flow relations

The evolution of the inelastic deformation gradients $\mathbf{F}_\mathrm{p}$ and $\mathbf{F}_\mathrm{i}$ is given in terms of their respective velocity gradients $\mathbf{L}_\mathrm{p}$ and $\mathbf{L}_\mathrm{i}$ by the following flow rules

$$\dot{\mathbf{F}}_\mathrm{p} = \mathbf{L}_\mathrm{p}\mathbf{F}_\mathrm{p}, \tag{46a}$$

$$\dot{\mathbf{F}}_\mathrm{i} = \mathbf{L}_\mathrm{i}\mathbf{F}_\mathrm{i}. \tag{46b}$$

The inelastic velocity gradients are additively composed from individual contributions (indexed by n) and are driven by their work conjugate stress measures, *i.e.* the Mandel stresses $\mathbf{M}_\mathrm{p}$ and $\mathbf{M}_\mathrm{i}$:

$$\mathbf{L}_\mathrm{p} = \sum_n f_n(\mathbf{M}_\mathrm{p}, \ldots), \tag{47a}$$

$$\mathbf{L}_\mathrm{i} = \sum_n f_n(\mathbf{M}_\mathrm{i}, \ldots). \tag{47b}$$

The Mandel stresses $\mathbf{M}_\mathrm{p}$ and $\mathbf{M}_\mathrm{i}$ are calculated from the second Piola–Kirchhoff stress $\mathbf{S}$ (see Appendix C), which is determined by an elastic constitutive law (Section 6.1) that expresses $\mathbf{S}$ as a function of its work conjugate, the Green–Lagrange strain $\mathbf{E}$ in the plastic configuration:

$$\mathbf{S} = f(\mathbf{E}, \ldots), \quad \text{with } \mathbf{E} \coloneqq \frac{1}{2}\mathbf{F}_\mathrm{i}^\mathrm{T}(\mathbf{F}_\mathrm{e}^\mathrm{T}\mathbf{F}_\mathrm{e} - \mathbf{I})\mathbf{F}_\mathrm{i}. \tag{48}$$

Integrating Eq. (46) over the given time interval Δt results in

$$\mathbf{F}_\mathrm{p}(t) = \mathbf{F}_\mathrm{p}(t_0) + \int_{t_0}^{t} \mathbf{L}_\mathrm{p}(\tau)\mathbf{F}_\mathrm{p}(\tau)\,\mathrm{d}\tau = \exp\left[\int_{t_0}^{t} \mathbf{L}_\mathrm{p}(\tau)\,\mathrm{d}\tau\right]\mathbf{F}_\mathrm{p}(t_0) \text{ and} \tag{49a}$$

$$\mathbf{F}_\mathrm{i}(t) = \mathbf{F}_\mathrm{i}(t_0) + \int_{t_0}^{t} \mathbf{L}_\mathrm{i}(\tau)\mathbf{F}_\mathrm{i}(\tau)\,\mathrm{d}\tau = \exp\left[\int_{t_0}^{t} \mathbf{L}_\mathrm{i}(\tau)\,\mathrm{d}\tau\right]\mathbf{F}_\mathrm{i}(t_0) \tag{49b}$$

and allows to solve Eq. (45) for given $\mathbf{F}$.

5.2.1.1. Numerical solution strategy. The resulting closed set of Eqs. (45), (46), (47), and (49) needs to be solved numerically. The exact time integral of the velocity gradients (Eq. (49)) is approximated in an implicit manner at a fixed material state as

$$\frac{\mathbf{F}_\mathrm{p}(t) - \mathbf{F}_\mathrm{p}(t_0)}{\Delta t} = \mathbf{L}_\mathrm{p}(t)\mathbf{F}_\mathrm{p}(t) \text{ and} \tag{50a}$$

$$\frac{\mathbf{F}_\mathrm{i}(t) - \mathbf{F}_\mathrm{i}(t_0)}{\Delta t} = \mathbf{L}_\mathrm{i}(t)\mathbf{F}_\mathrm{i}(t), \tag{50b}$$

which results in the inelastic deformation gradients at the end of the time increment being

[9] The partitioned quantities $\mathbf{F}^{(g)}$ and $\mathbf{P}^{(g)}$ are, for brevity, referred to as $\mathbf{F}$ and $\mathbf{P}$ in what follows.

[10] In this setting, rate-independent models are expressed as the kinetic limit of the corresponding rate-dependent model.

$$\mathbf{F}_\mathrm{p}(t) = (\mathbf{I} - \Delta t \mathbf{L}_\mathrm{p}(t))^{-1} \mathbf{F}_\mathrm{p}(t_0) \text{ and} \tag{51a}$$

$$\mathbf{F}_\mathrm{i}(t) = (\mathbf{I} - \Delta t \mathbf{L}_\mathrm{i}(t))^{-1} \mathbf{F}_\mathrm{i}(t_0), \tag{51b}$$

from which $\mathbf{F}_\mathrm{e}$ can be calculated using Eq. (45). The linearization procedure yields a system of nonlinear algebraic equations with three unknowns $\mathbf{F}_\mathrm{e}$, $\mathbf{F}_\mathrm{i}$, and $\mathbf{F}_\mathrm{p}$. Its solution provides a stress state for a consistent decomposition (Eq. (45)) that fulfills the constitutive laws, which are encapsulated as generic functions (Eqs. (47) and (48)) and provided by the Constitutive Level (Section 6).

The solution scheme is implemented using a two-level predictor–corrector scheme for $\mathbf{L}_\mathrm{p}$ and $\mathbf{L}_\mathrm{i}$ (see Fig. 5), based on minimizing the residuals

$$\mathbf{R}_\mathrm{p}(\widetilde{\mathbf{L}}_\mathrm{p}, \widetilde{\mathbf{L}}_\mathrm{i}) = \widetilde{\mathbf{L}}_\mathrm{p} - \mathbf{L}_\mathrm{p}(\mathbf{M}_\mathrm{p}(\widetilde{\mathbf{L}}_\mathrm{p}, \widetilde{\mathbf{L}}_\mathrm{i})) \text{ and} \tag{52a}$$

$$\mathbf{R}_\mathrm{i}(\widetilde{\mathbf{L}}_\mathrm{p}, \widetilde{\mathbf{L}}_\mathrm{i}) = \widetilde{\mathbf{L}}_\mathrm{i} - \mathbf{L}_\mathrm{i}(\mathbf{M}_\mathrm{i}(\widetilde{\mathbf{L}}_\mathrm{p}, \widetilde{\mathbf{L}}_\mathrm{i})), \tag{52b}$$

where $\widetilde{\mathbf{L}}_\mathrm{p}$ and $\widetilde{\mathbf{L}}_\mathrm{i}$ denote the predicted values of $\mathbf{L}_\mathrm{p}$ and $\mathbf{L}_\mathrm{i}$. The coupled system of Eqs. (52a) and (52b) is solved using a modified Newton–Raphson scheme with variable step length α within a staggered iterative loop until a consistent solution is achieved. The solution algorithm is outlined in Algorithm 2. The Newton–Raphson scheme is regarded converged when the residual drops below a given tolerance

$$\varepsilon_\mathrm{p} = \max(\varepsilon_\mathrm{a}, \varepsilon_\mathrm{r} \|\mathbf{L}_\mathrm{p}\|_2, \varepsilon_\mathrm{r} \|\widetilde{\mathbf{L}}_\mathrm{p}\|_2) \text{ and} \tag{53a}$$

$$\varepsilon_\mathrm{i} = \max(\varepsilon_\mathrm{a}, \varepsilon_\mathrm{r} \|\mathbf{L}_\mathrm{i}\|_2, \varepsilon_\mathrm{r} \|\widetilde{\mathbf{L}}_\mathrm{i}\|_2) \tag{53b}$$

that depends on specified values of absolute and relative errors (ε_a and ε_r).

Algorithm 2. Self-consistent integration of kinematic quantities at a fixed internal material state.

Data: $[\mathbf{F}]_{t_n}$, $[\mathbf{F}_\mathrm{p}]_{t_{n-1}}$, $[\mathbf{F}_\mathrm{i}]_{t_{n-1}}$
Result: $[\mathbf{F}_\mathrm{p}]_{t_n}$, $[\mathbf{F}_\mathrm{i}]_{t_n}$, $[\mathbf{F}_\mathrm{e}]_{t_n}$, $[\mathbf{S}]_{t_n}$

Initialisation:

$[\widetilde{\mathbf{L}_\mathrm{p}}]^0_{t_n} = [\mathbf{L}_\mathrm{p}]_{t_{n-1}}$,
$[\widetilde{\mathbf{L}_\mathrm{i}}]^0_{t_n} = [\mathbf{L}_\mathrm{i}]_{t_{n-1}}$,

$j = 1$
$\mathbf{L}_\mathrm{i}$ loop:
while $\|\mathbf{R}_\mathrm{i}\|_2 \geq \epsilon_\mathrm{i}$ **do**
  $[\mathbf{F}_\mathrm{i}]_{t_n} = \left(\mathbf{I} - \triangle t [\widetilde{\mathbf{L}_\mathrm{i}}]^{j-1}_{t_n}\right)^{-1} [\mathbf{F}_\mathrm{i}]_{t_{n-1}}$
  $k = 1$
  $\mathbf{L}_\mathrm{p}$ loop:
  while $\|\mathbf{R}_\mathrm{p}\|_2 \geq \epsilon_\mathrm{p}$ **do**
    $[\mathbf{F}_\mathrm{p}]_{t_n} = \left(\mathbf{I} - \triangle t [\widetilde{\mathbf{L}_\mathrm{p}}]^{k-1}_{t_n}\right)^{-1} [\mathbf{F}_\mathrm{p}]_{t_{n-1}}$
    $[\mathbf{F}_\mathrm{e}]_{t_n} = [\mathbf{F}]_{t_n} [\mathbf{F}_\mathrm{p}{}^{-1}]_{t_n} [\mathbf{F}_\mathrm{i}{}^{-1}]_{t_n}$
    $[\mathbf{S}]_{t_n} = f\left([\mathbf{F}_\mathrm{e}]_{t_n}, [\mathbf{F}_\mathrm{i}]_{t_n}\right)$
    $\mathbf{R}_\mathrm{p} = [\widetilde{\mathbf{L}_\mathrm{p}}]^{k-1}_{t_n} - \mathbf{L}_\mathrm{p}\left([\mathbf{S}]_{t_n}, [\mathbf{F}_\mathrm{i}]_{t_n}\right)$
    $[\widetilde{\mathbf{L}_\mathrm{p}}]^{k}_{t_n} = [\widetilde{\mathbf{L}_\mathrm{p}}]^{k-1}_{t_n} - \alpha_\mathrm{p} \left(\partial_{\widetilde{\mathbf{L}_\mathrm{p}}} \mathbf{R}_\mathrm{p}\right)^{-1} \mathbf{R}_\mathrm{p}$
    $k = k+1$
  end
  $\mathbf{R}_\mathrm{i} = [\widetilde{\mathbf{L}_\mathrm{i}}]^{j-1}_{t_n} - \mathbf{L}_\mathrm{i}\left([\mathbf{S}]_{t_n}, [\mathbf{F}_\mathrm{i}]_{t_n}\right)$
  $[\widetilde{\mathbf{L}_\mathrm{i}}]^{j}_{t_n} = [\widetilde{\mathbf{L}_\mathrm{i}}]^{j-1}_{t_n} - \alpha_\mathrm{i} \left(\partial_{\widetilde{\mathbf{L}_\mathrm{i}}} \mathbf{R}_\mathrm{i}\right)^{-1} \mathbf{R}_\mathrm{i}$
  $j = j+1$
end

5.2.2. Internal material state

Above the Constituent Level, the internal material state ω is treated as an abstract container that encapsulates all model-specific aspects of its evolution (Section 6). The state ω evolves simultaneously with the kinematic quantities at a rate

$$\dot{\omega} = g(\mathbf{S}, \omega). \tag{54}$$

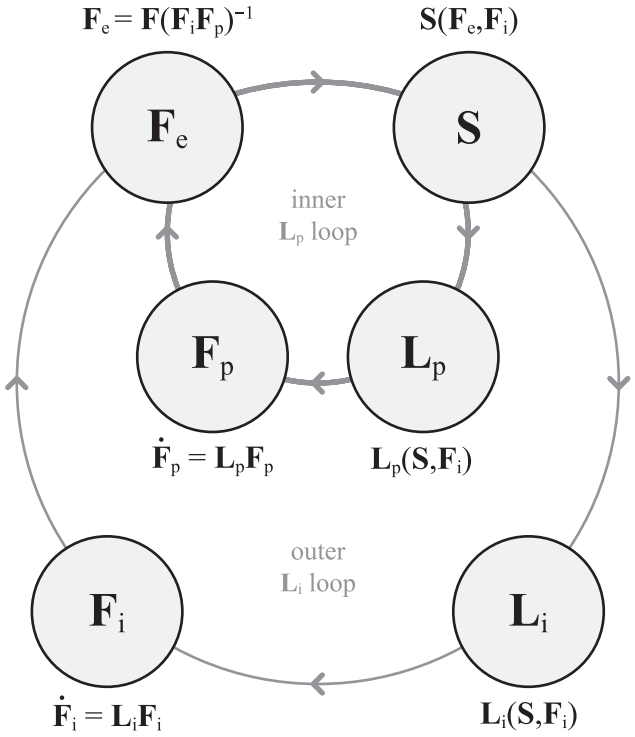

Fig. 5. Self-consistent integration of kinematic quantities at a fixed internal material state.

In some cases, it might be necessary in the constitutive description to express a change in the state in terms of an instantaneous jump rather than by a rate of change. For this case, an additional rate-independent constitutive equation is defined:

$$\Delta\omega = g_\Delta(\mathbf{S}, \omega). \tag{55}$$

The time integration of the inelastic flow relations (Fig. 5) is staggered with respect to the integration of ω (Fig. 6). Different schemes can be used to accomplish the state integration. The following schemes are implemented and a comparison of their performance within DAMASK has been compiled by Kords [124].

5.2.2.1. Fixed-point iteration. This implicit Euler scheme, used by, for instance, Kalidindi et al. [125], iteratively evaluates the state and the stress until a consistent solution is found. The residual (change between iterations) of the fixed point scheme is used as the convergence criterion, however, a converged solution is not guaranteed. To improve convergence and stability, the iterative state correction is adaptively controlled in DAMASK. This time integration scheme will always be first-order accurate for the typical case of a viscous state evolution. A schematic of the integration procedure is given in Fig. 7(a).

5.2.2.2. Explicit Euler integrator. This simple integration scheme consists of a single explicit time step without any control of stability:

$$\omega(t) = \omega(t_0) + \dot{\omega}(t_0)\Delta t + \Delta\omega(t_0). \tag{56}$$

The stress is calculated *after* the state update, so that it is consistent with the state. A schematic of the integration procedure is given in Fig. 7(b).

5.2.2.3. Adaptive Euler integrator. The explicit Euler integrator is enhanced by using a second evaluation of the state integration to estimate the error:

$$\varepsilon = \frac{\Delta t}{2}(\dot{\omega}(t) - \dot{\omega}(t_0)). \tag{57}$$

This error estimate is used to reduce the time step in case a predefined tolerance is not achieved. Since a cutback of the time step would have

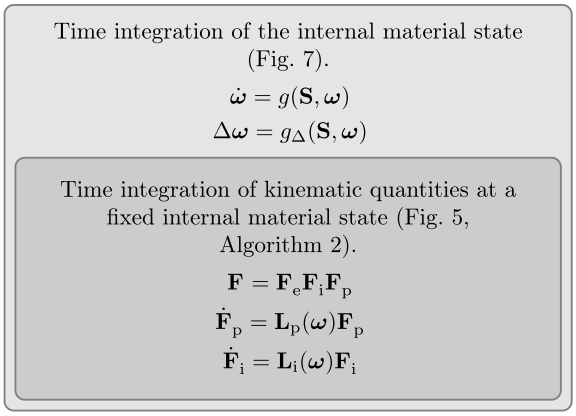

Fig. 6. Self-consistent staggered time integration of inelastic flow rules and the internal material state. Figure adopted from [124].

no influence on an instantaneous jump in the state, it is natural to not include the state jump in the error estimate. As for the explicit Euler integrator, the stress is calculated after the state evolution. A schematic of the integration procedure is given in Fig. 7(c).

5.2.2.4. Fourth-order explicit Runge–Kutta integrator. The Euler integration schemes described above are first-order accurate, *i.e.* they produce a temporal error of the order of Δt. Higher-order integration schemes reduce this error. The fourth-order Runge–Kutta integrator is such a scheme with an error of the order of Δt^4. In this scheme, the material state at the end of the increment is calculated on the basis of a weighted average of four different rates:

1. $\mathbf{g}_1^{\mathrm{RK}}$ at the beginning of the increment based on the state $\omega(t_0)$,
2. $\mathbf{g}_2^{\mathrm{RK}}$ in the middle of the increment based on the state $\omega(t_0) + \frac{1}{2}\mathbf{g}_1^{\mathrm{RK}}\Delta t$,
3. $\mathbf{g}_3^{\mathrm{RK}}$ in the middle of the increment based on the state $\omega(t_0) + \frac{1}{2}\mathbf{g}_2^{\mathrm{RK}}\Delta t$, and
4. $\mathbf{g}_4^{\mathrm{RK}}$ at the end of the increment based on the state $\omega(t_0) + \mathbf{g}_3^{\mathrm{RK}}\Delta t$.

For state evaluations at the intermediate time step $t_0 + \Delta t/2$, the stress is calculated coincidentally using only half the deformation increment. Therefore, a total of four state and stress evaluations are required. This additional computational cost often pays off in nonlinear problems, since it allows much larger time increments than first-order methods for a given temporal tolerance. A schematic of the integration procedure is given in Fig. 7(d) and the Butcher tableau in Table 1(a).

5.2.2.5. Fifth-order adaptive Runge–Kutta integrator. This fifth-order adaptive Runge–Kutta integrator [126] combines the high-order solution of the fourth-order explicit Runge–Kutta integrator with the possibility of the adaptive Euler integrator to control the error by an additional evaluation of stress and state. The Butcher tableau (see Table 1(b)) is constructed in such a way that the additional evaluation can also be used for the final solution, thus increasing its order to five. A schematic of the integration procedure is given in Fig. 7(e).

5.3. Stress tangent

Depending on the numerical method, the solution of the mechanical equilibrium Eq. (3) might require the tangent of stress with respect to the deformation gradient. For constitutive laws where no closed form solution of this tangent is available, it is typically determined by a numerical perturbation technique [64,125,127]. This is, however, computationally expensive as the constituent response (see Section 5.2) has to be evaluated for each perturbation direction.

In DAMASK, the stress tangent is analytically derived. The first Piola–Kirchhoff stress $\mathbf{P}$ is related to the second Piola–Kirchhoff stress $\mathbf{S}$ through

$$\mathbf{P} = \mathbf{F}_\mathrm{e}\mathbf{F}_\mathrm{i}\mathbf{S}\mathbf{F}_\mathrm{p}^{-\mathrm{T}} = \mathbf{F}\mathbf{F}_\mathrm{p}^{-1}\mathbf{S}\mathbf{F}_\mathrm{p}^{-\mathrm{T}}. \tag{58}$$

Therefore, the sought tangent is given as

$$\begin{aligned}\frac{\mathrm{d}\mathbf{P}}{\mathrm{d}\mathbf{F}} = {} & [\mathbf{I} \boxtimes (\mathbf{F}_\mathrm{p}^{-1}\mathbf{S}\mathbf{F}_\mathrm{p}^{-\mathrm{T}})] : \mathbb{I} + [\mathbf{F} \boxtimes (\mathbf{S}\mathbf{F}_\mathrm{p}^{-\mathrm{T}})] : \frac{\mathrm{d}\mathbf{F}_\mathrm{p}^{-1}}{\mathrm{d}\mathbf{F}} \\ & + [(\mathbf{F}\mathbf{F}_\mathrm{p}^{-1}) \boxtimes \mathbf{F}_\mathrm{p}^{-\mathrm{T}}] : \frac{\mathrm{d}\mathbf{S}}{\mathrm{d}\mathbf{F}} + [(\mathbf{F}\mathbf{F}_\mathrm{p}^{-1}\mathbf{S}) \boxtimes \mathbf{I}] : \frac{\mathrm{d}\mathbf{F}_\mathrm{p}^{-\mathrm{T}}}{\mathrm{d}\mathbf{F}}.\end{aligned} \tag{59}$$

Using the chain-rule, $\mathrm{d}\mathbf{S}/\mathrm{d}\mathbf{F}$ can be expressed as

$$\frac{\mathrm{d}\mathbf{S}}{\mathrm{d}\mathbf{F}} = \frac{\partial \mathbf{S}}{\partial \mathbf{F}_\mathrm{e}} : \frac{\mathrm{d}\mathbf{F}_\mathrm{e}}{\mathrm{d}\mathbf{F}} + \frac{\partial \mathbf{S}}{\partial \mathbf{F}_\mathrm{i}} : \frac{\mathrm{d}\mathbf{F}_\mathrm{i}}{\mathrm{d}\mathbf{F}}, \tag{60}$$

where the sensitivities $\partial\mathbf{S}/\partial\mathbf{F}_\mathrm{e}$ and $\partial\mathbf{S}/\partial\mathbf{F}_\mathrm{i}$ are given by the elastic constitutive law (see Appendix D for details). The total derivative of Eq. (45) yields

$$\frac{\mathrm{d}\mathbf{F}_\mathrm{e}}{\mathrm{d}\mathbf{F}} = [\mathbf{I} \boxtimes (\mathbf{F}_\mathrm{p}^{-1}\mathbf{F}_\mathrm{i}^{-1})] + [\mathbf{F} \boxtimes \mathbf{F}_\mathrm{i}^{-1}] : \frac{\mathrm{d}\mathbf{F}_\mathrm{p}^{-1}}{\mathrm{d}\mathbf{F}} + [(\mathbf{F}\mathbf{F}_\mathrm{p}^{-1}) \boxtimes \mathbf{I}] : \frac{\mathrm{d}\mathbf{F}_\mathrm{i}^{-1}}{\mathrm{d}\mathbf{F}} \tag{61}$$

and the differential

$$\frac{\mathrm{d}\mathbf{F}_\mathrm{i}}{\mathrm{d}\mathbf{F}} = -[\mathbf{F}_\mathrm{i} \boxtimes \mathbf{F}_\mathrm{i}] : \frac{\mathrm{d}\mathbf{F}_\mathrm{i}^{-1}}{\mathrm{d}\mathbf{F}} \tag{62}$$

can be expressed based on the differential of its inverse. Taking total derivatives of Eqs. (51a) and (51b) provides the differentials of the inverse components $\mathbf{F}_\mathrm{p}^{-1}$ and $\mathbf{F}_\mathrm{i}^{-1}$ as

$$\begin{aligned}\frac{\mathrm{d}\mathbf{F}_\mathrm{p}^{-1}}{\mathrm{d}\mathbf{F}} &= -\Delta t\,[\mathbf{F}_{\mathrm{p}0}^{-1} \boxtimes \mathbf{I}] : \frac{\mathrm{d}\mathbf{L}_\mathrm{p}}{\mathrm{d}\mathbf{S}} : \frac{\mathrm{d}\mathbf{S}}{\mathrm{d}\mathbf{F}} \\ &= -\Delta t\,[\mathbf{F}_{\mathrm{p}0}^{-1} \boxtimes \mathbf{I}] : \left[\frac{\partial \mathbf{L}_\mathrm{p}}{\partial \mathbf{S}} + \frac{\partial \mathbf{L}_\mathrm{p}}{\partial \mathbf{F}_\mathrm{i}} : \frac{\mathrm{d}\mathbf{F}_\mathrm{i}}{\mathrm{d}\mathbf{S}}\right] : \frac{\mathrm{d}\mathbf{S}}{\mathrm{d}\mathbf{F}}\end{aligned} \tag{63a}$$

and

$$\begin{aligned}\frac{\mathrm{d}\mathbf{F}_\mathrm{i}^{-1}}{\mathrm{d}\mathbf{F}} &= -\Delta t\,[\mathbf{F}_{\mathrm{i}0}^{-1} \boxtimes \mathbf{I}] : \frac{\mathrm{d}\mathbf{L}_\mathrm{i}}{\mathrm{d}\mathbf{S}} : \frac{\mathrm{d}\mathbf{S}}{\mathrm{d}\mathbf{F}} \\ &= -\Delta t\,[\mathbf{F}_{\mathrm{i}0}^{-1} \boxtimes \mathbf{I}] : \left[\frac{\partial \mathbf{L}_\mathrm{i}}{\partial \mathbf{S}} + \frac{\partial \mathbf{L}_\mathrm{i}}{\partial \mathbf{F}_\mathrm{i}} : \frac{\mathrm{d}\mathbf{F}_\mathrm{i}}{\mathrm{d}\mathbf{S}}\right] : \frac{\mathrm{d}\mathbf{S}}{\mathrm{d}\mathbf{F}}.\end{aligned} \tag{63b}$$

The sensitivities $\partial\mathbf{L}_\mathrm{p}/\partial\mathbf{S}$ and $\partial\mathbf{L}_\mathrm{i}/\partial\mathbf{S}$ are provided by the constitutive laws (see Appendix D for details). $\mathrm{d}\mathbf{F}_\mathrm{i}/\mathrm{d}\mathbf{S}$, required in Eqs. (63a) and (63b), is obtained by taking the total derivative of Eq. (51b):

$$\frac{\mathrm{d}\mathbf{F}_\mathrm{i}}{\mathrm{d}\mathbf{S}} = -[\mathbf{F}_\mathrm{i} \boxtimes \mathbf{F}_\mathrm{i}] : \frac{\mathrm{d}\mathbf{F}_\mathrm{i}^{-1}}{\mathrm{d}\mathbf{S}} = \Delta t\,[\mathbf{F}_\mathrm{i}\mathbf{F}_{\mathrm{i}0}^{-1} \boxtimes \mathbf{F}_\mathrm{i}] : \left[\frac{\partial \mathbf{L}_\mathrm{i}}{\partial \mathbf{S}} + \frac{\partial \mathbf{L}_\mathrm{i}}{\partial \mathbf{F}_\mathrm{i}} : \frac{\mathrm{d}\mathbf{F}_\mathrm{i}}{\mathrm{d}\mathbf{S}}\right], \tag{64}$$

resulting in the implicit equation

$$\left[\mathbb{I} - \Delta t\,[\mathbf{F}_\mathrm{i}\mathbf{F}_{\mathrm{i}0}^{-1} \boxtimes \mathbf{F}_\mathrm{i}] : \frac{\partial \mathbf{L}_\mathrm{i}}{\partial \mathbf{F}_\mathrm{i}}\right] : \frac{\mathrm{d}\mathbf{F}_\mathrm{i}}{\mathrm{d}\mathbf{S}} = \Delta t\,[\mathbf{F}_\mathrm{i}\mathbf{F}_{\mathrm{i}0}^{-1} \boxtimes \mathbf{F}_\mathrm{i}] : \frac{\partial \mathbf{L}_\mathrm{i}}{\partial \mathbf{S}}, \tag{65}$$

which can be solved for $\mathrm{d}\mathbf{F}_\mathrm{i}/\mathrm{d}\mathbf{S}$. This allows the evaluation of Eqs. (61) and (62), which is substituted back into Eq. (60), to obtain:

$$\begin{aligned}\Bigg[\mathbb{I} + \Delta t\frac{\partial \mathbf{S}}{\partial \mathbf{F}_\mathrm{e}} : [(\mathbf{F}\mathbf{F}_{\mathrm{p}0}^{-1}) \boxtimes \mathbf{F}_\mathrm{i}^{-1}] : \frac{\mathrm{d}\mathbf{L}_\mathrm{p}}{\mathrm{d}\mathbf{S}} + \Delta t\frac{\partial \mathbf{S}}{\partial \mathbf{F}_\mathrm{e}} : [(\mathbf{F}\mathbf{F}_\mathrm{p}^{-1}\mathbf{F}_{\mathrm{p}0}^{-1}) \boxtimes \mathbf{I}] : \frac{\mathrm{d}\mathbf{L}_\mathrm{i}}{\mathrm{d}\mathbf{S}} \\ - \Delta t\frac{\partial \mathbf{S}}{\partial \mathbf{F}_\mathrm{i}} : [(\mathbf{F}_\mathrm{i}\mathbf{F}_{\mathrm{i}0}^{-1}) \boxtimes \mathbf{F}_\mathrm{i}] : \frac{\mathrm{d}\mathbf{L}_\mathrm{i}}{\mathrm{d}\mathbf{S}}\Bigg] : \frac{\mathrm{d}\mathbf{S}}{\mathrm{d}\mathbf{F}} = \frac{\partial \mathbf{S}}{\partial \mathbf{F}_\mathrm{e}} : [\mathbf{I} \boxtimes (\mathbf{F}_\mathrm{p}^{-1}\mathbf{F}_\mathrm{i}^{-1})],\end{aligned} \tag{66}$$

which is solved for $\mathrm{d}\mathbf{S}/\mathrm{d}\mathbf{F}$ and used together with Eq. (63a) to evaluate Eq. (59).

6. Constitutive laws

The Constitutive Level forms the foundation of the hierarchical DAMASK structure. It is comprised of constitutive laws describing the

$i = 0$
$\mathbf{S}_0 = \mathbf{S}(t_0)$
$\boldsymbol{\omega}_0 = \boldsymbol{\omega}(t_0) + g(\mathbf{S}_0, \boldsymbol{\omega}(t_0))\Delta t$
  $i = i + 1$
  calculate $\mathbf{S}_i = \mathbf{S}(\boldsymbol{\omega}_{i-1})$
  $\boldsymbol{\omega}_i = \boldsymbol{\omega}(t_0) + g_\Delta(\mathbf{S}_i, \boldsymbol{\omega}_{i-1})$
  $\boldsymbol{\omega}_i = \boldsymbol{\omega}_i + \alpha_i\, g(\mathbf{S}_i, \boldsymbol{\omega}_i)\Delta t + (1 - \alpha_i)\, g(\mathbf{S}_0, \boldsymbol{\omega}_0)\Delta t$
Until $|\,||\boldsymbol{\omega}_i||_\infty - ||\boldsymbol{\omega}_{i-1}||_\infty\,| < \epsilon_{\mathrm{tol}}$
$\boldsymbol{\omega}(t) = \boldsymbol{\omega}_i$; $\mathbf{S}(t) = \mathbf{S}_i$

(a) Fixed-point integration scheme with adaptive damping factor α_i.

$\boldsymbol{\omega} = \boldsymbol{\omega}(t_0)$; $\mathbf{S} = \mathbf{S}(t_0)$
$\boldsymbol{\omega} = \boldsymbol{\omega} + g_\Delta(\mathbf{S}, \boldsymbol{\omega})$
$\boldsymbol{\omega} = \boldsymbol{\omega} + g(\mathbf{S}, \boldsymbol{\omega})\Delta t$
calculate $\mathbf{S}(\boldsymbol{\omega})$
$\boldsymbol{\omega}(t) = \boldsymbol{\omega}$; $\mathbf{S}(t) = \mathbf{S}$

(b) Explicit EULER integration scheme.

$\boldsymbol{\omega} = \boldsymbol{\omega}(t_0)$; $\mathbf{S} = \mathbf{S}(t_0)$; $\mathbf{g}_1^{\mathrm{RK}} = 0$
For $i = 1, ..., 3$
  $\widetilde{\Delta t} = c_{i+1}\Delta t$
  $\widetilde{\mathbf{F}}(t) = \mathbf{F}(t_0) + c_{i+1}\Delta\mathbf{F}$
  $\mathbf{g}_i^{\mathrm{RK}} = g(\mathbf{S}, \boldsymbol{\omega})$
  $\boldsymbol{\omega} = \boldsymbol{\omega}(t_0) + \sum_{j=2}^{i+1} A_{ji}\, \mathbf{g}_{j-1}^{\mathrm{RK}}\, \Delta t$
  $\boldsymbol{\omega} = \boldsymbol{\omega} + g_\Delta(\mathbf{S}, \boldsymbol{\omega})$
  calculate $\mathbf{S}(\boldsymbol{\omega}, \mathbf{F} = \widetilde{\mathbf{F}}, \Delta t = \widetilde{\Delta t})$
$\mathbf{g}_4^{\mathrm{RK}} = g(\mathbf{S}, \boldsymbol{\omega})$
$\boldsymbol{\omega} = \boldsymbol{\omega}(t_0) + \sum_{i=1}^{4} b_i\, \mathbf{g}_i^{\mathrm{RK}}\, \Delta t$
$\boldsymbol{\omega} = \boldsymbol{\omega} + g_\Delta(\mathbf{S}, \boldsymbol{\omega})$
integrate $\mathbf{S}(\boldsymbol{\omega})$
$\boldsymbol{\omega}(t) = \boldsymbol{\omega}$; $\mathbf{S}(t) = \mathbf{S}$

(d) Fourth-order RUNGE–KUTTA integration scheme. Coefficients **A**, **b**, and **c** are given in Table 1(a).

$\boldsymbol{\omega} = \boldsymbol{\omega}(t_0)$; $\mathbf{S} = \mathbf{S}(t_0)$; $\mathbf{g}_1^{\mathrm{RK}} = 0$
$\boldsymbol{\omega} = \boldsymbol{\omega} + g_\Delta(\mathbf{S}, \boldsymbol{\omega})$
$\epsilon = -\frac{1}{2}\, g(\mathbf{S}, \boldsymbol{\omega})\Delta t$
$\boldsymbol{\omega} = \boldsymbol{\omega} + g(\mathbf{S}, \boldsymbol{\omega})\Delta t$
calculate $\mathbf{S}(\boldsymbol{\omega})$
$\epsilon = \epsilon + \frac{1}{2}\, g(\mathbf{S}, \boldsymbol{\omega})\Delta t$
Yes / $\epsilon < \epsilon_{\mathrm{tol}}$ / No
$\boldsymbol{\omega}(t) = \boldsymbol{\omega}$; $\mathbf{S}(t) = \mathbf{S}$ | cutback

(c) Adaptive EULER integration scheme.

$\boldsymbol{\omega} = \boldsymbol{\omega}(t_0)$; $\mathbf{S} = \mathbf{S}(t_0)$; $\mathbf{g}_1^{\mathrm{RK}} = 0$
For $i = 1, ..., 5$
  $\widetilde{\Delta t} = c_{i+1}\Delta t$
  $\widetilde{\mathbf{F}}(t) = \mathbf{F}(t_0) + c_{i+1}\Delta\mathbf{F}$
  $\mathbf{g}_i^{\mathrm{RK}} = g(\mathbf{S}, \boldsymbol{\omega})$
  $\boldsymbol{\omega} = \boldsymbol{\omega}(t_0) + \sum_{j=2}^{i+1} A_{ji}\, \mathbf{g}_{j-1}^{\mathrm{RK}}\, \Delta t$
  $\boldsymbol{\omega} = \boldsymbol{\omega} + g_\Delta(\mathbf{S}, \boldsymbol{\omega})$
  calculate $\mathbf{S}(\boldsymbol{\omega}, \mathbf{F} = \widetilde{\mathbf{F}}, \Delta t = \widetilde{\Delta t})$
$\mathbf{g}_6^{\mathrm{RK}} = g(\mathbf{S}, \boldsymbol{\omega})$
$\boldsymbol{\omega} = \boldsymbol{\omega}(t_0) + \sum_{i=1}^{6} b_i\, \mathbf{g}_i^{\mathrm{RK}}\, \Delta t$
$\epsilon = \sum_{i=1}^{6} d_i\, \mathbf{g}_i^{\mathrm{RK}}\, \Delta t$
$\boldsymbol{\omega} = \boldsymbol{\omega} + g_\Delta(\mathbf{S}, \boldsymbol{\omega})$
integrate $\mathbf{S}(\boldsymbol{\omega})$
$\boldsymbol{\omega}(t) = \boldsymbol{\omega}$; $\mathbf{S}(t) = \mathbf{S}$

(e) Fifth-order RUNGE–KUTTA CASH–KARP integration scheme. Coefficients **A**, **b**, **c** and **d** are given in Table 1(b).

Fig. 7. Integration schemes for the internal material state $\boldsymbol{\omega}$. Figure adopted from [124].

mechanical, thermal, and damage response of each constituent. Each constitutive law is internally parametrized by a set of state variables. The choice of state variables reflects the degree of sophistication of the constitutive law, ranging from empirical descriptions, which are computationally efficient yet limited in accuracy, to physics-based descriptions with higher computational demands and accuracy. While empirical descriptions rely solely on data fitting, physics-based parameters can in many cases be determined by lower scale simulations or direct experimental observations.

The objective of the CONSTITUTIVE LEVEL is therefore twofold: (i) to provide the fluxes, sources, and inelastic velocity gradients associated with the mechanical, thermal, and damage behavior, and (ii) to provide

Table 1
Butcher tableaus for higher-order Runge–Kutta integration schemes. The notation is given in the upper right corner.

(a) Fourth-order Runge–Kutta integration scheme.

0	0		**c**	**A**
$\frac{1}{2}$	$\frac{1}{2}$	0		$\mathbf{b}^{\mathrm{T}}$
$\frac{1}{2}$	0	$\frac{1}{2}$	0	
1	0	0	1	0
	$\frac{1}{6}$	$\frac{1}{3}$	$\frac{1}{3}$	$\frac{1}{6}$

(b) Fifth-order Runge–Kutta Cash–Karp integration scheme.

0	0				**c**	**A**
$\frac{1}{5}$	$\frac{1}{5}$	0				$\mathbf{b}^{\mathrm{T}}$
$\frac{3}{10}$	$\frac{3}{40}$	$\frac{9}{40}$	0			$\mathbf{d}^{\mathrm{T}}$
$\frac{3}{5}$	$\frac{3}{10}$	$-\frac{9}{10}$	$\frac{6}{5}$	0		
1	$-\frac{11}{54}$	$\frac{5}{2}$	$-\frac{70}{27}$	$\frac{35}{27}$	0	
$\frac{7}{8}$	$\frac{1631}{55296}$	$\frac{175}{512}$	$\frac{575}{13824}$	$\frac{44275}{110592}$	$\frac{253}{4096}$	0
	$\frac{37}{378}$	0	$\frac{250}{621}$	$\frac{125}{594}$	0	$\frac{512}{1771}$
	$\frac{2825}{27648}$	0	$\frac{18575}{48384}$	$\frac{13525}{55296}$	$\frac{277}{14336}$	$\frac{1}{4}$

laws for the evolution of the respective internal state variables.

DAMASK provides modules for elastic, plastic, thermal, and damage behavior described in the following.

6.1. Elasticity

The purpose of an elastic law is to provide the second Piola–Kirchhoff stress associated with the elastic Green–Lagrange strain $\mathbf{E}$ (Eq. (48)).

6.1.1. Generalized Hooke's law

The generalized Hooke's law

$$\mathbf{S} = \mathbb{C} : \mathbf{E} \tag{67}$$

relates the Green–Lagrange strain $\mathbf{E}$ to the second Piola–Kirchhoff stress by an elastic stiffness $\mathbb{C}$, inheriting the symmetry of the underlying crystal lattice.[11]

6.2. Plasticity

The purpose of the plasticity law is to provide the plastic velocity gradient $\mathbf{L}_\mathrm{p}$ as a function of the applied Mandel stress $\mathbf{M}_\mathrm{p}$ (Eq. (47a)). This, typically non-linear, relation depends on a set of evolving internal state variables. Therefore, a set of evolution equations for these state variables must be additionally provided (Eqs. (54) and (55)).

Plasticity, in crystalline materials, occurs on well-defined deformation systems[12] specific to the crystallographic lattice. The plastic velocity gradient $\mathbf{L}_\mathrm{p}$ is thus calculated as the sum over the individual shear contributions $\dot{\gamma}^\alpha$ on those systems α:

$$\mathbf{L}_\mathrm{p} = \sum_\alpha \dot{\gamma}^\alpha \underbrace{(\mathbf{s}_\mathrm{s}^\alpha \otimes \mathbf{n}_\mathrm{s}^\alpha)}_{=:\mathbf{P}^\alpha_\mathrm{Schmid}}, \tag{68}$$

with $\mathbf{s}_\mathrm{s}^\alpha$ and $\mathbf{n}_\mathrm{s}^\alpha$ being unit vectors along the shear direction and shear plane normal. DAMASK contains definitions of slip system families for face-centered cubic (fcc), body-centered cubic (bcc), hexagonal (hex) and body-centered tetragonal (bct) lattice types as specified in Table 21.

The driving force τ^α for $\dot{\gamma}^\alpha$ is typically given by Schmid's law [131–135]

$$\tau^\alpha = \mathbf{M}_\mathrm{p} : \mathbf{P}^\alpha_\mathrm{Schmid}. \tag{69}$$

A deviation from Schmid's law that is exhibited by some bcc materials [25,26,136–139] can be represented by augmenting the driving force by non-Schmid contributions

$$\tau^\alpha = \mathbf{M}_\mathrm{p} : (\mathbf{P}^\alpha_\mathrm{Schmid} + \mathbf{P}^\alpha_\mathrm{non\text{-}Schmid}). \tag{70}$$

The specific plasticity models implemented in DAMASK are described in the following.

6.2.1. Isotropic plasticity

The isotropic plasticity model combines an isochoric response due to the deviatoric stress $\mathbf{M}_\mathrm{p}^\mathrm{dev} = \mathbf{M}_\mathrm{p} - \operatorname{tr}\mathbf{M}_\mathrm{p}/3$ (in the lattice configuration) with a dilatational response that arises from the hydrostatic pressure (mean stress $\mathbf{M}_\mathrm{i}^\mathrm{sph} = \mathbf{I}\operatorname{tr}\mathbf{M}_\mathrm{i}/3$ in the intermediate configuration). This formulation of plasticity deliberately ignores any orientation dependent behavior, *i.e.* does not explicitly account for slip or twin systems. The internal state parameterization and kinetics of this model are inspired by the phenomenological crystal plasticity model that was introduced by Peirce et al. [140] and postulates an internal deformation resistance, termed ξ, and a power-law relation between driving force and deformation rate.

The strain rate connected to isochoric deformation is driven by J_2, *i.e.* the second invariant of $\mathbf{M}_\mathrm{p}^\mathrm{dev}$:

$$\dot{\gamma}_\mathrm{p} = \dot{\gamma}_0 \left(\frac{\sqrt{3J_2}}{M\xi}\right)^n = \dot{\gamma}_0 \left(\sqrt{\frac{3}{2}}\frac{\|\mathbf{M}_\mathrm{p}^\mathrm{dev}\|_\mathrm{F}}{M\xi}\right)^n, \tag{71}$$

where $\dot{\gamma}_0$ denotes a reference strain rate, n the stress exponent, and M the orientation (Taylor) factor. The associated plastic velocity gradient $\mathbf{L}_\mathrm{p}$, acting in the lattice configuration, is then formulated as

$$\mathbf{L}_\mathrm{p} = \frac{\dot{\gamma}_\mathrm{p}}{M}\frac{\mathbf{M}_\mathrm{p}^\mathrm{dev}}{\|\mathbf{M}_\mathrm{p}^\mathrm{dev}\|_\mathrm{F}}. \tag{72}$$

To allow for dilatational responses (for instance in a void region of the geometry), a similar constitutive law is formulated for the dilatational rate $\dot{\gamma}_\mathrm{i}$ and the dilatational velocity gradient $\mathbf{L}_\mathrm{i,plastic}$ in the intermediate configuration as

$$\begin{aligned}\mathbf{L}_\mathrm{i,plastic} &= \frac{\dot{\gamma}_\mathrm{i}}{M}\frac{\mathbf{M}_\mathrm{i}^\mathrm{sph}}{\|\mathbf{M}_\mathrm{i}^\mathrm{sph}\|_\mathrm{F}} \\ &= \frac{\dot{\gamma}_0}{M}\left(\sqrt{\frac{3}{2}}\frac{\|\mathbf{M}_\mathrm{i}^\mathrm{sph}\|_\mathrm{F}}{M\xi}\right)^n \frac{\mathbf{M}_\mathrm{i}^\mathrm{sph}}{\|\mathbf{M}_\mathrm{i}^\mathrm{sph}\|_\mathrm{F}}.\end{aligned} \tag{73}$$

Analogous to the phenomenological Crystal Plasticity (CP) hardening model of Hutchinson [141] and the Phenomenological Crystal Plasticity presented later on, the scalar resistance ξ to plastic flow evolves asymptotically from its initial value ξ_0 towards a final value

$$\xi^*_\infty = \xi_\infty + \frac{(\operatorname{arsinh}(\dot{\gamma}/c_1)^{1/c_2})^{1/c_3}}{c_4(\dot{\gamma}/\dot{\gamma}_0)^{1/n}} \tag{74}$$

that can be made dependent on the rate of shear through adjustment constants c_1–c_4. The kinetics of resistance evolution

$$\dot{\xi} = \dot{\gamma}(h_0 + h_\mathrm{ln}\ln\dot{\gamma})\left|1 - \frac{\xi}{\xi^*_\infty}\right|^a \operatorname{sgn}\left(1 - \frac{\xi}{\xi^*_\infty}\right) \tag{75}$$

are controlled by the initial hardening h_0, strain rate sensitivity parameter h_ln, and exponent a and are proportional to the shear rate that is determined either by the full or deviatoric component of $\mathbf{M}_\mathrm{p}$, depending

[11] For non-crystalline materials, isotropic and orthotropic symmetries are defined.

[12] This assumption is typically justified for dislocation slip [128] and, when spatially resolved twin formation is not of interest, for mechanical twinning [129,130].

on whether the dilatational aspects of this constitutive law are considered, respectively:

$$\dot{\gamma} = \dot{\gamma}_0 \left(\sqrt{\frac{3}{2}} \frac{\|\mathbf{M}_\mathrm{p}\|_\mathrm{F}}{M\xi} \right)^n . \tag{76}$$

6.2.2. Phenomenological crystal plasticity

This widely used and simple model was first described by Hutchinson [141] for fcc crystals and extended for twinning by Kalidindi [129]. It is implemented in modified form in DAMASK for all available crystal structures. The plastic component of the internal state is parametrized in terms of resistances ξ on $N_{\mathrm{s+tw}} = N_\mathrm{s} + N_\mathrm{tw}$ slip and twin systems.

The resistances on the $\alpha = 1, \ldots, N_\mathrm{s}$ slip systems evolve from their initial value ξ_0 asymptotically to a system-dependent saturation value and depend on shear on slip and twin systems (see Appendix E) according to the relationship

$$\begin{aligned} \dot{\xi}^\alpha = {} & h_0^{\text{s-s}} (1 + c_1 (f_\mathrm{tw}^\mathrm{tot})^{c_2}) (1 + h_\mathrm{int}^\alpha) \\ & \times \sum_{\alpha'=1}^{N_\mathrm{s}} |\dot{\gamma}^{\alpha'}| \left| 1 - \frac{\xi^{\alpha'}}{\xi_\infty^{\alpha'}} \right|^a \operatorname{sgn}\left(1 - \frac{\xi^{\alpha'}}{\xi_\infty^{\alpha'}} \right) h^{\alpha\alpha'} + \sum_{\beta'=1}^{N_\mathrm{tw}} \dot{\gamma}^{\beta'} h^{\alpha\beta'}, \end{aligned} \tag{77}$$

where $f_\mathrm{tw}^\mathrm{tot}$ is the total twin volume fraction, h are the components of the slip–slip [142,143] and slip–twin interaction matrices respectively, $h_0^{\text{s-s}}$, h_int, c_1, and c_2 are model-specific fitting parameters, and ξ_∞ is bounding the resistance evolution.

The resistances on the $\beta = 1, \ldots, N_\mathrm{tw}$ twin systems evolve in a similar way:

$$\dot{\xi}^\beta = h_0^{\text{tw-s}} \left(\sum_{\alpha=1}^{N_\mathrm{s}} |\gamma^\alpha| \right)^{c_3} \sum_{\alpha'=1}^{N_\mathrm{s}} |\dot{\gamma}^{\alpha'}| \, h^{\beta\alpha'} + h_0^{\text{tw-tw}} (f_\mathrm{tw}^\mathrm{tot})^{c_4} \sum_{\beta'=1}^{N_\mathrm{tw}} \dot{\gamma}^{\beta'} h^{\beta\beta'}, \tag{78}$$

where $h_0^{\text{tw-s}}$, $h_0^{\text{tw-tw}}$, c_3, and c_4 are model-specific fitting parameters.

Given a set of current slip resistances, shear on each slip system evolves at a rate of

$$\dot{\gamma}^\alpha = (1 - f_\mathrm{tw}^\mathrm{tot}) \dot{\gamma}_0^\alpha \left| \frac{\tau^\alpha}{\xi^\alpha} \right|^n \operatorname{sgn}(\tau^\alpha). \tag{79}$$

Again, slip due to mechanical twinning is handled in a slightly different way that accounts for the unidirectional character of twin formation:

$$\dot{\gamma} = (1 - f_\mathrm{tw}^\mathrm{tot}) \dot{\gamma}_0 \left| \frac{\tau}{\xi} \right|^n \mathcal{H}(\tau), \tag{80}$$

where $\mathcal{H}$ is the Heaviside or unit step function.

The total twin volume fraction is given by

$$f_\mathrm{tw}^\mathrm{tot} = \max\left(\sum_{\beta=1}^{N_\mathrm{tw}} \underbrace{\gamma^\beta / \gamma_\mathrm{char}^\beta}_{=: f_\mathrm{tw}^\beta}, 1.0 \right), \tag{81}$$

where γ_char is the characteristic shear due to mechanical twinning, the value of which depends on the twin system.

6.2.3. Dislocation density based crystal plasticity

This dislocation density-based model follows the approach presented by Ma and Roters [144]—itself an extension of the Three Internal Variable Model (3IVM) by Roters et al. [145]—and the subsequent Finite Element Method (FEM) implementations [65,146] for dislocation glide. This physics-based approach increases complexity due to the larger state and the associated evolution equations but has the advantage that the values, or at least their order of magnitude, are known for most parameters. Deformation twinning is incorporated following the analytical Twinning Induced Plasticity (TWIP) model suggested by Steinmetz et al. [18]. To account for the Transformation Induced Plasticity (TRIP) behavior of fcc metals, the $\gamma \rightarrow \varepsilon$ martensitic transformation is included, such that the current constitutive model has the capability to simulate the evolution of dislocation densities, twin volume fractions, and ε-martensite volume fractions [19]. Furthermore, Jia et al. [147,148] enriched the model by shear-banding deformation modes (see Section 7.7).

The TWIP/TRIP constitutive model is built on internal microstructure variables and their respective kinetics. This means that the constitutive equations are parametrized in terms of the dislocation density ϱ, the dipole dislocation density ϱ_di, the twin volume fraction f_tw, and the ε-martensite volume fraction f_tr on $\chi = 1, \ldots, N_\mathrm{tr}$ transformation systems.

Following the approach of Kalidindi [129], the contribution of mechanical twinning and phase transformation are taken into account as additional terms in the plastic velocity gradient:

$$\begin{aligned} \mathbf{L}_\mathrm{p} = {} & (1 - f_\mathrm{tw}^\mathrm{tot} - f_\mathrm{tr}^\mathrm{tot}) \sum_{\alpha=1}^{N_\mathrm{s}} \dot{\gamma}^\alpha \mathbf{s}_\mathrm{s}^\alpha \otimes \mathbf{n}_\mathrm{s}^\alpha + \sum_{\beta=1}^{N_\mathrm{tw}} \dot{\gamma}^\beta \mathbf{s}_\mathrm{tw}^\beta \otimes \mathbf{n}_\mathrm{tw}^\beta \\ & + \sum_{\chi=1}^{N_\mathrm{tr}} \dot{\gamma}^\chi \mathbf{s}_\mathrm{tr}^\chi \otimes \mathbf{n}_\mathrm{tr}^\chi . \end{aligned} \tag{82}$$

The Orowan equation [149] gives the shear rate on a slip system as:

$$\dot{\gamma} = \varrho \, b_\mathrm{s} \, v_0 \exp\left[-\frac{Q_\mathrm{s}}{k_\mathrm{B} T} \left\{ 1 - \left(\frac{|\tau_\mathrm{eff}|}{\tau_\mathrm{sol}} \right)^{p_\mathrm{s}} \right\}^{q_\mathrm{s}} \right] \operatorname{sgn}(\tau) \tag{83}$$

where b_s is the length of the Burgers vector for slip, v_0 is a reference velocity, Q_s is the activation energy for slip, k_B is the Boltzmann constant, T is the temperature, τ_eff is the effective resolved shear stress, and τ_sol is the solid solution strength. The fitting parameters $0 < p_\mathrm{s} \leqslant 1$ and $1 \leqslant q_\mathrm{s} \leqslant 2$ control the glide resistance profile [150].

The effective shear stress τ_eff is computed as

$$\tau_\mathrm{eff} = \begin{cases} |\tau| - \tau_\mathrm{pass} & \text{for } |\tau| > \tau_\mathrm{pass} \\ 0 & \text{for } |\tau| \leqslant \tau_\mathrm{pass} \end{cases} \tag{84}$$

and the passing stress τ_pass is given by

$$\tau_\mathrm{pass}^\alpha = G b_\mathrm{s}^\alpha \left(\sum_{\alpha'=1}^{N_\mathrm{s}} h^{\alpha\alpha'} (\varrho^{\alpha'} + \varrho_\mathrm{di}^{\alpha'}) \right)^{1/2} \tag{85}$$

with the shear modulus G. The components of the slip–slip interaction matrices $h^{\alpha\alpha'}$ for the three most relevant crystal structures have been successfully determined using Dislocation Dynamics (DDD) simulations [151–154].

Following the work of Blum and Eisenlohr [155], the evolution of dislocation densities is related to dislocation multiplication, dislocation annihilation, and dipole formation. The evolution of the dislocation densities are given by the following equations:

$$\dot{\varrho} = \frac{|\dot{\gamma}|}{b_\mathrm{s} \Lambda_\mathrm{s}} - \frac{2\hat{d}}{b_\mathrm{s}} \varrho |\dot{\gamma}| \tag{86a}$$

$$\dot{\varrho}_\mathrm{di} = \frac{2(\hat{d} - \check{d})}{b_\mathrm{s}} \varrho |\dot{\gamma}| - \frac{2\check{d}}{b_\mathrm{s}} \varrho_\mathrm{di} |\dot{\gamma}| - \varrho_\mathrm{di} \frac{4 v_\mathrm{cl}}{\hat{d} - \check{d}} . \tag{86b}$$

The terms in Eq. (86a) correspond to generation of (unipolar) dislocation density due to multiplication and its reduction due to dipole formation. The terms in Eq. (86b) correspond to the formation of dislocation dipoles (less spontaneous annihilation of unipolar dislocations), the spontaneous annihilation of dipoles with (unipolar) dislocations, and the annihilation of dipoles due to dislocation climb.

The dislocation climb velocity is given by

$$v_\mathrm{cl} = \frac{G D_0 V_\mathrm{cl}}{\pi (1 - \nu) k_\mathrm{B} T} \frac{1}{\hat{d} + \check{d}} \exp\left(-\frac{Q_\mathrm{cl}}{k_\mathrm{B} T} \right), \tag{87}$$

where D_0 is the pre-factor of the self-diffusion coefficient, V_cl is the activation volume for climb, and Q_cl is the activation energy for climb.

The glide plane distance $\hat{d}$ below which two dislocations form a stable dipole and the distance $\check{d}$ below which two dislocations annihilate are, respectively, calculated as

$$\hat{d} = \frac{3Gb_\mathrm{s}}{16\pi|\tau|} \tag{88a}$$

and

$$\check{d} = D_\mathrm{a} b_\mathrm{s}, \tag{88b}$$

where D_a is a fitting parameter.

In the Kocks–Mecking model [17], dislocation density is the primary state variable for describing the hardening behavior. Strain hardening is described here in terms of a dislocation Mean Free Path (MFP) approach, where the mean free path is denoted by Λ. The MFP for slip has confining contributions due to the pileup of dislocations in front of grain boundaries, dislocation–dislocation interaction, the formation of twins, and the formation of ε-martensite and is composed as

$$\frac{1}{\Lambda_\mathrm{s}} = \frac{1}{D} + \frac{1}{\lambda_\mathrm{s}} + \frac{1}{\lambda_\mathrm{tw}} + \frac{1}{\lambda_\mathrm{tr}}, \tag{89}$$

with

$$\frac{1}{\lambda_\mathrm{s}^\alpha} = \frac{1}{i_\mathrm{s}}\left(\sum_{\alpha'=1}^{N_\mathrm{s}} p^{\alpha\alpha'}\left(\varrho^{\alpha'} + \varrho_\mathrm{di}^{\alpha'}\right)\right)^{1/2}, \tag{90a}$$

$$\frac{1}{\lambda_\mathrm{tw}^\alpha} = \sum_{\beta=1}^{N_\mathrm{tw}} h^{\alpha\beta}\frac{f_\mathrm{tw}^\beta}{t_\mathrm{tw}\left(1 - f_\mathrm{tw}^\mathrm{tot}\right)}, \tag{90b}$$

$$\frac{1}{\lambda_\mathrm{tr}^\alpha} = \sum_{\chi=1}^{N_\mathrm{tr}} h^{\alpha\chi}\frac{f_\mathrm{tr}^\chi}{t_\mathrm{tr}\left(1 - f_\mathrm{tr}^\mathrm{tot}\right)}, \tag{90c}$$

where D is the average grain size, i_s is a fitting parameter, t_tw is the average twin thickness, and t_tr is the average ε-martensite thickness. $p^{\alpha\alpha'}$ are projections for the forest dislocation density as introduced in [144]. The use of such physics-based formulations and the possibility to derive the associated parameters from models at a lower scale are a distinct advantage over the Phenomenological Crystal Plasticity model.

The MFP for twinning and the MFP for transformation are computed, respectively, as

$$\frac{1}{\Lambda_\mathrm{tw}^\beta} = \frac{1}{i_\mathrm{tw}}\left(\frac{1}{D} + \sum_{\beta'=1}^{N_\mathrm{tw}} h^{\beta\beta'} f_\mathrm{tw}^{\beta'}\frac{1}{t_\mathrm{tw}\left(1 - f_\mathrm{tw}^\mathrm{tot}\right)}\right) \tag{91a}$$

and

$$\frac{1}{\Lambda_\mathrm{tr}^\chi} = \frac{1}{i_\mathrm{tr}}\left(\frac{1}{D} + \sum_{\chi'=1}^{N_\mathrm{tr}} h^{\chi\chi'} f_\mathrm{tr}^{\chi'}\frac{1}{t_\mathrm{tr}\left(1 - f_\mathrm{tr}^\mathrm{tot}\right)}\right), \tag{91b}$$

where i_tw and i_tr are fitting parameters.

The nucleation rates for twins and ε-martensite are given as

$$\dot{N} = \dot{N}_0 P_\mathrm{ncs} P, \tag{92}$$

where $\dot{N}_0$ is the number density of potential twin or ε-martensite nuclei per unit time, which is assumed to be the same for twinning or ε-martensite because the dislocation reactions are assumed to be equally likely to form twin nuclei or ε-martensite nuclei.

The probability that cross-slip does not occur, which would allow a sufficient number of dislocations to pile up and form the stress concentration necessary to form a twin or ε-martensite nucleus, is formulated as

$$P_\mathrm{ncs} = 1 - \exp\left[-\frac{V_\mathrm{cs}}{k_\mathrm{B}T}\left(\tau_\mathrm{r} - \tau\right)\right], \tag{93}$$

where V_cs is the cross-slip activation volume.

The stress required to bring two partials within a critical distance x_c to form the twin nucleus without help from an external applied shear stress amounts to

$$\hat{\tau}_\mathrm{r} = \frac{Gb_\mathrm{s}}{2\pi\left(x_0 + x_\mathrm{c}\right)} + \frac{Gb_\mathrm{s}\cos(\pi/3)}{2\pi x_0}. \tag{94}$$

The equilibrium separation of Shockley partials in fcc metals is calculated as [156]

$$x_0 = \frac{G}{\Gamma_\mathrm{sf}}\frac{b_\mathrm{s}^2}{8\pi}\frac{2+\nu}{1-\nu}, \tag{95}$$

where Γ_sf is the stacking fault energy and ν is Poisson's ratio.

The probability P in Eq. (92) that a nucleus bows out to form a twin or ε-martensite is

$$P_\mathrm{tw} = \exp\left[-\left(\frac{\hat{\tau}_\mathrm{tw}}{\tau}\right)^{p_\mathrm{tw}}\right], \tag{96a}$$

$$P_\mathrm{tr} = \exp\left[-\left(\frac{\hat{\tau}_\mathrm{tr}}{\tau}\right)^{p_\mathrm{tr}}\right], \tag{96b}$$

where p_tw and p_tr are fitting parameters.

The critical stresses for twin and ε-martensite growth have been derived as [19]

$$\hat{\tau}_\mathrm{tw} = \frac{\Gamma_\mathrm{sf}}{3b_\mathrm{tw}} + \frac{3Gb_\mathrm{tw}}{L_\mathrm{tw}}, \tag{97a}$$

$$\hat{\tau}_\mathrm{tr} = \frac{2\sigma^{\gamma/\varepsilon}}{3b_\mathrm{tr}} + \frac{3Gb_\mathrm{tr}}{L_\mathrm{tr}} + \frac{h\Delta G^{\gamma\to\varepsilon}}{3b_\mathrm{tr}}, \tag{97b}$$

where b_tw and b_tr are the magnitudes of the Burgers vector for, respectively, twinning and transformation, L_tw and L_tr are the widths of the respective nuclei, $\sigma^{\gamma/\varepsilon}$ is the interface energy between γ- and ε-phase, and $\Delta G^{\gamma\to\varepsilon}$ is the change in Gibbs free energy per unit volume from the fcc to the hexagonal close-packed (hcp) phase.

The evolution of the twin and ε-martensite volume fractions follow a rate

$$\dot{f} = \left(1 - f_\mathrm{tw}^\mathrm{tot} - f_\mathrm{tr}^\mathrm{tot}\right)V\dot{N}. \tag{98}$$

Assuming new twins and new ε-martensite laths are thin discs, their volumes are computed as

$$V = \frac{\pi}{4}\Lambda^2 t. \tag{99}$$

The shearing rates on the β twin system and the χ transformation system are then computed as

$$\dot{\gamma} = \gamma_\mathrm{char}\dot{f}. \tag{100}$$

6.2.4. Atomistically-informed crystal plasticity for Tungsten

This dislocation density-based model implements a velocity law for the movement of dislocations in bcc Tungsten (W) that is parametrized based on knowledge obtained from atomistic simulations [26]. While the presented model is specific to W, the approach is general and can be applied to a wide range of materials [25,157]. The hardening model is equivalent to the one of the Dislocation Density Based Crystal Plasticity presented above.

At low to medium homologous temperatures, the shear rate in W and other bcc metals is determined by the thermally-activated motion of $\frac{1}{2}\langle 1\,1\,1\rangle$ screw dislocations [158,159], which proceed via the nucleation of kink pairs and their subsequent lateral relaxation. As kink relaxation is a significantly faster process than nucleation of kink pairs, it is assumed that no new kink pairs will be nucleated while lateral kink motion is underway. Such assumption leads to the following expression for the time t required for a kink pair to nucleate and relax laterally:

$$\begin{aligned} t &= t_\mathrm{n} + t_\mathrm{k} \\ &= J(\tau, T)^{-1} + \frac{\lambda - w}{2 v_\mathrm{ki}}, \end{aligned} \tag{101}$$

where t_n is the mean time to nucleate a kink pair and t_k is the time needed for a kink to sweep half the segment length λ. J is the kink pair nucleation rate, w is the kink-pair separation, and v_ki is the kink velocity. The kink pair nucleation rate

$$J(\tau, T) = \frac{\nu_\mathrm{a}(\lambda - w)}{b_\mathrm{s}} \exp\left(-\frac{\Delta H_\mathrm{kp}}{k_\mathrm{B} T}\right) \tag{102}$$

follows an Arrhenius formulation [160] with attempt frequency ν_a and activation enthalpy of a kink pair

$$\Delta H_\mathrm{kp} = \Delta H_\mathrm{kp,0} \left\{1 - \left(\frac{|\tau_\mathrm{eff}|}{\tau_\mathrm{Peierls}}\right)^{p_\mathrm{s}}\right\}^{q_\mathrm{s}} \tag{103}$$

that depends on $\Delta H_\mathrm{kp,0}$ and the resolved shear stress.

The kink velocity is assumed as

$$v_\mathrm{ki} = \frac{b_\mathrm{s} \tau}{B}, \tag{104}$$

with constant friction coefficient B.

The shear rate is calculated from the Orowan equation [149] as

$$\dot{\gamma} = \varrho b_\mathrm{s} \frac{h}{t}, \tag{105}$$

where h is the distance between two consecutive Peierls valleys.

Since Schmid's law is known to break down for bcc crystal structures due to the topological complexity of the atomic arrangements in the dislocation core [137,161], non-Schmid components of the stress tensor are included in the driving force according to Gröger et al. [162,163] and Gröger and Vitek [157]. More precisely, the parameters of $\mathbf{P}_\text{non-Schmid}$ to calculate τ in Eq. (70) have been obtained using the molecular dynamics code LAMMPS [164]. This allows to reproduce the experimentally observed temperature-dependent yield behavior of W single crystals [165].

6.2.5. Crystal plasticity including dislocation flux

More recent approaches of CP, mainly dealing with plasticity at small scales, are non-local models, *i.e.* the material response does not only depend on the state of the material point under consideration, but also on the state of the adjacent points.[13] In contrast to most existing non-local models [65,121,166–168], the model presented here [124,169] does not rely on strain or shear gradients to derive excess dislocations, ϱ_Δ, but explicitly treats the dislocation fluxes, where excess dislocations emerge from any uncompensated flux balance. The ϱ_Δ is required to calculate the Kröner–Nye tensor [117,170] $\boldsymbol{\alpha}$ as

$$\varrho_\Delta \mathbf{l} \otimes \mathbf{b} = \boldsymbol{\alpha} = -\mathrm{curl}(\gamma\, \mathbf{n} \otimes \mathbf{s}), \tag{106}$$

where $\mathbf{l}$ is the dislocation line direction.

Classical dislocation density-based constitutive models (Sections 6.2.3 and 6.2.4) neglect the dislocation transport and describe the change of dislocation densities ϱ^α per slip system α by evolution equations of the following form:

$$\frac{\partial \varrho^\alpha}{\partial t} = \sum_r \dot{\varrho}^\alpha_r, \tag{107}$$

where $\dot{\varrho}_r$ describes different processes that either increase or decrease the dislocation density, *e.g.* dislocation multiplication, annihilation, and cross slip (see Eqs. (86) and (145) or Eqs. (75) and (77)). In contrast, the dislocation flux model is based on the following modified equation:

$$\frac{\partial \varrho^\alpha}{\partial t} + \mathrm{div}\underbrace{(\varrho^\alpha \mathbf{v}^\alpha)}_{=:\mathbf{f}^\alpha} = \sum_r \dot{\varrho}^\alpha_r. \tag{108}$$

The term $\mathrm{div}(\varrho\mathbf{v}) =: \mathrm{div}(\mathbf{f})$, with $\mathbf{f}$ being the dislocation flux, incorporates the time evolution of $\boldsymbol{\alpha}$ (Eq. (106)). This addition renders Eq. (108) into a system of Partial Differential Equations (PDEs) that requires additional numerical efforts to solve when compared to the usual Ordinary Differential Equations (ODEs) (Eq. (107)). This model is, therefore, computationally very expensive. In DAMASK, the transport equation is solved using a Finite Volume Method (FVM) discretization.

As the terms on the right hand side of Eq. (108) are very similar to those described in Section 6.2.3, here the parametrization of the dislocation structure and the derivation of the dislocation flux term is given only. A full description of the model can be found in [124,169].

6.2.5.1. Dislocation parametrization. In contrast to the Dislocation Density Based Crystal Plasticity model, a somewhat more sophisticated distinction between the different dislocation types on a specific slip system is made in the dislocation flux model via:

- dislocation character c: edge (subscript "ed") or screw (subscript "sc")
- dislocation polarity: monopolar density of positive or negative sign (subscript + or −), or unsigned dipolar density (subscript ±).

Monopolar Dislocation Density: A positive or negative sign reflects the monopolar nature of a single dislocation's stress field. Fig. 8 illustrates the convention adopted for the sign of edge and screw dislocations on a slip plane. The signed character of these dislocations entails a directionality of their motion under a given resolved shear stress. According to Fig. 8, for a positive shear increment, *i.e.* increase in the slipped area by loop expansion, these directions of motion $\mathbf{m}$ follow as:

$$\mathbf{m}_{\mathrm{ed}+} = +\mathbf{s}, \tag{109a}$$

$$\mathbf{m}_{\mathrm{ed}-} = -\mathbf{s}, \tag{109b}$$

$$\mathbf{m}_{\mathrm{sc}+} = +\mathbf{n} \times \mathbf{s}, \tag{109c}$$

$$\mathbf{m}_{\mathrm{sc}-} = -\mathbf{n} \times \mathbf{s}. \tag{109d}$$

Accordingly, the plastic shear rate

$$\dot{\gamma} = \sum_p \dot{\gamma}_p = \sum_p \varrho_p v_p b_\mathrm{s} \tag{110}$$

is composed from four parts reflecting the four types $p \in \{\mathrm{ed}+, \mathrm{ed}-, \mathrm{sc}+, \mathrm{sc}-\}$ of monopolar dislocation populations. In addition to the monopolar density, which is considered here as a mobile entity, a blocked density of all types is also considered. The blocked density is directional, since blocking, *e.g.* by a grain boundary, always applies to one direction of motion only. Furthermore, the direction of motion can change when the direction of the resolved shear stress changes, in which case the blocked density is re-mobilized. Blocked density does not contribute to the transport relations but only contributes to the slip resistance (Eq. (85)).

Dipole Dislocation Density: The presence of stable dipoles enables dislocation annihilation. Stable dipoles contain two monopolar dislocations of the same character but opposite sign, hence two dipole densities, $\varrho_{\mathrm{ed}\pm}$ and $\varrho_{\mathrm{sc}\pm}$, are tracked and sum up to the overall dipole density

$$\varrho_\pm = \varrho_{\mathrm{ed}\pm} + \varrho_{\mathrm{sc}\pm}. \tag{111}$$

These dipole densities are quantitatively equivalent to the dislocation density of both signs, thus dislocations changing between monopolar and dipolar state do not alter the total of both densities.

A dipole is stable against dissociation under the resolved shear stress τ if the mutual elastic interaction between the two constituents is strong enough, *i.e.* if the distance between the glide planes of the two dislocations does not exceed

[13] When considering non-local models, only the use of a single constituent per material point is physically meaningful. Therefore, the use of such models in DAMASK is restricted to full-field simulations (Section 4.1.1).

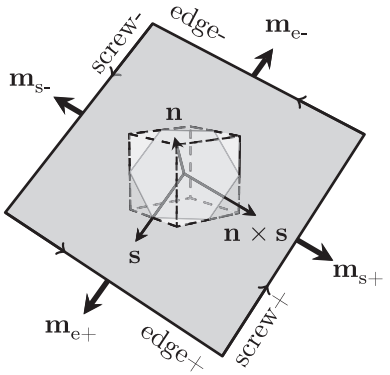

Fig. 8. Schematic dislocation loop (dark shade) on its slip plane with normal $\mathbf{n}$ and slip direction $\mathbf{s}$. Arrows along the loop periphery indicate positive line direction giving rise to the convention for signed dislocation characters as shown. The small (dashed line) interior cube illustrates the crystal unit cell orientation. A displacement step by $\mathbf{b}$ occurs when passing from below to above the shaded slip plane, *i.e.* along its normal $\mathbf{n}$. Figure adopted from [124,169] with permission from Elsevier.

$$\widehat{d}_{\mathrm{ed}} = \frac{G\,b_{\mathrm{s}}}{8\pi\,(1-\nu)}\,\frac{1}{|\tau|}, \tag{112a}$$

$$\widehat{d}_{\mathrm{sc}} = \frac{G\,b_{\mathrm{s}}}{4\pi}\,\frac{1}{|\tau|}. \tag{112b}$$

Total and Excess Dislocation Densities: The polar nature of dislocation densities allows to discriminate between the accumulated (total) measures according to

$$\varrho = \varrho_{\mathrm{ed}} + \varrho_{\mathrm{sc}} \tag{113a}$$

$$\varrho_{\mathrm{ed}} = \varrho_{\mathrm{ed}+} + \varrho_{\mathrm{ed}-} + \varrho_{\mathrm{ed}\pm} \tag{113b}$$

$$\varrho_{\mathrm{sc}} = \varrho_{\mathrm{sc}+} + \varrho_{\mathrm{sc}-} + \varrho_{\mathrm{sc}\pm} \tag{113c}$$

and the signed excess densities of edge and screw character

$$\varrho_{\Delta\mathrm{ed}} = \varrho_{\mathrm{ed}+} - \varrho_{\mathrm{ed}-} \tag{113d}$$

$$\varrho_{\Delta\mathrm{sc}} = \varrho_{\mathrm{sc}+} - \varrho_{\mathrm{sc}-}. \tag{113e}$$

Forest dislocation density: Following Ma and Roters [144], the density on any particular system α' can be projected with respect to system α into a corresponding forest density. By summation of the contribution of each slip system α', the overall forest density on system α results as

$$\varrho_{\mathrm{f}}^{\alpha} = \sum_{\alpha'=1}^{N_{\mathrm{s}}} \left(\varrho_{\mathrm{ed}}^{\alpha'}\,|\mathbf{n}^{\alpha}\cdot(\mathbf{n}^{\alpha'}\times\mathbf{s}^{\alpha'})| + \varrho_{\mathrm{sc}}^{\alpha'}\,|\mathbf{n}^{\alpha}\cdot\mathbf{s}^{\alpha'}|\right). \tag{114}$$

The MFP can be derived from the forest dislocation density as

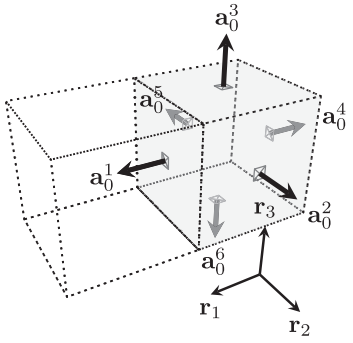

Fig. 9. Exemplary orthogonal cell with basis triad $\mathbf{r}_1$, $\mathbf{r}_2$, $\mathbf{r}_3$ in reference configuration $\mathcal{B}_0$. Interfaces between neighboring material points are characterized by their outward pointing normals $\mathbf{a}_0^n$ and have an area of A_0^n. Figure adopted from [124].

$$\Lambda_{\mathrm{s}}^{\alpha} = \frac{i_{\mathrm{s}}}{\sqrt{\varrho_{\mathrm{f}}^{\alpha}}}. \tag{115}$$

6.2.5.2. Dislocation flux. The Finite Volume Method (FVM) used in DAMASK to solve the dislocation transport PDEs (Eq. (108)) is briefly outlined in the following sections. A more detailed description can be found in [124].

Finite Volume Discretization: Finite volume cells are defined around each material point. In the case of an FEM simulation this would correspond to a cell around an integration point of an arbitrarily shaped finite element.[14] The cell volume is denoted by V. Each cell has N nearest neighbors. In the reference configuration $\mathcal{B}_0$, a shared interface with area A_0^n is situated between neighboring cell volumes and is characterized by its outward pointing unit normal $\mathbf{a}_0^n$ (see Fig. 9).

Each cell undergoes a deformation that is defined by the deformation gradient associated with its material point. Therefore, the relevant unit normals $\mathbf{a}^n$ and interface areas A^n are defined in the deformed configuration. As these measures are always shared between two neighboring material points (see Fig. 9), their values in the deformed configuration result, to a first-order approximation, from averaging the two deformation gradients $\mathbf{F}$ and $\mathbf{F}^n$ of the central and the neighboring material points, respectively. The average deformation gradient is used to define a common deformed configuration. Both, $\mathbf{a}_0^n$ and A_0^n, are pushed forward to this common deformed configuration and pulled back to the individual plastic configuration.

Finite Volume Upwind Scheme: The PDE describing dislocation transport (Eq. 108) is integrated over the finite volume cells. By means of the Stokes theorem, the volume integral of the flux divergence,

$$\int_V \operatorname{div}\mathbf{f}\,\mathrm{d}V = \oint_{\partial V}\mathbf{f}\cdot\mathbf{a}\,\mathrm{d}A = \sum_n \widetilde{\mathbf{f}}^n\cdot\mathbf{a}^n A^n, \tag{116}$$

is replaced by summing the fluxes[15] that pass through the volume surfaces A^n with outward unit normal $\mathbf{a}^n$ (see Fig. 10). The mean dislocation flux $\widetilde{\mathbf{f}}^n$ at the interface n takes either the value $\mathbf{f}$ from the central point or $\mathbf{f}^n$ from a neighboring point n such that it fulfills the following upwind scheme:

$$\widetilde{\mathbf{f}}^n = \begin{cases} \mathbf{f} & \text{if } \mathbf{f}\cdot\mathbf{a}^n > 0 \\ \mathbf{f}^n & \text{if } \mathbf{f}\cdot\mathbf{a}^n \leqslant 0 \text{ and } \mathbf{f}^n\cdot\mathbf{a}^n < 0. \\ 0 & \text{otherwise} \end{cases} \tag{117}$$

At free surfaces, $\mathbf{f}^n$ is set to zero.

While this scheme is only first-order accurate and can produce significant numerical diffusion, it is unconditionally bounded, highly stable, and ensures that dislocation density portions are transferred only in the directions of the actual dislocation motion.

Grain and phase boundaries are treated as interfaces with reduced transmissivity for dislocations. Therefore, a transmissivity factor $0 \leqslant \chi \leqslant 1$ is introduced into Eq. (116) so that only a fraction of the fluxes enters the neighboring cells

$$\int_V \operatorname{div}\mathbf{f}\,\mathrm{d}V = \sum_n \chi^n\,\widetilde{\mathbf{f}}^n\cdot\mathbf{a}^n A^n, \tag{118}$$

where the transmissivity is set to one in the case of material point neighbors that share the same orientation and phase. Any remainder of the dislocation flux that is not transmitted to the neighboring cell, *i.e.* the equivalent of the flux multiplied by $(1-\chi)$, gets stored in front of the grain boundary and is converted into blocked dislocation density.

The discretization of the spatial domain into cells entails an upper bound for the propagation speed of dislocations. Within a time step Δt,

[14] In general, the volume center of such a cell does not have to coincide with the corresponding integration point.

[15] The dislocation type p and the slip system α are dropped for brevity in notation.

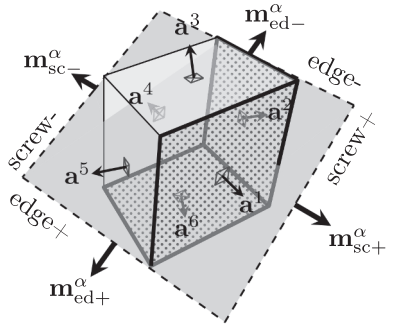

Fig. 10. Deformed material point with exemplary slip plane α (inclined) in intermediate configuration. Interface normals correspond to those of Fig. 9. Vectors on slip plane periphery indicate directions of dislocation motion for the indicated type and a positive shear increment (loop expansion). Positive screw dislocations, traveling along $\mathbf{m}_{\mathrm{sc}+}$, leave the material point volume (and enter the neighboring volume, if existent) through the dotted interfaces on the right, front, and bottom. Figure adopted from [124].

on average all dislocations that exceed a velocity $\hat{v}$ will have crossed the entire cell volume.

$$\hat{v} = \frac{\sqrt[3]{V}}{\Delta t}. \tag{119}$$

To ensure that no dislocation can move further than the next neighboring cell, the dislocation velocity will be limited to $\hat{v}$. An adaptive sub-cycling scheme is used to fulfill Eq. (119) by choosing an appropriate time step. The scheme, in principle, allows each material point to have its own time step. Nonetheless, if a material point does not converge and undergoes a cutback, then all neighbors will be cut back as well, so that non-converged material points are always surrounded by a layer of already converged material points, all subjected to the same time integration step [124].

6.3. Temperature

The thermal constitutive description is comprised of models for heat transport and generation. In addition, an eigenstrain contribution to $\mathbf{F}_{\mathrm{i}}$ resulting from thermal expansion can also be considered.

6.3.1. Heat flux

The heat flux $\mathbf{f}_T$ is the transport of thermal energy required to equlibrate temperature differences. In solids, the dominant mechanism for this transport is through conduction. Hence, in DAMASK, heat conduction models are used to describe $\mathbf{f}_T$ in Eq. (4).

6.3.1.1. Fourier's law. The heat flux in this model is based on Fourier's law of thermal conduction. An ansiotropic thermal conduction tensor $\mathbf{K}$ relates the temperature gradient to the heat flux

$$\mathbf{f}_T = -\mathbf{K}\ \mathrm{Grad}\ T. \tag{120}$$

6.3.2. Heat generation

The purpose of the heat generation model is to specify the source term f_T in Eq. (4). The heat generation rate can be composed of multiple sources.

6.3.2.1. Plastic dissipation. Heat generation due to plastic deformation is given by

$$f_T = \varkappa\, \mathbf{S}\cdot\mathbf{L}_{\mathrm{p}}, \tag{121}$$

where $\varkappa$ is the Taylor–Quinney factor [171,172], *i.e.* the fraction of plastic work that is dissipated as heat.

6.3.2.2. External heat source. In addition, a user-defined external heat source can be prescribed in tabulated form

$$f_T(t_{\mathrm{n}}) = c_n \tag{122}$$

and the actual value at time t is linearly interpolated in time between constants c_n.

6.3.3. Thermal expansion

The purpose of the thermal expansion model is to specify the thermal contribution to the eigenstrain in Eq. (47b).

6.3.3.1. Linear thermal expansion. In the linear model for thermal expansion, the expansion rate is given by

$$\mathbf{L}_{\mathrm{i,thermal}} = \dot{T}\mathbf{A}, \tag{123}$$

where $\mathbf{A}$ is an anisotropic thermal expansion coefficient tensor.

6.4. Damage

The damage constitutive description is comprised of models for the gradient term in gradient damage models and the driving force for the damage process.

6.4.1. Phase field damage

In phase field models for damage, the flux $\mathbf{f}_\varphi$ in Eq. (5), derives from the gradient contribution to the interface energy of an evolving crack surface.

6.4.1.1. Griffith's criterion. In the phase field formulation of Griffith's criterion, there is a continuous release of the stored mechanical energy density from an undamaged state, *i.e.* $\varphi = 1$, to a fully damaged state, *i.e.* $\varphi = 0$. The damage process also results in the creation of an internal surface area, *i.e.* the interface between an undamaged and fully damaged region, and an associated surface tension $\mathcal{G}$. In the phase field method, the atomically sharp interface is approximated by a much wider diffuse interface, resulting in the following form of the surface energy that is created upon crack opening:

$$\mathcal{W}_{\mathrm{surface}} = \frac{1}{2}\mathcal{G}\, l_c\, |\mathrm{Grad}\ \varphi|^2 + \frac{\mathcal{G}}{l_c}(1-\varphi), \tag{124}$$

where l_c is the length scale of the diffused interface.

The resulting flux follows from the minimization of the surface energy density

$$\mathbf{f}_\varphi = \frac{\partial \mathcal{W}_{\mathrm{surface}}}{\partial \mathrm{Grad}\ \varphi} = -\mathcal{G}\, l_c\ \mathrm{Grad}\ \varphi. \tag{125}$$

6.4.2. Damage driving force

The model for the damage driving force specifies the source term f_φ in Eq. (5). The driving force for damage can be composed of multiple sources.

6.4.2.1. Brittle damage. In the brittle damage model, the damage process is assumed to be driven by the release of stored elastic energy at a material point. The following form of the elastic energy density is used:

$$\mathcal{W}_{\mathrm{elastic}} = \frac{1}{2}\varphi^2 \mathbf{S}\cdot\mathbf{E}, \tag{126}$$

where there is a continuous release of the stored elastic energy density $\mathcal{W}_{\mathrm{elastic}}$ from an undamaged state, *i.e.* $\varphi = 1$, to a fully damaged state, *i.e.* $\varphi = 0$.

The damage driving force follows from the minimization of the total free energy density

$$f_\varphi = -\left[\frac{\partial \mathcal{W}_{\mathrm{elastic}}}{\partial \varphi} + \frac{\partial \mathcal{W}_{\mathrm{surface}}}{\partial \varphi}\right] = \frac{\mathcal{G}}{l_c} - \varphi \mathbf{S}\cdot\mathbf{E}. \tag{127}$$

The coupling of the damage evolution with the stored elastic energy results in the following modified Hooke's law (Eq. (67))

$$\mathbf{S} = \frac{\partial \mathcal{W}_{\text{elastic}}}{\partial \mathbf{E}} = \varphi^2 \mathbb{C} : \mathbf{E}. \tag{128}$$

6.4.2.2. Ductile damage. In the ductile damage model implementation, the damage process is assumed to be driven by the plastic energy dissipation at a material point. The following form of the plastic energy dissipation is used:

$$\mathcal{W}_{\text{plastic}} = \frac{1}{2}\varphi^2 \int \mathbf{M}_{\text{p}} \cdot \mathbf{L}_{\text{p}} \mathrm{d}t. \tag{129}$$

The resulting damage driving force follows from the minimization of the total free energy density

$$f_\varphi = -\left[\frac{\partial \mathcal{W}_{\text{plastic}}}{\partial \varphi} + \frac{\partial \mathcal{W}_{\text{surface}}}{\partial \varphi}\right] = \frac{\mathcal{G}}{l_c} - \varphi \int \mathbf{M}_{\text{p}} \cdot \mathbf{L}_{\text{p}} \mathrm{d}t. \tag{130}$$

The coupling of the damage evolution with the dissipated plastic energy results in the following modification to the plasticity laws

$$\mathbf{L}_{\text{p}} = f\left(\frac{\mathbf{M}_{\text{p}}}{\varphi^2}\right). \tag{131}$$

7. Application examples

The following application examples aim at illustrating the versatility of the DAMASK framework and the models incorporated therein. All presented simulations have been performed on standard workstations with 1 to 16 cores. More application examples not presented here can be found in [26,37,41,165,173–213].

In the following, the examples are sorted according to the considered length scale: From the single grain level all the way up to the component scale. Eventually, starting with Section 7.15, results are given that were obtained with models currently not included in the standard DAMASK distribution. These applications show how the presented framework can be readily extended to include practically arbitrary custom-designed modeling elements for tackling specific scientific and engineering questions. Depending on their general applicability, such extensions provided by external users will also be gradually incorporated into the standard distribution in the future. The constitutive model for the plastic response of Tungsten (W) presented in Section 6.2.4 is one such example of a constitutive model provided by the community.

7.1. "Virtual Single Crystal" experiments for identification of crystal plasticity constitutive parameters

The identification of model parameters is a key prerequisite in any kind of simulation. In mechanics, this is often achieved by fitting the parameters of the constitutive model in such way that the result of a macroscopic mechanical test, *e.g.* a tensile test, is reproduced. Depending on the complexity of the model and the number of test results available it is, however, often difficult to find a unique parameter set. This is especially true for Crystal Plasticity (CP) models as the constitutive equations are defined for individual deformation modes, *e.g.* slip or twinning systems (Appendix E), while the experimental data usually is obtained from macroscopic tests [214]. While it is in principle possible to perform experiments on single crystals oriented in a way to activate a single deformation system only, such tests are very complex and time-consuming in practice and are therefore rarely used to identify model parameters [142,143,215].

A methodology to fit parameters to "virtual single crystal" experiments has been introduced by Zambaldi and Raabe [216] and Zambaldi et al. [24]. In this approach, nanoindentations are performed on individual grains using a spherical indenter. The obtained pile-up pattern around the indents strongly depends on the activated deformation systems and, hence, the crystal orientation. It was the idea of Zambaldi and Raabe [216] to use the information provided by this pattern, *i.e.* the height profile around the indent, together with the force–displacement curve to determine the parameter set of a CP constitutive model. While the method was originally used for hexagonal γ-Titanium Aluminum (TiAl) and the phenomenological model introduced in Section 6.2.2 [24], it can in principle be used for any crystal lattice structure and any constitutive model. Using a (large) number of indents on differently oriented single crystals enables the (unique) identification of the parameters for the different deformation systems involved, using *e.g.* a Nelder–Mead [217] optimization algorithm [24,197]. Fig. 11 shows the comparison of measured and simulated height profiles for four different indents in α-Titanium (Ti).

The methodology is especially useful for the extraction of individual mechanical properties in dual- or multi-phase materials. It has for example been applied to obtain the ferrite properties for the simulations shown in Section 7.11 [218].

For facilitating corresponding indentation simulations, the open source software Slip Transfer Analysis Toolbox (STABiX) and corresponding GUIs have been developed by Mercier et al. [182] which can be used in combination with DAMASK.

7.2. Advanced generation techniques for synthetic dual phase steel microstructures

In order to predict the performance of existing and novel materials and microstructures in, *e.g.* forming processes, accurate microstructure models are needed to exploit the predictive capabilities of CP models. In cases where the use of real microstructures (Section 7.11) is prohibitive, synthetic microstructures reproducing the topological features of modern complex single- and multi-phase materials are a viable alternative [219,220].

Constructing virtual microstructures by employing Voronoi tesselation to construct Representative Volume Elements (RVEs) has been established as a powerful tool for the evaluation of field quantities [221]. Setting up such models in a continuum micromechanical framework allowed to study the response of ferritic–austenitic duplex stainless steels in thermo-mechanical loading scenarios [222] or the deformation behavior of ferritic–martensitic Dual Phase (DP) steels [223,224]. Besides the determination of microstructure-dependent stress and strain partitioning in such virtual steel microstructures, it is

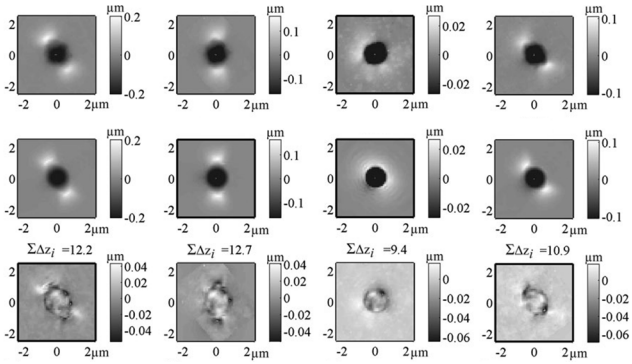

Fig. 11. Experimental (top row) and simulated (middle row) topographies of indentations in α-Titanium. The bottom row shows the difference between these surface profiles which was used to calculate the topography contribution to the objective function. Both left columns show results used to identify Crystal Plasticity (CP) parameters while the two right columns show results used to verify these parameters. Note that the gray scale ranges of the surface upheaval are consistent only per column. Figure adopted from [24] with permission from Cambridge University Press.

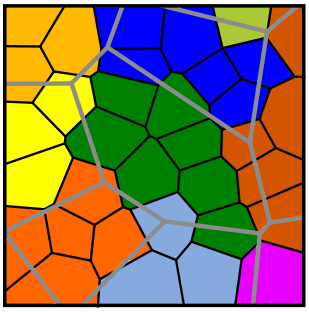

Fig. 12. Schematics of the multilevel Voronoi tessellation: Cells from the first-level (black lines) are grouped according to a second tessellation (gray lines) to form complex-shaped "grains" (indicated by colors). (For interpretation of the references to color in this figure, the reader is referred to the web version of this article.)

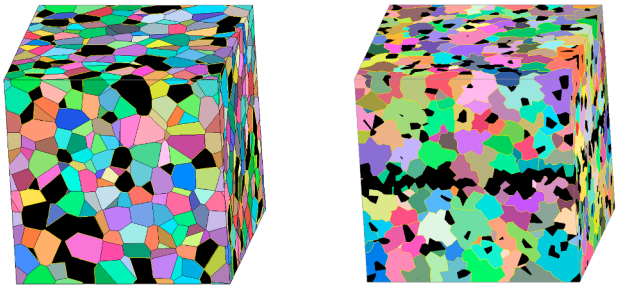

(a) Standard Voronoi tessellation for constructing synthetic microstructures.

(b) Multilevel Voronoi tessellation for constructing more complex and banded microstructure topologies.

Fig. 13. 3D Dual Phase (DP) microstructures consisting of 1000 grains. Both microstructures have a second phase volume fraction of 15.6% (indicated in black color). Colors represent crystallographic orientations.

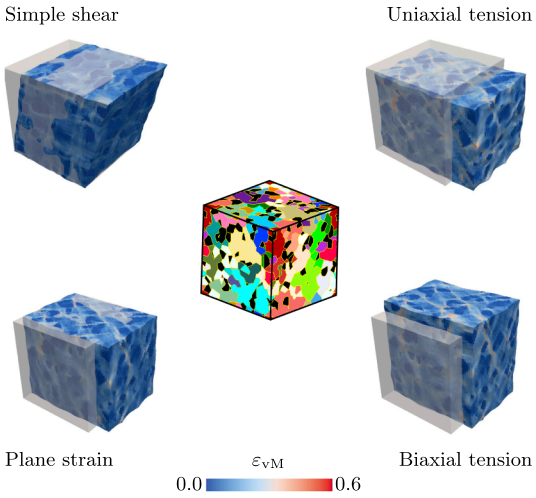

Fig. 14. Equivalent strain distributions after different deformation modes in a Dual Phase (DP) steel microstructure. In the central image, which shows the undeformed volume element, colors indicate the crystallographic orientation of the ferritic grains except for the black regions which indicate martensitic grains. (For interpretation of the references to color in this figure, the reader is referred to the web version of this article.)

also possible to identify phase-transformation induced effects resulting from the volume expansion occurring during production of these steels when part of the austenite transforms into martensite. Thereby eigenstresses are generated which could be made responsible for the experimentally observed tension–compression asymmetry at plastic strains below 1% and the very high initial work-hardening of such steels [225,226]. Furthermore, the investigation of material instability criteria and their application to predict localization-limit and forming-limit curves for DP steels turned out to be valuable for the identification of those DP steel microstructures being especially suited for deep drawing operations [227].

Using this approach in DAMASK allows to develop engineering alloy grades with specific types of microstructuress with tailored mechanical properties covering a broad range of specific combinations of functions on formability, strength, and energy absorption. This toolset enables to systematically vary microstructure topology parameters of complex alloys, understand their influence on the mechanical properties, and derive guidelines for tailored materials. An advanced microstructure design tool based on multilevel Voronoi tessellation, which is able to generate complex grain morphologies incorporating spatial and size distributions of various microstructural features, developed by Tata Steel for this purpose is presented in this section. These microstructures can be directly transferred to input data for the spectral solver introduced in Section 3.2.2. This makes exhaustive CP-based parameter studies on realistic microstructures in 2D or 3D for various steel grade families (see [228] for many examples) feasible within time scales acceptable for multiple industrial applications.

The basic principle of the multilevel approach, in more detail explained by Yadegari et al. [229], is the combination of a fine tessellation with a standard Voronoi algorithm followed by a grouping procedure to construct complex-shaped grains. The second-level tessellation is performed using a slightly modified Voronoi algorithm: a second-level grain is formed by all first-level grains whose seed point is closest to a second-level seed point, see Fig. 12. To illustrate the difference between both approaches, two 3D examples have been created that share the same volume fraction of a second phase (15.6%) as well as the same number of matrix phase grains (1000). The following differences between a standard Voronoi tessellation and the more advanced possibilities of the multilevel Voronoi approach can be observed in Fig. 13: (i) The standard Voronoi algorithm (Fig. 13(a)) creates convex shaped cells, while more complex-shaped cells can be generated with the multilevel approach (Fig. 13(b)). (ii) Different grain sizes of the second phase can be realized with the multilevel algorithm. In the example given, the average diameter of the second phase is 20% of that of the matrix phase while the standard Voronoi tessellation assigns the same average diameter to both phases. (iii) Instead of randomly distributing the second phase grains, the multilevel approach enables the localization within banded regions.

Fig. 14 shows an example of simulations on a periodic DP steel microstructure with 20% martensite embedded in a ferritic matrix. The center image shows the undeformed microstructure, where black grains represent martensite and the colors represent different crystal orientations within the ferrite grains. The volume element has been deformed in plane strain, simple shear, and uniaxial and biaxial tension with a total deformation of 12% for each load case. Fig. 14 reveals that the different deformation modes also have an effect on the heterogeneity of the strain distribution. The heterogeneity is dominated by the amount and spatial distribution of the martensite. Less dominant, but still of influence is the morphology of the ferrite grains and their misorientations relative to the neighboring grains. The average response of the RVE can be used to perform virtual testing on a macroscale.

As outlined in Section 7.13, yield surfaces (Fig. 40) can also be calibrated from such virtual experiments. Using synthetic microstructures, the influence of a wide array of topological and crystallographic microstructural parameters such as, *e.g.* the size and spatial distributions of second phase particles in multi-phase steel grades, grain morphology, crystallographic orientation, and misorientation distributions on the mechanical performance can hence be systematically investigated with the aim to identify microstructures that best match a targeted loading and/or forming scenario. Therefore, new insights and

Table 2
Constitutive parameters of aluminum employed for the oligocrystal simulation using the models presented in Sections 6.2.1 and 6.2.2.

Property	Value			Unit
	Plate	Void		
		Elastic	Dilatational	
C_{11}	100	0.1	10	GPa
C_{12}	60	0	0	GPa
C_{44}	30	0.05	5	GPa
$\dot{\gamma}_0$	1.0×10^{-3}		1.0×10^{-3}	s^{-1}
ξ_0	30		0.3	MPa
ξ_∞	60		0.6	MPa
h_0	80		1	MPa
n	20.0		20.0	
a	2.0		2.0	

the partial substitution of time-consuming laboratory experiments are enabled by this microstructure and texture oriented tools in conjunction with DAMASK.

7.3. Free surfaces in spectral solver simulations

The periodicity inherent to Fourier spectral solvers can be overcome by introducing buffer layers with high stiffness contrast to the sample material [11]. Maiti and Eisenlohr [230] studied how different material models can be used to consider free surfaces. To this end, they compared measured to simulated local deformation behavior of a thin oligocrystalline Aluminum (Al) tension sample. In the experimental investigation by Zhao et al. [7], serving as a reference, the grain structure on the sample front and back face were acquired by Electron Backscatter Diffraction (EBSD) before and after straining to about 0.1. The local in-plane deformation field was acquired using Digital Image Correlation (DIC) at strain increments of 5×10^{-4}. Since most of the about 20 grains in the thin gauge section are almost columnar, the modeled geometry was based on a through-thickness extrusion of the grain structure on the front face. Contrary to the Finite Element Method (FEM) simulations conducted by Zhao et al. [7], three different boundary conditions are considered here, namely "fully periodic" (periodic copies of the hexahedral dogbone gauge section), "semi-periodic" (periodic along thickness direction, *i.e.* infinite thickness), and "free surface" conditions. The geometries are discretized by a regular grid of 273×112 points and either 10 (fully periodic and quasi-periodic) or 20 points (free surface) across the thickness. A buffer layer of either the dilatational (Eq. (73)) or an isotropic soft-elastic material (see Table 2) encases the dogbone geometry for the semi-periodic and free surface boundary conditions to arrive at a periodic hexahedral cell required by the spectral solver (see left column in Fig. 15). Uniaxial tension up to a strain of 0.1 along the y-direction, discretized into 1000 individual time increments, is enforced by setting the average deformation gradient rate and complementary first Piola–Kirchhoff stress to

$$\frac{\dot{\bar{\mathbf{F}}}}{10^{-3}\mathrm{s}^{-1}} = \begin{bmatrix} * & 0 & 0 \\ 0 & 1 & 0 \\ 0 & 0 & * \end{bmatrix} \quad \text{and} \quad \frac{\bar{\mathbf{P}}}{\mathrm{Pa}} = \begin{bmatrix} 0 & * & * \\ * & * & * \\ * & * & 0 \end{bmatrix}. \tag{132}$$

Fig. 15 shows the local in-plane von Mises strain and lattice orientation (as Inverse Pole Figure, IPF) of the three simulated boundary conditions using a dilatational buffer layer, the experiment, and the free surface boundary condition using a soft-elastic layer (top to bottom). In the boundary condition sequence using a dilatational layer (first to third row), the in-plane von Mises strain is most homogeneous for the fully periodic case, a simulation result which differs significantly from the measured strain distribution. For the semi-periodic and free surface

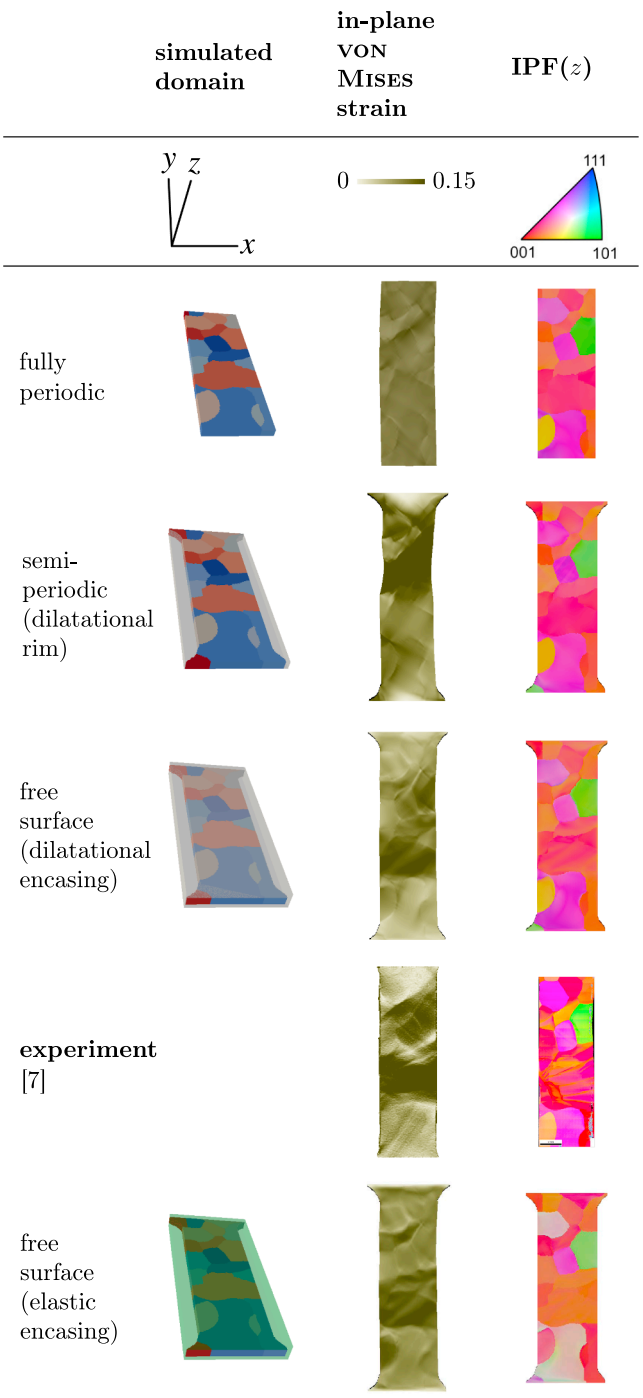

Fig. 15. Model setup and results of the aluminum oligocrytsal simulation compared to experimetal results by Zhao et al. [7]. Gray (green) semi-transparent volume in the simulated domain column uses the proposed dilatational (isotropically elastic) material model; regions of constant color reflect individual grains. IPF (last column) coloring of lab direction z is mapped on the undeformed configuration, except for the measured result (fourth row). Figure adopted from [230] with permission from Elsevier. (For interpretation of the references to color in this figure, the reader is referred to the web version of this article.)

boundary conditions, the strain localizes in grains with kinematically softer crystallographic orientation (*i.e.* higher Schmid factor) enabled by the non-compactness of the simulated geometry. The regions of strain localization differ significantly between the semi-periodic and free surface case. Only the simulations conducted by using free surface boundary conditions with either the dilatational or soft-elastic layer are

able of capturing the most relevant strain localization features (third and last row) observed in the DIC measurement. Despite this agreement, only with the dilatational layer does the simulation properly capture the experimentally observed crystal lattice re-orientations (last column). The extent and location of strain heterogeneity is not only influenced by microtexture as reported, for instance, by Raabe et al. [231], but it is also essential to reflect the correct boundary conditions in a simulation when matching experimental and simulated data one-to-one.

7.4. Wedge indentation

The dislocation density-based constitutive model including dislocation flux (Section 6.2.5) is especially suited for small scale simulations in which the assumption of a local dislocation density evolution cannot be justified. As a suitable reference example for benchmarking simulation results obtained with this model and studying the influence of the dislocation flux, experiments published by Kysar et al. [232] have been used. In this experimental study, pure single-crystalline face-centered cubic (fcc) Nickel (Ni) was indented by a 90° wedge indenter to an indentation depth of about 200 µm. The indent was placed into a (0 0 1) oriented surface; the indenter ridge was aligned parallel to the [1 1 0] lattice direction (see Fig. 16). Kysar et al. [232] pointed out that these specific loading conditions lead to a plane-strain deformation state. After indentation, the sample was cut in half normal to the [1 1 0] direction and the exposed surface was analyzed by EBSD.

The experiment had then been modeled in an FEM simulation (Msc.Marc) with a planar mesh of 1092 hexahedral elements with quadratic interpolation functions and reduced integration capacity, Fig. 16. Except for the indented surface, all nodes on outer surfaces of the model were constrained to in-plane motion, *i.e.* displacement normal to the respective surface was prohibited. In particular, displacement in direction of the wedge indent was constrained to be zero on the front and back surfaces in Fig. 16 in order to mimic plane-strain conditions. Due to the plane-strain conditions, one element in thickness direction suffices and was chosen here. The lateral extent of the FEM mesh does not cover the complete sample domain (which was approximately $1 \times 1 \times 1\,\mathrm{cm}^3$), but had been chosen sufficiently large for the boundaries to not influence the predictions. The wedge indenter was modeled by two rigid surfaces that form an angle of 90° and a flat tip surface of 5 µm width (see blow-up in Fig. 16). Contact conditions between the indenter and material surface were modeled using the Coulomb friction law with a friction coefficient of 0.3. A list of all material parameters used is given in Table 3.

Kysar et al. [232] measured the lattice rotations around the indent by EBSD. Fig. 17 juxtaposes maps of the experimentally obtained lattice rotation in the *y*–*z* plane (Fig. 17(b)) and the simulated rotation maps using the model with (Fig. 17(a)) and without (Fig. 17(c)) the flux terms. All maps reveal the same features, although, in general, the simulation slightly overestimates the rotations compared to the experiment. Regions of high rotation can be found on both flanks of the indent and directly below the tip of the indent. A boundary running vertically down from the indenter tip divides the sample into two halves with symmetric rotation patterns but inverted sign. However, the simulation without flux (Fig. 17(c)) results in orientation features not visible in the experiments. The out-of-plane rotations were negligibly small in both, experiment and simulation.

From the experimentally obtained lattice rotations Kysar et al. [232] derived lower bounds for the L_1 norm of the Geometrically Necessary Dislocation (GND) density, *i.e.* for the sum of the absolute values of edge and screw GNDs over all slip systems. This lower bound is equivalent to the actual value in case of only one or two effective slip systems being active. The experimentally obtained map of the GND density is shown in the center of Fig. 18 and the corresponding simulated excess dislocation density on the left (with flux) and the right (without flux). The experimental and simulated dislocation densities match very well both qualitatively and quantitatively. Nevertheless, the simulation without flux again results in features not found in the experiment. In particular, the highest densities of GNDs are seen around the evolving boundary beneath the indenter. Neglecting dislocation flux results in a clear maximum right beneath the indenter which is not seen in the experiment. To both sides of this boundary, GNDs of about ten times lower density extend into the material and form bands that draw an angle of about ± 45° with the deformation-induced boundary. The same feature with similar angles occurs in the simulations, yet not as finely patterned due to the limited mesh resolution and the disregard of the discreteness of dislocation sources.

As shown here and in [124,169], incorporating the dislocation fluxes into the constitutive model is the essential prerequisite to match the prediction of the experimental benchmark exhibiting large gradients. With the constitutive model presented in Section 6.2.5 it is therefore possible to predict the crystal rotations correctly as well as the quantitatively correct densities of geometrically necessary dislocations in the wedge indentation on a Ni single crystal.

7.5. Single crystalline pillar compression

Another example demonstrating the coupling of a CP constitutive law and commercial FEM software (see Section 3.2.1) is the simulation of pillar compression. Specifically, the phenomenological constitutive law described in Section 6.2.2 is used together with Msc.Marc to reveal the influence of complex boundary conditions on the *in situ* single crystalline micro-pillar compression tests. The pillar-shaped compression samples for the simulations are modeled as perfect cylinders placed on a large substrate (see the inset in the bottom of Fig. 20 and at the top of Fig. 21). The pillar and the substrate share the same crystallographic orientation and mechanical properties. The sample geometry is typical for samples cut in a Focused Ion Beam (FIB) device (see the top of Fig. 21).

Here two effects had been investigated: (i) the effect of friction between the compression tool and the sample surface on Cu pillars [233]; (ii) the effect of the misalignment of the compression tool on Ni pillars [234]. The model parameters used for Copper (Cu) and Ni are listed in Table 4.

7.5.1. Copper pillar: effect of friction

Fig. 19 shows the stress distribution mapped on the deformed pillar and the corresponding crystallographic orientation distributions (initial normal orientation [1 1 12]) for a friction coefficient between the

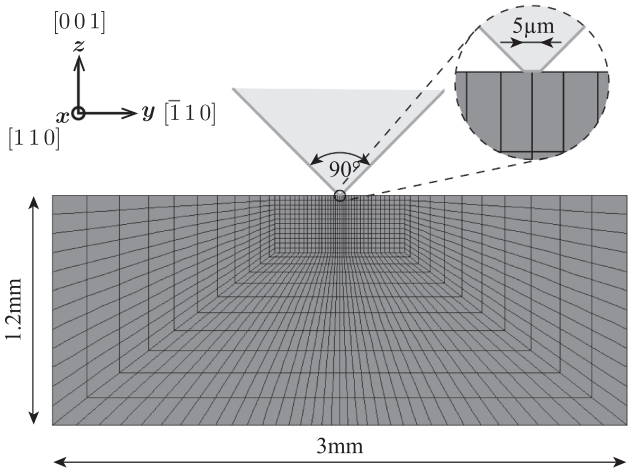

Fig. 16. Finite element mesh used for the simulation of wedge indentation. The indenter is modeled by two flat surfaces that have an inclination angle of 90° and a flat tip of 5 µm width. Figure adopted from [124,169] with permission from Elsevier.

Table 3
Constitutive parameters of single-crystalline Nickel employed for the simulation of the wedge indent using the model presented in Section 6.2.2.

Property	Value	Unit
C_{11}	246.5	GPa
C_{12}	147.3	GPa
C_{44}	124.7	GPa
b	0.248	nm
$\check{d}_{ed}$	2.6	nm
$\check{d}_{sc}$	12	nm
k_1	0.1	
k_2	45	
k_3	0.01	
ϱ_0	2.88×10^{12}	m^{-2}
Q_S	1.12	eV
c_{at}	5.0×10^{-7}	
τ_S	8.3	MPa
ν_a	50	GHz
B	0.248	$m\,s^{-1}\,MPa^{-1}$

compression tool and the sample surface ranging from 0.0 (left) to 0.1 (right) at an engineering strain (ε_{eng}) of 0.1 (top) and 0.4 (bottom). The sample deformed with zero friction (left column) shows a very strong trend to undergo deformation-induced crystallographic reorientation. The other two specimens which were deformed under non-zero friction conditions undergo less pronounced orientation changes. Moreover, the overall spread in the deformation-induced orientation distribution is in both cases with non-zero friction much smaller than in the case with zero friction. The shape changes of the pillars also reveal clear differences among the three samples as shown in Fig. 19: The sample which was deformed under zero-friction conditions undergoes very strong buckling while the two specimens that are deformed with non-zero friction conditions reveal a more stable evolution of the shape, *i.e.* less buckling.

The influence of friction is also revealed in the stress–strain curves (Fig. 20). For the case of vanishing friction the stress-strain curve shows features of plastic flow instability. This observation matches the shape change presented in the top of Fig. 19. To further investigate the stability of the deformation, the corresponding flow curve had been analyzed in terms of the Considére criterion (inset in Fig. 20). The point of intersection between the hardening curve and the stress–strain curve occurs at an engineering strain of 0.185. The unstable stress–strain curve for zero friction reflects the shape instability of the zero-friction specimen. The two stress–strain curves for non-zero friction conditions (friction coefficients 0.05 and 0.10) are much more stable and do not exhibit geometrical softening. Further details on the influence of friction and buckling effects can be found in the original publication [234].

7.5.2. Nickel pillar: effect of misalignment

Fig. 21 shows (i) the *in situ* Ni pillar compression sample used in the experiment and the FEM mesh for the simulation, and (ii) the average shear rate of the 12 slip systems in fcc crystals as a function of the engineering strain. In the simulation, the compression tool is set to be 2.0° off the ideal punch direction, and the contact between the compression tool and the sample surface is assumed to be frictionless.

The red line in Fig. 21 shows the shear rate evolution of the geometrically predicted $(\bar{1}\,1\,1)[1\,0\,1]$ slip plane, which is expected to be dominant in an ideal uniaxial compression experiment (with a Schmid factor of 0.47). When using a tool inclination of 2.0°, however, the simulation predicts at the beginning of loading the activity of two slip systems that are geometrically unexpected, *i.e.* the $(1\,1\,1)[1\,0\,\bar{1}]$ system with a Schmid factor of 0.35 and the $(1\,1\,1)[0\,1\,\bar{1}]$ system with a Schmid factor of 0.18. Only at a strain above 0.3% kinematically expected slip system becomes prevalent. This simulation result matches the experimental observation of plasticity on an unexpected observed slip plane, although the transition to the kinematically expected system occurs at a smaller strain in the simulation [234].

7.6. Single crystalline cellular materials

This example is provided to demonstrate the capability of the mixed variational formulation implemented in the spectral based method (see Section 3.2.2) to approach problems with high phase contrast. Particularly, in this example—presented in full length by Ma et al. [236,237]—the single crystalline stochastic honeycombs consist of two phases, Gold (Au) and voids, the latter with a stiffness close to zero.

For a systematic investigation of the effects of texture and topological details, four honeycomb structures were generated from 200 randomly arranged seed points using a periodic Voronoi tessellation on a 512×512 grid (see Fig. 22). The relative densities are approximately 0.6 that of bulk Au. From a statistical view, these four honeycomb structures have the same distributions of the cell wall length and their inclinations (see Fig. 3 in [237]). Eight different initial crystallographic orientations (see Table 6) were assigned to all four structures and loaded under in-plane compression. The phenomenological constitutive description in DAMASK introduced above (Section 6.2.2) was used with constitutive parameters for Au listed in Table 5.

A comparison of the average stress components normalized by the average stress in loading direction ($\bar{\sigma}_{33}$) at an early loading stage ($\bar{\varepsilon}_{33} = -0.001$) reveals that the elastic anisotropy of the bulk single crystal is inherited by the honeycombs. A large scatter of $\bar{\sigma}_{13}/\bar{\sigma}_{33}$ is observed in comparison to the other normalized stress components, which indicates that it is more sensitive to the local geometric details of the statistically equivalent honeycomb structures.

Fig. 23 shows the cumulative probability of the stress components of the honeycombs upon in-plane compression at $\bar{\varepsilon}_{33} = -0.1\%$. The

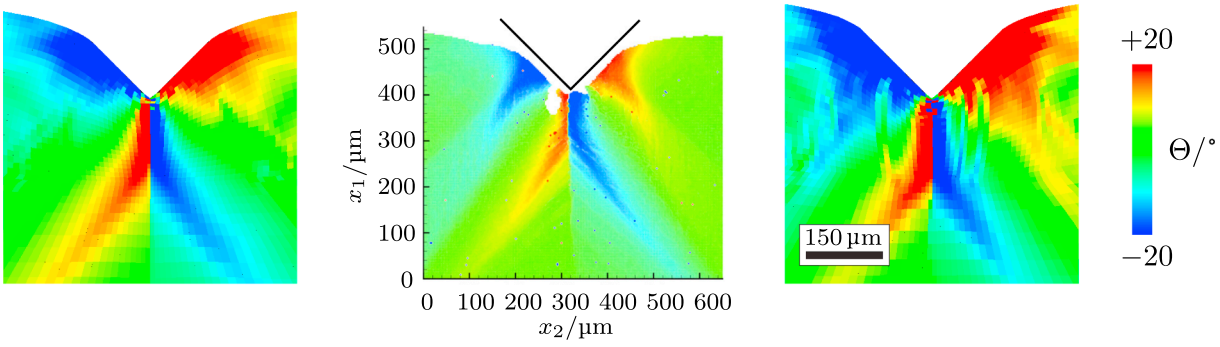

(a) Simulation with flux (b) Experimental reference (c) Simulation without flux

Fig. 17. In-plane lattice rotation Θ as experimentally obtained by Kysar et al. [232] in comparison to the simulation results. Figure adopted from [124,169] with permission from Elsevier.

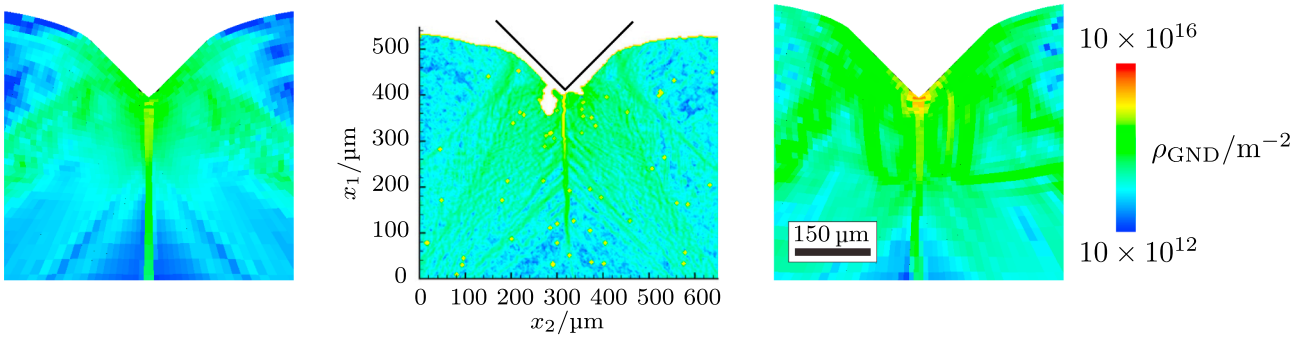

(a) Simulation with flux (b) Experimental reference (c) Simulation without flux

Fig. 18. Geometrically Necessary Dislocation (GND) density ρ_{GND} on a logarithmic scale as experimentally obtained by Kysar et al. [232] in comparison to the simulation results. Figure adopted from [124,169] with permission from Elsevier.

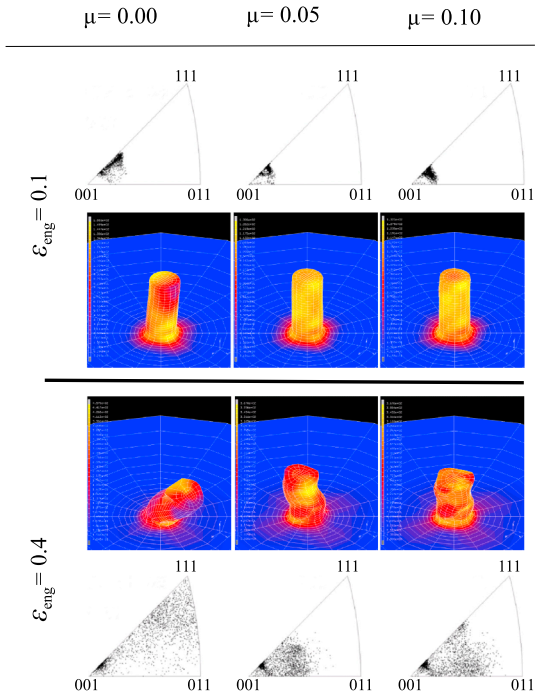

Fig. 19. Crystal Plasticity (CP) simulation of Copper pillar compression: Pillar geometry and corresponding crystallographic orientation distribution at an engineering strain of 0.1 (top) and 0.4 (bottom) with different friction coefficients (from left column to right, 0.00, 0.05, and 0.10). Color code: equivalent VON MISES stress from blue (low values) to yellow (high values). Figure adopted from [233] with permission from Elsevier. (For interpretation of the references to color in this figure, the reader is referred to the web version of this article.)

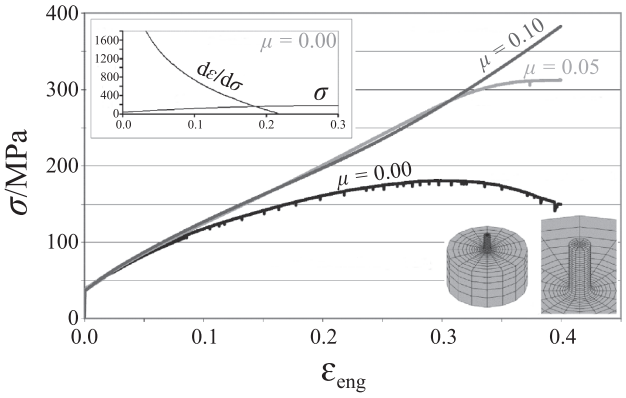

Fig. 20. Results of the Copper pillar compression simulation: Engineering stress-strain curves (bottom) for the three cases with different friction coefficients (σ: stress, $d\sigma/d\varepsilon$: hardening). Figure adopted from [233] with permission from Elsevier.

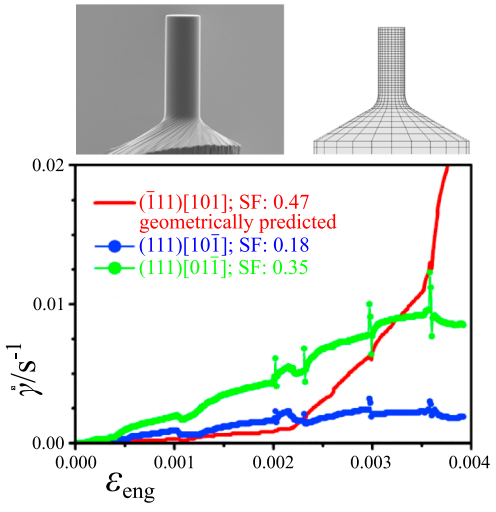

Fig. 21. Nickel pillar compression: Initial pillar geometry from experiment and simulation (top). Average shear rates on the dominant slip systems as a function of the engineering strain (bottom); SF: SCHMID factor. Figure adopted from [234] with permission from Elsevier.

cumulative probabilities of σ_{11} and σ_{13} reveal a normal distribution with a mean value of zero. This means that the dominant deformation mode is bending. Two main observations were made: (i) The in-plane stress (x–z plane) components, σ_{11}, σ_{33}, and σ_{13}, were nearly independent of the crystallographic orientation. (ii) The out-of-plane stress (x–y plane and y–z plane) components, σ_{22}, σ_{23}, and σ_{12}, were dependent on the initial orientation.

Fig. 24 shows IPFs of the honeycombs at $\bar{\varepsilon}_{33} = -0.03$. Most of the crystallographic reorientation follows a rigid rotation about the y-axis, which indicates that mostly bending of the cell walls was responsible for the crystallographic reorientation. In addition to the brief summary given here, Ma et al. [236,237] studied specific deformation details that were observed to be associated with the underlying texture components.

7.7. Shear banding

Shear bands are commonly observed across many material classes and loading conditions as non-crystallographic band-like deformation regions of concentrated plastic flow that frequently occur in bulk materials subjected to large plastic deformation [238,239]. In cases where

Table 4
Constitutive parameters of single-crystalline Copper and Nickel employed for the simulation of the pillar compression using the model presented in Section 6.2.2.

Property	Value		Unit
	Cu	Ni	
C_{11}	168.0	251.0	GPa
C_{12}	121.0	150.0	GPa
C_{44}	75.4	124.0	GPa
$\dot{\gamma}_0$	1.0×10^{-3}	1.0×10^{-3}	s^{-1}
ξ_0	16.0	26.1	MPa
ξ_∞	148.0	240.0	MPa
h_0	180.0	365.0×10^3	MPa
a	2.25	1.0	
n	83.3	83.3	

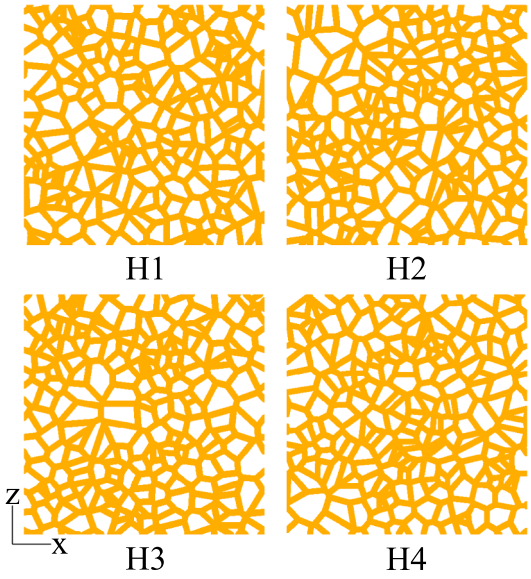

Fig. 22. The four instances of the periodic honeycomb structures, called H1–H4. Figure adopted from [236,237] with permission from Elsevier.

Table 5
Constitutive parameters of single-crystalline Gold employed for the simulation of cellular materials using the model presented in Section 6.2.2.

Property	Value	Unit
C_{11}	191.0	GPa
C_{12}	162.0	GPa
C_{44}	42.2	GPa
$\dot{\gamma}_0$	1.0×10^{-3}	s^{-1}
ξ_0	26.25	MPa
ξ_∞	53.0	MPa
h_0	75.0	MPa
a	1.0	
n	83.3	

homogeneous and compatible dislocation glide or twinning deformation is hampered, shear banding sets on as a local mechanism of concentrated plastic deformation. Formation of shear bands is promoted if homogeneous dislocation slip is hampered and the local strain hardening capacity of the material is exhausted.

Shear banding has been simulated by introducing a non-crystallographic mesoscopic deformation mechanism into the dislocation density-based constitutive model presented in Section 6.2.3. Inspired by the work of Kalidindi [130], the plastic velocity gradient $\mathbf{L}_\mathrm{p}$ has additional contributions from 6 additional "virtual" shear band systems, where the number of these additional degrees of freedom is identified in DAMASK by N_SB, which leads to an extension of Eq. (82):

$$\mathbf{L}_\mathrm{p} = \ldots + \sum_{\xi=1}^{N_\mathrm{SB}} \dot{\gamma}^\xi \mathbf{n}^\xi \otimes \mathbf{s}^\xi. \tag{133}$$

Ignoring their respective volume fractions in the additional term assumes that twinned and transformed volumes can be deformed by shear bands in a manner that is compatible to the surrounding matrix.

The kinematic and constitutive details of the shear banding contribution follow the model originally developed by Anand and Su [240]. In their approach, the specific non-crystallographic shear banding systems are defined relative to the three principal directions of the second Piola–Kirchhoff stress $\mathbf{S}$. The spectral decomposition of $\mathbf{S}$ reads:

$$\mathbf{S} = \sum_{i=1}^{3} \hat{S}_i \hat{\mathbf{e}}_i \otimes \hat{\mathbf{e}}_i, \tag{134}$$

where $\hat{S}_i$ are the principal stresses and $\hat{\mathbf{e}}_i$ are the orthonormal principal directions of $\mathbf{S}$. In agreement with the model of Anand and Su [240], the plastic flow due to shear banding is considered on six potential systems in the planes constructed by these three principal stress directions. In each ($\hat{\mathbf{e}}_i$-$\hat{\mathbf{e}}_j$)-plane, the two potential shear band systems are defined by:

$$\begin{aligned} \mathbf{s}^1 &= c\,\hat{\mathbf{e}}_i + s\,\hat{\mathbf{e}}_j \qquad \mathbf{n}^1 = s\,\hat{\mathbf{e}}_i - c\,\hat{\mathbf{e}}_j \\ \mathbf{s}^2 &= c\,\hat{\mathbf{e}}_i - s\,\hat{\mathbf{e}}_j \qquad \mathbf{n}^2 = s\,\hat{\mathbf{e}}_i + c\,\hat{\mathbf{e}}_j \end{aligned} \tag{135}$$

with $s := \sin(\pi/4)$; $c := \cos(\pi/4)$; $i, j \in (1, 2, 3)$ and $i \neq j$. The shear rate on system ξ is then formulated in analogy to that for dislocation slip systems in Eq. (84):

$$\dot{\gamma} = \dot{\gamma}_0 \exp\left[-\frac{Q_\mathrm{SB}}{k_\mathrm{B} T}\left\{1 - \left(\frac{|\tau|}{\tau_\mathrm{SB}}\right)^{p_\mathrm{SB}}\right\}^{q_\mathrm{SB}}\right] \mathrm{sgn}(\tau), \tag{136}$$

where Q_SB is the activation energy and τ_SB is the constant threshold stress for shear banding.

In the following, two examples of simulating shear banding-related behavior are presented. The first example shows simulations of the rolling texture evolution in low Stacking Fault Energy (SFE) fcc polycrystals [147]. The second example is the simulation of co-deformation and shear localization in a plane strain compressed Copper Silver (Cu–Ag) hetero-phase bicrystal [148]. In both simulation series the usual $N_\mathrm{s} = 12$ $\{1\,1\,1\}\langle 1\,1\,0\rangle$ dislocation slip systems and $N_\mathrm{tw} = 12$ $\{1\,1\,1\}\langle 1\,1\,2\rangle$ twin systems for fcc materials (see Tables 21(a) and 22(a)) are used together with the $N_\mathrm{SB} = 6$ shear band systems introduced above. The model presented here is able to capture the shear banding-related phenomena including not only the micromechanical behavior but also the associated local lattice rotation in hetero-phase composites. More details have been presented in the original references by Jia et al. [241,242].

7.7.1. Texture evolution in α-brass polycrystals during cold rolling

Shear banding is known to have pronounced influence on texture evolution [243]. Here the crystallographic texture evolution in α-brass polycrystals during cold rolling is investigated. The mesh that was used for the simulation with Msc.Marc in conjunction with DAMASK consists of 250 eight-noded, isoparametric, three-dimensional brick elements with eight integration points. Four different orientations were assigned to each integration point such that 8000 crystallographic orientations represented the random initial texture of the as-received material. At each integration point, the 4 constituents were homogenized using the Taylor isostrain homogenization approach (Section 4.1.2). The rolling process was approximated by imposing a global plane strain compression state with a strain rate of $1 \times 10^{-3}\,s^{-1}$ in conjunction with periodic boundary conditions. Fig. 25 shows the obtained orientation

Table 6
Investigated crystallographic orientations. See Raabe et al. [235] for naming convention.

Name	Euler angles/°		
	φ_1	Φ	φ_2
Brass	35	45	0
Copper	90	35	45
Cube	0	0	0
Goss	0	45	0
Rotated cube	45	0	0
S	60	32	65
RZ	32	85	85
Less symmetric	0	13	71

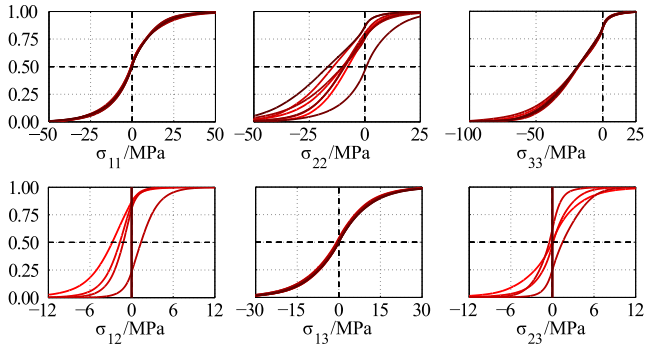

Fig. 23. Cumulative probability of the stress components at $\bar{\varepsilon}_{33} = -0.001$ for all investigated crystallographic orientations (indicated by color). Each cumulative probability of σ_{ij} contains the complete set of σ_{ij} values from all four honeycomb structures. Figure adopted from [237] with permission from Elsevier.

densities along the α- and τ-fibers in comparison to corresponding texture measurements on Cu-30 wt.%Zn published by Hirsch and Lücke [238]. The simulated textures were obtained from three sets of simulations using different combinations of deformation mechanisms: (i) dislocation slip only, denoted as "Slip" model; (ii) dislocation slip and mechanical twinning, referred to as "Slip + Twin" model; (iii) dislocation slip, twinning and shear banding, denoted as "Slip + Twin + SB" model, where two different values for τ_{SB} were used. At 20% thickness reduction, the {011}⟨100⟩ (Goss), {011}⟨211⟩ (Brass), and {112}⟨111⟩ (Copper, Cu) texture components were reproduced by all three models. However, after 40% reduction, differences among the model predictions were observed. This is for example revealed on the τ-fiber in terms of the Cu texture component, see Fig. 25(b): A significant increase of the Cu- and {123}⟨634⟩ (S-) components was predicted by the Slip and Slip + Twin models. At higher strains, in both simulations an additional increase of the {111}⟨211⟩ texture component (Brass-R) was identified. This prediction matched the earlier reported experimental observations [243]. Moreover, the Cu-component had further developed and a very pronounced Cu-type texture component had appeared at 80% and 90% reductions. Less increase of the Cu-component was predicted by the Slip + Twin model. Yet, it was found that both simulations (Slip and Slip + Twin) deviated from the experimental results which always exhibited a stronger Brass-component compared to the Cu-component at large thickness reductions. The experimental textures at reduction levels above 80% are apparently not of Cu-type as would be expected from homogeneous dislocation shear deformation, suggesting that shear band formation is responsible for the observed texture evolution in low SFE fcc materials. Using the Slip + Twin + SB model in conjunction with a critical stress to initiate shear banding of $\tau_{SB} = 0.3$ GPa, stronger Brass-type textures were predicted compared to the simulations without shear banding, as revealed by the α-fiber at 60% reduction. Moreover, the Cu- and the Brass-R-components were less pronounced when compared to the predictions obtained by the Slip and the Slip + Twin models. When using a critical stress of $\tau_{SB} = 0.18$ GPa for shear banding, the Brass-component was continuously strengthened with increasing deformation up to a strain of 90%. The Goss-component did not show a significant increase as predicted by the Slip + Twin + SB model when using $\tau_{SB} = 0.3$ GPa as critical stress. Furthermore comparison of the two shear band simulations with different threshold stresses showed that an easier activation of shear banding ($\tau_{SB} = 0.18$ GPa) leads to a more pronounced suppression of the development of the Cu- and S-components.

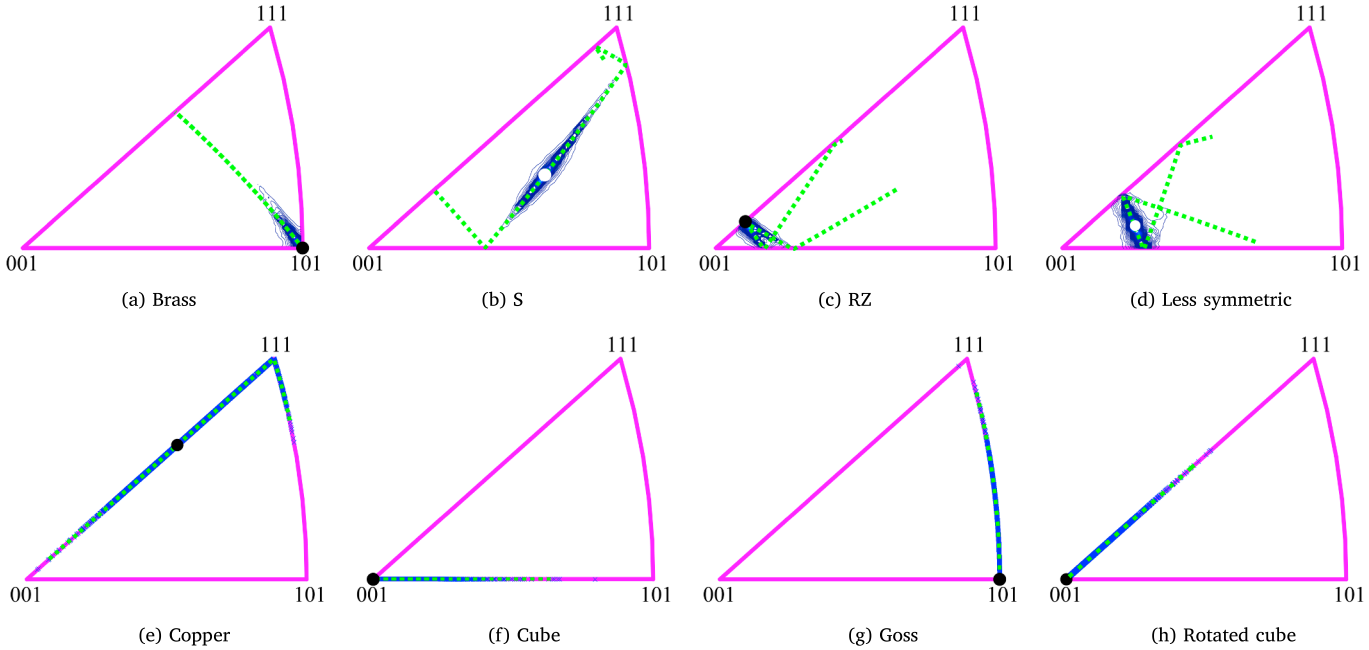

Fig. 24. Inverse Pole Figures (IPFs) of variant H1 of the honeycomb structures at $\bar{\varepsilon}_{33} = -0.03$. Top row shows contour plots and bottom shows discrete plots. The circle denotes the original orientation. Figure adopted from [237] with permission from Elsevier.

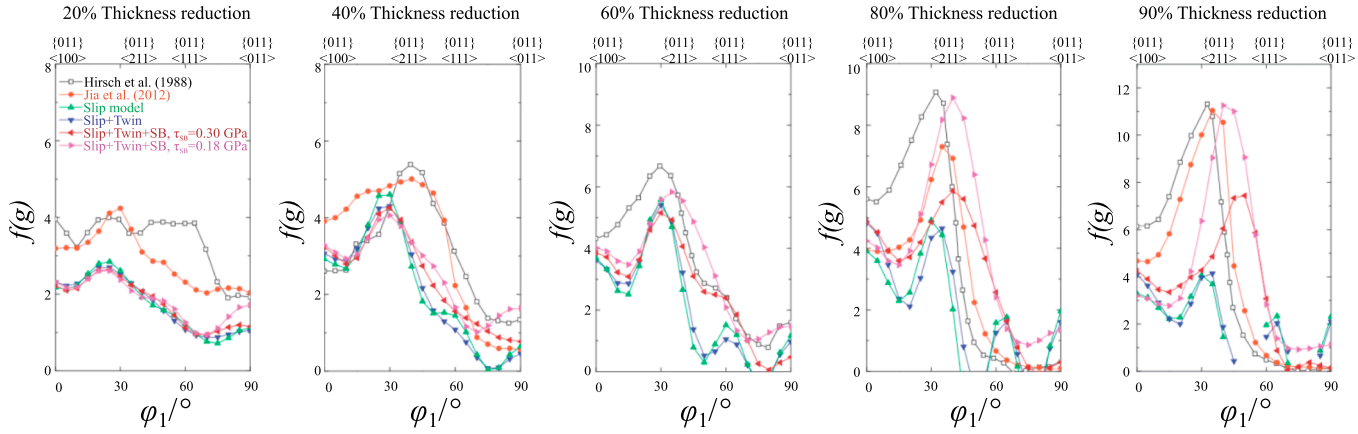

(a) α-fiber with constant EULER angles $\Phi = 45^\circ$, $\varphi_2 = 0^\circ$.

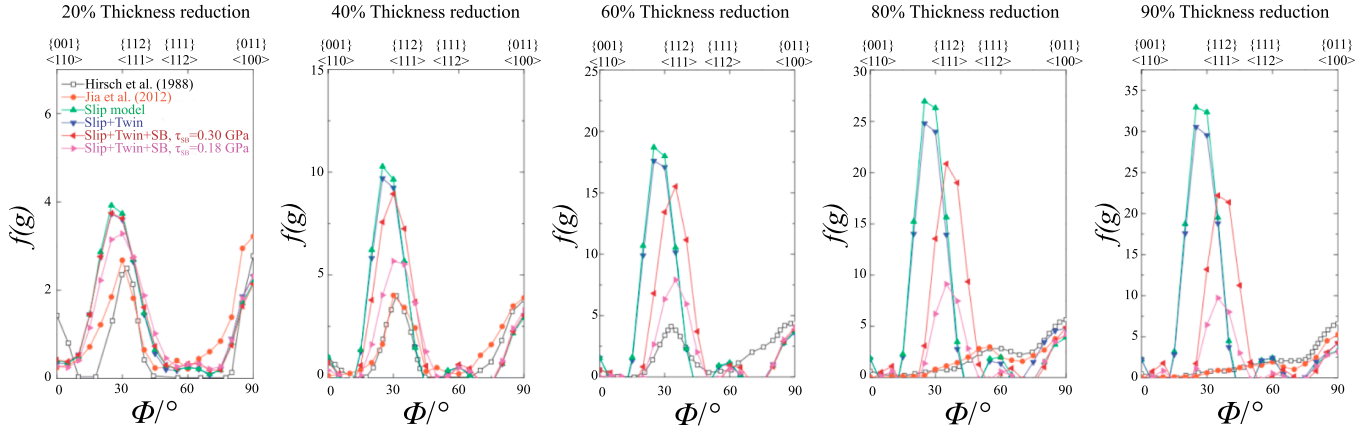

(b) τ-fiber with constant EULER angles $\varphi_1 = 0^\circ$, $\varphi_2 = 45^\circ$.

Fig. 25. Texture evolution of cold rolled *α*-brass at different thickness reduction levels in fiber representation. Figure adopted from [147] with permission from Elsevier.

7.7.2. Co-deformation and shear localization in a plane strain-compressed Copper-Silver bicrystal

For the study of shear banding in Cu-Ag composites with hetero-phase interfaces using DAMASK, suitable crystallographic orientations for both phases had to be selected. Preliminary simulations had revealed [241] that Cu-oriented crystals show the largest tendency to initiate shear banding. Therefore, simulations of a bicrystal consisting of $(1\,1\,2)[1\,1\,\bar{1}]$ orientented Cu and Silver (Ag) were performed. To mimic an initial eutectic composition of Cu-68.3 vol.%-Ag [244], a thickness ratio between Cu and Ag crystals of 6:13 was adopted to approximate the starting microstructure. The modeled region was a portion of bulk material with length L_0 and thickness $H_0 = 2 \times L_0$ in undeformed state, Fig. 26. While the right edge was free to move in the Elongation Direction (ED) direction, the left and bottom edges were constrained from moving in the ED and Normal Direction (ND) directions, respectively. Multi-point constraints were applied to maintain the right edge straight during deformation and a compression displacement constraint was imposed to the top edge with a strain rate of $1 \times 10^{-3}\,\mathrm{s}^{-1}$.

As shown in Fig. 27, at 20% deformation a strong strain localization with a width below five elements is predicted in the Ag phase. In the Cu phase, the deformation was localized in the region adjacent to the strain localization zone that had formed in the Ag phase. It was further observed that the initiation of the shear band systems in both phases did not necessarily correspond to the occurrence of localized strain. It was found that the shear band zones in the upper Cu crystal were triggered by stress concentration at the phase boundaries introduced by shear banding appearing in the adjacent Ag crystal below. Shear bands appeared to cross the phase boundaries, apparently extending into the adjacent Ag phase. The phase boundaries were generally straight although some inclination with respect to ED at small angles was observed. In the interior of the crystals, different directions of strain localization developed. Also, the stress in the Cu phase was larger than that in the Ag phase. In the respective phases, the area with larger stress coincided with the material points where shear banding had initiated. When the thickness reduction reached 40%, significant curvature of the phase boundaries was observed in regions where zones of strong strain localization had penetrated through the hetero-phase boundaries. Strain localization was pronounced in both phases, with a maximum contrast of approximately 3.5. In the upper Cu crystal and in both Ag crystals two families of shear bands were activated.

These different simulation results clearly revealed that shear bands are triggered by stress concentrations resulting from incompatibility of deformation modes at the phase boundaries. The observed very large local strains, significant bending of the hetero-phase interface regions, and sharp strain localization that propagates across the interfaces agree well with experimental observations made on co-deformed composites [244].

7.8. Grain-scale micromechanics of Magnesium

With its very low mass density of only $1.74\,\mathrm{g\,cm}^{-3}$, Magnesium (Mg) is the lightest structural engineering metal. Mg and its alloys are, thus, attractive for applications in lightweight automotive, train, and aerospace design. Yet, manufacturing parts of wrought Mg is challenging due its low formability at ambient temperatures. The low

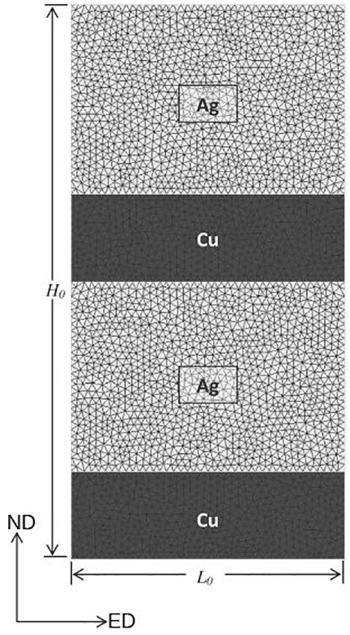

Fig. 26. Schematic of the hetero-phase bicrystal model consisting of triangular elements. To simulate plane strain compression, a prescribed displacement corresponding to the thickness reduction is applied to the top edge. The left and bottom edges are constrained from moving in the Elongation Direction (ED) and Normal Direction (ND) directions, respectively. The right edge is free to move in the Elongation Direction (ED) direction. Figure adopted from [241] with permission from Elsevier.

formability is due to the strong crystallographic basal texture developed during rolling and to the lack of a sufficient number of easily activated deformation systems, which is characteristic of many alloys with hexagonal lattice structure [247–250].

Besides non-basal dislocation slip, twinning can accommodate strain along the crystal c-axis, providing additional degrees of freedom for matching the von Mises criterion of compatible plastic deformation [251]. The deformation modes which are primarily active at room temperature in Mg and its alloys are basal slip and $\{10\bar{1}2\}$ tension twinning. Both are easy to activate and have Critical Resolved Shear Stress (CRSS) values of only a few MPa [252]. The prevalence of basal dislocation slip produces a fiber texture where the basal planes are closely aligned with the primary material flow direction, hence exhausting the contribution of the basal slip system to further deformation [10].

It was observed that the compatible deformation condition according to von Mises [251] does not have to be fulfilled in each grain individually but that also local collective cluster type deformation modes among a group of adjacent grains can provide a sufficient number of shear degrees of freedom [10]. For understanding these crystal cluster co-deformation modes in Mg polycrystals, the microstructure and texture evolution of Mg during *in situ* compression tests was studied. For the experimental analysis combined *in situ* EBSD and Electron Channeling Contrast Imaging (ECCI) observations on deformed sample surfaces to determine active slip and twinning systems via orientation mapping and slip trace analysis were applied. The corresponding CP simulations were conducted using the Phenomenological Crystal Plasticity model (parameters are given in Table 7) together with the spectral solver (Section 3.2.2). The experimental and numerical observed collective grain deformation modes were compared and discussed based on a detailed analysis of the underlying grain-to-grain strain transfer mechanisms and kinematics.

The experiments revealed strain localization and the formation of early stage shear bands in Mg during compressive deformation below 5% engineering strain, Fig. 28(a). Percolative strain patterns in grain clusters with prevalent basal slip as a precursor for shear band formation were observed. The strong basal texture and the associated grain clusters being characterized by similar basal orientations in the recrystallized pure Mg were identified as an important factor responsible for strain localization.

The CP simulations revealed a percolation of concentrated basal slip activity across grain boundaries as the main mechanism for shear band initiation, Fig. 28(b). Slip trace analysis, Schmid factor calculation and deformation transfer analysis at the grain boundaries were performed for the activated twins. The activation of tension twins which could not be predicted from the applied macroscopic compression load was frequently observed. This observation, sometimes termed “non-Schmid” behavior, is a direct consequence of the locally inhomogeneous stress state and should not be confused with the activation of slip systems observed in body-centered cubic (bcc) crystal structures violating Schmid’s law (Section 6.2). Tension twins were activated specifically in regions with high local stresses, for instance inside shear bands. Twinning thus appeared frequently as a local mechanism of

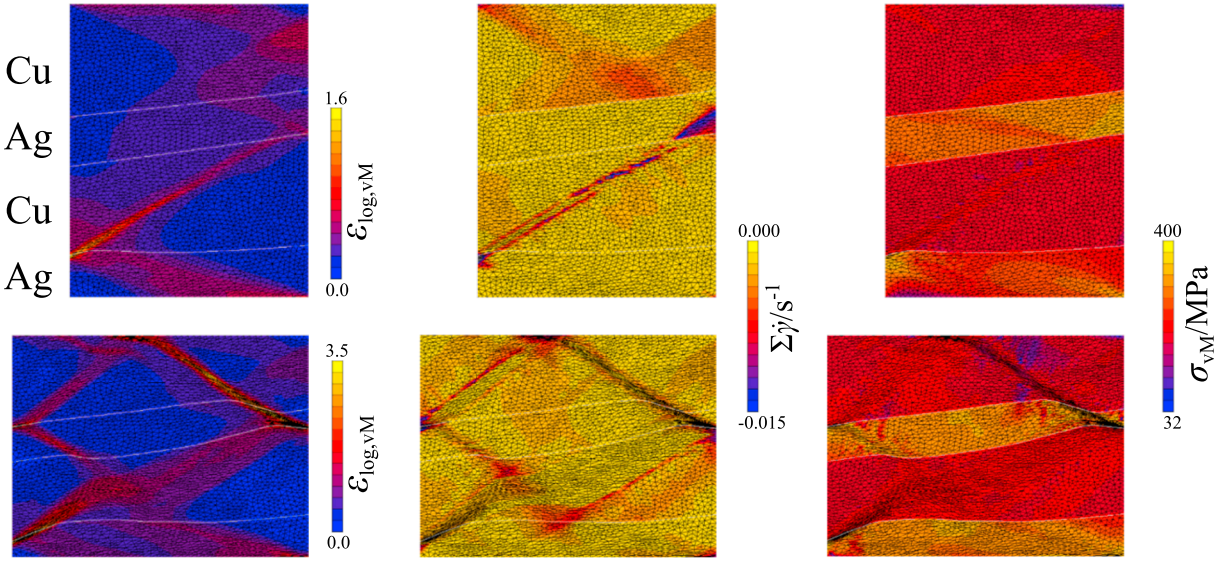

Fig. 27. Simulation results of equivalent logarithmic strain, sum of shear rates on the shear band systems and equivalent Cauchy stress for the Copper-Silver bicrystal at 20% (top) and 40% (bottom) thickness reductions. Figure adopted from [241] with permission from Elsevier.

Table 7
Plastic constitutive parameters for Magnesium employed for the simulation of a measured microstructure using the model presented in Section 6.2.2. Based on values from Tromans [245] and Agnew et al. [246].

Property	Value	Unit
C_{11}	59.3	GPa
C_{33}	61.5	GPa
C_{44}	16.4	GPa
C_{12}	25.7	GPa
C_{13}	21.4	GPa
c/a	1.6235	
$\xi_{0,\mathrm{basal}}$	10.0	MPa
$\xi_{\infty,\mathrm{basal}}$	40.0	MPa
$\xi_{0,\mathrm{prism}}$	55.0	MPa
$\xi_{\infty,\mathrm{prism}}$	135.0	MPa
$\xi_{0,\mathrm{pyr}\langle a\rangle}$	60.0	MPa
$\xi_{\infty,\mathrm{pyr}\langle a\rangle}$	150.0	MPa
$\xi_{0,\mathrm{pyr}\langle c+a\rangle}$	60.0	MPa
$\xi_{\infty,\mathrm{pyr}\langle c+a\rangle}$	150.0	MPa
$h_0^{\mathrm{s-s}}$	500.0	MPa
$h_0^{\mathrm{s-tw}}$	0.0	MPa
$\xi_{0,\mathrm{T1}}$	40.0	MPa
$h_0^{\mathrm{tw-tw}}$	50.0	MPa
$h_0^{\mathrm{tw-s}}$	150.0	MPa

accommodating local strain rather than a response to macroscopic strain.

The usage of CP simulations enabled to complement the experimental investigation with the local stress tensor. Analysis of the Luster–Morris alignment parameter and the (global) Schmid factors for the activated tension twins revealed that twinning follows Schmid's law in orientations favorable for twinning, while in orientations where twinning was not favored by the macroscopic stress state twinning acted indeed more as a process of accommodating local strain mismatch, thereby maintaining strain compatibility at grain boundaries [10].

7.9. Temperature dependent activation of twinning induced plasticity and transformation induced plasticity in high-Manganese steel

This example demonstrates the capability of the constitutive model introduced in Section 6.2.3 to capture the Transformation Induced Plasticity (TRIP) and the Twinning Induced Plasticity (TWIP) effects at different temperatures. Validation of the model was conducted using experimental data for a TRIP/TWIP Fe-22Mn-0.6C steel [19].

Tensile tests were carried out on the material within a temperature range of 123–773 K and at a quasi-static initial strain rate of 0.001 s^{-1}. High energy synchrotron X-ray Diffraction (XRD) was used to study the evolution of the ε-martensite fraction and EBSD analysis was employed to determine the twin volume fraction. The twin volume fraction of the material was determined from EBSD measurements prior to fracture of each sample while the ε-martensite volume fraction was measured in pre-strained tensile samples at macroscopic strains of 0.05, 0.10, 0.20, 0.30, 0.40 and also after fracture of the specimen.

RVE simulations were conducted using the spectral solver introduced in Section 3.2.2. A grid of dimensions $16 \times 16 \times 16$ comprising 100 grains generated using a standard Voronoi tessellation approach serves as an RVE on which periodic boundary conditions hold. Mechanical loading on the RVE was imposed by uniaxial tension with the same strain rate of 0.001 s^{-1} as in the experiments. The material was assumed to have a random texture and thus the crystallographic orientations of the grains were randomly assigned.

The constitutive parameters for the TRIP/TWIP model were determined by fitting the macroscopic stress-strain and the strain hardening curves obtained from the uniaxial tension experiments. The constitutive parameters used in the simulations are shown in Table 8. The fcc single crystal elastic constants for the austenite phase in Iron (Fe)-22Manganese (Mn)-0.6Carbon (C) steel were estimated from *ab initio* calculations by Music et al. [254] for Fe-Mn alloys, while the hexagonal close-packed (hcp) single crystal elastic constants for the ε-martensite phase were calculated from the fcc elastic constants using the procedure proposed by Martin [255,256], the values used are specified in Table 9. The SFE for the material used in this study is calculated using the thermodynamic approach by Dumay et al. [253] and the calculated values of the SFE at each temperature are shown in Table 10. Since the yield strength of the material varies as a function of temperature, the solid solution strength, τ_{sol}, was also varied to achieve this difference in the simulated stress–strain curves. The values of τ_{sol} used for each temperature are also shown in Table 10.

The comparison between the experimental and simulated stress-strain curves is shown in Fig. 29(a), the comparison between the experimental and simulated hardening curves in Fig. 29(b), and the comparison of the measured and simulated twin volume fractions in Fig. 29(c). There is qualitative agreement between the measured and computed twin volume fractions, where twinning decreases with decreasing temperature. Although the computed twin volume fraction at 123 K is not zero as in the experiment, the computed twin volume fraction is very small. However, the model tends to overpredict the twin

(a) Experimental result obtained by Electron Channeling Contrast Imaging (ECCI).

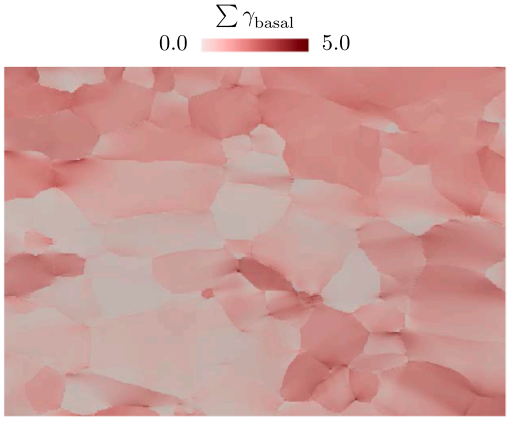

(b) Results of the Crystal Plasticity (CP) simulations: Magnitude of shear on all basal slip systems.

Fig. 28. Comparison of microstructural results at 5% compressive strain obtained from simulation and experiment. Compression direction is vertical. Figure adopted from [10,191] with permission from Elsevier.

Table 8
Constitutive parameters for the plastic behavior of Fe-22Mn-0.6C steel employed for the simulation of temperature dependent tensile behavior using the model presented in Section 6.2.3.

Property	Value	Unit
p_{tw}	5.0	
p_{tr}	8.0	
p_s	1.15	
q_s	1.0	
D	5.0	μm
V_{cs}	1	b_s^3
V_{cl}	1.5	b_s^3
v_0	1×10^{-4}	$m\,s^{-1}$
D_a	2.0	
D_0	4×10^{-5}	$m^2\,s^{-1}$
i_s	30.0	
i_{tw}	10.0	
i_{tr}	3.0	
t_{tw}	0.05	µm
t_{tr}	0.1	µm
L_{tw}	0.192	µm
L_{tr}	0.128	µm
Q_s	3.5×10^{-19}	J
Q_{cl}	3.0×10^{-19}	J
b_s	256	pm
b_{tw}	120	pm
b_{tr}	147	pm

Table 9
Single crystal elastic constants for face-centered cubic (fcc) austenite and hexagonal close-packed (hcp) ε-martensite used in the simulations.

Component	Value / GPa	
	Austenite	ε-martensite
C_{11}	175.0	242.3
C_{12}	115.0	117.7
C_{13}		45.0
C_{33}		315.0
C_{44}	135.0	40.5

Table 10
Temperature-dependent input parameters for the model presented in Section 6.2.3. The solid solution strength τ_{sol} is determined from fitting the experimental stress-strain curves shown in Fig. 29. The Stacking Fault Energy (SFE) Γ_{sf} and the Gibbs free energy $\Delta G^{\gamma\to\varepsilon}$ are calculated using the approach by Dumay et al. [253], assuming values for the interface energy $\sigma^{\gamma/\varepsilon}$ as shown in the table.

T/K	τ_{sol}/MPa	Γ_{sf}/mJ m^{-2}	$\Delta G^{\gamma\to\varepsilon}$/J mol^{-1}	$\sigma^{\gamma/\varepsilon}$/mJ m^{-2}
123	250	14.33	−266.25	15
233	160	19.45	−9.42	10
293	130	25.37	91.30	10
373	130	39.03	323.32	10
423	100	48.60	486.02	10
673	60	98.32	1330.78	10
773	35	118.41	1672.13	10

volume fractions at 373 K and 423 K while it slightly underpredicts the twin volume fractions at 233 K and 293 K. Although the twin volume fractions were not measured for the high temperature curves at 673 K and 773 K, the model predicts that twinning does not occur at those temperatures, which is the expected behavior [18,257]. For the ε-martensite volume fractions which are shown in Fig. 29(d), the measured and computed volume fractions decrease with increasing temperature. The martensitic transformation is more active at lower temperatures because of the lower SFE and more difficult cross-slip. Martensitic phase transformation decreases at higher temperatures as the SFE and Gibbs free energy increase.

The model is able to predict, based on the temperature, which in turn changes the SFE of the material, the activation of martensitic phase transformation at low temperatures, the predominance of twinning at intermediate temperatures, and plastic deformation solely by slip at high temperatures. It is observed that in Fe-22Mn-0.6C, the $\gamma \to \varepsilon$ transformation occurs at low temperatures and increases as the temperature decreases. Twinning occurs starting at room temperature and increases as the temperature increases. Therefore, determination of the temperature dependent SFE as well as of the Gibbs free energy is important to accurately predict the onset of twinning and ε-martensitic phase transformation. Implementation of a first-principles based model for solid solution strengthening [258] can further improve the predictive capabilities of the model.

7.10. Damage in martensitic steel

Lath martensite, the non-equilibrium high-strength phase found in carbon steels after rapid cooling from the austenitic phase-region, typically has a complex hierarchical microstructure [259–261]. Therefore, investigations on plasticity in martensite require on the one side a high spatial resolution to capture the behavior of the smallest building blocks—the name-giving laths—and on the other side a large field of view to include further hierarchical components, *i.e.* subblocks, blocks and packets, up to full prior austenite grains [39]. Here, a coupled damage–CP study is presented which is based on the EBSD characterization of a martensitic microstructure.

A model alloy with composition Fe-0.13C-5.1Ni (in wt.%) produced by ArcelorMittal Research was austenitized at 900°C for 5 min and subsequently water quenched to obtain a fully martensitic microstructure. Further details of the experimental investigations are presented in [262]. Using the *TSL OIM* EBSD analysis software, a single crystallographic orientation has been assigned to individual “grains”, *i.e.* (sub-)blocks. The IPF of the resulting microstructure is shown in Fig. 30. Since the tetragonal distortion of the lattice is small for martensite in low carbon steels, a bcc structure is assumed. The employed material parameters for the Phenomenological Crystal Plasticity model are given in Table 11. Isotropic damage is modeled following Diehl et al. [41], *i.e.* assuming Griffith’s Criterion using the Brittle Damage driving force. The parameters for the damage model are given in Table 12. A uniaxial tensile load at a strain rate of $1 \times 10^{-3}\,s^{-1}$ was applied with an initial time step of 1.0 s. To temporally resolve crack propagation the time step had been reduced to 0.0002 s after damage initiation.

The resulting stress distribution evolution from damage initiation until the development of a percolating crack network is shown in Fig. 31. A significant stress redistribution can be observed when comparing Fig. 31(a) and (c). The dominant crack initiates in the region where severe plastic deformation was experimentally observed by Morsdorf et al. [262]. While the stress normal to this crack path is relaxed, characteristic stress concentrations can be seen at the crack tips (Fig. 31(b) and (c)). Moreover, damage initiates also at several other sites, but further development into cracks is inhibited by the surrounding microstructure. The remaining material between the two largest cracks shows an especially high stress, as can be seen in Fig. 31(b) and (c).

This example clearly demonstrates how enhancing CP modeling by continuum damage approaches provides new insights into the mechanics of complex materials as the stress distribution changes profoundly upon damage initiation. However, it should be mentioned that including damage imposes additional challenges: First, computation times increase significantly, which is mainly due to the necessity of using smaller time steps and the additional iterations required to arrive at a self-consistent solution (Fig. 6). Second, the identification of suitable damage models and their associated parameters introduces additional efforts. Finally, also the CP model needs to be parametrized to give appropriate results in the quasi-static loading regime as well as at high strain rates during catastrophic failure.

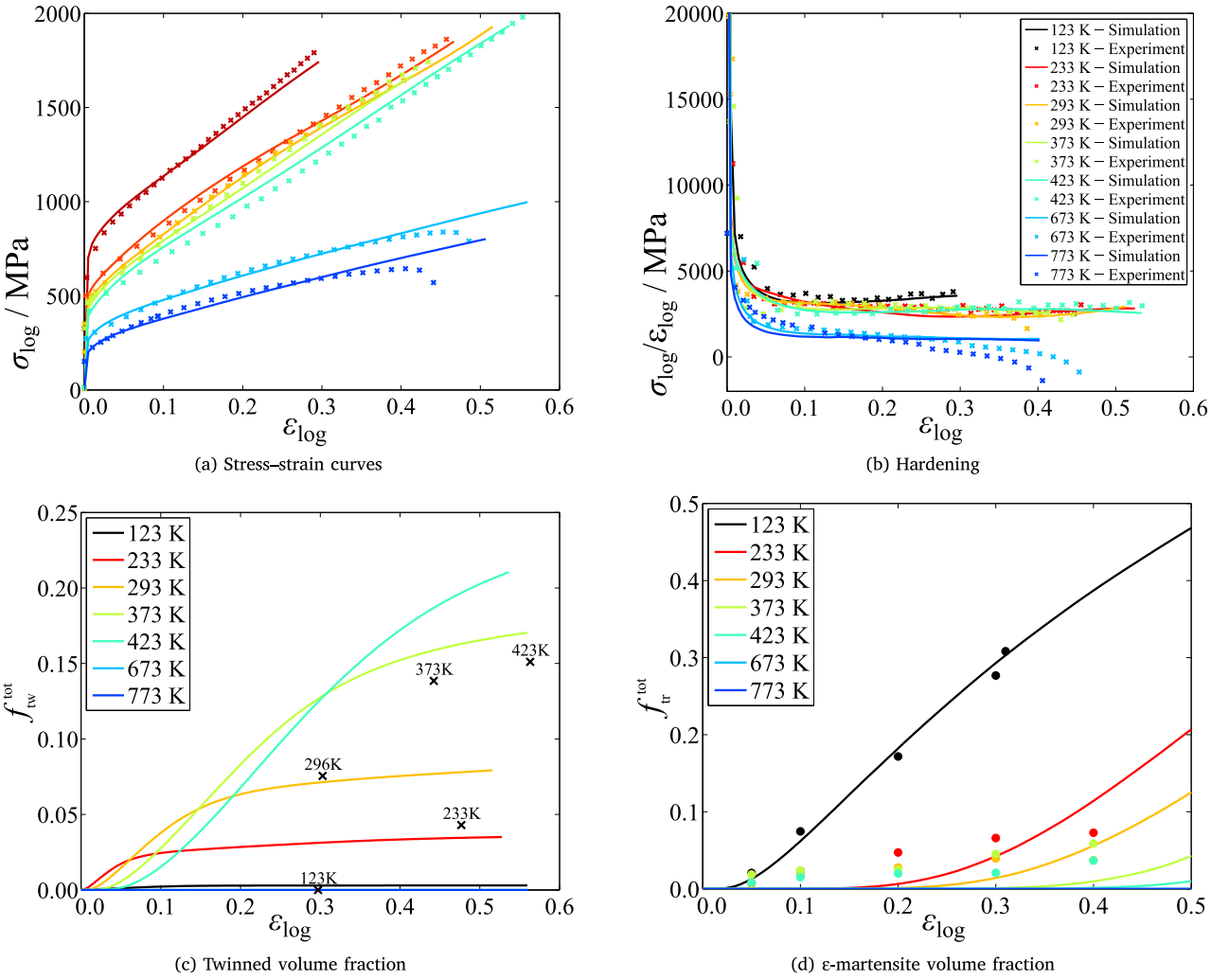

(a) Stress–strain curves

(b) Hardening

(c) Twinned volume fraction

(d) ε-martensite volume fraction

Fig. 29. Comparison between experimental (indicated by crosses and dots) and simulated (indicated by lines) results using the TRIP/TWIP model for Fe-22Mn-0.6C steel. Figure adopted from [19] with permission from Elsevier.

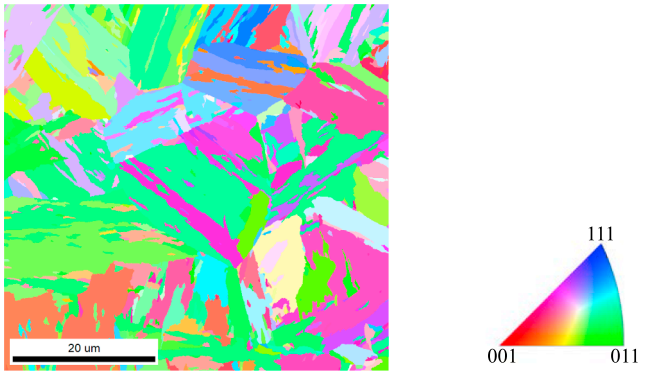

Fig. 30. Martensitic microstructure formed out of approximately 15 former austenitic grains after assigning a single orientation to each (sub-)block. Color indicates crystallographic orientation in Inverse Pole Figure (IPF) notation parallel to the out-of-plane direction. (For interpretation of the references to color in this figure, the reader is referred to the web version of this article.)

Table 11
Plastic constitutive parameters for body-centered cubic (bcc) martensite employed for the coupled Crystal Plasticity-Phase Field Method for Fracture (CP-PFMF) simulation of a measured martensitic steel microstructure using the model presented in Section 6.2.2.

Property	Value	Unit
C_{11}	417.4	GPa
C_{12}	242.4	GPa
C_{44}	211.1	GPa
$\dot{\gamma}_0$	1.0×10^{-3}	s^{-1}
$\xi_{0,\{110\}}$	406	MPa
$\xi_{\infty,\{110\}}$	873	MPa
$\xi_{0,\{112\}}$	457	MPa
$\xi_{\infty,\{112\}}$	971	MPa
h_0	563	GPa
$h^{\alpha\alpha'}$	1.0	
n	20.0	
a	2.25	

7.11. Dual phase steel micromechanics

Dual Phase (DP) steels achieve their excellent mechanical properties through the combination of two phases: Hard martensitic inclusions in a softer ferritic matrix enable simultaneous improvement of strength and ductility, making DP steels a viable option in automotive engineering [263]. Despite the successful application of DP steels and a large number of detailed studies on modeling their mechanical behavior, a complete understanding of the local stress and strain

Table 12
Damage constitutive parameters for body-centered cubic (bcc) martensite employed for the coupled Crystal Plasticity-Phase Field Method for Fracture (CP-PFMF) simulation of a measured martensitic steel microstructure using the model presented in Sections 6.4.1.1 and 6.4.2.1.

Property	Value	Unit
G	5.0	$\mathrm{J\,m^{-2}}$
l_c	0.1	µm
μ_ϕ	1.0	Pa s

partitioning, which is responsible for the mechanical properties, has still not been achieved.

Here, two examples of simulating experimentally characterized DP steel microstructures with DAMASK are presented. The first example aims at a strong coupling between experiment and simulation adapted from Tasan et al. [12,218] and is limited to 2D models. Since reducing micromechanical simulations to 2D slices of the real 3D microstructure may lead to errors [37,189,191,264,265], in a second example a 3D DP steel microstructure obtained by serial sectioning and subsequent EBSD measurements has been modeled by Diehl et al. [34].

The phenomenological constitutive formulation described in Section 6.2.2 has been used to model, ferrite and martensite phases (model parameters are given in Table 13). Retained austenite regions with fcc crystal structure, which are often found in DP steels [263], have been treated as martensite since it is known from experimental observations that the austenite transforms to martensite at early deformation states in the considered material.

7.11.1. 2D Simulations of dual phase steel: coupling experiments and simulations

For the coupled 2D experimental-simulation study, a tensile strain at the same rate as in the accompanying experiment ($6 \times 10^{-4}\,\mathrm{s^{-1}}$) has been applied to the microstructural patch (Fig. 32(a)) for 170 s, *i.e.* until a final average strain of approximately $\bar{\varepsilon} = 0.08$ was reached. The out-of-plane direction of the 2D model is set to be stress-free to reflect the experimental situation of a free surface. As a characteristic feature of the employed spectral solution method, the microstructure is periodically repeated in all three directions, *i.e.* the prescribed Boundary Conditions (BCs) are volume averages.

Comparing the overall strain distributions obtained from the experiments by a DIC approach [266] given in Fig. 32(b) to those obtained from the simulations (Fig. 33(a)) reveals that many features are in good agreement, especially: (i) A strong strain partitioning is observed among ferrite and martensite (compare *e.g.* rightmost images

Table 13
Constitutive parameters of ferrite and body-centered cubic (bcc) martensite employed for the simulation of real Dual Phase (DP) microstructures using the model presented in Section 6.2.2.

Property	Value		Unit
	Ferrite	Martensite	
C_{11}	233.3	417.4	GPa
C_{12}	235.5	242.4	GPa
C_{44}	128.0	211.1	GPa
$\dot{\gamma}_0$	1.0×10^{-3}	1.0×10^{-3}	$\mathrm{s^{-1}}$
$\xi_{0,\{110\}}$	95	406	MPa
$\xi_{\infty,\{110\}}$	222	873	MPa
$\xi_{0,\{112\}}$	96	457	MPa
$\xi_{\infty,\{112\}}$	412	971	MPa
h_0	1	563	GPa
$h^{\alpha\alpha'}$	1.0	1.0	
n	20.0	20.0	
a	2.25	2.25	

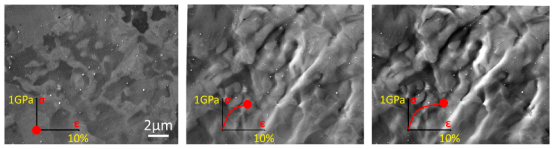

(a) Secondary Electron (SE) images. Insets show global stress–strain curves.

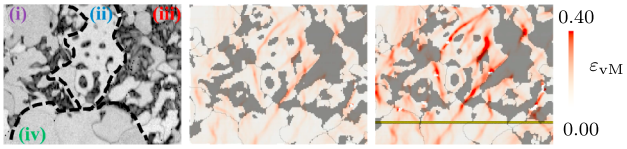

(b) Strain maps obtained experimentally with µDIC. DIC: Digital Image Correlation.

Fig. 32. Results of the *in situ* deformation experiments in the undeformed state (left) and at an average strain in horizontal loading direction of $\bar{\varepsilon} = 0.05$ (center) and $\bar{\varepsilon} = 0.08$ (right). Figure adopted from [12,191] with permission from Elsevier.

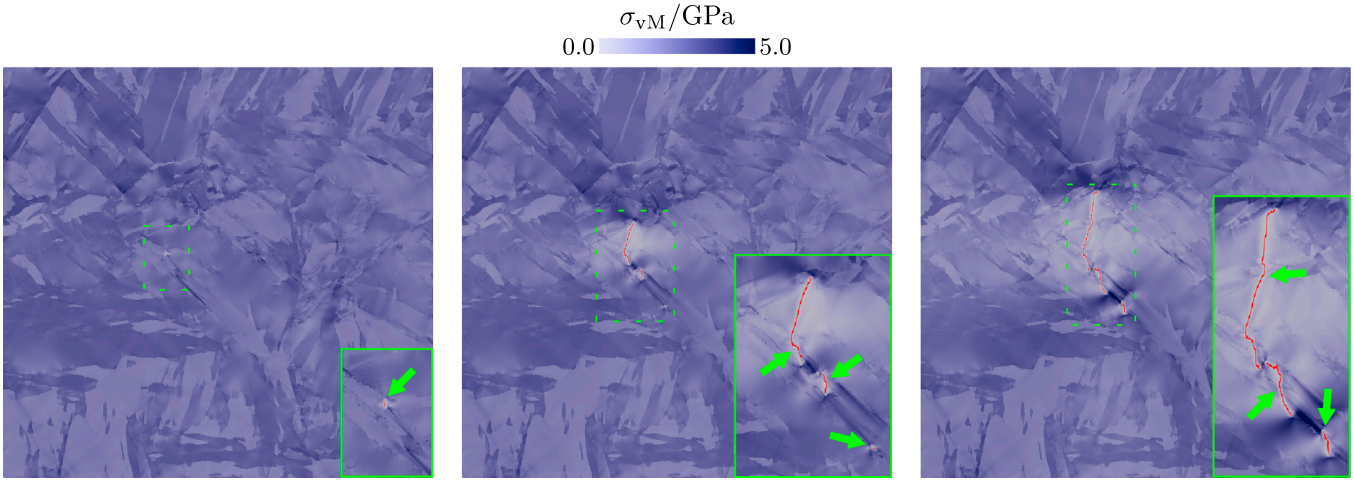

(a) Directly after formation of the first crack. (b) After a crack network has formed. (c) Later stage of the crack network formation.

Fig. 31. Simulated equivalent stress in the martensitic microstructure where cracks are colored in red. The loading direction is horizontal. The insets (green solid lines) show a magnification of the region around the cracks (green dashed lines) in which individual cracks are indicated by green arrows. (For interpretation of the references to color in this figure, the reader is referred to the web version of this article.)

in Fig. 32(b) and Fig. 33(a)). (ii) There is also good qualitative agreement in the level of scatter observed in the ferritic regions. A large scatter ($\varepsilon_{vM} = 0.02$–0.35 for a nominal strain of $\bar{\varepsilon}_{vM} = 0.010$, *i.e.* $\bar{\varepsilon} = 0.08$) corresponds to the highly heterogeneous nature of strain distribution in ferrite, which is clearly seen in Fig. 32(b) and Fig. 33(a). (iii) The strain in many ferritic regions is localized in bands oriented at 45–50° w.r.t. the loading direction.

Given this correlation of the strain distribution between simulation and experiment, von Mises stress maps obtained from simulations (Fig. 33(b)) are considered to be representative for the stress partitioning in the microstructure during the *in situ* experiments. It can be observed that long and thin martensite connections aligned with the loading direction experience the highest local stresses while smaller and globular shaped martensite areas show rather small stress concentrations. The stress partitioning is spatially relatively constant over time: This means that the local stress peaks that had been built up at the beginning of loading remained essentially stationary during further deformation. Significant stress heterogeneities are observed in martensitic regions, *e.g.* in the large martensite grains in the upper right region, which can be attributed to the complex hierarchical microstructure of martensite (see Section 7.10 for details).

The overall success in capturing the qualitatively similar strain distribution trends in simulations and experiments (see Fig. 32(b) and Fig. 33(a)) underlines the fidelity of the simulations also for cases of complex engineering microstructures. However, differences are observed in some cases, for example regarding the position of the highly strained bands. More specifically, the simulations reveal strain bands in the ferritic grains mainly in regions with higher martensite content and low strain gradients elsewhere, while the experimental results show high strain gradients also in ferritic regions remote from martensite.

The main limitation for the experiments is that Scanning Electron Microscopy (SEM) is a surface analysis technique and cannot (at least in a non-destructive manner) be used to reveal 3D microstructural information. Due to this lack of subsurface information, the microstructure in the DP simulation model is assumed to be columnar, while in reality there may be martensite layers below the surface ferrite grains, or vice versa (see also [189]). However, as shown by Tasan et al. [218], a *post mortem* serial sectioning methodology allows to asses the role of the underlying microstructure and can partially explain the deviations resulting from the 2D approach.

7.11.2. 3D simulations of dual phase steel: simulating a measured microstructure

The integrated experimental–numerical methodology presented above is able to capture many of the quantitative aspects such as strain and stress partitioning in a realistic way. However, the simplifications associated with a 2D microstructure approximation prevent a better match between experimental and simulated results. Therefore, here results of extending this approach to 3D are shown. As the microstructure was in this case obtained through a serial sectioning approach, a comparison to experimental strain maps is not possible.

The applied serial sectioning approach consists of multiple cycles of mechanical polishing and EBSD imaging [33,267]. To this end, first a sample with two parallel sides of high surface quality was prepared by mechanical grinding and polishing. For each measurement cycle, the sample was polished with a Silicon (Si) Oxide Particle Suspension (OPS) which resulted in an approximately constant removal rate of 0.13 µm per step. In total, 22 slices, each sized 70 µm × 20 µm (Transverse Direction (TD) × Rolling Direction (RD)) at an in-plane EBSD step size of 0.2 µm had been acquired and combined to a 3D model using the Cube software [268]. To avoid artifacts at the boundaries, the model (see Fig. 34) has been mirrored at each side.

The local strain in loading direction for the final increment is shown in Fig. 35. A strong strain partitioning is observed, where the martensite exhibits the smallest strain while narrow ferrite regions in between martensite portions are significantly strained far above the average deformation. In agreement with the findings from the 2D simulations, the spatial stress and strain distribution remains constant during loading, *i.e.* "hot" and "cold" spots do not change (not shown here). In contrast with the 2D simulations, the localization bands are much less pronounced and a more homogeneous pattern is observed [34].

The 3D example illustrates that—except for increased computation times—the limitation to 2D in CP modeling, when using real microstructures, is mainly caused by experimental constraints. While the selected 3D EBSD approach enables acquisition at high spatial resolution, its destructive nature prohibits the direct comparison to experiments. Synchrotron measurements [269], in contrast, require even higher experimental efforts especially when high spatial resolution including in-grain orientation scatter is of importance.

7.12. Texture evolution during plate rolling

Crystallographic textures are formed by plastic deformation, recrystallization and phase transformation. Since crystallographic textures have substantial effects on the mechanical properties and their anisotropy, their reliable prediction is of high relevance for adjusting complex engineering process chains such as for instance sheet and plate production. CP simulations have been successfully used to investigate the evolution of the deformation textures under various types of processing conditions [272–274]. However, there are so far only few systematic simulation studies on texture analysis during hot rolling processes. In this section, the temperature dependent dislocation-based model, presented in Section 6.2.3, was therefore exemplarily used for simulating a steel plate hot rolling process. Special attention was placed in that context on studying specifically the influence of controlled rolling on the crystallographic texture evolution through the sheet thickness. Studying hot rolling textures is of special importance as the textures and microstructures that are formed during this process are substantially altered when the material is exposed to the subsequent down-stream processing steps. Hence, the hot band textures are as a rule often not directly accessible to measurements. Also, it is challenging to evaluate texture evolution in steel plate production quantitatively by experiments due to limitations in achieving realistic heating and rolling conditions in laboratory settings.

The macroscopic deformation resistance, viz. the flow stress, during hot rolling can be approximated by the empirical equation of Misaka and Yoshimoto [275]:

$$\sigma = \exp(0.126 - 1.75C + 0.9545C^2) \times \exp\left(\frac{2851 + 2968C - 1120C^2}{T}\right)\varepsilon^{0.21}\dot{\varepsilon}^{0.13}. \tag{137}$$

Here, C is a fitting parameter and reflects the amount of alloying elements. The material parameters (Table 14) for the fcc slip systems were determined by fitting Eq. (137), Fig. 36. Except for some deviation at

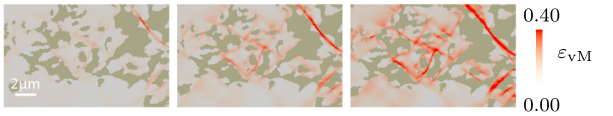

(a) von Mises strain in ferrite, martensite shown in grey.

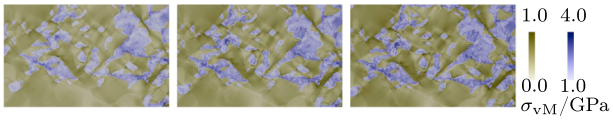

(b) von Mises stress in ferrite and martensite. Different color codes are used for both phases because of the largely different properties.

Fig. 33. Results obtained from the Crystal Plasticity (CP) simulations at an average strain of $\bar{\varepsilon} = 0.03$ (left), $\bar{\varepsilon} = 0.05$ (center) and $\bar{\varepsilon} = 0.08$ (right). Figure adopted from [12,191] with permission from Elsevier.

Fig. 34. 3D model obtained from serial sectioning Electron Backscatter Diffraction (EBSD) used for the Dual Phase (DP) steel simulations. The dimensions are 70.0 µm × 20.0 µm × 2.9 µm. Color indicates Inverse Pole Figure (IPF) along the horizontal loading direction.

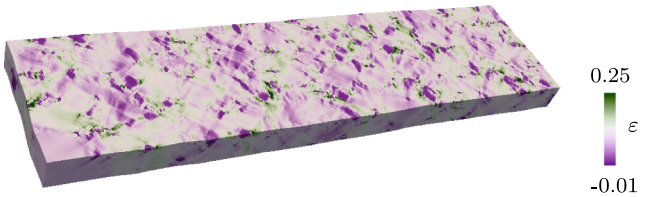

Fig. 35. Strain in loading direction mapped onto the microstructure in deformed configuration. Gray color indicates the average strain of $\bar{\varepsilon} = 0.12$.

small strains the agreement between the CP simulation and Eq. (137) is satisfactory.

The plate rolling process was simulated with the commercial FEM code Abaqus explicit 6.14 using DAMASK as a user material subroutine (`Vumat`). Reverse rolling was modeled using rigid work rolls with a diameter of 1220 mm. The work piece was discretized by three-dimensional isoparametric elements with reduced integration (C3D8RT); 10 elements in the Normal Direction (ND), 5 elements in the TD and 12 elements in the RD. Generalized plane strain boundary conditions were applied along TD. ND surfaces were kept straight by multi-point constraints. The thickness of the plate was reduced from 40 mm to 20 mm by three-pass rolling according to Table 15 with a rolling speed of 3.3 m s^{-1} and a plate entry velocity of 3 m s^{-1}. The friction coefficient was set to 0.4. Adaptive meshing was used to improve the distortion of the elements at large plastic deformation, *i.e.* mesh smoothing methods, volume smoothing, and Laplacian smoothing were applied in each increment. The initial temperatures for the coupled thermo-mechanical analysis were set to 1173 K and 373 K for work piece and work rolls, respectively. Air cooling and heat transfer from the material to the work rolls were considered. Also, dissipative deformation and frictional heating were considered in the work piece elements. To mimic a random starting texture, five constituents with random orientations were assigned to each element, resulting in a total number of 3000 orientations.

Fig. 37 shows the total accumulated slip and the temperature during each rolling pass. Almost no accumulated slip is seen at the center of the work piece and, despite a random initial texture, a strong plastic strain partitioning is observed. In the last rolling pass, friction caused large plastic deformation at the plate surfaces.

The Orientation Distribution Function (ODF) was calculated from the crystallographic orientations after each rolling pass. For studying the texture gradients along the ND through the sheet thickness, the surface and center texture were evaluated separately. The deformation texture after the final rolling pass was converted into its corresponding transformation texture by using the Kurdjumov–Sachs (KS) relationship without imposing any specific variant selection.

Fig. 38 shows the deformation texture evolution obtained from the CP simulation in terms of $\varphi_2 = 45°$ ODF sections for the surface layer and at the center layer of the rolled sheet. In the surface region of the sheet, the textures predicted are the rotated cube ($\{0\,0\,1\}\langle 1\,1\,0\rangle$)[16] and γ-fiber ($\langle 1\,1\,1\rangle \parallel$ ND) components, since the surface texture is affected by friction and the rolling pass direction, which together can promote shear textures. For the mid thickness textures (*i.e.* at the center layer) high intensities of $\{2\,1\,1\}\langle 1\,1\,1\rangle$ and $\{1\,1\,0\}\langle 1\,1\,2\rangle$ are predicted. The quarter thickness textures are predicted to be intermediate between surface and mid thickness (not shown here).

Next, the corresponding transformation textures resulting from the simulations and an experimental reference texture were compared to each other. Tomida et al. [271] have studied the transformation textures resulting from a typical hot rolling process. The center texture after transformation obtained from the simulation indeed corresponds roughly to this experimentally obtained reference texture. However, the surface texture after transformation obtained from the DAMASK simulation includes some other orientations that differ from those observed in the experimental reference texture. It is conjectured that the differences between the predicted and the experimentally obtained surface textures depend on the influence of friction conditions and on the variant selection during transformation.

The influence of various rolling conditions on deformation texture evolution was evaluated in the non-recrystallized region of the rolled sheets. In this study, the friction coefficient and the rolling pass direction were changed. The friction coefficient was decreased from the reference condition (0.40–0.10) and the rolling pass direction was changed from reverse rolling (alternating forward–backward rolling) to tandem rolling (sequential unidirectional rolling). The other conditions assumed for the analysis remained the same (Table 15).

Fig. 39 shows the influence of these rolling conditions on deformation texture evolution in terms of ODF sections for $\varphi_2 = 45°$. The mid-thickness texture was not affected by the rolling conditions, since any of these modifications in the boundary conditions produced similar simulated deformation textures with high intensities of $\{2\,1\,1\}\langle 1\,1\,1\rangle$ and $\{1\,1\,0\}\langle 1\,1\,2\rangle$. However, the predicted surface textures were affected by the rolling conditions. In cases where the friction coefficient between the work roll and the sheet was decreased in the simulations, the surface texture became similar to the center layer texture, *i.e.* the deformation state was approaching a global plane strain state everywhere in the sheet. When tandem rolling was assumed as boundary condition, *i.e.* when accumulative unidirectional rolling was applied, the surface texture was predicted to show a higher intensity of the gamma fiber ($\langle 1\,1\,1\rangle \parallel$ ND) in comparison to the textures obtained after reverse rolling. These trends reveal that the surface textures can depend substantially on the near-surface shear profiles associated with the imposed friction and rolling pass conditions. These results qualify DAMASK as a helpful modeling toolbox for investigating and tuning industrial rolling processes owing to its capability of predicting texture, microstructure, and mechanical response in complex through-process scenarios.

7.13. The Virtual Laboratory

While CP simulations include many of the details of the underlying deformation mechanisms, in many cases they are still computationally

Table 14
Constitutive parameters of austenite employed for the simulation of plate rolling using the model presented in Section 6.2.2.

Property	Value	Unit
C_{11}	124.8	GPa
C_{12}	53.5	GPa
C_{44}	35.7	GPa
D	50.0	µm
τ_S	20.0	MPa
b	256	pm
ϱ_0	1.0	m m^{-3}
v_0	1.0	m s^{-1}
Q_s	3.12	eV
p	10.0	
q	0.30	

[16] $\{0\,0\,1\}$ parallel to ND and $\langle 1\,1\,0\rangle$ parallel to RD.

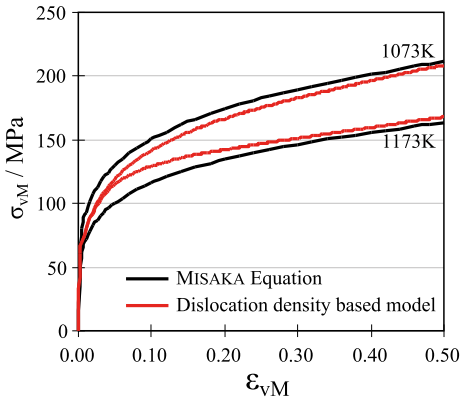

Fig. 36. Flow curves for two selected temperatures. Comparison of the prediction by Eq. (138) to the behavior of the employed Crystal Plasticity (CP) model (see Section 6.2.3 and Table 14). Figure adopted from [270].

Table 15
Rolling pass schedule for hot rolling of austenitic plate steel at 1173 K.

Pass	Thickness / mm		Reduction / %
	Initial	Final	
1	40	30	25
2	30	24	20
3	24	20	20

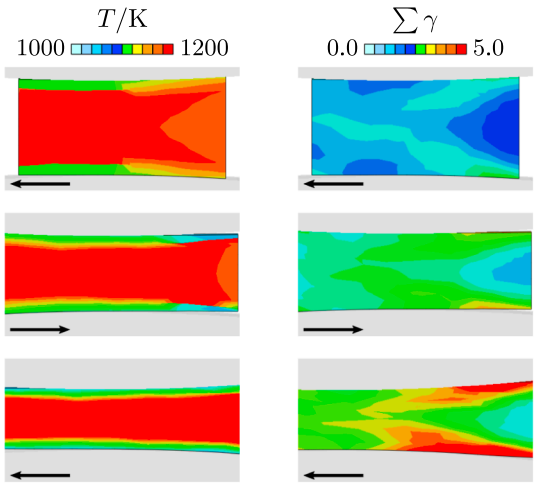

(a) Temperature (b) Accumulated slip

Fig. 37. Results from the hot rolling simulation, quantities mapped onto the work piece in the mill from first (top) to third pass (bottom). Arrows indicate Rolling Direction (RD). Figure adopted from [270].

much too expensive for direct inclusion into large-scale forming simulations. Therefore, simulations at the component scale are typically conducted using the concept of yield surfaces to model the transition from elastic to elasto-plastic deformation. The yield surface is usually described as a convex analytical function in the six-dimensional stress space. The best-known and probably to date most-used yield surface descriptions are the VON MISES yield surface [251] for isotropic behavior and the HILL48 yield surface [284] for anisotropic behavior. The parameters of these functionals are usually calibrated based on a number of experimental tests (see Fig. 40). However, with increasingly advanced yield surface formulations, the number and complexity of the necessary experimental tests for calibration are also increased and so are the associated costs. This is where the VIRTUAL LABORATORY [1], also termed numerical homogenization, comes in. Instead of conducting multiple

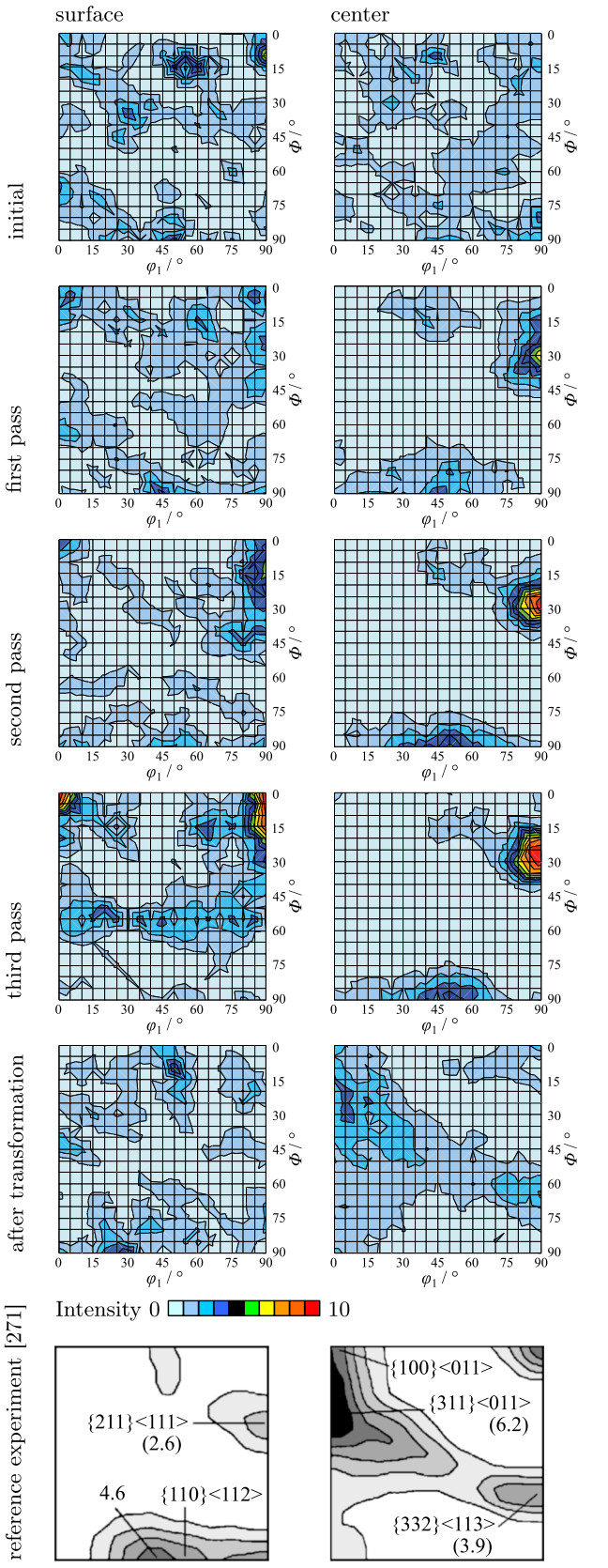

Fig. 38. Texture evolution at the surface and at the center of the simulated rolled sheet in terms of Orientation Distribution Function (ODF) sections at $\varphi_2 = 45°$. Figure adopted from [270,271] with permission from the Iron and Steel Institute of Japan.

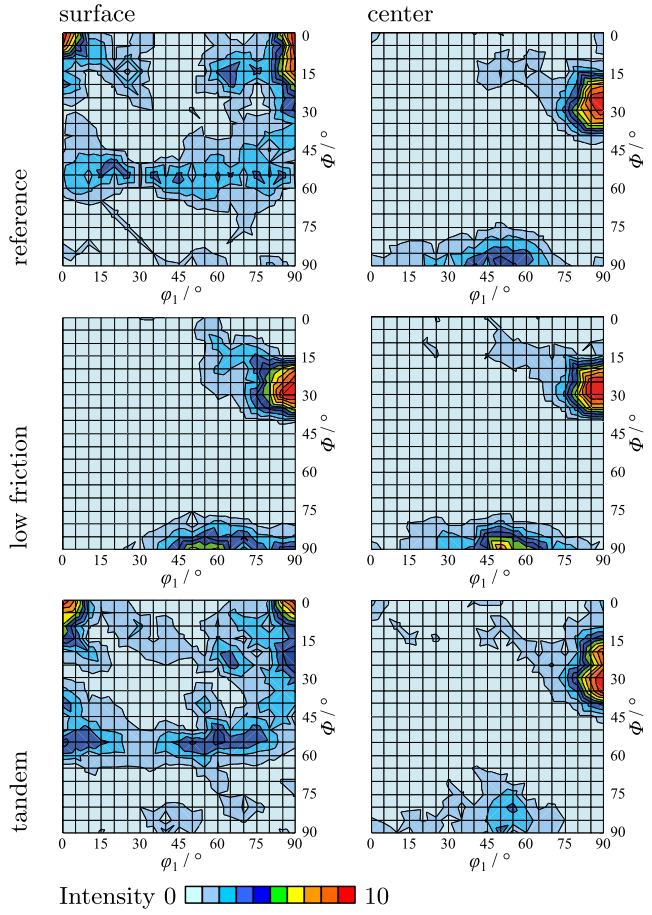

Fig. 39. Influence of rolling conditions on the final rolling texture shown in terms of Orientation Distribution Function (ODF) sections at $\varphi_2 = 45°$. Figure adopted from [270].

time-consuming and expensive experiments, only a small number of very basic mechanical tests to calibrate a CP constitutive law have to be performed. Then, in lieu of doing all calibrations experimentally, a number of additional virtual tests are done on the basis of RVEs using *e.g.* the efficient spectral solver (Section 3.2.2). This approach has the additional advantage that many tests, which experimentally can hardly be done at all, are easy to perform in a simulation.

In this example, several yield surface descriptions have been calibrated for the description of the anisotropy of cold rolled Al alloy 3104. First, the parameters of the phenomenological constitutive law (Section 6.2.2) were calibrated to a simple tensile test, see Fig. 41 and Table 16. Then a large number of tests were simulated for the yield surface calibration. As the cold rolled material shows some additional anisotropy due to the elongated grain shape, different RVEs were used for each loading direction as shown in three examples in Fig. 42. A Levenberg–Marquardt optimization was used to determine the parameters of different yield surface descriptions. Details of the different yield surface descriptions and the fitted parameters can be found in Zhang et al. [27]. Fig. 43 shows the resulting yield surfaces together with the simulated and some experimental points. It was found that the CP simulations can indeed be very efficiently used to calibrate complex analytical yield surfaces that are commonly used in industrial manufacturing.

These results show that the use of DAMASK-based numerical homogenization schemes in conjunction with the spectral solver and high resolution RVEs can serve as a powerful Virtual Laboratory for meeting simulation challenges in advanced manufacturing involving complex forming operations. The fitted yield surfaces can be directly used in forming simulations on the component scale, by that bridging scales from the motion of dislocations to the resulting anisotropic behavior of sheet metal [1].

7.14. Deep drawing of dual phase steel

In this example the Relaxed Grain Cluster (RGC) homogenization scheme (Section 4.1.3) was used for the multi-scale simulation of a deep drawing process (see Fig. 44(a) for the simulation setup). In order to highlight the predictive capability of the RGC scheme under demanding micromechanical conditions, a multi-phase material with strong property contrast between its constituent phases, namely a DP steel, has been considered. A $2 \times 2 \times 2$ cluster, of which two constituents (or "grains") represent martensite, was used at each integration point. For the ferrite phase a set of orientations with size equal to the number of Material Points times six, closely representing the measured crystallographic texture, was drawn using the HybridIA algorithm (Section 4, [97]). These orientations were then randomly assigned to the respective cluster constituents. For the martensite a random orientation distribution was assumed. The local constitutive response of the individual phases was described by the phenomenological CP model (Section 6.2.2); the constitutive parameters are given in Table 17. DAMASK was used as a `Hypela2` subroutine in Msc.Marc.

Fig. 45(a) and (b) shows the distribution of the major (or the most dominant) principal strain component on the cup exterior and interior surfaces, respectively. In general, the upper part of the cup wall had undergone compressive strain, particularly in the circumferential direction. The middle part of the cup wall was dominated by tensile strain in the radial direction. The strain level in the lower part and base of the cup was relatively low. The results moreover revealed that there was no prominent "earing", *i.e.* undesired texture-dependent variation in cup height. This was to be expected, since in this case the initial crystallographic texture was close to random and therefore does not induce any anisotropic behavior.

The results of the deep drawing simulations using the RGC scheme are compared in Fig. 46 to results obtained by simulations using the simpler Taylor homogenization scheme (Section 4.1.2) as well as to experimental investigations. It can be seen that the RGC scheme provides in general a better prediction than the uniform strain Taylor model for the measures considered: wall thickness (Fig. 46(a,b)), earing profile (Fig. 46(c)), and punch force (Fig. 46(d)). The evolution of the force applied to the moving punch is depicted as a function of the position of the punch in Fig. 46(d). Comparison to the benchmark experimental data reveals that both, the uniform strain Taylor model and

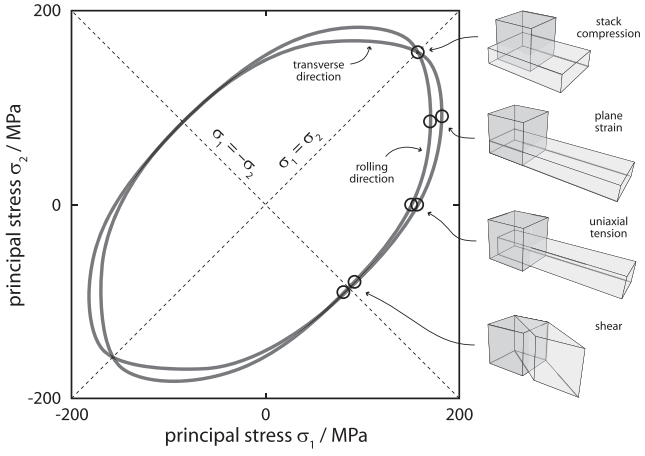

Fig. 40. The Vegter yield surface [276–278] derived from virtual test data. The corresponding associated individual simulated or experimentally conducted deformation tests are schematically depicted on the right hand side. Figure adopted from [1] with permission from Elsevier.

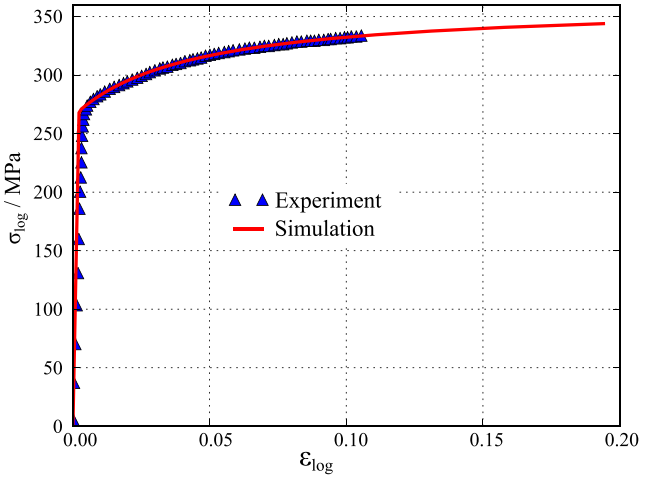

Fig. 41. Experimentally obtained and fitted stress-strain curves of cold-rolled AA3104. The experimental result is taken from the work of Wu et al. [279]. Figure adopted from [27] with permission from Elsevier.

Table 16
Constitutive parameters of single-crystalline aluminum employed for the virtual tests using the model presented in Section 6.2.2.

Property	Value	Unit
C_{11}	206	GPa
C_{12}	118	GPa
C_{44}	54	GPa
$\dot{\gamma}_0$	1.0×10^{-3}	s^{-1}
ξ_0	88	MPa
ξ_∞	118	MPa
h_0	2.483	GPa
a	2	
n	50	

the RGC scheme lead to an overprediction of the experimental punch force magnitude (32 kN), with the RGC model being in better agreement (39 kN) than the uniform strain Taylor model (48 kN).

As a result of the improved strain partitioning (kinematics), the RGC scheme allows for accurate plastic flow in local grain deformation compared to the Taylor scheme, leading to a more realistic prediction of the final cup geometry (both height and thickness). The comparison to the experimental results shows that the presented model is able to adequately bridge the gap between the governing deformation mechanism at the microscale and the overall behavior of the sample at the macroscopic, *i.e.* engineering, scale. A more detailed description of this application example can be found in Tjahjanto et al. [285].

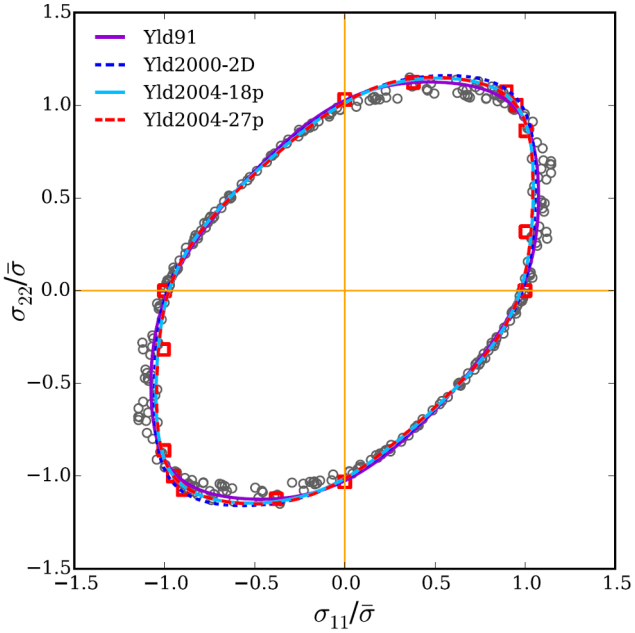

Fig. 43. Yield surfaces ($\sigma_{12} = 0$) of the cold-rolled AA3104 aluminum alloy predicted by the identified yield functions. $\bar{\sigma}$ denotes the uniaxial tensile yield stress along the Rolling Direction (RD) obtained from the virtual tests. Open circles denote the yield stress points obtained from the Virtual Laboratory simulations, open squares denote experimental data from Wu et al. [279]. Yld91, Yld2000-2D (for the plane stress state), and Yld2004-18p are the yield functions proposed by Barlat et al. [280–282], Yld2004-27p is the one proposed by Aretz et al. [283]. Figure adopted from [27] with permission from Elsevier.

7.15. Continuum dislocation dynamics

This example shows how a novel CDD theory [286,287] can be used to study the evolution of the dislocation density in torsion of a microshaft when implemented into DAMASK. The presented CDD CP model is based on three internal state variables per slip system, namely the total dislocation density ϱ, the dislocation density vector $\boldsymbol{\varrho}$, and the dislocation curvature density q. As presented in Ebrahimi et al. [288], the evolution equations on a slip system are formulated as:

$$\dot{\varrho} = -\operatorname{div}(v\boldsymbol{\varrho}^{\perp}) + vq, \tag{138}$$

$$\dot{\boldsymbol{\varrho}} = \operatorname{curl}(\dot{\varrho} v \boldsymbol{n}), \tag{139}$$

$$\dot{q} = -\operatorname{div}\left(v\frac{q}{\varrho}\boldsymbol{\varrho}^{\perp} + \frac{1}{2|\boldsymbol{\varrho}|^2}[(\varrho + |\boldsymbol{\varrho}|)\boldsymbol{\varrho} \otimes \boldsymbol{\varrho} - (\varrho - |\boldsymbol{\varrho}|)\boldsymbol{\varrho}^{\perp} \otimes \boldsymbol{\varrho}^{\perp}]\cdot\operatorname{grad} v\right), \tag{140}$$

for a given velocity v. Here, $\boldsymbol{\varrho}^{\perp}$ denotes the dislocation density vector tilted clockwise by 90° within the glide plane, $\boldsymbol{\varrho}^{\perp} = -\mathbf{n} \times \boldsymbol{\varrho}$. It is worth mentioning that on each slip system the Kröner–Nye tensor $\boldsymbol{\alpha}$ is

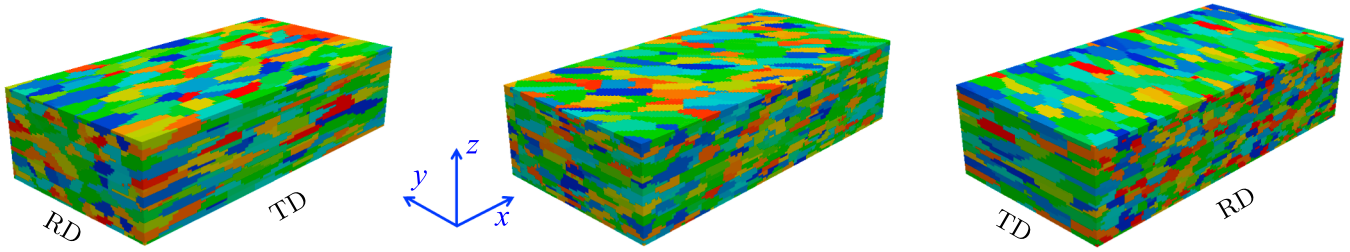

(a) Θ = 0° (b) Θ = 45° (c) Θ = 90°

Fig. 42. Representative Volume Elements (RVEs) of size = 160 × 80 × 40 with 500 randomly distributed grains used for uniaxial tensile tests along different loading directions characterized by angle Θ, x is the loading direction, z is the (sheet) normal direction. Figure adopted from [27] with permission from Elsevier.

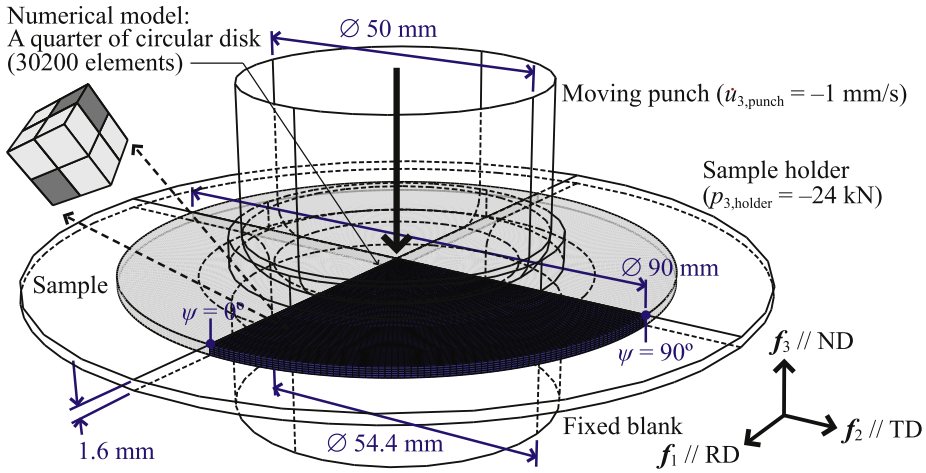

Fig. 44. Setup of the deep drawing simulations. RD: Rolling Direction, ND: Normal Direction, TD: Transverse Direction. Figure adopted from [285] with permission from IOP Publishing.

Table 17
Constitutive parameters of ferrite and body-centered cubic (bcc) martensite employed for the simulation of deep drawing using the models presented in Sections 4.1.3 and 6.2.2.

Property	Value		Unit
	Ferrite	Martensite	
C_{11}	233	417	GPa
C_{12}	135	242	GPa
C_{44}	118	211	GPa
$\dot{\gamma}_0$	1.0×10^{-3}	1.0×10^{-3}	s^{-1}
ξ_0	102	702	MPa
ξ_∞	235	1510	MPa
h_0	0.61	563	GPa
$h^{\alpha\alpha'}$	1.0	1.0	
n	20	20	
a	1.0	2.0	

Initial grain dimensions $r_1 \times r_2 \times r_3 = 4 \times 4 \times 2\ \mu m^3$.
Length of Burgers vector $b = 0.25$ nm.

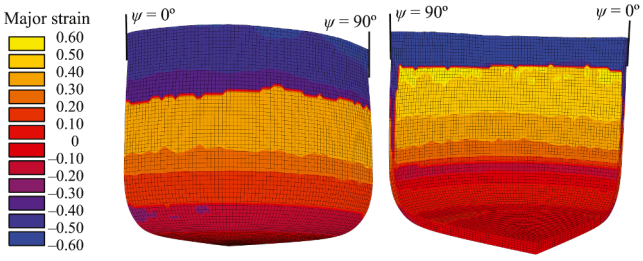

Fig. 45. Distribution of major strain resulting from the deep drawing process. Figure adopted from [285] with permission from IOP Publishing.

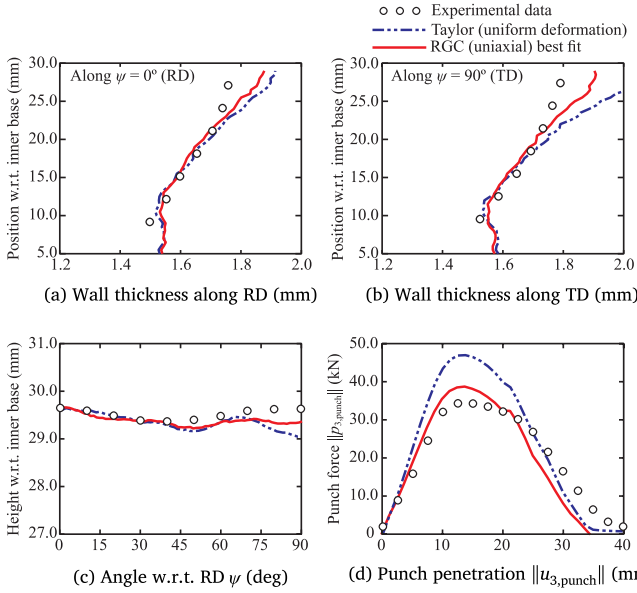

Fig. 46. Results of the deep drawing simulations using the Relaxed Grain Cluster (RGC) and the Taylor scheme in comparison to experimental investigations. RD: Rolling Direction, TD: Transverse Direction. Figure adopted from [285] with permission from IOP Publishing.

decomposable into a tensor product of the dislocation density vector $\boldsymbol{\varrho}$ and the Burgers vector $\mathbf{b}$ as $\boldsymbol{\alpha} = \boldsymbol{\varrho} \otimes \mathbf{b}$.

In Eqs. (138)–(140), the velocity v is computed using the thermodynamically consistent form introduced by Hochrainer [289]. It is defined as $v = \text{sgn}(\tau_{\text{net}})\langle|\tau_{\text{net}}| - \tau_f\rangle/B$, where B is a dislocation drag coefficient, τ is the resolved shear stress on the slip system, τ_f is a Taylor-type flow stress, and $\langle\cdot\rangle$ denotes the Macaulay brackets. The net shear stress is defined as $\tau_{\text{net}} = \tau + \tau_g - \tau_{lt} - \tau_b$, which contains the mesoscopic shear stress contributions τ_g, τ_{lt}, and τ_b, ensures thermodynamic consistency, and depends on (gradients of) the density variables [289].

The implementation of the flux-based formulation of CDD, Eqs. (138)–(140), is based on the non-local constitutive model (Section 6.2.5). For this simulation example DAMASK has been used as a user material subroutine (`Umat`) for the commercial Abaqus FEM solver.

A first fully-coupled three-dimensional CDD simulation of bending of a micro-beam with only one activated slip system has been presented by Ebrahimi and Hochrainer [290]. This contribution presents a simulation of torsion of a cylindrical micro-shaft in a multi-slip situation. The geometry and the applied boundary conditions are schematically depicted in Fig. 47. The micro-shaft has been clamped from one side and surface traction inducing a pure torsion moment is applied on the shaft's opposite free surface. The shaft was modeled as an fcc single crystal with the torsion axis aligned along the [0 0 1] direction. Isotropic elastic constants $E = 70$ GPa and $\nu = 0.34$ and a Burgers vector length $b = 0.255$ nm had been used.

As initial condition, a total dislocation density of $\varrho_0 = 20\ \mu m^{-2}$ of only Statistically Stored Dislocations (SSDs) was prescribed. The initial dislocation density vector $\boldsymbol{\varrho}_0$ and the initial curvature density q_0 were set to zero. An outflow boundary condition for the density variables was

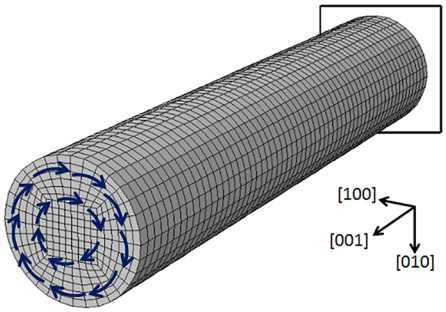

Fig. 47. Finite element mesh and boundary conditions of the simulated shaft with radius 2 µm and length 20 µm.

defined such that the last layer of integration point volumes close to the free surfaces was only serving as a buffer that does not belong to the sample. No initial dislocation densities were assigned to these volumes and they remain empty during the simulation.

The predicted dislocation densities have then been qualitatively compared with results from Discrete Dislocation Dynamics (DDD) simulations taken from the literature [291,292]. Fig. 48 shows the total dislocation densities on different slip systems on a section perpendicular to the shaft torsion axis. Dislocations left the shaft at the free surfaces and they accumulated around the shaft torsion axis. This is in contrast with predictions from conventional CP simulations [291] but similar to dislocation pile-ups observed in DDD simulations of torsion of shafts with rectangular cross sections, see, *e.g.* Fig. 7(a) in Jones et al. [291] and Fig. 6(e) in Senger et al. [292].

7.16. Dislocation patterning during cyclic loading

This example shows how the non-local dislocation density-based model introduced in Section 6.2.5 has been modified to reproduce dislocation structures forming during cyclic deformation of fcc metals [295] at the sub-micrometer length scale. Under the single slip conditions studied here, dislocation substructures consist of high dislocation density regions, called veins, and low dislocation density regions, referred to as dislocation channels. The veins contain mostly edge dislocations, while screw dislocations in the channels accommodate the plastic deformation (Fig. 49). The motion of screw dislocations creates new edge dislocation segments at the vein–channel interface [296]. This specific behavior can be reproduced by dislocation-based models if the curvature of dislocation segments at the vein–channel interface is higher than in the channels.

The modified dislocation rate equations that have been used for this application example are based on eight state variables for every slip system, compared with four state variables used in the original dislocation flux model (Section 6.2.5). Four state variables (edge ± and screw ± in Fig. 50) represent dislocation segments with zero curvature, oriented parallel and perpendicular to the Burgers vector direction, while the other four densities shown in Fig. 50 represent dislocation segments with an orientation that is intermediate between edge and screw dislocations. An average segment curvature $\bar{k}$ is assigned to these four densities.

Only the motion of the four curved dislocation density populations contributes to the generation of straight edge and screw density components. For instance, the dislocation multiplication law for ϱ_{s+}, according to Grilli et al. [297], is given by:

$$\dot{\varrho}_{s+,\mathrm{mult}} = |v_{e+,s+}|\,\bar{k}\varrho_{e+,s+} + |v_{e-,s+}|\,\bar{k}\varrho_{e-,s+}. \tag{141}$$

The annihilation rate of edge and screw dislocations is the same as in Eq. (86a).

The new generation law has been validated on a small volume with a dislocation density representing two interacting dislocation segments, as shown in Fig. 51: One straight edge dislocation had been kept immobile. A second dislocation segment had an edge part, forming a dislocation dipole with the first dislocation, and a screw part. At the intersection between the edge and the screw segment a curved density $\varrho_{e+,s+}$ was present. The screw dislocation moved when a resolved shear stress was applied. According to the newly introduced generation law, the edge dislocation density increased in the elements which contain the immobile edge segment and, after the transit of the density $\varrho_{e+,s+}$, it had doubled in value. This result indicates that two edge dislocations are present in those elements in agreement with the behavior found in equivalent discrete systems.

A continuum rate equation for double cross-slip was then used to model the density evolution of curved dislocation segments [297]. In this simple model the dislocation loops emitted on primary slip planes after a double cross-slip event were considered [298]. The rate at which new curved dislocation density is created was introduced as:

$$\dot{\varrho}_{e+,s+,\mathrm{cs}} = \frac{\nu_{\mathrm{a}}\,(\varrho_{s+} + \varrho_{s-})}{w\bar{k}}\,\exp\left(-\frac{\tau_{\mathrm{III}}\,V_{\mathrm{cs}}}{k_{\mathrm{B}}\,T}\right), \tag{142}$$

where τ_{III} is the stage three stress and w is the average width of a cross-slipping screw dislocation segment [299].

Simulations of cyclic shear deformation of a Cu single crystal oriented for single slip were then carried out on the rectangular geometry shown in Fig. 52 using an element size of 200 nm. A strain amplitude $\varepsilon = 0.1\%$ was applied along the Burgers vector direction. After 25 deformation cycles, the edge dislocation density started to self-organize and a distinct pattern became visible, see Fig. 52(a). The dislocation density walls were mainly oriented perpendicular to the Burgers vector direction and the characteristic spacing between two neighboring walls was of the order of 1 µm.

The strain amplitude was increased to $\varepsilon = 0.2\%$ after cycle 30. The dislocations in the larger veins did not rearrange and the vein size increased, as shown in Fig. 52(b). Therefore, the channels become shorter, satisfying the similitude principle [300]. This leads to an increase of the volume fraction of veins for higher strain amplitudes [301]. A more detailed description of the model and other simulation results can be found in [297]. An extension of the model suitable to describe multiple slip situations and to predict labyrinth dislocation structures has been presented by Grilli et al. [302].

7.17. Glissile junction formation

In this example, the addition of a new multiplication mechanism based on glissile junction formation to the dislocation density-based CP model (Section 6.2.3) is presented. Dislocation junctions are usually

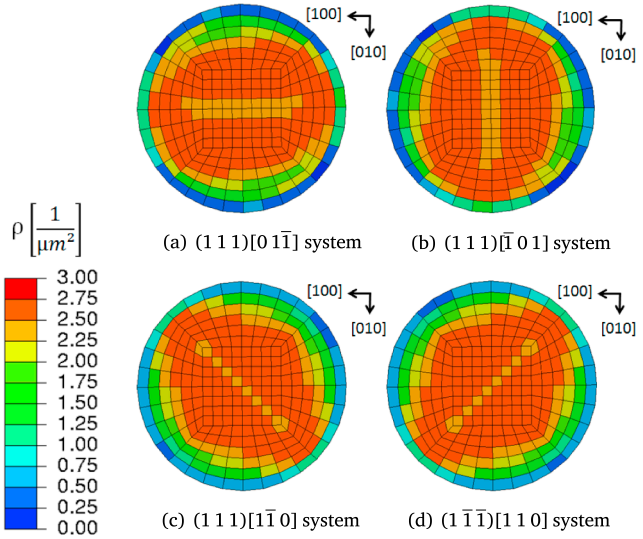

Fig. 48. Accumulation of total dislocation density on a section perpendicular to the shaft's torsion axis and on four different slip systems.

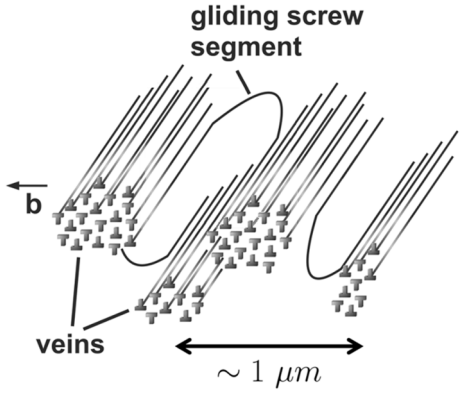

Fig. 49. Representation of veins and the gliding motion of screw dislocations inside the channels. Figure adopted from [293] with permission from Elsevier.

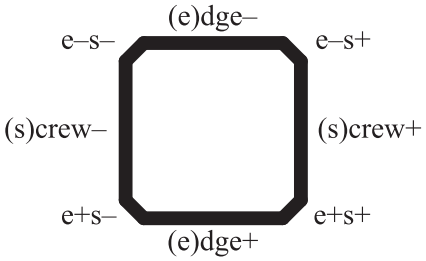

Fig. 50. Parametrization of the dislocation loop used to define state variables.

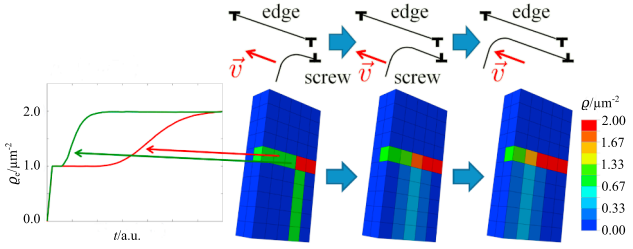

Fig. 51. Simulation of two interacting dislocation segments using the dislocation density based model for cyclic fatigue. Figure adopted from [294].

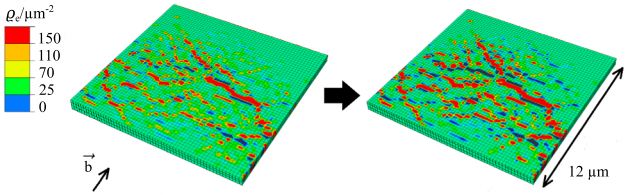

(a) ε = 0.1% (b) ε = 0.2%

Fig. 52. Edge dislocation density after (a) N = 25 cycles at a strain amplitude ε = 0.1% and (b) after 12 more cycles at a strain amplitude ε = 0.2%. Figure adopted from [294].

only considered in the context of strain hardening (*e.g.* [153,304,305]). Recent investigations of the glissile junction formation in fcc crystals [306,307] using DDD simulations [308–310] show, however, that it substantially alters both, the dislocation density evolution and the plastic strain contributions of the active glide systems. A glissile junction is formed when two non-coplanar glide dislocations react such that the vectorial sum of their Burgers vectors is also a Burgers vector coplanar with one of the reactant glide planes. Crystallographically, 48 out of the 144 possible combinations of glide systems form glissile junctions in fcc crystals, which makes it the most frequent reaction. In glide system notation the reaction reads $(\mathbf{n}_1, \mathbf{b}_1) + (\mathbf{n}_2, \mathbf{b}_2) = (\mathbf{n}_2, \mathbf{b}_3)$, where the indices 1 and 2 denote the primary systems and 3 the respective glissile system of Burgers vector $\mathbf{b}$ and plane normal $\mathbf{n}$.

In order to include the glissile mechanism, determined at the level of discrete dislocation dynamics, rate equations for the dislocation density evolution of the concerned systems have been proposed by Stricker and Weygand [307] following the approach of Ma and Roters [144] and Ma et al. [65]. In the model, the collision frequency ν^{α} of glide system α moving with the average velocity v^{α} through a forest system α' having an average dislocation spacing of $L^{\alpha'}$, which is proportional to the dislocation density through the relationship $L^{\alpha'} = 1/\sqrt{\varrho^{\alpha'}}$ is calculated as:

$$\nu^{\alpha} = \frac{v^{\alpha}}{L^{\alpha'}}. \tag{143}$$

The crystallography of the fcc crystal dictates a symmetry for the formation rate of glissile junctions on the third system. The dislocation density increase due to this mechanism is, hence, given by

$$\dot{\varrho}^{\alpha''} = C\left(\sqrt{\varrho^{\alpha'}}\ |\dot{\gamma}^{\alpha}| + \sqrt{\varrho^{\alpha}}\ |\dot{\gamma}^{\alpha'}|\right), \tag{144}$$

where the indices α and α' are the respective primary glide systems, which produce a dislocation density contribution on system α'', $\dot{\gamma}$ denotes the plastic shear rates and the prefactor C is assumed to be constant (for details refer to [307]). This prefactor can be estimated from DDD simulations. The formation of dislocation density from the glissile junctions is completed by subtracting the newly formed $\dot{\varrho}^{\alpha''}$ from both primary systems forming the reaction:

$$\begin{aligned}\dot{\varrho}^{\alpha,\mathrm{eff}} &= \dot{\varrho}^{\alpha} - \dot{\varrho}^{\alpha''},\\ \dot{\varrho}^{\alpha',\mathrm{eff}} &= \dot{\varrho}^{\alpha'} - \dot{\varrho}^{\alpha''}.\end{aligned} \tag{145}$$

The determination of the prefactor C is not straightforward as both, normal dislocation multiplication and reactions, lead to a change in dislocation density. Furthermore, the reaction is occurring as a discrete change in the microstructure in the DDD simulations, but the initial segment length, right after the formation, is too small for being relevant at the continuum level. This means that the glissile dislocation first has to extend before it is able to contribute to plastic slip. Therefore, a lower bound for the prefactor C has been estimated by measuring the dislocation density increase on glide systems with a Schmid factor of zero for a tensile test along a ⟨1 0 0⟩ direction.

The increase in dislocation density on these systems occurs only through deposition of a dislocation density contribution by formation of glissile junctions and not as a result of the motion of dislocations due to an applied stress. Fig. 53 shows the result of this measurement on each zero Schmid factor glide system from a series of 300 DDD simulations as

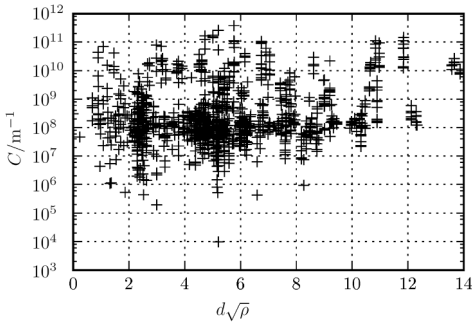

Fig. 53. Prefactor C as a function of smallest outer sample dimension d and square root of the dislocation density ϱ. Measured from the deposition of dislocation density on zero Schmid factor systems in Discrete Dislocation Dynamics (DDD) simulations. Figure adopted from [303] with permission from KIT Scientific Publishing. Licensed under CC BY-SA 4.0.

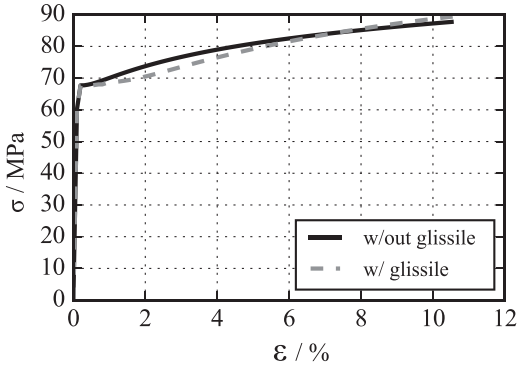

Fig. 54. Simulated stress-strain response obtained for the original dislocation based constitutive model and for the advanced model considering glissile junction formation. Figure adopted from [303] with permission from KIT Scientific Publishing. Licensed under CC BY-SA 4.0.

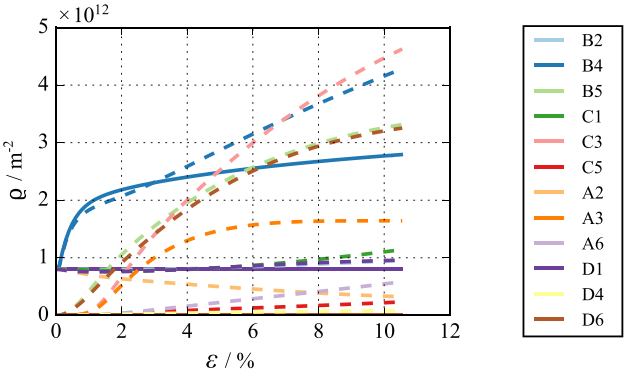

Fig. 55. Dislocation density evolution of individual glide systems as a function of strain for the tensile tests shown in Fig. 54. Dashed lines represent the enhanced model including dislocation multiplication by glissile junction formation. New glide systems are populated and contribute to the plastic deformation as opposed to the original model, where only glide system B4 shows an increase in dislocation density and contributes to plastic deformation. For legend notation see Table 18. Figure adopted from [303] with permission from KIT Scientific Publishing. Licensed under CC BY-SA 4.0.

a function of the product between the smallest sample dimension d and the square root of the total dislocation density ϱ after deformation.

The value $d\sqrt{\varrho} \approx 14$ represents samples with a volume of 24 μm^3 and a dislocation density of $\varrho \approx 5 \times 10^{13}$ m^{-2}. Since the mean values of C are on the order of 10^4 m^{-1} and converging to this value for larger $d\sqrt{\varrho}$, this value has been adopted as a lower bound. The mean values of C are on the order of 10^8 m^{-1} and the lowest value is of the order of 10^4 m^{-1}. Since the lowest value is an outlier, a lower bound of $C = 10^5$ m^{-1} is assumed. The implementation of the glissile junction formation includes a reaction matrix, similar to the ones used for strain hardening (Eq. (77)). For the considered case of fcc crystals, one of the twelve target glide systems can be populated due to the glissile junctions from two pairs of primary glide systems. Table 18 lists all possible combinations for glide systems to form a glissile junction on the target glide system in an fcc crystal. The rate per glide system is determined by Eqs. (144) and (145).

To show the multiplication as well as the deposition of dislocation density by the reaction, a very restricted initial density distribution has been chosen and the prefactor of Eq. (144) is set to $C = 5 \times 10^6$ m^{-1}. In a strain rate controlled tensile test along the [1 0 0]-axis, all zero Schmid factor glide systems (B2, C1, A2, and D1 in Schmid–Boas notation) are populated as well as one system with a non-zero Schmid factor (glide systems B4: $m = 0.408$). Fig. 54 shows the difference in the stress-strain responses of both the original (Section 6.2.3) and the enhanced model. The macroscopic stress response is only slightly changed and quite similar to results obtained from DDD simulations.

However, when a microstructural measure is used, such as the dislocation density evolution of individual glide systems, as depicted in Fig. 55, a significant difference in the predictions becomes apparent: While the original model behaves *classically* in the sense that the dislocation density on zero Schmid factor glide systems (B2, C1, A2, and D1) does not change during loading, the enhanced model (dashed lines) shows that an additional dislocation density portion is generated on the other non-zero systems by the new multiplication mechanism as well as deposited on the zero systems. During the deformation glide systems are populated by the glissile junction mechanism, leading to an overall positive effective rate for multiplication.

This proof of concept conducted on a [1 0 0] tensile test with an inhomogeneous initial dislocation density distribution showed that the glissile junction is able to populate glide systems which are initially not populated and deposit also a dislocation density contribution on zero Schmid factor systems. While this mechanism might not be important for all loading conditions, it helps the microstructure to plastically accommodate settings in which large gradients prevail.

7.18. Thermo-mechanics of microelectronic devices

In this example, thermo-mechanically coupled CP simulations have been used to gain insights on the role that the microstructure of the metallic components plays on the reliability of microelectronic devices. Growing demands on the lifetime in power electronic devices require an understanding of typical failure mechanisms such as the occurrence of short circuits and the evolution of surface roughening. These devices operate under complex thermo-mechanical loadings caused by the current flow within the conducting metallic components and the mismatch in thermal expansion of the involved materials. The left hand side image in Fig. 56 shows a cross section of an experimental test structure presented by Smorodin et al. [311] illustrating its layered structure. Aluminum (Al) conductor paths (colored in gray) are embedded in a Si-oxide insulator (Interlayer Dielectric (ILD)), which is covered by a metallic layer of Al (metallization plate). Power pulses are applied to the polysilicon heater in order to subject the device to a thermal loading comparable to that imposed during operation but without having a current flow within the conductor paths. The heating plate is not modeled but the power pulses are directly applied as a heat source within the conductor paths in the simulation. The corresponding temperature field and its evolution are depicted in Fig. 58 and they agree well with the experimental observations published by Smorodin et al. [311] and Kanert [314]. These authors report also that cyclic thermal loading results in a continuous accumulation of plastic deformation in the metallic components causing crack initiation within the ILD. As visualized in Fig. 57, the crack is subsequently filled with Al

Table 18
Reaction table for glissile junction formation in DAMASK for all slip system of the face-centered cubic (fcc) slip family given in Table 21(a) using the Schmid–Boas notation.

Target system	Primary systems	
B2	B4 + C5	B5 + D4
B4	B2 + C5	B5 + A2
B5	B2 + D4	B4 + A2
C1	B5 + C3	C5 + A3
C3	B5 + C1	C5 + D1
C5	C1 + A3	C3 + D1
A2	C3 + A6	A3 + D6
A3	B2 + A6	A2 + D6
A6	B2 + A3	C3 + A2
D1	B4 + D6	A6 + D4
D4	C1 + D6	A6 + D1
D6	B4 + D1	C1 + D4

and induces a short circuit resulting in a loss of functionality of the device.

In this study, the influence of the microstructure of the metallic components on the probability of crack initiation is revealed. All parts consisting of Al are assigned a microstructure made up of polyhedral grains derived from Voronoi tessellations, see Fig. 59. Their mechanical behavior is described by the phenomenological CP model presented in Section 6.2.2. An excerpt of the material properties is summarized in Table 19. The material model was enhanced by incorporating eigenstrains due to thermal expansion, temperature dependent material properties, and taking into account grain size effects by means of the Hall–Petch relation. A more detailed description can be found in [312,313,315]. The Si substrate and the ILD are assumed to behave purely elastic and are temperature dependent. The probability of crack initiation is qualitatively investigated by monitoring the maximum principal stress between two neighboring conductor paths, as this measure indicates the occurrence of brittle failure. Fig. 60 illustrates the averaged stress distribution within the ILD after 50 load cycles along the output paths depicted in Fig. 56. To investigate its influence on crack initiation, the texture of the conductor paths is varied. A ⟨1 1 1⟩- and a ⟨0 0 1⟩-fiber texture (⟨1 1 1⟩ respectively ⟨0 0 1⟩|| z-direction) as well as a configuration without any texture labeled as "random" have been considered, whereby the ⟨1 1 1⟩-texture is predominant in a real device. The ⟨1 1 1⟩-texture of the metallization plate is kept unchanged for all three simulations.

The load on the ILD was observed to be especially high for all the crystallographic textures considered (Fig. 60) in the region of the highest temperature amplitude ($0 \leqslant x \leqslant 50$ µm) which is the domain where cracks are likely to occur. The crystallographic texture affects the stress level after cooling as well as after heating, however, the impact becomes more apparent after cooling (Fig. 60(b)). The diagrams in Fig. 61 show how the von Mises stress and the stress in x-direction along the central line of the conductor paths differ depending on their texture. The stress within the conductor paths is supposed to be the dominating factor for a continuous material flow from the region at low temperature to the domain at high temperature. After heating as well as after cooling, this is highest in the case of a ⟨1 1 1⟩-texture. However, after 50 load cycles no considerable difference in plastic deformation based on the texture is observed.

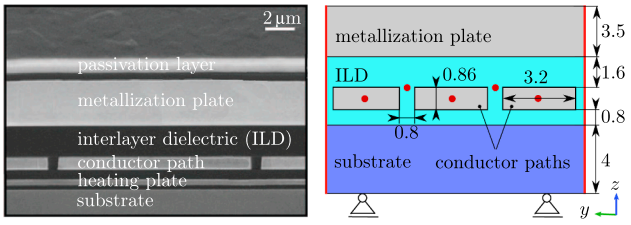

Fig. 56. Cross section image on the left side and the derived simulation model on the right side with its dimensions in µm. The (red) dots mark the position where the stress is probed for Fig. 60 (Interlayer Dielectric, ILD) and Fig. 61 (conductor path). Figure adopted from [311,312] with permission from IEEE.

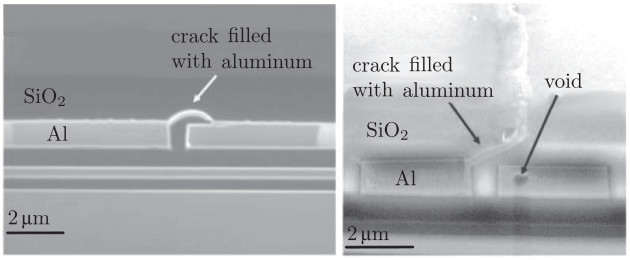

Fig. 57. Cross section images showing points of failure. Figure adopted from [311,312] with permission from IEEE.

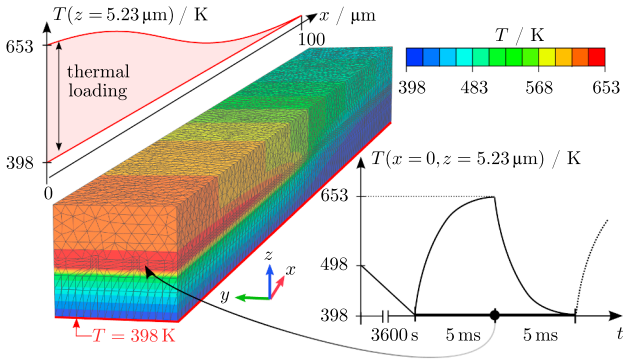

Fig. 58. The right hand side diagram shows the temperature history within the conductor paths. After an initial homogeneous cooling from 498 K to 398 K, 50 inhomogeneous thermal load cycles are applied reaching a maximum temperature of 653 K. The left image illustrates the temperature distribution after heating. Figure adopted from [312,313].

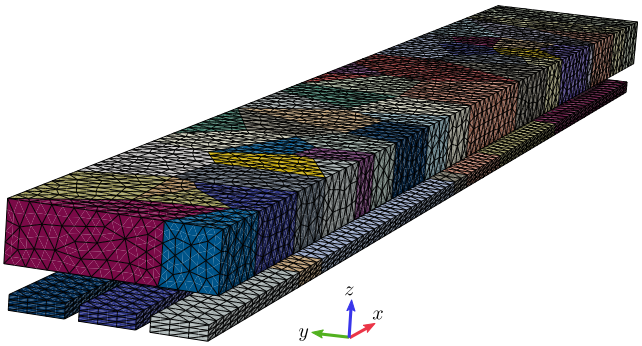

Fig. 59. Meshed simulation model whereby only the aluminum components (metallization plate and conductor paths) with their characteristic microstructure are shown. The colors indicate different grains. (For interpretation of the references to color in this figure, the reader is referred to the web version of this article.)

Table 19
Constitutive parameters of aluminum valid for a grain diameter of 0.8 µm and a temperature of 293 K employed for the simulation of cyclic thermal loading of microelectronic devices using the model presented in Section 6.2.2.

Property	Value	Unit
C_{11}	114.3	GPa
C_{12}	64.3	GPa
C_{44}	30.75	GPa
$\dot{\gamma}_0$	1.0×10^{-3}	s^{-1}
ξ_0	88	MPa
ξ_∞	132	MPa
h_0	1	GPa
$h^{\alpha\alpha'}$	1.0	
a	20.0	
n	1.75	

In this example, the stress load on the ILD was examined, which is directly linked with the probability of brittle failure. Using the same approach, Meier et al. [312] investigated the effect of grain refinement of the conductor path grains on crack initiation and in [315] the influence of grain size and grain orientation of the metallization plate on surface roughening is analyzed.

7.19. Mechanics of biological structural materials

Modeling the micromechanical behavior of biological structural materials such as bone, shells, or arthropod exoskeletons is challenging

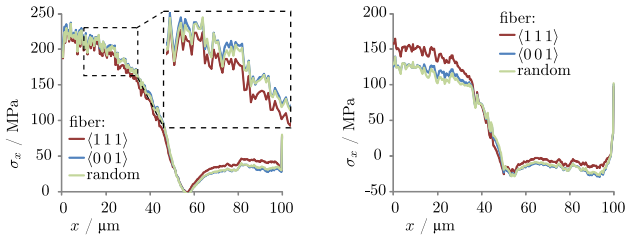

(a) after heating (b) after cooling

Fig. 60. Distribution of the maximum principal stress within the Interlayer Dielectric (ILD) after 50 load cycles averaged along the positions depicted in Fig. 56.

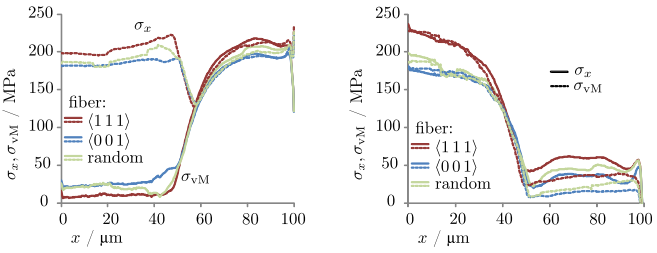

(a) after heating (b) after cooling

Fig. 61. Distribution of the stress in x-direction and the von Mises stress within the conductor paths after 50 load cycles averaged along the positions depicted in Fig. 56.

because they are hierarchically structured organic-inorganic nanocomposites. Thus, the mechanical response of the bulk material is a result of both the mechanical behavior of the individual constituents and their structural arrangement on different length scales within the composite [318,319]. Therefore, computational determination of the material properties as a function of composition, constituents, and structural arrangement requires multi-scale modeling that considers all length scales [320]. Here, a multi-scale modeling approach is presented for predicting the elastic properties of the mineralized cuticle forming the exoskeletons of two species of crustaceans, namely the lobster *Homarus americanus* and the crab *Cancer pagurus*. The organic matrix of the composite consists of polysaccharide chitin and various proteins organized into fibrils. These are arranged in horizontal layers forming a twisted plywood structure that incorporates numerous vertical pore canals [321,322]. Both, the rotation angles of the plywood as well as size and shape of the pore canals, are species-specific [323,324]. In the lobster, the inorganic constituents are nanoparticles of Amorphous Calcium Carbonate (ACC), while the crab incorporates larger calcite particles [318,323–328]. Following the experimentally determined structural characteristics and composition of the cuticle of both species [324,329–331], the model consists of different RVEs corresponding to the main building blocks (Fig. 62) [316,317,332].

The properties of α-chitin (I and II in Fig. 62) and the calcite mineral phase (IIIb in Fig. 62) were obtained from *ab initio* calculations using Molecular Dynamics (MD), Tight Binding (TB), and Density Functional Theory (DFT) [333–337]. At the mesoscale (IV in Fig. 62), successive homogenization modeling is applied [316,332,338–340]. The local stress and strain fields for different loadings on the exact cuticle geometry (Figs. 62 and 63) are investigated using the spectral method (Section 3.2.2) [317].

At the mesoscale, the computed elastic properties were compared to data obtained from nanoindentation experiments (Fig. 62) [324,341] for the mineralized chitin-protein planes. The Young's modulus along the chitin fibrils is about 60% larger than perpendicular to the fibrils, rendering the planes mechanically anisotropic. Nevertheless, due to their twisted plywood arrangement, the in-plane stiffness of the bulk material appears

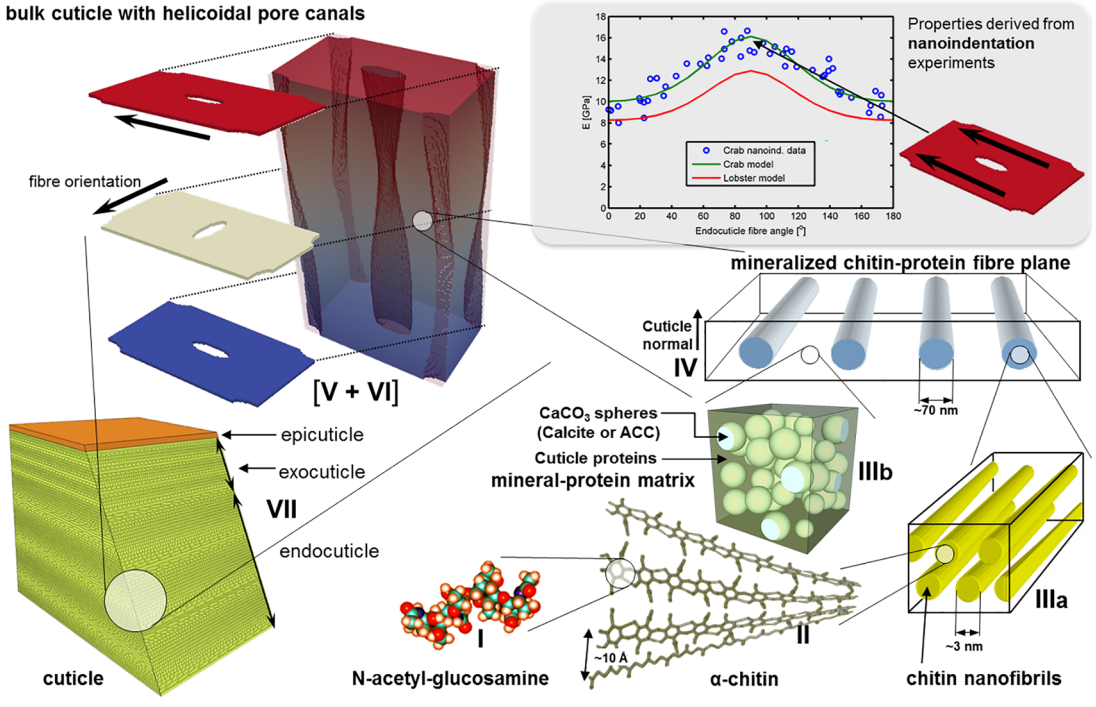

Fig. 62. Multi-scale hierarchical modeling of crustacean cuticle showing the Representative Volume Elements (RVEs) used at different length scales. The properties of α-chitin (I and II) and the calcite mineral phase (IIIb) were obtained from *ab initio* calculations using Molecular Dynamics (MD), Tight Binding (TB) and Density Functional Theory (DFT). Their elastic constants are introduced into a continuum-scale model of the chitin nanofibrils (IIIa), which are represented as rods, and a protein/mineral matrix (IIIb), where the properties of the proteins are estimated from literature data. The properties of the mineralized chitin-protein fiber layer tissue (IV) are obtained by homogenization. The RVE of the bulk cuticle is composed of single fiber planes (V and VI) where the properties are derived from nanoindentation (inset). Every plane has a directional vector assigned and features pore canal voids arranged in a regular hexagonal array, thus representing an accurate reconstruction of the structure of the endocuticle layer (VII). Figure adopted from [316] with permission from John Wiley and Sons.

isotropic at the macroscopic scale and is greatly enhanced by the presence of chitin fibrils. As these experiments can only be performed correctly on dry cuticle surfaces, the properties of dry material are assessed.

The endocuticle of both crustacean species is represented by RVEs of periodic unit cells discretized by means of a regular three-dimensional grid. Each RVE has two phases, cuticular material and pore canals. The pore canals are modeled as a compressible medium with negligible stiffness. Structurally, the endocuticles of lobster (Fig. 63(a)) and crab (Fig. 63(b)) differ in their stacking height and the size and distribution of pore canals [323,324]. The stack of the chitin-protein fiber layers completes a 180° rotation over a distance of 30 µm in the lobster and 15 µm in the crab. In both species, the ellipsoidal cross sections of the pore canals are about 2 µm wide (Fig. 63(a)). However, in the crab the open lumina of the pore canals have an oval shape and are only about 1 µm wide because the narrow edges of each pore canal are reinforced with mineralized chitin-protein fibers oriented in normal direction with respect to the bulk endocuticle. In the RVE, this is accounted for by introducing a third phase at the pore canal edges with the same properties as the rest of the cuticular material, but oriented vertically (Fig. 63(b)). The two RVEs encompass a fiber plane rotation of 180° from top to bottom. The one for lobster is discretized by approximately 4.9 million material points and the one for crab by approximately 2.8 million. The twisted plywood is discretized in 100 planes for lobster and 50 planes for crab to obtain a resolution that is high enough to observe even small changes in the local stress and strain fields. However, the shape and distribution of pore canals is idealized to maintain periodicity of the RVEs.

Experimentally, the dry endocuticles of both species exhibit linear elastic behavior. The mean in-plane Young's modulus for lobster claws is in the range of 5.8–7 GPa [329] and about 11.9 GPa for crab carapace. The cuticle fails abruptly at a strain of approximately 0.7% and 0.3% in the lobster and the more heavily mineralized crab, respectively. Therefore, tensile strains along the x-axis of 0.7% for the lobster endocuticle (Fig. 64(a)) and of 0.3% for the crab endocuticle (Fig. 64(b)–(d)) are applied to the RVEs to obtain the local stress–strain state just before failure. To study the influence of the pore canal reinforcements on the local stress fields in the case of crab, three different RVEs are used: one corresponding to the actual microstructure including the reinforcements (Fig. 64(b)), one without the reinforcement phase with pore canals modeled corresponding to the actual hollow tubes within the cuticle (Fig. 64(c)), and a hypothetical case without reinforcement phase leaving the entire space taken up by pore canals empty (Fig. 64). The resulting von Mises stress fields are shown in Fig. 64(b)–(d).

The regions where stress concentrations occur represent the most likely sites where damage is initiated before failure. In all four cases, the highlighted voxels in Fig. 64 represent stress concentrations with values far higher than the experimentally determined stresses at failure. In both, lobster and crab endocuticle, high stresses are confined to small, localized regions. In case of the lobster, the highest stress concentrations are observed in regions where the long axes of the ellipsoidal pore canals are oriented at about 45° with respect to the loading direction. In these regions of the RVE, the solid material separating the pore canals is thinnest (see highlighted planes in Fig. 64(a)) and the chitin fibers are subject to shear stress. In the crab endocuticle, a similar behavior is found only in the hypothetical case where the pore canal reinforcement phase is omitted exposing the entire volume of the ellipsoidal pore canals (Fig. 64(d)). Considering only the actual pore canal volume with its oval cross section and further assuming that they are surrounded by mineralized twisted plywood (Fig. 64(c)), the regions with high stress concentrations become larger and relocate to the pore canal margins at the sides oriented perpendicular to the tensile direction, where the chitin fiber orientation is parallel to the tensile direction. The affected regions decrease in volume with increasing rotation angle and vanish shortly before the fiber orientation becomes perpendicular to the tensile direction. This result implies that wider pore canals affect the stability of the material more than smaller ones, where the orientation of the mineralized chitin fibers becomes the dominant factor. This is also observed in the RVE of the natural cuticle where the pore canal edges are reinforced with vertically oriented mineralized fibers (Fig. 64(b)). However, the reinforcement phase greatly reduces the region of high stress concentrations, indicating that one of its purposes is to prevent damage initiation caused by tensile stresses.

A thorough understanding of the structure–property relations in biological hard tissues is crucial for possible biomimetic applications. Modeling the structure and properties on each level of structural hierarchy provides the flexibility to account for inherent local structural and compositional variations of biological materials, especially on the macroscopic scale. By replacing the properties of cuticle constituents with those of synthetic materials, the model can be used for the knowledge-based design of new materials such as biomimetic fiber-based laminate composites with tailored porosity by virtual prototyping. Once validated, such a model can be used to identify optimal designs for specific purposes. Beyond the specific structure–property results discussed in this section the example shows also that DAMASK is well suited to solve complex micromechanical problems of biological matter and generally in composite materials that contain both soft polymeric and hard ingredients.

8. Workflow and usage philosophy

DAMASK is designed with the aim to enable conducting systematic parametric simulation studies. Using a Command Line Interface (CLI) allows for easy parameterization, for instance based on problem-specific shell scripts. Up-to-date manuals are available at https://damask.mpie.de.

8.1. Boundary value problem solver

The in-house spectral [and experimental Finite Element Method (FEM)] solvers use a CLI. For Abaqus and Msc.Marc, interface functions exist that allow to use these solvers in connection with DAMASK via a CLI. These solvers have their specific input files to specify geometry (*e.g.* the microstructure) and load. DAMASK is controlled by three configuration files, `material.config`, `numerics.config`, and `debug.config` placed in the current working directory. While the configuration for the material behavior needs to be defined in `material.config`, fine tuning of the numerical parameters via `numerics.config` and requesting additional debug output with `debug.config` are optional.

8.2. Pre- and postprocessing

A number of pre- and postprocessing tools is available within DAMASK. The design strategy follows the concept of "one tool per task" to create a flexible and modular tool system that derives its strength

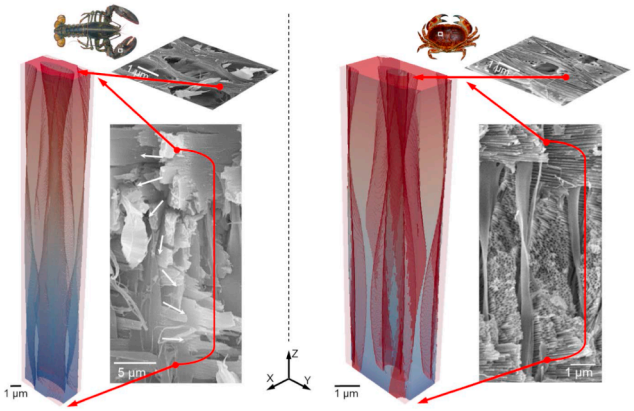

(a) *Homarus americanus* (b) *Cancer pagurus*

Fig. 63. Representative Volume Elements (RVEs) and corresponding scanning electron micrographs in cross-sectional and transverse orientations of the endocuticle.

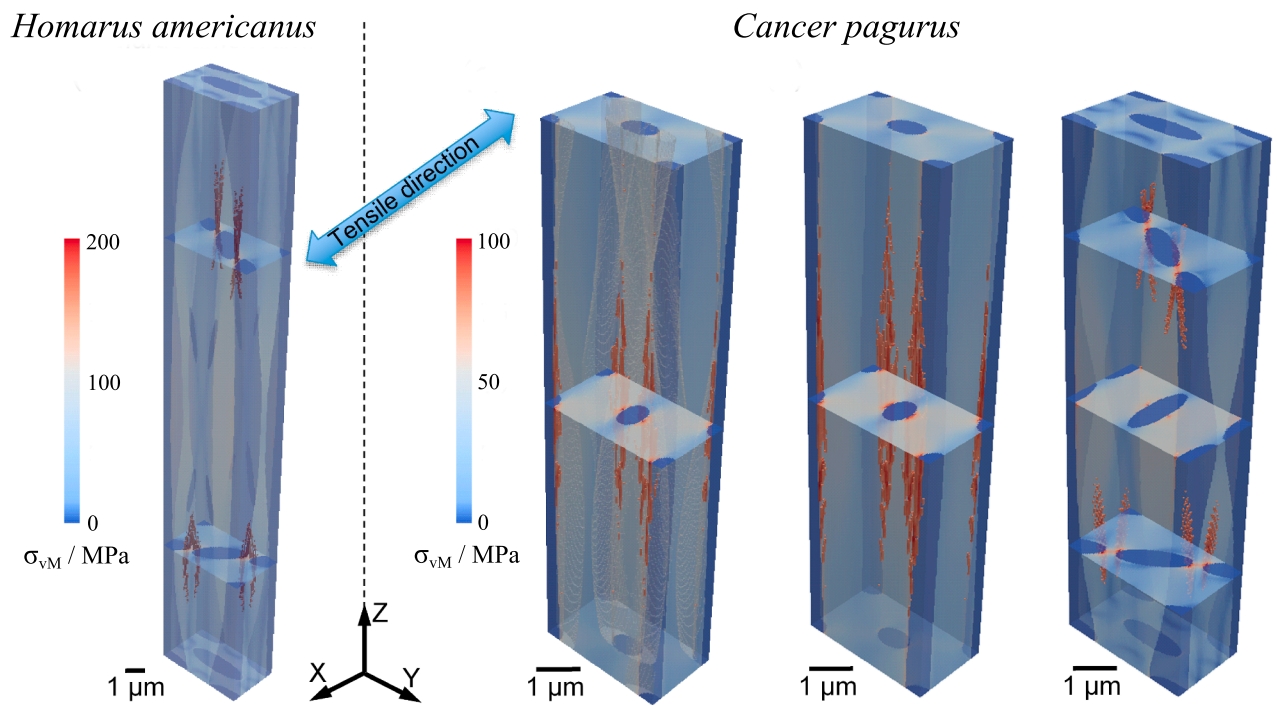

(a) real geometry (b) real geometry (c) no reinforcement (d) empty pore canals

Fig. 64. 3D von Mises stress field maps obtained from spectral method calculations applying in-plane uniaxial tension at strains that are close to experimental fracture values obtained for endocuticle of the lobster (a), and the crab (b–d). Representative Volume Elements (RVEs) (a) and (b) represent geometries as found in nature, while (c) and (d) represent hypothetical cases where structural parameters of the pore canals were altered by removing the pore canal reinforcement phase and modifying the pore canal volumes. Figure adopted from [317] with permission from the Institute of Chemical Engineering-BAS.

from the numerous possible pipelines, combinations, and workflows that can be constructed out of the individual building blocks.

8.2.1. Preprocessing

The preprocessing tools enable the semi-automated generation of geometry descriptions including material parametrization and load definition. While the geometry creation of the commercial FEM solvers is partly left to the respective tools provided by the vendors (*i.e.* Msc.Mentat for Msc.Marc and Cae for Abaqus), some additional tools do exist for writing and modifying the input files. Various in-house tools are available for the spectral solver to create and modify the geometry definition file. In addition, the functionality of various external tools, such as the multilevel Voronoi tool described in Section 7.2, Dream.3D [219], Neper [342], *etc.*, can be used for this purpose. In the following, three exemplary routes are presented.

8.2.1.1. Importing synthetic microstructures from Dream.3D. Dream.3D [219] is a flexible software for the evaluation and modification of measured and synthetically created microstructures. In a previous study [34], Dream.3D was used to create different grain-resolved microstructures based on the statistical description of microstructures of a steel exhibiting Twinning Induced Plasticity (TWIP) behavior. These microstructures were then used to investigate the effect of cold-rolling on the mechanical response of the material. More specifically, DAMASK contains a script to create the spectral solver geometry (microstructure description) and the crystallographic orientation information of the `material.config` file from a Dream.3D file. The material specific part of `material.config`, *i.e.* the specification of the constitutive parameters of the model presented in Section 6.2.3 as well as the definition of the load case, had to be conducted manually with the help of a standard text editor.

8.2.1.2. Selecting a set of discrete orientations from an orientation distribution function. For multi-scale simulations (Sections 7.12 and 7.14) or Virtual Laboratory approaches (Section 7.13), computational restrictions often require to select a relatively small number of discrete orientations from an Orientation Distribution Function (ODF). To accurately represent the macro-texture, the HybridIA algorithm [97] has been implemented in DAMASK (Section 4). Based on a binned representation of the ODF, each constituent of a Material Point in the model is assigned a single orientation ("Texture-Component CPFEM"). Alternatively, for the creation of synthetic microstructures, the set of discrete orientations can be used to initialize all material points belonging to one grain with a homogeneous orientation that can include some random scatter. In this case, the grain geometry needs to be provided from, for instance, Voronoi tessellation approaches as presented in Section 7.2 [342–344].

8.2.1.3. Direct use of electron backscatter diffraction data. As demonstrated in Sections 7.8, 7.10, and 7.11, the spectral solvers are often used to perform simulations based on experimentally characterized microstructures. In this case, the acquired voxelized microstructure representation is easily converted into a geometric description readable by DAMASK. In a similar way, the pointwise orientation data can be used to populate `material.config`, giving each point its individual orientation as obtained from Electron Backscatter Diffraction (EBSD). As this, particularly for larger measurements, results in very large `material.config` files, grain segmentation can be performed beforehand to assign average orientation data (with the option of including random scatter following a Gaussian distribution) to the undeformed grains. While such grain segmentation is a standard feature of EBSD analysis software (*e.g.* Dream.3D [219] or Mtex [345,346]), DAMASK also provides a script with basic functionality for this purpose.

8.2.2. Postprocessing

The postprocessing tools are designed to calculate additional quantities that are derived from simulation results. Moreover, they allow to convert and adapt the output for use with external tools to

enable in-depth analysis and visualization. In the following, three general visualization strategies sketched in Fig. 65 and their associated DAMASK workflows are presented.

8.2.2.1. Line plots. Line plots (Fig. 65(a)) are the simplest and probably most used representation of data. In the field of continuum simulation, average quantities, *e.g.* stress–strain curves, are shown in most cases. DAMASK, therefore, contains routines to compute the average of the complete model or subsets, *i.e.* individual phases or grains. Moreover, scripts are included to calculate derived quantities such as stress measures in different configurations (Table 20), various strain measures, and the von Mises equivalent or norm of tensorial quantities. The provided Python interface enables the straightforward use of sophisticated tools such as Matplotlib [347], but the output as plain `ASCII` file is suitable for many other plotting tools as well.

8.2.2.2. Mapped field quantities. Visualization of field quantities, as shown in Fig. 65(b), is a popular representation of spatially resolved data on surfaces or—with limitations—in volumes. Spatially resolved DAMASK results can be stored as `vtk` files that can be visualized by a number of commercial or freely available tools, *e.g.* Paraview [348]. Besides the general tools for the calculation of additional quantities (Section 8.2.2), special routines for spatially resolved visualization of scalars, vectors, and tensors are available. This includes scripts for Inverse Pole Figures (IPFs) color mapping with given crystal symmetry, the calculation of the nodal displacements in finite-strain spectral solver simulations [57], and the construction of perceptually uniform colormaps [349].

8.2.2.3. Statistical evaluation. Especially for Representative Volume Element (RVE) simulations, statistical evaluations aiming, for instance, at identifying "fingerprints" of microstructural features are of increasing importance. Common ways to represent such evaluations are "heat maps" [34,189,350] or "mechanism maps" [351]. DAMASK provides a number of scripts to calculate and extract such data, which can then be visualized with external tools such as Seaborn.

For more complex dependencies, which can only be partly visualized, machine-learning approaches can be used to detect underlying patterns and presently gain traction in various fields of materials science and engineering [352]. The DAMASK output is accessible to such approaches, but the large data sets impose challenges similar to the ones known from analyzing highly resolved microstructure maps obtained from experimental investigations [353].

9. Summary and outlook

DAMASK has been used to investigate mechanical structure–property relations in crystalline materials and has been successfully applied to study diverse phenomena in structures ranging from single crystals to components and even in biological tissue (Section 7).

In its current state, it is on the one hand a ready-to-use multi-physics simulation toolbox with a focus on Crystal Plasticity (CP) modeling. To lower the barrier for more experimentally-oriented scientists to use DAMASK as a robust tool for advanced structure–property predictions, we have coupled the actual Material Point Model to different numerical solvers and provide a large number of tools for pre- and post-processing. On the other hand, DAMASK is a rapidly growing, flexible, and extensible framework with a modular structure that enables an easy integration of additional (sub)-models (Sections 7.15–7.17). We invite and train interested members of the scientific community to use DAMASK as an open-source platform for the development of novel multi-physics models [192,194,210,354,355] and encourage its further dissemination. We especially appreciate the contribution of extensions that are of broader interest for the materials science community, such as model developments addressing the often encountered trade-off between computational efficiency and model accuracy.

DAMASK is a research code under active development. We currently work on the interoperability with evaluation and visualization tools such as Dream.3D [195,219], Mtex [345], or Paraview/`vtk` [348]. To improve the platform independence and performance, the DAMASK data format is intended to change to `Hdf5` [356,357]. Our current focus in model development is on exploiting the multi-physics capabilities of DAMASK and extending their use beyond full-field simulations. This includes the development of coupled constitutive models and homogenization schemes for chemo-thermo-mechanical problems. Such a fully coupled approach is key for studying complex phenomena such as hydrogen embrittlement or dynamic recrystallization, where physical processes, such as dislocation glide, phase transformation, grain boundary migration, or damage, are strongly influenced by local fluctuations in chemical composition and temperature.

With DAMASK we are aiming at building a community of users and developers to foster the open exchange of material models and application examples. If you are interested in contributing towards this goal, please let us know about your DAMASK-related work.

Acknowledgements

DAMASK development is performed in the *Theory and Simulation Group* at the Max-Planck-Institut für Eisenforschung (MPIE) in Düsseldorf, Germany for more than ten years and in the *Department of Chemical Engineering and Materials Science* of Michigan State University in East Lansing, USA, for more than four years. We acknowledge the contributions of numerous former and current group members. Many of the presented examples are based on work performed by our experimental colleagues and technical staff. We are grateful for the close and faithful cooperation. Finally, we thank Bob Svendsen, Tom Bieler, Martin Crimp, and Ricardo Lebensohn for discussions on theory, modeling, and implementation of the various modules of DAMASK.

The DAMASK development was financially supported by:

- The Deutsche Forschungsgemeinschaft (DFG) within SFB 761 *Steel - ab initio: Quantum mechanics guided design of new Fe based materials*,

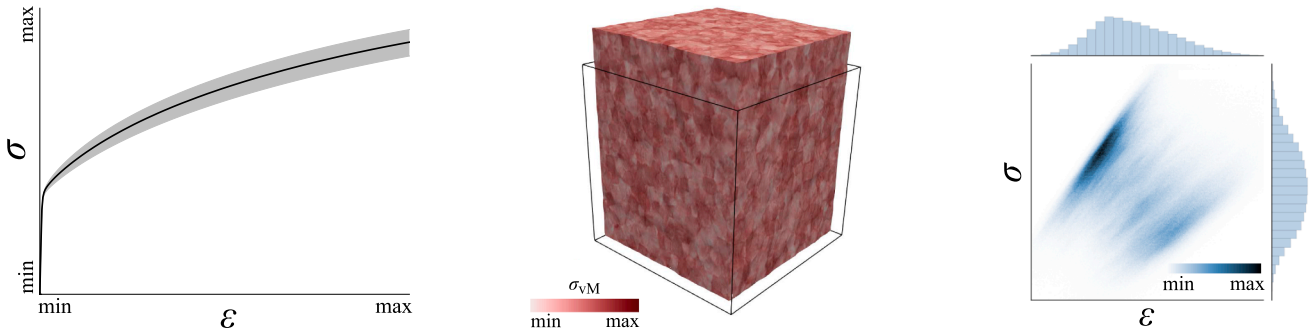

(a) Line plot (b) Mapped field quantity (c) Heat map

Fig. 65. Approaches for data evaluation, exemplary shown for the visualization of stress and strain. Figure adopted from [47] with permission from Cambridge publications.

SPP 1713 *Strong coupling of thermo-chemical and thermo-mechanical states in applied materials*, and contract No. EI 681/3-1.
- The Max-Planck–Fraunhofer initiative Computational Mechanics of Polycrystals (CMC^n).
- The materials innovation institute (M2i) via project No. M 41.2.10410.

The theoretical developments and simulations presented in Section 7.3 were supported by the National Science Foundation (NSF) through grant NSF-CMMI 1463006 and in part by Michigan State University through computational resources provided by the Institute for Cyber-Enabled Research.

The work presented in Section 7.7 has been supported by the Natural Science Foundation of China (NSFC) through Grant No. 51571057.

The work presented in Section 7.15 was financially supported by the research group FOR1650 *Dislocation based plasticity* funded by the DFG under contract number WE 3544/5-2, which is gratefully acknowledged. It was performed on the computational resource bwUniCluster funded by the Ministry of Science, Research and Arts and by the Universities of the State of Baden-Württemberg, Germany, within the framework program bwHPC, on the IC2 (funded by the DFG), and on the HC3 at the Steinbuch Centre for Computing at Karlsruhe Institute of Technology.

The work presented in Section 7.16 has been supported by the Swiss National Science Foundation (SNSF) (project No. 138240) and by the DFG (contract No. SA 2251/2-1).

The work presented in Section 7.18 has been supported by the DFG (contract No. SCHW 1347/3-1).

Appendix A. Obtain, use, contribute, and get support

The latest release version of DAMASK together with installation and usage instructions can be found on the DAMASK home page at https://damask.mpie.de. The bleeding edge of development, which is suitable for experienced users of DAMASK, can be downloaded at https://magit1.mpie.de/damask/damask.git using Git. Within this repository, the branch "release" contains the current release version, the branch "development" is the latest development version, and the branch "master" corresponds to the most recent development version that successfully passed the automated testing suite. To get support regarding installation, usage, or how to contribute to the development, please write an email to damask@mpie.de.

Appendix B. Scheme of notation

As a general scheme of notation, scalar quantities are written as lower case letter (*e.g.* a, b), vectors are written as boldface lowercase letters (*e.g.* **a**, **b**), second-order tensors as boldface capital letters (*e.g.* **A**, **B**), and fourth-order tensors as blackboard-bold capital letters (*e.g.* $\mathbb{A}$, $\mathbb{B}$). For vectors and tensors, Cartesian components are denoted as, respectively, a_i, A_{ij}, and A_{ijkl}. All inner products are indicated by a single dot between the tensorial quantities of the same order, *e.g.* $t = \mathbf{a}\cdot\mathbf{b}$ ($t = a_i b_i$ with implicit summation over repeated indices unless specified otherwise) for vectors and $t = \mathbf{A}\cdot\mathbf{B}$ ($t = A_{ij}B_{ij}$) for second-order tensors. The tensor (or dyadic) product between two vectors is denoted as $\mathbf{T} = \mathbf{a} \otimes \mathbf{b}$ ($T_{ij} = a_i b_j$). The action of a second-order tensor upon a vector is denoted as $\mathbf{t} = \mathbf{A}\mathbf{b}$ (in components $t_i = A_{ij}b_j$) and that of a fourth-order tensor upon a second order tensor is designated as $\mathbf{T} = \mathbb{A}\colon\mathbf{B}$ ($T_{ij} = A_{ijkl}B_{kl}$). The composition of two second-order tensors is denoted as $\mathbf{T} = \mathbf{A}\mathbf{B}$ ($T_{ij} = A_{ik}B_{kj}$). The tensor product $\mathbf{A} \boxtimes \mathbf{B}$ of two second-order tensors **A** and **B** is defined by $(\mathbf{A} \boxtimes \mathbf{B})\mathbf{C} \coloneqq \mathbf{A}\mathbf{C}\mathbf{B}$ ($T_{ijkl} = (A_{ij} \boxtimes B_{kl})$ such that $T_{ijkl}C_{kl} = A_{im}C_{mn}B_{nj}$). The transpose tensor product $\mathbf{A} \boxplus \mathbf{B}$ of two second-order tensors **A** and **B** is defined by $(\mathbf{A} \boxplus \mathbf{B})\mathbf{C} \coloneqq \mathbf{A}\mathbf{C}^{\mathrm{T}}\mathbf{B}$ ($T_{ijkl} = (A_{ij} \boxtimes B_{kl})$ such that $T_{ijkl}C_{kl} = A_{im}C_{nm}B_{nj}$). The dyadic product of two second-order tensors is denoted as $\mathbb{T} = \mathbf{A} \odot \mathbf{B}$ ($T_{ijkl} = A_{ij}B_{kl}$). $||\mathbf{A}||_{\mathrm{F}} = \sqrt{\mathrm{Tr}(\mathbf{A}\mathbf{A}^{\mathrm{T}})}$ designates the Frobenius norm of (real-valued) matrix **A**. The gradients $\mathbf{t} = \mathrm{Grad}\,(a)$ and $\mathbf{t} = \mathrm{grad}\,(a)$ of a scalar field a are defined by $t_i = \partial a/\partial x_i$ and $t_i = \partial a/\partial y_i$, respectively. The divergences $\mathbf{t} = \mathrm{Div}\,(\mathbf{A})$ and $\mathbf{t} = \mathrm{div}\,(\mathbf{A})$ of a tensor field **A** are defined by $t_i = \partial A_{ij}/\partial x_j$ and $t_i = \partial A_{ij}/\partial y_j$, respectively. The curls $\mathbf{T} = \mathrm{Curl}\,(\mathbf{A})$ and $\mathbf{T} = \mathrm{curl}\,(\mathbf{A})$ of a tensor field **A** are defined by $T_{ij} = \epsilon_{kli}\,\partial A_{jl}/\partial x_k$ and $T_{ij} = \epsilon_{kli}\,\partial A_{jl}/\partial y_k$, respectively, where ϵ is the permutation symbol.

Appendix C. Configurations

The formulas shown in Table 20 can be used for conversion of the three stress measures used in this work: the first Piola–Kirchhoff stress **P**, the second Piola–Kirchhoff stress **S**, and the Cauchy stress $\boldsymbol{\sigma}$.

To obtain the work conjugacy relations, the total stress power

$$\begin{aligned}\mathcal{P} &= \mathbf{P}\cdot\dot{\mathbf{F}}\\ &= \underbrace{\mathbf{P}\cdot(\dot{\mathbf{F}}_{\mathrm{e}}\mathbf{F}_{\mathrm{i}}\mathbf{F}_{\mathrm{p}})}_{\mathcal{P}_{\mathrm{e}}} + \underbrace{\mathbf{P}\cdot(\mathbf{F}_{\mathrm{e}}\dot{\mathbf{F}}_{\mathrm{i}}\mathbf{F}_{\mathrm{p}})}_{\mathcal{P}_{\mathrm{i}}} + \underbrace{\mathbf{P}\cdot(\mathbf{F}_{\mathrm{e}}\mathbf{F}_{\mathrm{i}}\dot{\mathbf{F}}_{\mathrm{p}})}_{\mathcal{P}_{\mathrm{p}}}\end{aligned} \tag{146}$$

is split into elastic, eigenstrain, and plastic contributions. The relation between $\dot{\mathbf{E}}$ and $\mathbf{L}_{\mathrm{e}} = \dot{\mathbf{F}}_{\mathrm{e}}\mathbf{F}_{\mathrm{e}}^{-1}$ is obtained by taking the time derivative of Eq. (48). Under the assumption of small elastic strains, *i.e.* $\mathbf{F}_{\mathrm{e}}^{\mathrm{T}}\mathbf{F}_{\mathrm{e}} \approx \mathbf{I}$, and isochoric plastic deformation, *i.e.* $\det \mathbf{F}_{\mathrm{p}} = 1$, this relation can be simplified to

$$\dot{\mathbf{E}} = \frac{1}{2}\mathbf{F}_{\mathrm{i}}^{\mathrm{T}}\mathbf{F}_{\mathrm{e}}^{\mathrm{T}}(\mathbf{L}_{\mathrm{e}} + \mathbf{L}_{\mathrm{e}}^{\mathrm{T}})\mathbf{F}_{\mathrm{e}}\mathbf{F}_{\mathrm{i}}. \tag{147}$$

Using Eq. (147), the elastic stress power term can be expressed in the plastic configuration to establish the work conjugacy between **S** and **E**

Table 20
Conversion between different stress measures. Note that the definition of the second Piola–Kirchhoff stress **S** differs from the definition used in standard nonlinear continuum mechanics [49].

	P	**S**	$\boldsymbol{\sigma}$
P	**P**	$\det\mathbf{F}_{\mathrm{p}}\mathbf{F}_{\mathrm{e}}\mathbf{F}_{\mathrm{i}}\mathbf{S}\mathbf{F}_{\mathrm{p}}^{-\mathrm{T}}$	$\det\mathbf{F}\boldsymbol{\sigma}\mathbf{F}^{-\mathrm{T}}$
S	$\frac{1}{\det\mathbf{F}_{\mathrm{p}}}\mathbf{F}_{\mathrm{i}}^{-1}\mathbf{F}_{\mathrm{e}}^{-1}\mathbf{P}\mathbf{F}_{\mathrm{p}}^{\mathrm{T}}$	**S**	$\det(\mathbf{F}_{\mathrm{e}}\mathbf{F}_{\mathrm{i}})\mathbf{F}_{\mathrm{i}}^{-1}\mathbf{F}_{\mathrm{e}}^{-1}\boldsymbol{\sigma}\mathbf{F}_{\mathrm{e}}^{-\mathrm{T}}\mathbf{F}_{\mathrm{i}}^{-\mathrm{T}}$
$\boldsymbol{\sigma}$	$\frac{1}{\det\mathbf{F}}\mathbf{P}\mathbf{F}^{\mathrm{T}}$	$\frac{1}{\det(\mathbf{F}_{\mathrm{e}}\mathbf{F}_{\mathrm{i}})}\mathbf{F}_{\mathrm{e}}\mathbf{F}_{\mathrm{i}}\mathbf{S}\mathbf{F}_{\mathrm{i}}^{\mathrm{T}}\mathbf{F}_{\mathrm{e}}^{\mathrm{T}}$	$\boldsymbol{\sigma}$

$$\begin{aligned}\mathcal{P}_\mathrm{e} &= \mathbf{P}\cdot(\mathbf{F}_\mathrm{e}^{-\mathrm{T}}\mathbf{F}_\mathrm{i}^{-\mathrm{T}}\dot{\mathbf{E}}\mathbf{F}_\mathrm{i}^{-1}\mathbf{F}_\mathrm{e}^{-1}\mathbf{F})\\ &= (\mathbf{F}_\mathrm{i}^{-1}\mathbf{F}_\mathrm{e}^{-1}\mathbf{P}\mathbf{F}_\mathrm{p}^{-\mathrm{T}})\cdot\dot{\mathbf{E}}\\ &= \mathbf{S}\cdot\dot{\mathbf{E}}.\end{aligned} \tag{148}$$

Work conjugacy between $\mathbf{M}_\mathrm{i}$ and $\mathbf{L}_\mathrm{i}$ can be established by considering the eigenstrain stress power term and using Eq. (48)

$$\begin{aligned}\mathcal{P}_\mathrm{i} &= \mathbf{P}\cdot(\mathbf{F}_\mathrm{e}\mathbf{L}_\mathrm{i}\mathbf{F}_\mathrm{i}\mathbf{F}_\mathrm{p})\\ &= (\mathbf{F}_\mathrm{i}\mathbf{S}\mathbf{F}_\mathrm{i}^{\mathrm{T}})\cdot\mathbf{L}_\mathrm{i}\\ &= \mathbf{M}_\mathrm{i}\cdot\mathbf{L}_\mathrm{i}\det\mathbf{F}_\mathrm{i}.\end{aligned} \tag{149}$$

Similarly, considering the plastic stress power, work conjugacy between $\mathbf{M}_\mathrm{p}$ and $\mathbf{L}_\mathrm{p}$ can be established

$$\begin{aligned}\mathcal{P}_\mathrm{p} &= \mathbf{P}\cdot(\mathbf{F}_\mathrm{e}\mathbf{F}_\mathrm{i}\mathbf{L}_\mathrm{p}\mathbf{F}_\mathrm{p})\\ &= (\mathbf{F}_\mathrm{i}^{\mathrm{T}}\mathbf{F}_\mathrm{e}^{\mathrm{T}}\mathbf{P}\mathbf{F}_\mathrm{p}^{\mathrm{T}})\cdot\mathbf{L}_\mathrm{p}\\ &= \mathbf{M}_\mathrm{p}\cdot\mathbf{L}_\mathrm{p}.\end{aligned} \tag{150}$$

The Mandel stresses in the plastic and in the eigenstrain configuration are then given as

$$\mathbf{M}_\mathrm{p} = \mathbf{F}_\mathrm{i}^{\mathrm{T}}\mathbf{F}_\mathrm{i}\mathbf{S} \text{ and} \tag{151a}$$

$$\mathbf{M}_\mathrm{i} = \det\mathbf{F}_\mathrm{i}^{-1}\mathbf{F}_\mathrm{i}\mathbf{S}\mathbf{F}_\mathrm{i}^{\mathrm{T}}. \tag{151b}$$

Appendix D. Partial derivative of the constitutive relations

For the time integration of the stress (Section 5.2) and the evaluation of the consistent stress tangent (Section 5.3), derivatives of the constitutive functions are required.

The second Piola–Kirchhoff stress $\mathbf{S}$ is expressed as a function of its work conjugate Green–Lagrange strain $\mathbf{E}$ in the plastic configuration. Therefore its derivates are given by:

$$\frac{\partial\mathbf{S}}{\partial\mathbf{F}_\mathrm{e}} = \frac{\mathrm{d}\mathbf{S}}{\mathrm{d}\mathbf{E}} : \frac{\partial\mathbf{E}}{\partial\mathbf{F}_\mathrm{e}}, \tag{152a}$$

$$\frac{\partial\mathbf{S}}{\partial\mathbf{F}_\mathrm{i}} = \frac{\mathrm{d}\mathbf{S}}{\mathrm{d}\mathbf{E}} : \frac{\partial\mathbf{E}}{\partial\mathbf{F}_\mathrm{i}}, \tag{152b}$$

where

$$\frac{\partial\mathbf{E}}{\partial\mathbf{F}_\mathrm{e}} = \frac{1}{2}[\mathbf{F}_\mathrm{i}^{\mathrm{T}}\mathbf{F}_\mathrm{e}^{\mathrm{T}} \boxtimes \mathbf{F}_\mathrm{i} + \mathbf{F}_\mathrm{i}^{\mathrm{T}} \boxplus \mathbf{F}_\mathrm{e}\mathbf{F}_\mathrm{i}], \tag{153a}$$

$$\frac{\partial\mathbf{E}}{\partial\mathbf{F}_\mathrm{i}} = \frac{1}{2}[\mathbf{F}_\mathrm{i}^{\mathrm{T}}(\mathbf{F}_\mathrm{e}^{\mathrm{T}}\mathbf{F}_\mathrm{e} - \mathbf{I}) \boxtimes \mathbf{I} + \mathbf{I} \boxplus (\mathbf{F}_\mathrm{e}^{\mathrm{T}}\mathbf{F}_\mathrm{e} - \mathbf{I})\mathbf{F}_\mathrm{i}]. \tag{153b}$$

Similarly, the derivatives of the plastic velocity gradient $\mathbf{L}_\mathrm{p}$ are expressed through its work conjugate plastic Mandel stress $\mathbf{M}_\mathrm{p}$:

$$\frac{\partial\mathbf{L}_\mathrm{p}}{\partial\mathbf{S}} = \frac{\mathrm{d}\mathbf{L}_\mathrm{p}}{\mathrm{d}\mathbf{M}_\mathrm{p}} : \frac{\partial\mathbf{M}_\mathrm{p}}{\partial\mathbf{S}}, \tag{154a}$$

$$\frac{\partial\mathbf{L}_\mathrm{p}}{\partial\mathbf{F}_\mathrm{i}} = \frac{\mathrm{d}\mathbf{L}_\mathrm{p}}{\mathrm{d}\mathbf{M}_\mathrm{p}} : \frac{\partial\mathbf{M}_\mathrm{p}}{\partial\mathbf{F}_\mathrm{i}}, \tag{154b}$$

where

$$\frac{\partial\mathbf{M}_\mathrm{p}}{\partial\mathbf{S}} = \mathbf{F}_\mathrm{i}^{\mathrm{T}}\mathbf{F}_\mathrm{i} \boxtimes \mathbf{I}, \tag{155a}$$

$$\frac{\partial\mathbf{M}_\mathrm{p}}{\partial\mathbf{F}_\mathrm{i}} = \mathbf{F}_\mathrm{i}^{\mathrm{T}} \boxtimes \mathbf{S} + \mathbf{I} \boxplus \mathbf{F}_\mathrm{i}\mathbf{S}. \tag{155b}$$

$\mathbf{L}_\mathrm{p}$ describes the plastic velocity gradient resulting from combined dislocation glide on all slip systems:[17]

$$\mathbf{L}_\mathrm{p}(\mathbf{M}_\mathrm{p}, \omega) = \mathbf{L}_\mathrm{p} = \sum_\alpha \mathbf{L}_\mathrm{p}^\alpha = \sum_\alpha \dot{\gamma}^\alpha \mathbf{s}^\alpha \otimes \mathbf{n}^\alpha. \tag{156}$$

Hence, the partial derivative of $\mathbf{L}_\mathrm{p}$ with respect to the plastic Mandel stress is defined by the sum of the derivatives of the plastic velocity gradient of the respective slip systems:

$$\mathbf{L}_\mathrm{p}(\mathbf{M}_\mathrm{p}, \omega)_{,\mathbf{M}_\mathrm{p}} = \mathbf{L}_{\mathrm{p},\mathbf{M}_\mathrm{p}} = \sum_\alpha \mathbf{L}_\mathrm{p}^{\alpha}{}_{,\mathbf{M}_\mathrm{p}}. \tag{157}$$

The individual derivatives can be obtained as follows:

[17] A similar procedure is applicable for twin systems.

$$\begin{aligned}\mathbf{L}_{\mathrm{p}}^{\alpha},_{\mathbf{M}_{\mathrm{p}}} &= (\dot{\gamma}^{\alpha}\,\mathbf{s}^{\alpha}\otimes\ \mathbf{n}^{\alpha}),_{\mathbf{M}_{\mathrm{p}}}\\ &= (\mathbf{s}^{\alpha}\otimes\ \mathbf{n}^{\alpha})\odot\dot{\gamma}^{\alpha},_{\mathbf{M}_{\mathrm{p}}}\\ &= \tfrac{\partial\dot{\gamma}^{\alpha}}{\partial\tau^{\alpha}}(\mathbf{s}^{\alpha}\otimes\ \mathbf{n}^{\alpha})\odot\tau^{\alpha},_{\mathbf{M}_{\mathrm{p}}}\\ &= \tfrac{\partial\dot{\gamma}^{\alpha}}{\partial\tau^{\alpha}}(\mathbf{s}^{\alpha}\otimes\ \mathbf{n}^{\alpha})\odot((\mathbf{s}^{\alpha}\otimes\ \mathbf{n}^{\alpha})\cdot\mathbf{M}_{\mathrm{p}}),_{\mathbf{M}_{\mathrm{p}}}\\ &= \tfrac{\partial\dot{\gamma}^{\alpha}}{\partial\tau^{\alpha}}(\mathbf{s}^{\alpha}\otimes\ \mathbf{n}^{\alpha})\odot(\mathbf{s}^{\alpha}\otimes\ \mathbf{n}^{\alpha}).\end{aligned} \tag{158}$$

The eigenstrain velocity gradient $\mathbf{L}_{\mathrm{i}}$ is expressed in terms of its pull-back to the plastic configuration, $\mathbf{L}_{\mathrm{i;p}} = \mathbf{F}_{\mathrm{i}}^{-1}\mathbf{L}_{\mathrm{i}}\mathbf{F}_{\mathrm{i}}^{\mathrm{T}}\det\mathbf{F}_{\mathrm{i}}^{-1}$, which is work conjugate with $\mathbf{S}$. Its derivates are, therefore, given by:

$$\frac{\partial\mathbf{L}_{\mathrm{i}}}{\partial\mathbf{S}} = (\mathbf{F}_{\mathrm{i}}\boxtimes\mathbf{F}_{\mathrm{i}}^{-\mathrm{T}}\det\mathbf{F}_{\mathrm{i}})\colon\frac{\mathrm{d}\mathbf{L}_{\mathrm{i;p}}}{\mathrm{d}\mathbf{S}}, \tag{159}$$

$$\frac{\partial\mathbf{L}_{\mathrm{i}}}{\partial\mathbf{F}_{\mathrm{i}}} = \mathbf{I}\boxtimes\mathbf{L}_{\mathrm{i;p}}\mathbf{F}_{\mathrm{i}}^{-\mathrm{T}}\det\mathbf{F}_{\mathrm{i}} - \mathbf{F}_{\mathrm{i}}\mathbf{L}_{\mathrm{i;p}}\mathbf{F}_{\mathrm{i}}^{-\mathrm{T}}\boxplus\mathbf{F}_{\mathrm{i}}^{-\mathrm{T}}\det\mathbf{F}_{\mathrm{i}} + \mathbf{L}_{\mathrm{i}}\odot\mathbf{F}_{\mathrm{i}}^{-\mathrm{T}}. \tag{160}$$

Appendix E. Deformation systems

DAMASK has definitions of slip systems for cubic materials such as face-centered cubic (fcc) and body-centered cubic (bcc), and for hexagonal (hex) and body-centered tetragonal (bct) crystal structures for which the c/a-ratio is adjustable. Table 21 lists all included slip families. Twin system families are implemented for fcc, bcc, and hex (where the exact geometry depends on c/a-ratio) crystal symmetries as specified in Table 22.

Table 21
Slip system families of the different lattice types as Miller or (for hexagonal lattices) Miller–Bravais indices.

Direction	Plane normal	Label
(a) Face-centered cubic (fcc) crystal structure		
⟨01$\bar{1}$⟩	{111}	
(b) Body-centered cubic (bcc) crystal structure		
⟨1$\bar{1}$1⟩	{011}	
⟨$\bar{1}$11⟩	{211}	
(c) Hexagonal (hex) crystal structure		
⟨2$\bar{1}\bar{1}$0⟩	{0001}	Basal
⟨2$\bar{1}\bar{1}$0⟩	{01$\bar{1}$0}	1st Prismatic
⟨01$\bar{1}$0⟩	{2$\bar{1}\bar{1}$0}	2nd Prismatic
⟨2$\bar{1}\bar{1}$0⟩	{01$\bar{1}$1}	Pyramidal ⟨a⟩
⟨2$\bar{1}\bar{1}$3⟩	{$\bar{1}$101}	Pyramidal ⟨c + a⟩
⟨2$\bar{1}\bar{1}$3⟩	{$\bar{2}$112}	Pyramidal ⟨c + a⟩
(d) Body-centered tetragonal (bct) crystal structure		
⟨001⟩	{100}	
⟨001⟩	{110}	
⟨010⟩	{100}	
⟨1$\bar{1}$0⟩	{110}	
⟨1$\bar{1}$0⟩	{110}	
⟨011⟩	{100}	
⟨010⟩	{001}	
⟨110⟩	{001}	
⟨01$\bar{1}$⟩	{011}	
⟨1$\bar{1}$1⟩	{011}	
⟨100⟩	{011}	
⟨01$\bar{1}$⟩	{211}	
⟨$\bar{1}$11⟩	{211}	

Table 22
Twin system families of the different lattice types as Miller or (for hexagonal lattices) Miller–Bravais indices.

Direction	Plane normal	Label
(a) Face-centered cubic (fcc) crystal structure		
$\langle\bar{2}11\rangle$	$\{111\}$	
(b) Body-centered cubic (bcc) crystal structure		
$\langle\bar{1}11\rangle$	$\{211\}$	
(c) Hexagonal (hex) crystal structure		
$\langle1\bar{1}01\rangle$	$\{\bar{1}102\}$	1st Extension
$\langle2\bar{1}\bar{1}6\rangle$	$\{\bar{2}111\}$	1st Compression
$\langle\bar{1}10\bar{2}\rangle$	$\{\bar{1}101\}$	2nd Extension
$\langle2\bar{1}\bar{1}\bar{3}\rangle$	$\{2\bar{1}\bar{1}2\}$	2nd Compression

References

[1] M. Kraska, M. Doig, D. Tikhomirov, D. Raabe, F. Roters, Virtual material testing for stamping simulations based on polycrystal plasticity, Comput. Mater. Sci. 46 (2) (2009) 383–392, https://doi.org/10.1016/j.commatsci.2009.03.025.

[2] J.H. Panchal, S.R. Kalidindi, D.L. McDowell, Key computational modeling issues in Integrated Computational Materials Engineering, Comp.-Aided Des. 45 (1) (2013) 4–25, https://doi.org/10.1016/j.cad.2012.06.006.

[3] G.J. Schmitz, U. Prahl (Eds.), Integrative Computational Materials Engineering, Wiley-VCH, Weinheim, 978-3-527-33081-2, 2012, , https://doi.org/10.1002/9783527646098.

[4] F. Roters, P. Eisenlohr, L. Hantcherli, D.D. Tjahjanto, T.R. Bieler, D. Raabe, Overview of constitutive laws, kinematics, homogenization, and multiscale methods in crystal plasticity finite element modeling: theory, experiments, applications, Acta Mater. 58 (4) (2010) 1152–1211, https://doi.org/10.1016/j.actamat.2009.10.058.

[5] D. Raabe, Z. Zhao, F. Roters, A finite element method on the basis of texture components for fast predictions of anisotropic forming operations, Steel Res. 72 (10) (2001) 421–426, https://doi.org/10.1002/srin.200100145.

[6] M. Sachtleber, Z. Zhao, D. Raabe, Experimental investigation of plastic grain interaction, Mater. Sci. Eng. A 336 (1-2) (2002) 81–87, https://doi.org/10.1016/S0921-5093(01)01974-8.

[7] Z. Zhao, M. Ramesh, D. Raabe, A.M. Cuitiño, R. Radovitzky, Investigation of three-dimensional aspects of grain-scale plastic surface deformation of an aluminum oligocrystal, Int. J. Plast. 24 (12) (2008) 2278–2297, https://doi.org/10.1016/j.ijplas.2008.01.002.

[8] L. Wang, R.I. Barabash, Y. Yang, T.R. Bieler, M.A. Crimp, P. Eisenlohr, W. Liu, G.E. Ice, Experimental characterization and crystal plasticity modeling of heterogeneous deformation in polycrystalline α-Ti, Metal. Mater. Trans. A 42 (3) (2011) 626–635, https://doi.org/10.1007/s11661-010-0249-8.

[9] S-H Choi, E-Y Kim, W. Woo, S.H. Han, J.H. Kwak, The effect of crystallographic orientation on the micromechanical deformation and failure behaviors of DP980 steel during uniaxial tension, Int. J. Plast. 45 (2013) 85–102, https://doi.org/10.1016/j.ijplas.2012.11.013.

[10] F. Wang, S. Sandlöbes, M. Diehl, L. Sharma, F. Roters, D. Raabe, In situ observation of collective grain-scale mechanics in Mg and Mg–rare earth alloys, Acta Mater. 80 (2014) 77–93, https://doi.org/10.1016/j.actamat.2014.07.048.

[11] R. Pokharel, J. Lind, A.K. Kanjarla, R.A. Lebensohn, S.F. Li, P. Kenesei, R.M. Suter, A.D. Rollett, Polycrystal plasticity: comparison between grain-scale observations of deformation and simulations, Ann. Rev. Cond. Matter Phys. 5 (1) (2014) 317–346, https://doi.org/10.1146/annurev-conmatphys-031113-133846.

[12] C.C. Tasan, J.P.M. Hoefnagels, M. Diehl, D. Yan, F. Roters, D. Raabe, Strain localization and damage in dual phase steels investigated by coupled in-situ deformation experiments-crystal plasticity simulations, Int. J. Plast. 63 (2014) 198–210, https://doi.org/10.1016/j.ijplas.2014.06.004.

[13] C. Pinna, Y. Lan, M.F. Kiu, P. Efthymiadis, M. Lopez-Pedrosa, D. Farrugia, Assessment of crystal plasticity finite element simulations of the hot deformation of metals from local strain and orientation measurements, Int. J. Plast. 73 (2015) 24–38, https://doi.org/10.1016/j.ijplas.2015.05.015.

[14] V.V.C. Wan, M.A. Cuddihy, J. Jiang, D.W. MacLachlan, F.P.E. Dunne, An HR-EBSD and computational crystal plasticity investigation of microstructural stress distributions and fatigue hotspots in polycrystalline copper, Acta Mater. 115 (2016) 45–57, https://doi.org/10.1016/j.actamat.2016.05.033.

[15] Y. Guan, B. Chen, J. Zou, T.B. Britton, J. Jiang, F.P.E. Dunne, Crystal plasticity modelling and HR-DIC measurement of slip activation and strain localization in single and oligo-crystal Ni alloys under fatigue, Int. J. Plast. 88 (2017) 70–88, https://doi.org/10.1016/j.ijplas.2016.10.001.

[16] F. Roters, P. Eisenlohr, T.R. Bieler, D. Raabe, Crystal Plasticity Finite Element Methods in Materials Science and Engineering, Wiley-VCH, Weinheim, Germany, 978-3-527-32447-7, 2010, https://doi.org/10.1002/9783527631483.

[17] H. Mecking, U.F. Kocks, Kinetics of flow and strain hardening, Acta Metal. 29 (11) (1981) 1865–1875, https://doi.org/10.1016/0001-6160(81)90112-7.

[18] D.R. Steinmetz, T. Jäpel, B. Wietbrock, P. Eisenlohr, I. Gutierrez-Urrutia, A. Saeed-Akbari, T. Hickel, F. Roters, D. Raabe, Revealing the strain-hardening behavior of twinning-induced plasticity steels: theory, simulations, experiments, Acta Mater. 61 (2) (2013) 494–510, https://doi.org/10.1016/j.actamat.2012.09.064.

[19] S.L. Wong, M. Madivala, U. Prahl, F. Roters, D. Raabe, A crystal plasticity model for twinning- and transformation-induced plasticity, Acta Mater. 118 (2016) 140–151, https://doi.org/10.1016/j.actamat.2016.07.032.

[20] C. Ayas, V.S. Deshpande, N.A. Fleck, A fracture criterion for the notch strength of high strength steels in the presence of hydrogen, J. Mech. Phys. Solids 63 (2014) 80–93, https://doi.org/10.1016/j.jmps.2013.10.002.

[21] M. Koyama, E. Akiyama, Y-K Lee, D. Raabe, K. Tsuzaki, Overview of hydrogen embrittlement in high-Mn steels, Int. J. Hydrogen Energy 42 (17) (2017) 12706–12723, https://doi.org/10.1016/j.ijhydene.2017.02.214.

[22] A.D. Rollett, Overview of modeling and simulation of recrystallization, Prog. Mater. Sci. 42 (1-4) (1997) 79–99, https://doi.org/10.1016/S0079-6425(97)00008-X.

[23] M. Jafari, M. Jamshidian, S. Ziaei-Rad, D. Raabe, F. Roters, Constitutive modeling of strain induced grain boundary migration via coupling crystal plasticity and phase-field methods, Int. J. Plast. 99 (2017) 19–42, https://doi.org/10.1016/j.ijplas.2017.08.004.

[24] C. Zambaldi, Y. Yang, T.R. Bieler, D. Raabe, Orientation informed nanoindentation of α-titanium: Indentation pileup in hexagonal metals deforming by prismatic slip, J. Mater. Res. 27 (1) (2012) 356–367, https://doi.org/10.1557/jmr.2011.334.

[25] A. Köster, A. Ma, A. Hartmaier, Atomistically informed crystal plasticity model for body-centered cubic iron, Acta Mater. 60 (9) (2012) 3894–3901, https://doi.org/10.1016/j.actamat.2012.03.053.

[26] D. Cereceda, M. Diehl, F. Roters, P. Shanthraj, D. Raabe, J.M. Perlado, J. Marian, Linking atomistic, kinetic Monte Carlo and crystal plasticity simulations of single-crystal Tungsten strength, GAMM-Mitteilungen 38 (2) (2015) 213–227, https://doi.org/10.1002/gamm.201510012.

[27] H. Zhang, M. Diehl, F. Roters, D. Raabe, A virtual laboratory for initial yield surface determination using high resolution crystal plasticity simulations, Int. J. Plast. 80 (2016) 111–138, https://doi.org/10.1016/j.ijplas.2016.01.002.

[28] D. Helm, A. Butz, D. Raabe, P. Gumbsch, Microstructure-based description of the deformation of metals: theory and application, JOM 63 (4) (2011) 26–33, https://doi.org/10.1007/s11837-011-0056-8.

[29] F. Fritzen, T. Böhlke, Three-dimensional finite element implementation of the nonuniform transformation field analysis, Int. J. Numer. Meth. Eng. 84 (7) (2010) 803–829, https://doi.org/10.1002/nme.2920.

[30] L. Scheunemann, D. Balzani, D. Brands, J. Schröder, D. Raabe, Statistically similar RVE construction based on 3D dual-phase steel microstructures, in: A. Zingoni (Ed.), Research and Applications in Structural Engineering, Mechanics and Computation – Proceedings of the 5th International Conference on Structural Engineering, Mechanics and Computation, SEMC, CRC Press, 411, 2013, p. 416 ISBN 978-1-315-8078-8.

[31] J-C Michel, P. Suquet, A model-reduction approach to the micromechanical analysis of polycrystalline materials, Comput. Mech. 57 (3) (2016) 483–508, https://doi.org/10.1007/s00466-015-1248-9.

[32] A.J. Schwartz, M. Kumar, B.L. Adams, D.P. Field (Eds.), Electron Backscatter Diffraction in Materials Science, Springer, Boston, 978-0-387-88135-5, 2009, , https://doi.org/10.1007/978-0-387-88136-2.

[33] S. Zaefferer, S.I. Wright, D. Raabe, Three-dimensional orientation microscopy in a focused ion beam–scanning electron microscope: a new dimension of microstructure characterization, Metal. Mater. Trans. A 39 (2) (2008) 374–389, https://doi.org/10.1007/s11661-007-9418-9.

[34] M. Diehl, D. An, P. Shanthraj, S. Zaefferer, F. Roters, D. Raabe, Crystal plasticity study on stress and strain partitioning in a measured 3D dual phase steel microstructure, Phys. Mesomech. 20 (3) (2017) 311–323, https://doi.org/10.1134/S1029959917030079.

[35] B.C. Larson, W. Yang, G.E. Ice, J.D. Budai, J.Z. Tischler, Three-dimensional X-ray structural microscopy with submicrometre resolution, Nature 415 (6874) (2002) 887–890, https://doi.org/10.1038/415887a.

[36] B. Zhou, T.R. Bieler, T-K Lee, W. Liu, Characterization of recrystallization and microstructure evolution in lead-free solder joints using EBSD and 3D-XRD, J. Electron. Mater. 42 (2) (2013) 319–331, https://doi.org/10.1007/s11664-012-2307-z.

[37] C. Zhang, H. Li, P. Eisenlohr, W.J. Liu, C.J. Boehlert, M.A. Crimp, T.R. Bieler, Effect of realistic 3D microstructure in crystal plasticity finite element analysis of polycrystalline Ti-5Al-2.5Sn, Int. J. Plast. 69 (2015) 21–35, https://doi.org/10.1016/j.ijplas.2015.01.003.

[38] C. Miehe, F. Welschinger, M. Hofacker, Thermodynamically consistent phase-field models of fracture: variational principles and multi-field FE implementations, Int. J. Numer. Meth. Eng. 83 (10) (2010) 1273–1311, https://doi.org/10.1002/nme.2861.

[39] P. Shanthraj, M.A. Zikry, Optimal microstructures for martensitic steels, J. Mater. Res. 27 (12) (2012) 1598–1611, https://doi.org/10.1557/jmr.2012.127.

[40] P. Shanthraj, M.A. Zikry, Microstructurally induced fracture nucleation and propagation in martensitic steels, J. Mech. Phys. Solids 61 (4) (2013) 1091–1105, https://doi.org/10.1016/j.jmps.2012.11.006.

[41] M. Diehl, M. Wicke, P. Shanthraj, F. Roters, A. Brueckner-Foit, D. Raabe, Coupled crystal plasticity–phase field fracture simulation study on damage evolution around a void: pore shape versus crystallographic orientation, JOM 69 (5) (2017) 872–878, https://doi.org/10.1007/s11837-017-2308-8.

[42] P. Shanthraj, L. Sharma, B. Svendsen, F. Roters, D. Raabe, A phase field model for damage in elasto-viscoplastic materials, Comp. Meth. Appl. Mech. Eng. 312 (2016) 167–185, https://doi.org/10.1016/j.cma.2016.05.006.

[43] P. Shanthraj, M. Diehl, P. Eisenlohr, F. Roters, D. Raabe, Spectral solvers for crystal plasticity and multi-physics simulations, in: C.-H. Hsueh, S. Schmauder, C.-S. Chen, K.K. Chawla, N. Chawla, W. Chen, Y. Kagawa (Eds.), Handbook of Mechanics of Materials, Springer, Berlin, 978-981-10-6883-6, 2019.

[44] D. Raabe, F. Roters, F. Barlat, L.-Q. Chen (Eds.), Continuum Scale Simulation of Engineering Materials, Wiley-VCH, Weinheim, 978-3-527-30760-9, 2005, , https://doi.org/10.1002/3527603786.

[45] I. Steinbach, Phase-field models in materials science, Model. Simul. Mater. Sci. Eng. 17 (7) (2009) 073001, https://doi.org/10.1088/0965-0393/17/7/073001.

[46] G.Z. Voyiadjis (Ed.), Handbook of Damage Mechanics, Springer, New York, USA, 2015, , https://doi.org/10.1007/978-1-4614-8968-9.

[47] M. Diehl, Review and outlook: mechanical, thermodynamic, and kinetic continuum modeling of metallic materials at the grain scale, MRS Commun. 7 (4) (2017) 735–746, https://doi.org/10.1557/mrc.2017.98.

[48] F. Roters, Advanced Material Models for the Crystal Plasticity Finite Element Method – Development of a General CPFEM Framework, Habilitation thesis, RWTH Aachen, Aachen, 2011 http://darwin.bth.rwth-aachen.de/opus3/volltexte/2011/3874/.

[49] J. Bonet, R.D. Wood, Nonlinear Continuum Mechanics for Finite Element Analysis, second ed., Cambridge University Press, Cambridge, United Kingdom, 2009, https://doi.org/10.1017/CBO9780511755446.

[50] B. Bourdin, G.A. Francfort, J-J Marigo, Numerical experiments in revisited brittle fracture, J. Mech. Phys. Solids 48 (4) (2000) 797–826, https://doi.org/10.1016/S0022-5096(99)00028-9.

[51] S.M. Allen, J.W. Cahn, Ground state structures in ordered binary alloys with second neighbor interactions, Acta Metal. 20 (3) (1972) 423–433, https://doi.org/10.1016/0001-6160(72)90037-5.

[52] A.A. Griffith, The phenomena of rupture and flow in solids, Philos. Trans. R. Soc. A 221 (1921) 582–593, https://doi.org/10.1098/rsta.1921.0006.

[53] H. Moulinec, P. Suquet, A fast numerical method for computing the linear and nonlinear properties of composites, Comptes rendus de l'Académie des sciences. Série II, Mécanique, physique, chimie, astronomie 318 (1994) 1417–1423.

[54] R.A. Lebensohn, N-site modeling of a 3D viscoplastic polycrystal using fast Fourier transform, Acta Mater. 49 (14) (2001) 2723–2737, https://doi.org/10.1016/S1359-6454(01)00172-0.

[55] S. Kaßbohm, W.H. Müller, R. Feßler, Improved approximations of Fourier coefficients for computing periodic structures with arbitrary stiffness distribution, Comput. Mater. Sci. 37 (1–2) (2006) 90–93, https://doi.org/10.1016/j.commatsci.2005.12.010.

[56] J. Spahn, H. Andrä, M. Kabel, R. Müller, A multiscale approach for modeling progressive damage of composite materials using fast Fourier transforms, Comp. Meth. Appl. Mech. Eng. 268 (2014) 871–883, https://doi.org/10.1016/j.cma.2013.10.017.

[57] P. Eisenlohr, M. Diehl, R.A. Lebensohn, F. Roters, A spectral method solution to crystal elasto-viscoplasticity at finite strains, Int. J. Plast. 46 (2013) 37–53, https://doi.org/10.1016/j.ijplas.2012.09.012.

[58] F. Willot, Fourier-based schemes for computing the mechanical response of composites with accurate local fields, Comptes Rendus Mécanique 343 (3) (2015) 232–245, https://doi.org/10.1016/j.crme.2014.12.005.

[59] T.W.J. De Geus, J. Vondřejc, J. Zeman, R.H.J. Peerlings, M.G.D. Geers, Finite strain FFT-based non-linear solvers made simple, Comp. Meth. Appl. Mech. Eng. 318 (2017) 412–430, https://doi.org/10.1016/j.cma.2016.12.032.

[60] R. Courant, Variational methods for the solution of problems of equilibrium and vibrations, Bull. Am. Math. Soc. 49 (1) (1943) 1–23, https://doi.org/10.1090/S0002-9904-1943-07818-4.

[61] O.C. Zienkiewicz, The Finite Element Method in Structural and Continuum Mechanics, McGraw-Hill, New York, 1967.

[62] K.-J. Bathe, Finite Element Procedures, 2014, ISBN 978-0-9790049-5-7 http://web.mit.edu/kjb/www/Books/FEP_2nd_Edition_4th_Printing.pdf.

[63] O.C. Zienkiewicz, R.L. Taylor, J.Z. Zhu, The Finite Element Method: Its Basis and Fundamentals, seventh ed., Butterworth-Heinemann, Oxford, 978-1-85617-633-0, 2013, https://doi.org/10.1016/B978-1-85617-633-0.00019-8.

[64] D.D. Tjahjanto, Micromechanical Modeling and Simulations of Transformation-Induced Plasticity in Multiphase Carbon Steels, PhD thesis, TU Delft, 2008 http://resolver.tudelft.nl/uuid:32a7ae08-96fe-4f0e-baf3-1af379580708.

[65] A. Ma, F. Roters, D. Raabe, A dislocation density based constitutive model for crystal plasticity FEM including geometrically necessary dislocations, Acta Mater. 54 (8) (2006) 2169–2179, https://doi.org/10.1016/j.actamat.2006.01.005.

[66] J. Michel, H. Moulinec, P. Suquet, Effective properties of composite materials with periodic microstructure: a computational approach, Comp. Meth. Appl. Mech. Eng. 172 (1–4) (1999) 109–143, https://doi.org/10.1016/S0045-7825(98)00227-8.

[67] F. Grennerat, M. Montagnat, O. Castelnau, P. Vacher, H. Moulinec, P. Suquet, P. Duval, Experimental characterization of the intragranular strain field in columnar ice during transient creep, Acta Mater. 60 (8) (2012) 3655–3666, https://doi.org/10.1016/j.actamat.2012.03.025.

[68] R.A. Lebensohn, A. Needleman, Numerical implementation of non-local polycrystal plasticity using fast Fourier transforms, J. Mech. Phys. Solids 97 (2016) 333–351, https://doi.org/10.1016/j.jmps.2016.03.023.

[69] N. Lahellec, J.C. Michel, H. Moulinec, and P. Suquet, Analysis of inhomogeneous materials at large strains using fast Fourier transforms, in: C. Miehe (Ed.), IUTAM Symposium on Computational Mechanics of Solid Materials at Large Strains, Solid Mechanics and its Applications, vol. 108, Kluwer Academic Publishers; Dordrecht, 2001, pp. 247–258. ISBN 978-90-481-6239-0, https://doi.org/10.1007/978-94-017-0297-3_22.

[70] J. Zeman, T.W.J. De Geus, J. Vondřejc, R.H.J. Peerlings, M.G.D. Geers, A finite element perspective on non-linear FFT-based micromechanical simulations, Int. J. Numer. Meth. Eng. 111 (10) (2016) 903–926, https://doi.org/10.1002/nme.5481.

[71] D.J. Eyre, G.W. Milton, A fast numerical scheme for computing the response of composites using grid refinement, Euro. Phys. J.-Appl. Phys. 6 (1) (1999) 41–47, https://doi.org/10.1051/epjap:1999150.

[72] J.C. Michel, H. Moulinec, P. Suquet, A computational scheme for linear and non-linear composites with arbitrary phase contrast, Int. J. Numer. Meth. Eng. 52 (12) (2001) 139–160, https://doi.org/10.1002/nme.275.

[73] S. Brisard, L. Dormieux, FFT-based methods for the mechanics of composites: a general variational framework, Comput. Mater. Sci. 49 (3) (2010) 663–671, https://doi.org/10.1016/j.commatsci.2010.06.009.

[74] J. Zeman, J. Vondřejc, J. Novák, I. Marek, Accelerating a FFT-based solver for numerical homogenization of periodic media by conjugate gradients, J. Comput. Phys. 229 (21) (2010) 8065–8071, https://doi.org/10.1016/j.jcp.2010.07.010.

[75] V. Monchiet, G. Bonnet, A polarization-based FFT iterative scheme for computing the effective properties of elastic composites with arbitrary contrast, Int. J. Numer. Meth. Eng. 89 (11) (2012) 1419–1436, https://doi.org/10.1002/nme.3295.

[76] P. Shanthraj, P. Eisenlohr, M. Diehl, F. Roters, Numerically robust spectral methods for crystal plasticity simulations of heterogeneous materials, Int. J. Plast. 66 (2015) 31–45, https://doi.org/10.1016/j.ijplas.2014.02.006.

[77] M. Schneider, D. Merkert, M. Kabel, FFT-based homogenization for microstructures discretized by linear hexahedral elements, Int. J. Numer. Meth. Eng. 109 (10) (2016) 1461–1489, https://doi.org/10.1002/nme.5336.

[78] J.D. Eshelby, The determination of the elastic field of an ellipsoidal inclusion, and related problems, Proc. R. Soc. A: Math., Phys. Eng. Sci. 241 (1226) (1957) 376–396, https://doi.org/10.1098/rspa.1957.0133.

[79] T. Mura, Micromechanics of Defects in Solids, second ed., Martinus Nijhoff Publishers, Dordrecht, 978-94-009-3489-4, 1987, https://doi.org/10.1007/978-94-009-3489-4.

[80] M. Frigo, S.G. Johnson, The Design and Implementation of FFTW3, Proc. IEEE 93 (2) (2005) 216–231, https://doi.org/10.1109/JPROC.2004.840301.

[81] D. Gottlieb, C-W Shu, On the Gibbs phenomenon and its resolution, SIAM Rev. 39 (4) (1997) 644–668, https://doi.org/10.1137/S0036144596301390.

[82] A. Gelb, S. Gottlieb, The resolution of the Gibbs phenomenon for fourier spectral methods, in: A..J. Jerri (Ed.), Advances in the Gibbs Phenomenon, Sigma Sampling Publishers; Potsdam, 2008. ISBN 0-9673301-4-9.

[83] A. Vidyasagar, W.L. Tan, D.M. Kochmann, Predicting the effective response of bulk polycrystalline ferroelectric ceramics via improved spectral phase field methods, J. Mech. Phys. Solids 106 (2017) 133–151, https://doi.org/10.1016/j.jmps.2017.05.017.

[84] M. Schneider, F. Ospald, M. Kabel, Computational homogenization of elasticity on a staggered grid, Int. J. Numer. Meth. Eng. 105 (9) (2015) 693–720, https://doi.org/10.1002/nme.5008.

[85] M. Kabel, S. Fliegener, M. Schneider, Mixed boundary conditions for FFT-based homogenization at finite strains, Comput. Mater. Sci. 57 (2) (2016) 193–210, https://doi.org/10.1007/s00466-015-1227-1.

[86] H. Moulinec, P. Suquet, A numerical method for computing the overall response of nonlinear composites with complex microstructure, Comp. Meth. Appl. Mech. Eng. 157 (1–2) (1998) 69–94, https://doi.org/10.1016/S0045-7825(97)00218-1.

[87] L. Gélébart, R. Mondon-Cancel, Non-linear extension of FFT-based methods accelerated by conjugate gradients to evaluate the mechanical behavior of composite materials, Comput. Mater. Sci. 77 (2013) 430–439, https://doi.org/10.1016/j.commatsci.2013.04.046.

[88] C.T. Kelley, Iterative Methods for Linear and Nonlinear Equations, Frontiers in Applied Mathematics, vol. 16, Society for Industrial and Applied Mathematics, Philadelphia, 1995, ISBN 978-0-89871-352-7, https://doi.org/10.1137/1.9781611970944.

[89] C.W. Oosterlee, T. Washio, Krylov subspace acceleration of nonlinear multigrid with application to recirculating flows, SIAM J. Scient. Comput. 21 (5) (2000) 1670–1690, https://doi.org/10.1137/S1064827598338093.

[90] Y. Chen, C. Shen, A Jacobian-Free Newton-GMRES(m) method with adaptive preconditioner and its application for power flow calculations, IEEE Trans. Power Syst. 21 (3) (2006) 1096–1103, https://doi.org/10.1109/TPWRS.2006.876696.

[91] S. Balay, J. Brown, K. Buschelman, V. Eijkhout, W.D. Gropp, D. Kaushik, M.G. Knepley, L.C. McInnes, B.F. Smith, H. Zhang, PETSc Users Manual, Argonne National Laboratory, 2013.

[92] H.J. Bunge, Texture Analysis in Materials Science, Butterworth, London, 978-0-408-10642-9, 1982, https://doi.org/10.1016/B978-0-408-10642-9.50018-0.
[93] R. Hielscher, H. Schaeben, A novel pole figure inversion method: specification of the MTEX algorithm, J. Appl. Crystal. 41 (6) (2008) 1024–1037, https://doi.org/10.1107/S0021889808030112.
[94] U.F. Kocks, C.N. Tomé, H.-R. Wenk, Texture and Anisotropy: Preferred Orientations in Polycrystals and Their Effect on Materials Properties, Cambridge University Press, Cambridge, 978-0-521-79420-6, 2000.
[95] H-R Wenk, P. Van Houtte, Texture and anisotropy, Rep. Prog. Phys. 67 (8) (2004) 1367–1428, https://doi.org/10.1088/0034-4885/67/8/R02.
[96] L.S. Tóth, P. Van Houtte, Discretization techniques for orientation distribution functions, Text. Microstruct. 19 (4) (1992) 229–244, https://doi.org/10.1155/TSM.19.229.
[97] P. Eisenlohr, F. Roters, Selecting sets of discrete orientations for accurate texture reconstruction, Comput. Mater. Sci. 42 (4) (2008) 670–678, https://doi.org/10.1016/j.commatsci.2007.09.015.
[98] W. Voigt, Über die Beziehung zwischen den beiden Elastizitätskonstanten isotroper Körper, Annalen der Physik 38 (1889) 573–587, https://doi.org/10.1002/andp.18892741206.
[99] A. Reuss, Berechnung der Fließgrenze von Mischkristallen auf Grund der Plastizitätsbedingung für Einkristalle, Z. Angew. Math. Mech. 9 (1) (1929) 49–58, https://doi.org/10.1002/zamm.19290090104.
[100] G.I. Taylor, Plastic strain in metals, J. Inst. Metals 62 (1938) 307–324.
[101] G. Sachs, Mitteilungen der deutschen Materialprüfungsanstalten, chapter Zur Ableitung einer Fließbedingung, Springer, Berlin, Germany, 1929, pp. 94–97, https://doi.org/10.1007/978-3-642-92045-5_12.
[102] P. Van Houtte, L. Delannay, I. Samajdar, Quantitative prediction of cold rolling textures in low-carbon steel by means of the LAMEL model, Text. Microstruct. 8–9 (1999) 109–149, https://doi.org/10.1155/TSM.31.109.
[103] P. Van Houtte, S. Li, M. Seefeldt, L. Delannay, Deformation texture prediction: from the Taylor model to the advanced Lamel model, Int. J. Plast. 21 (3) (2005) 589–624, https://doi.org/10.1016/j.ijplas.2004.04.011.
[104] M. Crumbach, M. Goerdeler, G. Gottstein, Modelling of recrystallisation textures in aluminium alloys: I. Model set-up and integration, Acta Mater. 54 (12) (2006) 3275–3289, https://doi.org/10.1016/j.actamat.2006.03.017.
[105] D.D. Tjahjanto, P. Eisenlohr, F. Roters, A novel grain cluster-based homogenization scheme, Model. Simul. Mater. Sci. Eng. 18 (1) (2010) 015006, https://doi.org/10.1088/0965-0393/18/1/015006.
[106] R.A. Lebensohn, C.N. Tomé, A study of the stress state associated with twin nucleation and propagation in anisotropic materials, Philos. Magaz. A 67 (1) (1993) 187–206, https://doi.org/10.1080/01418619308207151.
[107] J. Gawad, A. Van Bael, P. Eyckens, G. Samaey, P. Van Houtte, D. Roose, Hierarchical multi-scale modeling of texture induced plastic anisotropy in sheet forming, Comput. Mater. Sci. 66 (2013) 65–83, https://doi.org/10.1016/j.commatsci.2012.05.056.
[108] R.J.M. Smit, W.A.M. Brekelmans, H.E.H. Meijer, Prediction of the mechanical behavior of nonlinear heterogeneous systems by multi-level finite element modeling, Comp. Meth. Appl. Mech. Eng. 155 (1–2) (1998) 181–192, https://doi.org/10.1016/S0045-7825(97)00139-4.
[109] C. Miehe, J. Schotte, J. Schröder, Computational micro-macro transitions and overall moduli in the analysis of polycrystals at large strains, Comput. Mater. Sci. 16 (1–4) (1999) 372–382, https://doi.org/10.1016/S0927-0256(99)00080-4.
[110] F. Feyel, J.L. Chaboche, FE^2 multiscale approach for modelling the elastoviscoplastic behaviour of long fibre SiC/Ti composite materials, Comp. Meth. Appl. Mech. Eng. 183 (3–4) (2000) 309–330, https://doi.org/10.1016/S0045-7825(99)00224-8.
[111] M.V. Upadhyay, J. Capek, S. Van Petegem, R.A. Lebensohn, H. Van Swygenhoven, Intergranular strain evolution during biaxial loading: a multiscale FE-FFT approach, JOM 69 (5) (2017) 839–847, https://doi.org/10.1007/s11837-017-2299-5.
[112] D.D. Tjahjanto, P. Eisenlohr, F. Roters, Relaxed Grain Cluster (RGC) homogenization scheme, Int. J. Mater. Form. 2 (1) (2009) 939–942, https://doi.org/10.1007/s12289-009-0619-1.
[113] M. Crumbach, M. Goerdeler, G. Gottstein, Modelling of recrystallisation textures in aluminium alloys: II. Model performance and experimental validation, Acta Mater. 54 (12) (2006) 3291–3306, https://doi.org/10.1016/j.actamat.2006.03.019.
[114] L. Delannay, S.R. Kalidindi, P. Van Houtte, Quantitative prediction of textures in aluminium cold rolled to moderate strains, Mater. Sci. Eng. A 336 (1–2) (2002) 233–244, https://doi.org/10.1016/S0921-5093(01)01966-9.
[115] P. Van Houtte, L. Delannay, S.R. Kalidindi, Comparison of two grain interaction models for polycrystal plasticity and deformation texture prediction, Int. J. Plast. 18 (3) (2002) 359–377, https://doi.org/10.1016/S0749-6419(00)00102-9.
[116] P. Eisenlohr, D.D. Tjahjanto, T. Hochrainer, F. Roters, D. Raabe, Texture prediction from a novel grain cluster-based homogenization scheme, Int. J. Mater. Form. 2 (1) (2009) 523–526, https://doi.org/10.1007/s12289-009-0561-2.
[117] J.F. Nye, Some geometrical relations in dislocated crystals, Acta Metal. 1 (2) (1953) 153–162, https://doi.org/10.1016/0001-6160(53)90054-6.
[118] B.A. Bilby, Types of dislocation source, in: Defects in Crystalline Solids, Report of the Conference of the International Union of Physics, The Physical Society, London, 1955, pp. 124–133.
[119] B.A. Bilby, R. Bullough, E. Smith, Continuous distributions of dislocations: a new application of the methods of non-Riemannian geometry, Proc. R. Soc. A: Math., Phys. Eng. Sci. 231 (1185) (1955) 263–273, https://doi.org/10.1098/rspa.1955.0171.
[120] M.E. Gurtin, A gradient theory of single-crystal viscoplasticity that accounts for geometrically necessary dislocations, J. Mech. Phys. Solids 50 (1) (2002) 5–32, https://doi.org/10.1016/S0022-5096(01)00104-1.
[121] L.P. Evers, D.M. Parks, W.A.M. Brekelmans, M.G.D. Geers, Crystal plasticity model with enhanced hardening by geometrically necessary dislocation accumulation, J. Mech. Phys. Solids 50 (11) (2002) 2403–2424, https://doi.org/10.1016/S0022-5096(02)00032-7.
[122] S. Turteltaub, A.S.J. Suiker, Transformation-induced plasticity in ferrous alloys, J. Mech. Phys. Solids 53 (8) (2005) 1747–1788, https://doi.org/10.1016/j.jmps.2005.03.004.
[123] P. Shanthraj, B. Svendsen, L. Sharma, F. Roters, D. Raabe, Elasto-viscoplastic phase field modelling of anisotropic cleavage fracture, J. Mech. Phys. Solids 99 (2017) 19–34, https://doi.org/10.1016/j.jmps.2016.10.012.
[124] C. Kords, On the Role of Dislocation Transport in the Constitutive Description of Crystal Plasticity, PhD thesis, RWTH Aachen, Berlin, 2013 http://darwin.bth.rwth-aachen.de/opus3/volltexte/2014/4862/.
[125] S.R. Kalidindi, C.A. Bronkhorst, L. Anand, Crystallographic texture evolution in bulk deformation processing of fcc metals, J. Mech. Phys. Solids 40 (3) (1992) 537–569, https://doi.org/10.1016/0022-5096(92)80003-9.
[126] J.R. Cash, A.H. Karp, A variable order Runge-Kutta method for initial value problems with rapidly varying right-hand sides, ACM Trans. Math. Softw. 16 (3) (1990) 201–222, https://doi.org/10.1145/79505.79507.
[127] F. Meier, C. Schwarz, E. Werner, Numerical calculation of the tangent stiffness matrix in materials modeling, Pamm 14 (1) (2014) 425–426, https://doi.org/10.1002/pamm.201410200.
[128] E. Schmid, W. Boas, Kristallplastizität, Springer, Berlin, Heidelberg, 978-3-662-34261-9, 1935, https://doi.org/10.1007/978-3-662-34532-0.
[129] S.R. Kalidindi, Incorporation of deformation twinning in crystal plasticity models, J. Mech. Phys. Solids 46 (2) (1998) 267–271, https://doi.org/10.1016/S0022-5096(97)00051-3.
[130] S.R. Kalidindi, Modeling anisotropic strain hardening and deformation textures in low stacking fault energy fcc metals, Int. J. Plast. 17 (6) (2001) 837–860, https://doi.org/10.1016/S0749-6419(00)00071-1.
[131] H. Mark, M. Polanyi, E. Schmid, Vorgänge bei der Dehnung von Zinkkristallen. I. Mitteilung: Allgemeine Beschreibung der Erscheinungen und Untersuchungsmethoden, Zeitschrift für Physik 12 (1) (1923) 58–77, https://doi.org/10.1007/BF01328082.
[132] H. Mark, M. Polanyi, E. Schmid, Vorgänge bei der Dehnung von Zinkkristallen. II. Mitteilung. Quantitative Festlegung des Dehnungsmechanismus, Zeitschrift für Physik 12 (1) (1923) 78–110, https://doi.org/10.1007/BF01328083.
[133] E. Siebel, Über die Kaltverformung kristallin bildsamer Körper, Zeitschrift für Physik 20 (1) (1923) 45–53, https://doi.org/10.1007/BF01327918.
[134] E. Schmid, Bemerkungen über die plastische Deformation von Kristallen, Zeitschrift für Physik 22 (1) (1924) 328–333, https://doi.org/10.1007/BF01328138.
[135] E. Schmid, Neuere Untersuchungen an Metallkristallen, in: C.B. Biezeno, J.M. Burgers (Eds.), Proceedings of the 1st International Congress for Applied Mechanics, Delft, The Netherlands, 1925, pp, 342–353 (Technische Boekhandel en Drukkerij J. Waltman Jr).
[136] J.W. Christian, Some surprising features of the plastic deformation of the body-centered cubic metals and alloys, Metall. Trans. A 14 (7) (1983) 1237–1256, https://doi.org/10.1007/BF02664806.
[137] R. Gröger, V. Vitek, Breakdown of the Schmid law in bcc molybdenum related to the effect of shear stress perpendicular to the slip direction, Mat. Sci. Forum 482 (2005) 123–126, https://doi.org/10.4028/www.scientific.net/MSF.482.123.
[138] D. Caillard, Kinetics of dislocations in pure Fe. Part I. In situ straining experiments at room temperature, Acta Mater. 58 (9) (2010) 3493–3503, https://doi.org/10.1016/j.actamat.2010.02.023.
[139] H. Lim, C.R. Weinberger, C.C. Battaile, T.E. Buchheit, Application of generalized non-Schmid yield law to low-temperature plasticity in bcc transition metals, Model. Simul. Mater. Sci. Eng. 21 (4) (2013) 045015, https://doi.org/10.1088/0965-0393/21/4/045015.
[140] D. Peirce, R.J. Asaro, A. Needleman, Material rate dependence and localized deformation in crystalline solids, Acta Metal. 31 (12) (1983) 1951–1976, https://doi.org/10.1016/0001-6160(83)90014-7.
[141] J.W. Hutchinson, Bounds and self-consistent estimates for creep of polycrystalline materials, Proc. R. Soc. A: Math., Phys. Eng. Sci. 348 (1652) (1976) 101–127, https://doi.org/10.1098/rspa.1976.0027.
[142] T-Y Wu, J.L. Bassani, C. Laird, Latent hardening in single crystals I. Theory and experiments, Proc. R. Soc. A: Math., Phys. Eng. Sci. 435 (1893) (1991) 1–19, https://doi.org/10.1098/rspa.1991.0127.
[143] J.L. Bassani, T-Y Wu, Latent hardening in single crystals II. Analytical characterization and predictions, Proc. R. Soc. A: Math., Phys. Eng. Sci. 435 (1893) (1991) 21–41, https://doi.org/10.1098/rspa.1991.0128.
[144] A. Ma, F. Roters, A constitutive model for fcc single crystals based on dislocation densities and its application to uniaxial compression of aluminium single crystals, Acta Mater. 52 (12) (2004) 3603–3612, https://doi.org/10.1016/j.actamat.2004.04.012.
[145] F. Roters, D. Raabe, G. Gottstein, Work hardening in heterogeneous alloys – a microstructural approach based on three internal state variables, Acta Mater. 48 (17) (2000) 4181–4189, https://doi.org/10.1016/S1359-6454(00)00289-5.
[146] A. Ma, F. Roters, D. Raabe, A dislocation density based constitutive law for BCC materials in crystal plasticity FEM, Comput. Mater. Sci. 39 (1) (2007) 91–95, https://doi.org/10.1016/j.commatsci.2006.04.014.
[147] N. Jia, F. Roters, P. Eisenlohr, C. Kords, D. Raabe, Non-crystallographic shear banding in crystal plasticity FEM simulations: example of texture evolution in α-brass, Acta Mater. 60 (3) (2012) 1099–1115, https://doi.org/10.1016/j.actamat.2011.10.047.

[148] N. Jia, P. Eisenlohr, F. Roters, D. Raabe, X. Zhao, Orientation dependence of shear banding in face-centered-cubic single crystals, Acta Mater. 60 (8) (2012) 3415–3434, https://doi.org/10.1016/j.actamat.2012.03.005.
[149] E. Orowan, Zur Kristallplastizität I–III, Zeitschrift für Physik 89 (1934) 605–659, https://doi.org/10.1007/BF01341478.
[150] U.F. Kocks, A.S. Argon, M.F. Ashby, Thermodynamics and Kinetics of Slip, Pergamon Press, Braunschweig, 978-0-08-017964-3, 1975.
[151] S. Queyreau, G. Monnet, B. Devincre, Slip systems interactions in alpha-iron determined by dislocation dynamics simulations, Int. J. Plast. 25 (2) (2009) 361–377, https://doi.org/10.1016/j.ijplas.2007.12.009.
[152] B. Devincre, Dislocation dynamics simulations of slip systems interactions and forest strengthening in ice single crystal, Philos. Magaz. 93 (1–3) (2013) 235–246, https://doi.org/10.1080/14786435.2012.699689.
[153] B. Devincre, L. Kubin, T. Hoc, Physical analyses of crystal plasticity by DD simulations, Scripta Mater. 54 (5) (2006) 741–746, https://doi.org/10.1016/j.scriptamat.2005.10.066.
[154] N. Bertin, C.N. Tomé, I.J. Beyerlein, M.R. Barnett, L. Capolungo, On the strength of dislocation interactions and their effect on latent hardening in pure Magnesium, Int. J. Plast. 62 (2014) 72–92, https://doi.org/10.1016/j.ijplas.2014.06.010.
[155] W. Blum, P. Eisenlohr, Dislocation mechanics of creep, Mater. Sci. Eng. A 510-511 (2009) 7–13, https://doi.org/10.1016/j.msea.2008.04.110.
[156] G. Gottstein, Physical Foundations of Material Science, Springer, Berlin, Germany, 978-3-642-07271-0, 2004, https://doi.org/10.1007/978-3-662-09291-0.
[157] R. Gröger, V. Vitek, Multiscale modeling of plastic deformation of molybdenum and tungsten. III. Effects of temperature and plastic strain rate, Acta Mater. 56 (19) (2008) 5426–5439, https://doi.org/10.1016/j.actamat.2008.07.027.
[158] V. Vitek, Core structure of screw dislocations in body-centred cubic metals: relation to symmetry and interatomic bonding, Philos. Magaz. 84 (3–5) (2004) 415–428, https://doi.org/10.1080/14786430310001611644.
[159] S. Wurster, B. Gludovatz, R. Pippan, High temperature fracture experiments on tungsten–rhenium alloys, Int. J. Refract. Metals Hard Mater. 28 (6) (2010) 692–697, https://doi.org/10.1016/j.ijrmhm.2010.03.002.
[160] A. Stukowski, D. Cereceda, T.D. Swinburne, J. Marian, Thermally-activated non-Schmid glide of screw dislocations in W using atomistically-informed kinetic Monte Carlo simulations, Int. J. Plast. 65 (2015) 108–130, https://doi.org/10.1016/j.ijplas.2014.08.015.
[161] V.V. Bulatov, O. Richmond, M.V. Glazov, An atomistic dislocation mechanism of pressure-dependent plastic flow in aluminum, Acta Mater. 47 (12) (1999) 3507–3514, https://doi.org/10.1016/S1359-6454(99)00154-8.
[162] R. Gröger, A.G. Bailey, V. Vitek, Multiscale modeling of plastic deformation of molybdenum and tungsten: I. Atomistic studies of the core structure and glide of 1/2 ⟨1 1 1⟩ screw dislocations at 0K, Acta Mater. 56 (19) (2008) 5401–5411, https://doi.org/10.1016/j.actamat.2008.07.018.
[163] R. Gröger, V. Racherla, J.L. Bassani, V. Vitek, Multiscale modeling of plastic deformation of molybdenum and tungsten: II. Yield criterion for single crystals based on atomistic studies of glide of 1/2 ⟨1 1 1⟩ screw dislocations, Acta Mater. 56 (19) (2008) 5412–5425, https://doi.org/10.1016/j.actamat.2008.07.037.
[164] S. Plimpton, Fast parallel algorithms for short-range molecular dynamics, J. Comput. Phys. 117 (1) (1995) 1–19, https://doi.org/10.1006/jcph.1995.1039.
[165] D. Cereceda, M. Diehl, F. Roters, D. Raabe, J.M. Perlado, J. Marian, Unraveling the temperature dependence of the yield strength in single-crystal tungsten using atomistically-informed crystal plasticity calculations, Int. J. Plast. 78 (2016) 242–265, https://doi.org/10.1016/j.ijplas.2015.09.002.
[166] N.A. Fleck, J.W. Hutchinson, Strain gradient plasticity, Adv. Appl. Mech. 33 (1997) 295–361, https://doi.org/10.1016/S0065-2156(08)70388-0.
[167] A. Acharya, J.L. Bassani, Lattice incompatibility and a gradient theory of crystal plasticity, J. Mech. Phys. Solids 48 (8) (2000) 1565–1595, https://doi.org/10.1016/S0022-5096(99)00075-7.
[168] A. Arsenlis, D.M. Parks, R. Becker, V.V. Bulatov, On the evolution of crystallographic dislocation density in non-homogeneously deforming crystals, J. Mech. Phys. Solids 52 (6) (2004) 1213–1246, https://doi.org/10.1016/j.jmps.2003.12.007.
[169] C. Reuber, P. Eisenlohr, F. Roters, D. Raabe, Dislocation density distribution around an indent in single-crystalline nickel: comparing nonlocal crystal plasticity finite element predictions with experiments, Acta Mater. 71 (2014) 333–348, https://doi.org/10.1016/j.actamat.2014.03.012.
[170] E. Kröner, Kontinuumstheorie der Versetzungen und Eigenspannungen, Springer, Berlin, 978-3-540-02261-9, 1958.
[171] W.S. Farren, G.I. Taylor, The heat developed during plastic extension of metals, Proc. R. Soc. A: Math., Phys. Eng. Sci. 107 (743) (1925) 422–451, https://doi.org/10.1098/rspa.1925.0034.
[172] G.I. Taylor, H. Quinney, The latent energy remaining in a metal after cold working, Proc. R. Soc. A: Math., Phys. Eng. Sci. 143 (849) (1934) 307–326, https://doi.org/10.1098/rspa.1934.0004.
[173] A. Alankar, P. Eisenlohr, D. Raabe, A dislocation density-based crystal plasticity constitutive model for prismatic slip in α-titanium, Acta Mater. 59 (18) (2011) 7003–7009, https://doi.org/10.1016/j.actamat.2011.07.053.
[174] A. Nonn, A.C. Cerrone, C. Stallybrass, H. Meuser, Microstructure-based modeling of high-strength linepipe steels, in: 6th International Pipeline Technology Conference, 2013, https://doi.org/10.13140/2.1.2797.4404.
[175] O. Güvenc, T. Henke, G. Laschet, B. Böttger, M. Apel, M. Bambach, G. Hirt, Modeling of static recrystallization kinetics by coupling crystal plasticity FEM and multiphase field calculations, Comp. Meth. Mater. Sci. 13 (2) (2013) http://www.cmms.agh.edu.pl/repo_file.php?f_id=456.
[176] M. Demura, D. Raabe, F. Roters, P. Eisenlohr, Y. Xu, T. Hirano, K. Kishida, Slip system analysis in the cold rolling of a Ni_3Al single crystal, Mater. Sci. Forum 783–786 (2014) 1111–1116, https://doi.org/10.4028/www.scientific.net/MSF.783-786.1111.
[177] R. Kebriaei, I.N. Vladimirov, S. Reese, Joining of the alloys AA1050 and AA5754—Experimental characterization and multiscale modeling based on a cohesive zone element technique, J. Mater. Process. Technol. 214 (10) (2014) 2146–2155, https://doi.org/10.1016/j.jmatprotec.2014.03.014.
[178] A. Yamanaka, Prediction of 3D microstructure and plastic deformation behavior in dual-phase steel using multi-phase field and crystal plasticity FFT methods, Key Eng. Mater. 651–653 (2015) 570–574, https://doi.org/10.4028/www.scientific.net/KEM.651-653.570.
[179] A. Yamanaka, Prediction of deformed- and recrystallized microstructures in metallic materials by crystal plasticity analysis and multi-phase-field method, J. Japan Inst. Light Metals 65 (11) (2015) 542–548, https://doi.org/10.2464/jilm.65.542.
[180] Y.F. Shen, N. Jia, Y.D. Wang, X. Sun, L. Zuo, D. Raabe, Suppression of twinning and phase transformation in an ultrafine grained 2 GPa strong metastable austenitic steel: experiment and simulation, Acta Mater. 97 (2015) 305–315, https://doi.org/10.1016/j.actamat.2015.06.053.
[181] B. Berisha, C. Raemy, C. Becker, M. Gorji, P. Hora, Multiscale modeling of failure initiation in a ferritic–pearlitic steel, Acta Mater. 100 (2015) 191–201, https://doi.org/10.1016/j.actamat.2015.08.035.
[182] D. Mercier, C. Zambaldi, T.R. Bieler, A Matlab toolbox to analyze slip transfer through grain boundaries, in: Proceedings of the 17th International Conference on Textures of Materials (ICOTOM-17), p. 012090, 2015, https://doi.org/1.1088/1757-899X/82/1/012090.
[183] G. Nayyeri, W.J. Poole, C.W. Sinclair, S. Zaefferer, P.J. Konijnenberg, C. Zambaldi, An instrumented spherical indentation study on high purity magnesium loaded nearly parallel to the c-axis, Mater. Sci. Eng. A 670 (2016) 132–145, https://doi.org/10.1016/j.msea.2016.05.112.
[184] C. Zambaldi, C. Zehnder, D. Raabe, Orientation dependent deformation by slip and twinning in magnesium during single crystal indentation, Acta Mater. 91 (2015) 267–288, https://doi.org/10.1016/j.actamat.2015.01.046.
[185] D. Cereceda, Multiscale Modeling of the Plastic Behaviour in Single Crystal Tungsten: From Atomistic to Crystal Plasticity Simulations, PhD thesis, Universidad Politecnica de Madrid, Madrid, 2015 https://oa.upm.es/36490/.
[186] X. Wu, D. Ma, P. Eisenlohr, D. Raabe, H-O Fabritius, From insect scales to sensor design: modelling the mechanochromic properties of bicontinuous cubic structures, Bioinsp. Biomimet. 11 (4) (2016) 045001, https://doi.org/10.1088/1748-3190/11/4/045001.
[187] P. Jagtap, P. Kumar, Macro and micro-texture study for understanding whisker growth in Sn coatings, in: 2016 IEEE 18th Electronics Packaging Technology Conference (EPTC), Singapore, 2016, pp. 165–170, https://doi.org/10.1109/EPTC.2016.7861464.
[188] S. Balachandran, Effect of Thermomechanical Processing on Microstructure and Microtexture Evolution in Titanium Alloys, PhD thesis, Indian Institute of Science, Bangalore, 2016, https://doi.org/10.13140/RG.2.1.2909.8487.
[189] M. Diehl, P. Shanthraj, P. Eisenlohr, F. Roters, Neighborhood influences on stress and strain partitioning in dual-phase microstructures. An investigation on synthetic polycrystals with a robust spectral-based numerical method, Meccanica 51 (2) (2016) 429–441, https://doi.org/10.1007/s11012-015-0281-2.
[190] Y. Su, C. Zambaldi, D. Mercier, P. Eisenlohr, T.R. Bieler, M.A. Crimp, Quantifying deformation processes near grain boundaries in alpha-titanium using nanoindentation and crystal plasticity modeling, Int. J. Plast. 86 (2016) 170–186, https://doi.org/10.1016/j.ijplas.2016.08.007.
[191] M. Diehl, High-Resolution Crystal Plasticity Simulations, Apprimus Verlag, Aachen, 2016, ISBN 978-3-86359-392-6.
[192] M. Lin, U. Prahl, A parallelized model for coupled phase field and crystal plasticity simulation journal, Comp. Meth. Mater. Sci. 16 (3) (2016) 156–162 http://www.cmms.agh.edu.pl/abstract.php?p_id=584.
[193] Z. Boufaida, J. Boisse, S. André, L. Farge, A Mechanical Study of a Glass Fabric-Thermoplastic Resin Composite: 3D-DIC and X-ray Tomographic Observations Explained by Numerical Simulations Based on a Spectral Solver, 2016 http://arxiv.org/abs/1605.00478v1.
[194] S. Papanikolaou, J. Thibault, C. Woodward, P. Shanthraj, F. Roters, Brittle to Quasi-Brittle Transition and Crack Initiation Precursors in Disordered Crystals, 2017 http://arxiv.org/abs/1707.04332v1.
[195] M. Diehl, M. Groeber, C. Haase, D.A. Molodov, F. Roters, D. Raabe, Identifying structure-property relationships through DREAM.3D representative volume elements and DAMASK crystal plasticity simulations: an integrated computational materials engineering approach, JOM 69 (5) (2017) 848–855, https://doi.org/10.1007/s11837-017-2303-0.
[196] P. Jagtap, A. Chakraborty, P. Eisenlohr, P. Kumar, Identification of whisker grain in Sn coatings by analyzing crystallographic micro-texture using electron backscatter diffraction, Acta Mater. 134 (2017) 346–359, https://doi.org/10.1016/j.actamat.2017.05.063.
[197] A. Chakraborty, P. Eisenlohr, Evaluation of an inverse methodology for estimating constitutive parameters in face-centered cubic materials from single crystal indentations, Euro. J. Mech./A Solids 66 (2017) 114–124, https://doi.org/10.1016/j.euromechsol.2017.06.012.
[198] M. Isaenkova, Y. Perlovich, D. Zhuk, O. Krymskaya, Crystal plasticity simulation of Zirconium tube rolling using multi-grain representative volume element, in: AIP Conference Proceedings 1896, 2017, pp. 160023-1–160023-6, https://doi.org/10.1063/1.5008198.
[199] D-F Zhu, S-H Tu, H-Sheng Ma, X-Wang Zhang, A 3D Voronoi and subdivision model for calibration of rock properties, Model. Simul. Mater. Sci. Eng. 25 (8) (2017) 085005, https://doi.org/10.1088/1361-651X/aa8f19.

[200] A. Irastorza-Landa, N. Grilli, H. Van Swygenhoven, Effect of pre-existing immobile dislocations on the evolution of geometrically necessary dislocations during fatigue, Model. Simul. Mater. Sci. Eng. 25 (5) (2017) 055010, https://doi.org/10.1088/1361-651X/aa6e24.
[201] J. Jung, J.I. Yoon, J.G. Kim, M.I. Latypov, J.Y. Kim, H.S. Kim, Continuum understanding of twin formation near grain boundaries of FCC metals with low stacking fault energy, NPJ Comput. Mater. 3 (1) (2017), https://doi.org/10.1038/s41524-017-0023-1.
[202] U. Prahl, M. Lin, M. Weikamp, C. Hueter, D. Schicchi, M. Hunkel, R. Spatschek, Multiscale, coupled chemo-mechanical modeling of bainitic transformation during press hardening, in: P. Mason, C.R. Fisher, R. Glamm, M.V. Manuel, G.J. Schmitz, A.K. Singh, A. Strachan (Eds.), Proceedings of the 4th World Congress on Integrated Computational Materials Engineering (ICME 2017), Springer, Cham, 2017, pp. 335–343. ISBN 978-3-319-57863-7, https://doi.org/10.1007/978-3-319-57864-4_31.
[203] K. Balusu, H. Huang, A CPFEM investigation of the effect of grain orientation on the surface profile during tensile plastic deformation of fcc polycrystals, in: ASME 2017 International Mechanical Engineering Congress and Exposition, 2017, pp. V009t12a046, https://doi.org/10.1115/IMECE2017-71763.
[204] T. Shiraiwa, F. Briffod, M. Enoki, Development of integrated framework for fatigue life prediction in welded structures, Eng. Fract. Mech. (2017), https://doi.org/10.1016/j.engfracmech.2017.11.012.
[205] F. Briffod, T. Shiraiwa, M. Enoki, Microstructure modeling and crystal plasticity simulations for the evaluation of fatigue crack initiation in α-iron specimen including an elliptic defect, Mater. Sci. Eng. A 695 (2017) 165–177, https://doi.org/10.1016/j.msea.2017.04.030.
[206] H. Zhang, J. Liu, D. Sui, Z. Cui, M.W. Fu, Study of microstructural grain and geometric size effects on plastic heterogeneities at grain-level by using crystal plasticity modeling with high-fidelity representative microstructures, Int. J. Plast. 100 (2018) 69–89, https://doi.org/10.1016/j.ijplas.2017.09.011.
[207] T. Shiraiwa, F. Briffod, M. Enoki, Uncertainty quantification of fatigue life prediction in welded structures using microstructure-based simulations, in: R.R. Ambriz, D. Jaramillo, G. Plascencia, M. Nait Abdelaziz (Eds.), Proceedings of the 17th International Conference on New Trends in Fatigue and Fracture, Springer, Cham, 2018, pp. 329–334. ISBN 978-3-319-70364-0, https://doi.org/10.1007/978-3-319-70365-7_38.
[208] K.H. Khafagy, T.M. Hatem, S.M. Bedair, Impact of embedded voids on thin-films with high thermal expansion coefficients mismatch, Appl. Phys. Lett. 112 (4) (2018) 042109, https://doi.org/10.1063/1.5011394.
[209] N. Fujita, N. Ishikawa, F. Roters, C.C. Tasan, D. Raabe, Experimental-numerical study on strain and stress partitioning in bainitic steels with martensite-austenite constituents, Int. J. Plast. 104 (2018) 39–53, https://doi.org/10.1016/j.ijplas.2018.01.012.
[210] C. Liu, P. Shanthraj, M. Diehl, F. Roters, S. Dong, J. Dong, W. Ding, D. Raabe, An integrated crystal plasticity-phase field model for spatially resolved twin nucleation, propagation, and growth in hexagonal materials, Int. J. Plast. (2018), https://doi.org/10.1016/j.ijplas.2018.03.009.
[211] M. Madivala, A. Schwedt, S.L. Wong, U. Prahl, F. Roters, W. Bleck, Temperature dependent strain hardening and fracture behavior of TWIP steel, Int. J. Plast. 104 (2018) 80–103, https://doi.org/10.1016/j.ijplas.2018.02.001.
[212] A. Chakkedath, T. Maiti, J. Bohlen, S. Yi, D. Letzig, P. Eisenlohr, C.J. Boehlert, Contraction twinning dominated tensile deformation and subsequent fracture in extruded Mg-1Mn (Wt Pct) at ambient temperature, Metal. Mater. Trans. A 49 (6) (2018) 2441–2454, https://doi.org/10.1007/s11661-018-4557-8.
[213] T. Maiti, A. Chakraborty, P. Eisenlohr, D. Kang, T.R. Bieler, A crystal plasticity study on influence of dislocation mean free path on stage II hardening in Nb single crystals, in: V.R.W. Schaa, Y. He, L. Li, N. Zhao (Eds.), Proceedings of the 18th International Conference on RF Superconductivity (SRF2017), Lanzhou, 2018, pp. 783–786, https://doi.org/10.18429/JACoW-SRF2017-THPB025.
[214] V. Herrera-Solaz, J. LLorca, E. Dogan, I. Karaman, J. Segurado, An inverse optimization strategy to determine single crystal mechanical behavior from polycrystal tests: application to AZ31 Mg alloy, Int. J. Plast. 57 (2014) 1–15, https://doi.org/10.1016/j.ijplas.2014.02.001.
[215] A.S. Keh, Work hardening and deformation sub-structure in iron single crystals deformed in tension at 298 K, Philos. Magaz. 12 (115) (1965) 9–30, https://doi.org/10.1080/14786436508224942.
[216] C. Zambaldi, D. Raabe, Plastic anisotropy of γ-TiAl revealed by axisymmetric indentation, Acta Mater. 58 (9) (2010) 3516–3530, https://doi.org/10.1016/j.actamat.2010.02.025.
[217] J.A. Nelder, R. Mead, A simplex method for function minimization, Comp. J. 7 (4) (1965) 308–313, https://doi.org/10.1093/comjnl/7.4.308.
[218] C.C. Tasan, M. Diehl, D. Yan, C. Zambaldi, P. Shanthraj, F. Roters, D. Raabe, Integrated experimental-numerical analysis of stress and strain partitioning in multi-phase alloys, Acta Mater. 81 (2014) 386–400, https://doi.org/10.1016/j.actamat.2014.07.071.
[219] M.A. Groeber, M.A. Jackson, DREAM.3D: a digital representation environment for the analysis of microstructure in 3D, Integ. Mater. Manuf. Innov. 3 (1) (2014) 5, https://doi.org/10.1186/2193-9772-3-5.
[220] J. Pagenkopf, A. Butz, M. Wenk, D. Helm, Virtual testing of dual-phase steels: effect of martensite morphology on plastic flow behavior, Mater. Sci. Eng. A 674 (2016) 672–686, https://doi.org/10.1016/j.msea.2016.07.118.
[221] E. Werner, T. Siegmund, H. Weinhandl, F.D. Fischer, Properties of random polycrystalline two-phase materials, Appl. Mech. Rev. 47 (1s) (1994) S231–S240, https://doi.org/10.1115/1.3122817.
[222] T. Siegmund, E. Werner, F.D. Fischer, On the thermomechanical deformation behavior of duplex-type materials, J. Mech. Phys. Solids 43 (4) (1995) 495–501, https://doi.org/10.1016/0022-5096(95)00003-2.
[223] U. Liedl, S. Traint, E. Werner, An unexpected feature of the stress-strain diagram of dual-phase steel, Comput. Mater. Sci. 25 (1-2) (2002) 122–128, https://doi.org/10.1016/S0927-0256(02)00256-2.
[224] A. Fillafer, C. Krempaszky, E. Werner, On strain partitioning and micro-damage behavior of dual-phase steels, Mater. Sci. Eng. A 614 (2014) 180–192, https://doi.org/10.1016/j.msea.2014.07.029.
[225] A. Fillafer, E. Werner, C. Krempaszky, On phase transformation induced effects controlling the initial flow behavior of ferritic-martensitic dual-phase steels, Mater. Sci. Eng. A 708 (2017) 556–562, https://doi.org/10.1016/j.msea.2017.10.005.
[226] A. Fillafer, E. Werner, C. Krempaszky, Advances in Mechanics of Materials and Structural Analysis, Chapter On Phase Transformation Induced Effects Controlling the Flow Behavior of Ferritic-Martensitic Dual-Phase Steels, vol. 80, Springer, Cham, 2018, pp. 47–58. ISBN 978-3-319-70562-0, https://doi.org/10.1007/978-3-319-70563-7.
[227] R. Wesenjak, C. Krempaszky, E. Werner, Prediction of forming-limit curves of dual-phase steels based on a multiple length scale modelling approach considering material instabilities, Comput. Mater. Sci. 111 (2016) 277–288, https://doi.org/10.1016/j.commatsci.2015.09.046.
[228] P.J.J. Kok, W. Spanjer, H. Vegter, A microstructure based model for the mechanical behavior of multiphase steels, Key Eng. Mater. 651–653 (2015) 975–980, https://doi.org/10.4028/www.scientific.net/KEM.651-653.975.
[229] S. Yadegari, S. Turteltaub, A.S.J. Suiker, P.J.J. Kok, Analysis of banded microstructures in multiphase steels assisted by transformation-induced plasticity, Comput. Mater. Sci. 84 (2014) 339–349, https://doi.org/10.1016/j.commatsci.2013.12.002.
[230] T. Maiti, P. Eisenlohr, Fourier-based spectral method solution to finite strain crystal plasticity with free surfaces, Scripta Mater. 145 (2018) 37–40, https://doi.org/10.1016/j.scriptamat.2017.09.047.
[231] D. Raabe, M. Sachtleber, Z. Zhao, F. Roters, S. Zaefferer, Micromechanical and macromechanical effects in grain scale polycrystal plasticity experimentation and simulation, Acta Mater. 49 (17) (2001) 3433–3441, https://doi.org/10.1016/S1359-6454(01)00242-7.
[232] J.W. Kysar, Y. Saito, M.S. Oztop, D. Lee, W.T. Huh, Experimental lower bounds on geometrically necessary dislocation density, Int. J. Plast. 26 (8) (2010) 1097–1123, https://doi.org/10.1016/j.ijplas.2010.03.009.
[233] D. Raabe, D. Ma, F. Roters, Effects of initial orientation, sample geometry and friction on anisotropy and crystallographic orientation changes in single crystal microcompression deformation: a crystal plasticity finite element study, Acta Mater. 55 (13) (2007) 4567–4583, https://doi.org/10.1016/j.actamat.2007.04.023.
[234] R. Maaß, S. Van Petegem, D. Ma, J. Zimmermann, D. Grolimund, F. Roters, H. Van Swygenhoven, D. Raabe, Smaller is stronger: the effect of strain hardening, Acta Mater. 57 (20) (2009) 5996–6005, https://doi.org/10.1016/j.actamat.2009.08.024.
[235] D. Raabe, Z. Zhao, S-J Park, F. Roters, Theory of orientation gradients in plastically strained crystals, Acta Mater. 50 (2) (2002) 421–440, https://doi.org/10.1016/S1359-6454(01)00323-8.
[236] D. Ma, P. Eisenlohr, P. Shanthraj, M. Diehl, F. Roters, D. Raabe, Analytical bounds of in-plane Young's modulus and full-field simulations of two-dimensional monocrystalline stochastic honeycomb structures, Comput. Mater. Sci. 109 (2015) 323–329, https://doi.org/10.1016/j.commatsci.2015.07.041.
[237] D. Ma, P. Eisenlohr, E. Epler, C.A. Volkert, P. Shanthraj, M. Diehl, F. Roters, D. Raabe, Crystal plasticity study of monocrystalline stochastic honeycombs under in-plane compression, Acta Mater. 103 (2016) 796–808, https://doi.org/10.1016/j.actamat.2015.11.016.
[238] J. Hirsch, K. Lücke, Overview no. 76: Mechanism of deformation and development of rolling textures in polycrystalline f.c.c. metals–I. Description of rolling texture development in homogeneous CuZn alloys, Acta Metal. 36 (11) (1988) 2863–2882, https://doi.org/10.1016/0001-6160(88)90172-1.
[239] H. Paul, A. Morawiec, J.H. Driver, E. Bouzy, On twinning and shear banding in a Cu–8 at.% Al alloy plane strain compressed at 77 K, Int. J. Plast. 25 (8) (2009) 1588–1608, https://doi.org/10.1016/j.ijplas.2008.10.003.
[240] L. Anand, C. Su, A theory for amorphous viscoplastic materials undergoing finite deformations, with application to metallic glasses, J. Mech. Phys. Solids 53 (6) (2005) 1362–1396, https://doi.org/10.1016/j.jmps.2004.12.006.
[241] N. Jia, F. Roters, P. Eisenlohr, D. Raabe, X. Zhao, Simulation of shear banding in heterophase co-deformation: example of plane strain compressed Cu–Ag and Cu–Nb metal matrix composites, Acta Mater. 61 (12) (2013) 4591–4606, https://doi.org/10.1016/j.actamat.2013.04.029.
[242] N. Jia, D. Raabe, X. Zhao, Texture and microstructure evolution during non-crystallographic shear banding in a plane strain compressed Cu–Ag metal matrix composite, Acta Mater. 76 (2014) 238–251, https://doi.org/10.1016/j.actamat.2014.05.036.
[243] T. Leffers, R.K. Ray, The brass-type texture and its deviation from the copper-type texture, Prog. Mater. Sci. 54 (3) (2009) 351–396, https://doi.org/10.1016/j.pmatsci.2008.09.002.
[244] S. Ohsaki, S. Kato, N. Tsuji, T. Ohkubo, K. Hono, Bulk mechanical alloying of Cu–Ag and Cu/Zr two-phase microstructures by accumulative roll-bonding process, Acta Mater. 55 (8) (2007) 2885–2895, https://doi.org/10.1016/j.actamat.2006.12.027.
[245] D. Tromans, Elastic anisotropy of hcp metal crystals and polycrystals, Int. J. Res. Rev. Appl. Sci. 6 (4) (2011) 462–483 http://www.arpapress.com/volumes/vol6issue4/ijrras_6_4_14.pdf.
[246] S.R. Agnew, D. Brown, C.N. Tomé, Validating a polycrystal model for the

elastoplastic response of magnesium alloy AZ31 using in situ neutron diffraction, Acta Mater. 54 (18) (2006) 4841–4852, https://doi.org/10.1016/j.actamat.2006.06.020.
[247] S.R. Agnew, J.A. Horton, T.M. Lillo, D.W. Brown, Enhanced ductility in strongly textured magnesium produced by equal channel angular processing, Scripta Mater. 50 (3) (2004) 377–381, https://doi.org/10.1016/j.scriptamat.2003.10.006.
[248] J. Bohlen, M.R. Nürnberg, J.W. Senn, D. Letzig, S.R. Agnew, The texture and anisotropy of magnesium–zinc–rare earth alloy sheets, Acta Mater. 55 (6) (2007) 2101–2112, https://doi.org/10.1016/j.actamat.2006.11.013.
[249] S. Sandlöbes, M. Friák, S. Zaefferer, A. Dick, S. Yi, D. Letzig, Z. Pei, L-F Zhu, J. Neugebauer, D. Raabe, The relation between ductility and stacking fault energies in Mg and Mg–Y alloys, Acta Mater. 60 (6–7) (2012) 3011–3021, https://doi.org/10.1016/j.actamat.2012.02.006.
[250] S. Sandlöbes, Z. Pei, M. Friák, L-F Zhu, F. Wang, S. Zaefferer, D. Raabe, J. Neugebauer, Ductility improvement of Mg alloys by solid solution: ab initio modeling, synthesis and mechanical properties, Acta Mater. 70 (2014) 92–104, https://doi.org/10.1016/j.actamat.2014.02.011.
[251] R. von Mises, Mechanik der plastischen Formänderung von Kristallen, ZAMM – Zeitschrift für Angewandte Mathematik und Mechanik 8 (3) (1928) 161–185, https://doi.org/10.1002/zamm.19280080302.
[252] A. Akhtar, E. Teghtsoonian, Solid solution strengthening of magnesium single crystals – 1: alloying behaviour in basal slip, Acta Metal. 17 (11) (1969) 1339–1349, https://doi.org/10.1016/0001-6160(69)90151-5.
[253] A. Dumay, J-P Chateau, S. Allain, S. Migot, O. Bouaziz, Influence of addition elements on the stacking-fault energy and mechanical properties of an austenitic Fe–Mn–C steel, Mater. Sci. Eng. A 483–484 (2008) 184–187, https://doi.org/10.1016/j.msea.2006.12.170.
[254] D. Music, T. Takahashi, L. Vitos, C. Asker, I.A. Abrikosov, J.M. Schneider, Elastic properties of Fe–Mn random alloys studied by ab initio calculations, Appl. Phys. Lett. 91 (19) (2007), https://doi.org/10.1063/1.2807677.
[255] R.M. Martin, Relation between elastic tensors of wurtzite and zinc-blende structure materials, Phys. Rev. B 6 (12) (1972) 4546–4553, https://doi.org/10.1103/PhysRevB.6.4546.
[256] E.R. Fuller, W.F. Weston, Relation between elastic-constant tensors of hexagonal and cubic structures, J. Appl. Phys. 45 (9) (1974) 3772–3776, https://doi.org/10.1063/1.1663858.
[257] A. Asghari, A. Zarei-Hanzaki, M. Eskandari, Temperature dependence of plastic deformation mechanisms in a modified transformation-twinning induced plasticity steel, Mater. Sci. Eng. A 579 (2013) 150–156, https://doi.org/10.1016/j.msea.2013.04.106.
[258] G.P.M. Leyson, L.G. Hector Jr., W.A. Curtin, Solute strengthening from first principles and application to aluminum alloys, Acta Mater. 60 (9) (2012) 3873–3884, https://doi.org/10.1016/j.actamat.2012.03.037.
[259] S. Morito, H. Tanaka, R. Konishi, T. Furuhara, T. Maki, The morphology and crystallography of lath martensite in Fe-C alloys, Acta Mater. 51 (6) (2003) 1789–1799, https://doi.org/10.1016/S1359-6454(02)00577-3.
[260] S. Morito, X. Huang, T. Furuhara, T. Maki, N. Hansen, The morphology and crystallography of lath martensite in alloy steels, Acta Mater. 54 (19) (2006) 5323–5331, https://doi.org/10.1016/j.actamat.2006.07.009.
[261] S. Morito, Y. Edamatsu, K. Ichinotani, T. Ohba, T. Hayashi, Y. Adachi, T. Furuhara, G. Miyamoto, N. Takayama, Quantitative analysis of three-dimensional morphology of martensite packets and blocks in iron-carbon-manganese steels, J. Alloys Comp. 577 (2013) S587–S592, https://doi.org/10.1016/j.jallcom.2012.02.004.
[262] L. Morsdorf, O. Jeannin, D. Barbier, M. Mitsuhara, D. Raabe, C.C. Tasan, Multiple mechanisms of lath martensite plasticity, Acta Mater. 121 (2016) 202–214, https://doi.org/10.1016/j.actamat.2016.09.006.
[263] C.C. Tasan, M. Diehl, D. Yan, M. Bechtold, F. Roters, L. Schemmann, C. Zheng, N. Peranio, D. Ponge, M. Koyama, K. Tsuzaki, D. Raabe, An overview of dual-phase steels: advances in microstructure-oriented processing and micromechanically guided design, Ann. Rev. Mater. Res. 45 (2015) 391–431, https://doi.org/10.1146/annurev-matsci-070214-021103.
[264] A. Zeghadi, F. N'guyen, S. Forest, A-F Gourgues, O. Bouaziz, Ensemble averaging stress–strain fields in polycrystalline aggregates with a constrained surface microstructure – part 1: anisotropic elastic behaviour, Philos. Magaz. 87 (8-9) (2007) 1401–1424, https://doi.org/10.1080/14786430601009509.
[265] A. Zeghadi, S. Forest, A-F Gourgues, O. Bouaziz, Ensemble averaging stress–strain fields in polycrystalline aggregates with a constrained surface microstructure – part 2: crystal plasticity, Philos. Magaz. 87 (8–9) (2007) 1425–1446, https://doi.org/10.1080/14786430601009517.
[266] D. Yan, C.C. Tasan, D. Raabe, High resolution in situ mapping of microstrain and microstructure evolution reveals damage resistance criteria in dual phase steels, Acta Mater. 96 (2015) 399–409, https://doi.org/10.1016/j.actamat.2015.05.038.
[267] M.D. Uchic, L. Holzer, B.J. Inkson, E.L. Principe, P. Munroe, Three-dimensional microstructural characterization using focused ion beam tomography, MRS Bull. 32 (5) (2007) 408–416, https://doi.org/10.1557/mrs2007.64.
[268] P.J. Konijnenberg, S. Zaefferer, S.B. Lee, A.D. Rollett, G.S. Rohrer, D. Raabe, Advanced methods and tools for reconstruction and analysis of grain boundaries from 3D-EBSD data sets, Mater. Sci. Forum 702–703 (2011) 475–478, https://doi.org/10.4028/www.scientific.net/MSF.702-703.475.
[269] L. Wang, M. Li, J. Almer, T. Bieler, R. Barabash, Microstructural characterization of polycrystalline materials by synchrotron X-rays, Front. Mater. Sci. 7 (2) (2013) 156–169, https://doi.org/10.1007/s11706-013-0201-0.
[270] N. Fujita, F. Roters, Texture evolution analysis in plate rolling by thermo-mechanical CPFEM, in: Proceedings of the 10th International Rolling Conference, 2016, 2016, pp. 1–8.
[271] T. Tomida, N. Imai, K. Miyata, S. Fukushima, M. Yoshida, M. Wakita, M. Etou, T. Sasaki, Y. Haraguchi, Y. Okada, Grain refinement of C–Mn steel to 1 μm by rapid cooling and short interval multi-pass hot rolling in stable austenite region, ISIJ Int. 48 (8) (2008) 1148–1157, https://doi.org/10.2355/isijinternational.48.1148.
[272] T. Morimoto, F. Yoshida, Y. Kusumoto, A. Yanagida, Development of recrystallization texture prediction method linking with deformation texture prediction model, ISIJ Int. 52 (4) (2012) 592–600, https://doi.org/10.2355/isijinternational.52.592.
[273] Y. Tanaka, T. Tomida, V. Mohles, Quantitative prediction of deformed austenite and transformed ferrite texture in hot-rolled steel sheet, IOP Conf. Ser.: Mater. Sci. Eng. 82 (2015) 012057, https://doi.org/10.1088/1757-899X/82/1/012057.
[274] Y. Ueda, Y. Goto, T. Yamaguchi, Y. Tomita, Y. Morita, E. Nakamachi, Two-scale thermo-crystal plasticity finite element analysis of dynamic-recrystallization texture evolution, ASME 2016 International Mechanical Engineering Congress and Exposition, (2016), https://doi.org/10.1115/IMECE2016-66437 V014T11A017.
[275] Y. Misaka, Y. Yoshimoto, Formularization of mean resistance to deformation of plain carbon steels at elevated temperature, J. Jpn. Soc. Technol. Plast. 8 (1967) 414–422.
[276] H. Vegter, Y. An, H.H. Pijlman, J. Huétink, Different approaches to describe the plastic material behaviour of steel and aluminium-alloys in sheet forming, in: J.A. Covas (Ed.), Proceedings of the 2nd ESAFORM Conference on Material Forming. Guimarães, 1999, pp. 127–132.
[277] H. Vegter, C. Ten Horn, Y. An, E. Atzema, H.H. Pijlman, A. Van Den Boogaard, J. Huétink, Characterisation and modelling of the plastic material behaviour and its application in sheet metal forming simulation, in: E. Oñate, D.R.J. Owen (Eds.), Proceedings of the 7th International Conference on Computational Plasticity, Barcelona, 2003.
[278] H. Vegter, A.H. Van Den Boogaard, A plane stress yield function for anisotropic sheet material by interpolation of biaxial stress states, Int. J. Plast. 22 (3) (2006) 557–580, https://doi.org/10.1016/j.ijplas.2005.04.009.
[279] P.D. Wu, M. Jain, J. Savoie, S.R. MacEwen, P. Tuğcu, K.W. Neale, Evaluation of anisotropic yield functions for aluminum sheets, Int. J. Plast. 19 (1) (2003) 121–138, https://doi.org/10.1016/S0749-6419(01)00033-X.
[280] F. Barlat, D.J. Lege, J.C. Brem, A six-component yield function for anisotropic materials, Int. J. Plast. 7 (7) (1991) 693–712, https://doi.org/10.1016/0749-6419(91)90052-Z.
[281] F. Barlat, J.C. Brem, J.W. Yoon, K. Chung, R.E. Dick, D.J. Lege, F. Pourboghrat, S-H Choi, E. Chu, Plane stress yield function for aluminum alloy sheets—part 1: theory, Int. J. Plast. 19 (9) (2003) 1297–1319, https://doi.org/10.1016/S0749-6419(02)00019-0.
[282] F. Barlat, H. Aretz, J.W. Yoon, M.E. Karabin, J.C. Brem, R.E. Dick, Linear transfomation-based anisotropic yield functions, Int. J. Plast. 21 (5) (2005) 1009–1039, https://doi.org/10.1016/j.ijplas.2004.06.004.
[283] H. Aretz, J. Aegerter, O. Engler, F. Barlat, Y.H. Moon, M.G. Lee, Analysis of earing in deep drawn cups, in: Proceedings of the 10th International Conference on Numerical Methods in Industrial Forming Processes, 2010, pp. 417–424, https://doi.org/10.1063/1.3457585.
[284] R. Hill, A theory of the yielding and plastic flow of anisotropic metals, Proc. R. Soc. A: Math., Phys. Eng. Sci. 193 (1033) (1948) 281–297, https://doi.org/10.1098/rspa.1948.0045.
[285] D.D. Tjahjanto, P. Eisenlohr, F. Roters, Multiscale deep drawing analysis of dual-phase steels using grain cluster-based RGC scheme, Model. Simul. Mater. Sci. Eng. 23 (2015) 045005, https://doi.org/10.1088/0965-0393/23/4/045005.
[286] T. Hochrainer, S. Sandfeld, M. Zaiser, P. Gumbsch, Continuum dislocation dynamics: towards a physical theory of crystal plasticity, J. Mech. Phys. Solids 63 (2014) 167–178, https://doi.org/10.1016/j.jmps.2013.09.012.
[287] T. Hochrainer, Multipole expansion of continuum dislocations dynamics in terms of alignment tensors, Philos. Magaz. 95 (12) (2015) 1321–1367, https://doi.org/10.1080/14786435.2015.1026297.
[288] A. Ebrahimi, M. Monavari, T. Hochrainer, Numerical implementation of continuum dislocation dynamics with the discontinuous-Galerkin method, MRS Proc. 1651 (2014), https://doi.org/10.1557/opl.2014.26.
[289] T. Hochrainer, Thermodynamically consistent continuum dislocation dynamics, J. Mech. Phys. Solids 88 (2016) 12–22, https://doi.org/10.1016/j.jmps.2015.12.015.
[290] A. Ebrahimi, T. Hochrainer, Three-dimensional continuum dislocation dynamics simulations of dislocation structure evolution in bending of a micro-beam, MRS Adv. 1 (24) (2016) 1791–1796, https://doi.org/10.1557/adv.2016.75.
[291] R.E. Jones, J.A. Zimmerman, G. Po, Comparison of dislocation density tensor fields derived from discrete dislocation dynamics and crystal plasticity simulations of torsion, J. Mater. Sci. Res. 5 (4) (2016) 44–62, https://doi.org/10.5539/jmsr.v5n4p44.
[292] J. Senger, D. Weygand, O. Kraft, P. Gumbsch, Dislocation microstructure evolution in cyclically twisted microsamples: a discrete dislocation dynamics simulation, Model. Simul. Mater. Sci. Eng. 19 (7) (2011) 074004, https://doi.org/10.1088/0965-0393/19/7/074004.
[293] H. Mughrabi. Microscopic mechanisms of metal fatigue, in: P. Haasen, V. Gerold, G. Kostorz (Eds.), Proceedings of the 5th International Conference on the Strength of Metals and Alloys (ICSMA 5), Pergamon Press, Oxford, 1980, pp. 1615–1633.
[294] N. Grilli, Constitutive Modeling for Crystal Plasticity Finite Element Computation of Cyclic Plasticity in Fatigue, PhD thesis, École polytechnique fédérale de Lausanne, Lausanne, 2016, https://doi.org/10.5075/epfl-thesis-7251.
[295] L.P. Kubin, Dislocation patterning, in: R.W. Cahn, P. Haasen, E.J. Kramer (Eds.), Materials Science and Technology, Wiley-VCH, Weinheim, 2006, , https://doi.

org/10.1002/9783527603978.mst0051.
[296] Y. Estrin, H. Braasch, Y. Brechet, A dislocation density based constitutive model for cyclic deformation, J. Eng. Mater. Technol. 118 (4) (1996) 441, https://doi.org/10.1115/1.2805940.
[297] N. Grilli, K.G.F. Janssens, H. Van Swygenhoven, Crystal plasticity finite element modelling of low cycle fatigue in fcc metals, J. Mech. Phys. Solids 84 (2015) 424–435, https://doi.org/10.1016/j.jmps.2015.08.007.
[298] U. Messerschmidt, M. Bartsch, Generation of dislocations during plastic deformation, Mater. Chem. Phys. 81 (2–3) (2003) 518–523, https://doi.org/10.1016/S0254-0584(03)00064-6.
[299] B. Escaig, Sur le glissement dévié des dislocations dans la structure cubique a faces centrées, J. Physique 29 (2–3) (1968) 225–239, https://doi.org/10.1051/jphys:01968002902-3022500.
[300] M. Sauzay, L.P. Kubin, Scaling laws for dislocation microstructures in monotonic and cyclic deformation of fcc metals, Prog. Mater. Sci. 56 (6) (2011) 725–784, https://doi.org/10.1016/j.pmatsci.2011.01.006.
[301] L. Buchinger, S. Stanzl, C. Laird, Dislocation structures in copper single crystals fatigued at low amplitudes, Philos. Magaz. A 50 (2) (1985) 275–298, https://doi.org/10.1080/01418618408244227.
[302] N. Grilli, K.G.F. Janssens, J. Nellessen, S. Sandlöbes, D. Raabe, Multiple slip dislocation patterning in a dislocation-based crystal plasticity finite element method, Int. J. Plast. 100 (2017) 104–121, https://doi.org/10.1016/j.ijplas.2017.09.015.
[303] M. Stricker, Die Übertragung von mikrostrukturellen Eigenschaften aus der diskreten Versetzungsdynamik in Kontinuumsbeschreibungen, PhD thesis, Karlsruher Institut für Technologie (KIT), Karlsruhe, 2017, https://doi.org/10.5445/IR/1000067987.
[304] P. Franciosi, M. Berveiller, A. Zaoui, Latent hardening in copper and aluminium single crystals, Acta Metal. 28 (3) (1980) 273–283, https://doi.org/10.1016/0001-6160(80)90162-5.
[305] B. Devincre, T. Hoc, L. Kubin, Dislocation mean free paths and strain hardening of crystals, Science 320 (5884) (2008) 1745–1748, https://doi.org/10.1126/science.1156101.
[306] D. Weygand, Mechanics and dislocation structures at the micro-scale: insights on dislocation multiplication mechanisms from discrete dislocation dynamics simulations, MRS Proc. 1651 (2014), https://doi.org/10.1557/opl.2014.362.
[307] M. Stricker, D. Weygand, Dislocation multiplication mechanisms – Glissile junctions and their role on the plastic deformation at the microscale, Acta Mater. 99 (2015) 130–139, https://doi.org/10.1016/j.actamat.2015.07.073.
[308] D. Weygand, L.H. Friedman, E. Van der Giessen, A. Needleman, Aspects of boundary-value problem solutions with three-dimensional dislocation dynamics, Model. Simul. Mater. Sci. Eng. 10 (4) (2002) 437–468, https://doi.org/10.1088/0965-0393/10/4/306.
[309] D. Weygand, P. Gumbsch, Study of dislocation reactions and rearrangements under different loading conditions, Mater. Sci. Eng. A 400–401 (2005) 158–161, https://doi.org/10.1016/j.msea.2005.03.102.
[310] D. Weygand, J. Senger, C. Motz, W. Augustin, V. Heuveline, P. Gumbsch, High performance computing and discrete dislocation dynamics: plasticity of micrometer sized specimens, in: W.E. Nagel, D.B. Kröner, M.M. Resch (Eds.), High Performance Computing in Science and Engineering'08, Springer, Berlin, 978-3-540-88301-2, 2009, pp. 507–523, , https://doi.org/10.1007/978-3-540-88303-6_36.
[311] T. Smorodin, J. Wilde, P. Alpern, M. Stecher, A temperature-gradient-induced failure mechanism in metallization under fast thermal cycling, IEEE Trans. Dev. Mater. Reliab. 8 (3) (2008) 590–599, https://doi.org/10.1109/TDMR.2008.2002359.
[312] F. Meier, C. Schwarz, E. Werner, Crystal-plasticity based thermo-mechanical modeling of Al-components in integrated circuits, Comput. Mater. Sci. 94 (2014) 122–131, https://doi.org/10.1016/j.commatsci.2014.03.020.
[313] F. Meier, E. Werner, Application of crystal plasticity in the field of microelectronics, Oberwolfach Rep. 13 (1) (2016) 835–838, https://doi.org/10.4171/Owr/2016/17.
[314] W. Kanert, Reliability challenges for power devices under active cycling, in: 2009 IEEE International Reliability Physics Symposium, 2009, pp. 409–415, https://doi.org/10.1109/IRPS.2009.5173288.
[315] E. Werner, R. Wesenjak, A. Fillafer, F. Meier, C. Krempaszky, Microstructure-based modelling of multiphase materials and complex structures, Contin. Mech. Thermodyn. 28 (5) (2016) 1325–1346, https://doi.org/10.1007/s00161-015-0477-7.
[316] S. Nikolov, M. Petrov, L. Lymperakis, M. Friák, C. Sachs, H-O Fabritius, D. Raabe, J. Neugebauer, Revealing the design principles of high-performance biological composites using ab initio and multiscale simulations: the example of lobster cuticle, Adv. Mater. 22 (4) (2010) 519–526, https://doi.org/10.1002/adma.200902019.
[317] S. Nikolov, H. Fabritius, M. Friák, D. Raabe, Integrated multiscale modeling approach for hierarchical biological nanocomposites applied to lobster cuticle, Bulg. Chem. Commun. 47 (Special Issue B) (2015) 423–432 http://bcc.bas.bg/BCC_Volumes/Volume_47_Special_B_2015/BCC-47-SI-B-60.pdf.
[318] H-O Fabritius, C. Sachs, P.R. Triguero, D. Raabe, Influence of structural principles on the mechanics of a biological fiber-based composite material with hierarchical organization: the exoskeleton of the lobster *Homarus americanus*, Adv. Mater. 21 (4) (2009) 391–400, https://doi.org/10.1002/adma.200801219.
[319] P. Fratzl, R. Weinkamer, Nature's hierarchical materials, Prog. Mater. Sci. 52 (8) (2007) 1263–1334, https://doi.org/10.1016/j.pmatsci.2007.06.001.
[320] M.J. Buehler, Nanomechanics of collagen fibrils under varying cross-link densities: Atomistic and continuum studies, J. Mech. Behav. Biomed. Mater. 1 (1) (2008) 59–67, https://doi.org/10.1016/j.jmbbm.2007.04.001.
[321] M-M Giraud-Guille, Plywood structures in nature, Curr. Opin. Solid State Mater. Sci. 3 (3) (1988) 221–227, https://doi.org/10.1016/S1359-0286(98)80094-6.
[322] N.F. Hadley, The arthropod cuticle, Sci. Am. 255 (1) (1986) 104–112, https://doi.org/10.1038/scientificamerican0786-104.
[323] D. Raabe, P. Romano, C. Sachs, H. Fabritius, A. Al-Sawalmih, S-B Yi, G. Servos, H.G. Hartwig, Microstructure and crystallographic texture of the chitin–protein network in the biological composite material of the exoskeleton of the lobster Homarus americanus, Mater. Sci. Eng. A 421 (1–2) (2006) 143–153, https://doi.org/10.1016/j.msea.2005.09.115.
[324] H-O Fabritius, E.S. Karsten, K. Balasundaram, S. Hild, K. Huemer, D. Raabe, Correlation of structure, composition and local mechanical properties in the dorsal carapace of the edible crab Cancer pagurus, Zeitschrift für Kristallographie – Crystal. Mater. 227 (11) (2012) 766–776, https://doi.org/10.1524/zkri.2012.1532.
[325] A. Al-Sawalmih, C. Li, S. Siegel, H. Fabritius, S. Yi, D. Raabe, P. Fratzl, O. Paris, Microtexture and chitin/calcite orientation relationship in the mineralized exoskeleton of the American lobster, Adv. Funct. Mater. 18 (20) (2008) 3307–3314, https://doi.org/10.1002/adfm.200800520.
[326] F. Boßelmann, P. Romano, H. Fabritius, D. Raabe, M. Epple, The composition of the exoskeleton of two crustacea: the American lobster *Homarus americanus* and the edible crab *Cancer pagurus*, Thermochim. Acta 463 (1–2) (2007) 65–68, https://doi.org/10.1016/j.tca.2007.07.018.
[327] H. Fabritius, C. Sachs, D. Raabe, S. Nikolov, M. Friák, J. Neugebauer, Chitin: Formation and Diagenesis, Chapter Chitin in the Exoskeletons of Arthropoda: From Ancient Design to Novel Materials Science, vol. 34, Springer, Dordrecht, 2011, pp. 35–60. ISBN 978-90-481-9683-8, https://doi.org/10.1007/978-90-481-9684-5_2.
[328] H-O Fabritius, A. Ziegler, M. Friák, S. Nikolov, J. Huber, B.H.M. Seidl, S. Ruangchai, F.I. Alagboso, S. Karsten, J. Lu, A.M. Janus, M. Petrov, L-F Zhu, P. Hemzalová, S. Hild, D. Raabe, J. Neugebauer, Functional adaptation of crustacean exoskeletal elements through structural and compositional diversity: a combined experimental and theoretical study, Bioinsp. Biomimet. 11 (5) (2016) 055006, https://doi.org/10.1088/1748-3190/11/5/055006.
[329] C. Sachs, H. Fabritius, D. Raabe, Experimental investigation of the elastic–plastic deformation of mineralized lobster cuticle by digital image correlation, J. Struct. Biol. 155 (3) (2006) 409–425, https://doi.org/10.1016/j.jsb.2006.06.004.
[330] C. Sachs, H. Fabritius, D. Raabe, Hardness and elastic properties of dehydrated cuticle from the lobster *Homarus americanus* obtained by nanoindentation, J. Mater. Res. 21 (08) (2006) 1987–1995, https://doi.org/10.1557/jmr.2006.0241.
[331] C. Sachs, H. Fabritius, D. Raabe, Influence of microstructure on deformation anisotropy of mineralized cuticle from the lobster *Homarus americanus*, J. Struct. Biol. 161 (2) (2008) 120–132, https://doi.org/10.1016/j.jsb.2007.09.022.
[332] S. Nikolov, H. Fabritius, M. Petrov, M. Friák, L. Lymperakis, C. Sachs, D. Raabe, J. Neugebauer, Robustness and optimal use of design principles of arthropod exoskeletons studied by ab initio-based multiscale simulations, J. Mech. Behav. Biomed. Mater. 4 (2) (2011) 129–145, https://doi.org/10.1016/j.jmbbm.2010.09.015.
[333] M. Friák, H-O Fabritius, S. Nikolov, M. Petrov, L. Lymperakis, C. Sachs, P. Elstnerová, J. Neugebauer, D. Raabe, Multi-scale modelling of a biological material: the arthropod exoskeleton, in: P. Fratzl, J.W.C. Dunlop, R. Weinkamer (Eds.), Materials Design Inspired by Nature: Function Through Inner Architecture, Royal Society of Chemistry, Cambridge, 2013, pp. 197–218, https://doi.org/10.1039/9781849737555-00197.
[334] M. Friák, L.F. Zhu, L. Lymperakis, H. Titrian, U. Aydin, A.M. Janus, H.O. Fabritius, A. Ziegler, S. Nikolov, P. Hemzalová, D. Raabe, J. Neugebauer, Quantum-mechanical study of single-crystalline and polycrystalline elastic properties of Mg-substituted calcite crystals, Key Eng. Mater. 592–593 (2013) 335–341, https://doi.org/10.4028/www.scientific.net/KEM.592-593.335.
[335] M. Petrov, L. Lymperakis, M. Friák, J. Neugebauer, Ab initio based conformational study of the crystalline α-chitin, Biopolymers 99 (1) (2012) 22–34, https://doi.org/10.1002/bip.22131.
[336] Z. Střelcová, P. Kulhánek, M. Friák, H-O Fabritius, M. Petrov, J. Neugebauer, J. Koča, The structure and dynamics of chitin nanofibrils in an aqueous environment revealed by molecular dynamics simulations, RSC Adv. 6 (36) (2016) 30710–30721, https://doi.org/10.1039/C6RA00107F.
[337] L-F Zhu, M. Friák, L. Lymperakis, H. Titrian, U. Aydin, A.M. Janus, H-O Fabritius, A. Ziegler, S. Nikolov, P. Hemzalová, D. Raabe, J. Neugebauer, Ab initio study of single-crystalline and polycrystalline elastic properties of Mg-substituted calcite crystals, J. Mech. Behav. Biomed. Mater. 20 (2013) 296–304, https://doi.org/10.1016/j.jmbbm.2013.01.030.
[338] T. Mori, K. Tanaka, Average stress in matrix and average elastic energy of materials with misfitting inclusions, Acta Metal. 21 (5) (1973) 571–574, https://doi.org/10.1016/0001-6160(73)90064-3.
[339] S. Torquato, Effective stiffness tensor of composite media: II. Applications to isotropic dispersions, J. Mech. Phys. Solids 46 (8) (1998) 1411–1440, https://doi.org/10.1016/S0022-5096(97)00083-5.
[340] S. Torquato, Random Heterogeneous Materials: Microstructure and Macroscopic Properties, Interdisciplinary Applied Mathematics vol. 16, Springer, New York, 978-0-387-95167-6, 2002, https://doi.org/10.1007/978-1-4757-6355-3.
[341] C. Sachs, Microstructure and Mechanical Properties of the Exoskeleton of the Lobster *Homarus americanus* as an Example of a Biological Composite Material, PhD thesis, RWTH Aachen, Aachen, 2008 http://publications.rwth-aachen.de/record/50251/files/Sachs_Christoph.pdf.
[342] R. Quey, P.R. Dawson, F. Barbe, Large-scale 3D random polycrystals for the finite element method: generation, meshing and remeshing, Comp. Meth. Appl. Mech. Eng. 200 (17–20) (2011) 1729–1745, https://doi.org/10.1016/j.cma.2011.01.

002.
[343] C. Geuzaine, J-F Remacle, Gmsh: a 3-D finite element mesh generator with built-in pre- and post-processing facilities, Int. J. Numer. Meth. Eng. 79 (11) (2009) 1309–1331, https://doi.org/10.1002/nme.2579.
[344] F. Fritzen, T. Böhlke, E. Schnack, Periodic three-dimensional mesh generation for crystalline aggregates based on Voronoi tessellations, Comput. Mech. 43 (5) (2009) 701–713, https://doi.org/10.1007/s00466-008-0339-2.
[345] F. Bachmann, R. Hielscher, H. Schaeben, Texture analysis with MTEX – free and open source software toolbox, Solid State Phenom. 160 (2010) 63–68, https://doi.org/10.4028/www.scientific.net/SSP.160.63.
[346] F. Bachmann, R. Hielscher, H. Schaeben, Grain detection from 2D and 3D EBSD data—specification of the MTEX algorithm, Ultramicroscopy 111 (12) (2011) 1720–1733, https://doi.org/10.1016/j.ultramic.2011.08.002.
[347] J.D. Hunter, Matplotlib: a 2D graphics environment, Comput. Sci. Eng. 9 (3) (2007) 90–95, https://doi.org/10.1109/Mcse.2007.55.
[348] W. Schroeder, K. Martin, B. Lorensen, The Visualization Toolkit, Kitware, forth ed., 2006. ISBN 978-1-930934-19-1.
[349] K. Moreland, Diverging color maps for scientific visualization, in: G. Bebis, R. Boyle, B. Parvin, D. Koracin, Y. Kuno, J. Wang, R. Pajarola, P. Lindstrom, A. Hinkenjann, M.L. Encarnação, C.T. Silva, D. Coming (Eds.), Proceedings of the 5th International Symposium on Visual Computing, 2009, pp. 92–103, , https://doi.org/10.1007/978-3-642-10520-3_9.
[350] T.W.J. De Geus, R.H.J. Peerlings, M.G.D. Geers, Microstructural topology effects on the onset of ductile failure in multi-phase materials: a systematic computational approach, Int. J. Solids Struct. 67–68 (2015) 326–339, https://doi.org/10.1016/j.ijsolstr.2015.04.035.
[351] A. Saeed-Akbari, L. Mosecker, A. Schwedt, W. Bleck, Characterization and prediction of flow behavior in high-manganese twinning induced plasticity steels: part I. Mechanism maps and work-hardening behavior, Metal. Mater. Trans. A 43 (5) (2012) 1688–1704, https://doi.org/10.1007/s11661-011-0993-4.
[352] S.R. Kalidindi, M. De Graef, Materials data science: current status and future outlook, Ann. Rev. Mater. Res. 45 (1) (2015) 171–193, https://doi.org/10.1146/annurev-matsci-070214-020844.
[353] R. Pokharel, J. Lind, S.F. Li, P. Kenesei, R.A. Lebensohn, R.M. Suter, A.D. Rollett, In-situ observation of bulk 3D grain evolution during plastic deformation in polycrystalline Cu, Int. J. Plast. 67 (2015) 217–234, https://doi.org/10.1016/j.ijplas.2014.10.013.
[354] B. Svendsen, P. Shanthraj, D. Raabe, Finite-deformation phase-field chemomechanics for multiphase, multicomponent solids, J. Mech. Phys. Solids 112 (2017) 619–636, https://doi.org/10.1016/j.jmps.2017.10.005.
[355] R. Darvishi Kamachali, C. Schwarze, M. Lin, M. Diehl, P. Shanthraj, U. Prahl, I. Steinbach, D. Raabe, Numerical benchmark of phase-field simulations with elastic strains: precipitation under chemo–mechanical coupling, Comput. Mater. Sci. 155 (2018) 541–553, https://doi.org/10.1016/j.commatsci.2018.09.011.
[356] M. Diehl, P. Eisenlohr, C. Zhang, J. Nastola, P. Shanthraj, F. Roters, A flexible and efficient output file format for grain-scale multiphysics simulations, Integ. Mater. Manuf. Innov. 6 (1) (2017) 83–91, https://doi.org/10.1007/s40192-017-0084-5.
[357] G.J. Schmitz, Microstructure modeling in integrated computational materials engineering (ICME) settings: can HDF5 provide the basis for an emerging standard for describing microstructures? JOM 68 (1) (2016) 77–83, https://doi.org/10.1007/s11837-015-1748-2.